DURBAN UNIVERSITY OF TECHNOLOGY
INYUVESI YASETHEKWINI YEZOBUCHWEPHESHE

ELECTROCHEMICAL APTASENSOR FOR THE DETECTION OF MYCOTOXINS IN FOOD SAMPLES BY EXPERIMENTAL AND COMPUTATIONAL METHODS

Kwanele Kunene

(Reg. No: 20803990)

Submitted in fulfillment of the requirements of the degree of Doctor of Philosophy in Chemistry in the Faculty of Applied Sciences at the Durban University of Technology

August 2021

DECLARATION

I, **Kwanele Kunene** declare that the thesis submitted for the degree of Doctor of Philosophy Science in Chemistry at the Durban University of Technology is the result of my own investigation and has not been accepted nor submitted by me or anyone else for any degree. The work in its totality was done by me.

Student Name: Kwanele Kunene

Student Signature: Date:.13./…08…../…2021

Supervisor Name: Professor K. Bisetty

Signature: …… Date:.17./…08…/…2021

Co-Supervisor Name: Dr. S Kanchi

Signature: Date:.15./…08…../…2021

Co-Supervisor Name: Dr. M Sabela

Signature: Date:.15./…08…../…2021…

DEDICATION

This thesis is dedicated to late Madoda Kunene and the late Makubheka "NtombikamaZwane" Kunene. I feel blessed, having been born and raised by you. I believe I am destined to achieve more good in life with all the lessons and love you gave to me and my beloved siblings.

ACKNOWLEDGEMENTS

"The *future belongs to those who believe in the beauty of their dreams". - Eleanor Roosevelt*

I would like to express my deep and sincere appreciation to my mentors **Prof. Krishna Bisetty** and **Dr. Mikhael Bechelany** for their expertise, kindness, guidance, perseverance, and optimism which helped a lot in instilling confidence in me. I honestly thank them for continuously orienting me in the correct research path and guiding me to write this dissertation through their persistent encouragement and guidance. They were very demonstrative and were prepared to help me even in the midst of their hectic schedule and without their supervision this dissertation would have been a distant possibility. I am very grateful to my co-supervisors **Dr. Myalowenkosi Sabela** and **Dr. Suvardhan Kanchi** for providing a welcoming and supportive atmosphere at work and valuable advice and perceptive remarks on my work. I am very grateful to my second family at the European Institute of Membranes for their guidance and supervision, especially to Dr. Matthieu Weber, Dr. Damien Voiry, and Dr. Yaovi Holade. I would like to thank Mrs. Mavis Xhakaza who have motivated and assisted me countless times throughout my project. I have received a generous support from the Computational Modelling and BioAnalytical Chemistry (CMBAC) group. The group has been a source of friendship, laughter, advice, and partnerships. I am forever grateful to my family and friends, **Nokalika, Nomathemba, Minister, Laree, Maneliza**, **Mandla**, who have never left my corner with every decision I have taken in my life. I would be negligent if I don't thank **Londie**, who deserve credit for providing much needed support with administrative tasks, reminding me of imminent deadlines. A very special word of thanks goes for my twin sister, **Dasie**, who have been great over the years and never raised an eyebrow when I claimed my dissertation would be completed 'in the next two weeks' for nearly a year. I am sincerely grateful to my son, **Zosukumizizwezonke** for being patient and understanding that I sometimes needed to spend extended time away from home. May he grow to be wise and respectful men. To my dear sister, **Mbali**, I am deeply grateful for your continued support of my dreams and for holding the fort while I was away on research visits. Thank you **Lethukuthula** for being always there for me throughout the journey and for providing emotional support. My appreciation also

goes out to Prof. **Theophilus Andrew** for he's encouragements and support through my studies. Some special words of appreciation go to: Zenande, Qamfuza, Thabiso, Nomakhephu, Gugu, Nonhlanhla, Dr. Thokozane Xaba, Yusuf Mia, Nondumiso Mathonsi, Njabulo Kudla, Cecil, Noxolo, Thobile, Phumezi, Msheshana, Khathide, Nazym, Mahmoud, Pelagie, and Queen who have constantly been a main source of support when things would get a bit depressing, thank you guys for always being there for me.

I owe my thanks to the Council of Scientific and Industrial Research (CSIR) and French Embassy scholarship for the fellowship. I bow my head in humility to izinyanya zasemaNtimandeni and Lord for giving me the knowledge to complete the work and guiding me all through my life.

ABSTRACT

Mycotoxins are secondary metabolites of fungi that are present in various foodstuff and feed commodities. A large number of mycotoxins exist, however only a limited number represent a major damages and toxic properties. Amongst them, the aflatoxins and ochratoxins are deemed to be the most poisonous and extensively circulated in the world and then, represent a real hazard to both human and animal. Depending on several factors like the consumption levels, exposure time, mechanisms of action, digestion and defense mechanisms, mycotoxins stimulate a wide spectrum of toxicological effects leading to both acute and chronic diseases, liver and kidney failure, skin rash, cancer, immune suppression, birth defects or even death.

To address the harmful impact of mycotoxin contaminants in food and feed, health authorities in various countries world-wide have established guidelines in order to protect human and animal from the possible damages instigated by these toxins. Authorities such as the European Commission, US Food and Drug Administration (FDA), World Health Organization (WHO) and the Food and Agriculture Organization of the United Nations (FAO) set up maximum level regulations for main mycotoxins in foods and feeds. To accomplish the expectations of these regulation levels, there is a great need for the development and validation of modern, uncomplicated, rapid, and detailed methodologies for the detection of toxins.

In this study, various approaches for the rapid, inexpensive and ultrasensitive biosensors for the detection of two major mycotoxins were developed. The electrochemical-based aptasensor and immunosensor were developed for the determination of aflatoxin B_1 (AFB_1) and ochratoxin A (OTA) in different food products. The fabricated biosensors demonstrated good practical analytical feasibility for mycotoxins detection in real samples such as Weet-Bix, yoghurt, coffee and in wine samples with excellent recoveries and RSD values. To avoid fouling on the sensor surface by the constituents present in real samples, the carbon screen printed electrode (C-SPE) and carbon felt electrode (CFE) surfaces were modified with different nanomaterials such as silver nanoparticle (AgNPs), palladium nanoparticles (PdNPs), palladium doped boron nitride (PdNPs-BN) and titanium nanoparticles doped with boron nitride BN-TiO_2. In addition, the aptamers and antibodies were immobilized on the

modified electrode in order to enhance the selectivity of the sensor towards the detection of OTA and AFB_1.

The electrochemical aptasensor for OTA permitted for highly sensitive detection in Weet-Bix with a wide linear range (0.002 - 0.016 mg L^{-1}) and limit of detection of 7×10^{-4} mg L^{-1}. It is worth prominence that it is the first time that carbon screen printed electrode (C-SPE) modified with AgNPs was used, opening new pathways for highly precise analysis. Experimental results were further supported computationally for a better understanding of the interaction between the aptamer and the analytes. Computational results were in good agreement with experimental results. The same procedure was also established in voltammetric detection of AFB_1 using CFE modified with BN-TiO_2 (CF/BN-TiO_2). A wide concentration range of 2.5 - 20 ng mL^{-1} with an excellent LOD of 0.002 ng mL^{-1} for AFB_1 was obtained. For the case study of wine samples tested for AFB_1 detection, a simple but very effective pretreatment method was effectively applied. The addition of acetonitrile to the wine reduces the non-specific interactions that might be accountable for inactivation of antibody and blocking of the sensor surface. Furthermore, the PdNPs-BN enhanced the electrical signal and the sensor sensitivity. Attained results allowed for AFB_1 detection at concentrations range from 1.0 - 10 ng mL^{-1} with limit of detection of 0.832 ng mL^{-1}. In the case study of the electrochemical immunosensor for the detection of OTA in coffee, a linear detection range of 0.5 - 20 ng mL^{-1} was achieved with LOD of 0.096 ng mL^{-1}.

The fabricated aptasensors and immunosensors in this study combines the most desirable characteristics of a good biosensor such as high sensitivity, inexpensive, rapid, and simple but portable method make proposed approaches an important and very promising tools for extensive biosensing applications.

TABLE OF CONTENTS

LIST OF FIGURES

LIST OF TABLES

LIST OF SCHEMES

LIST OF ACRONYMS AND SYMBOLS

AFB_1	Aflatoxin B_1
AL	Adsorption locator
AFM_1	Aflatoxin M_1
AFM	Atomic force microscope
ALD	Atomic layer deposition
ACN	Acetonitrile
AgNPs	Silver nanoparticles
ATR	Attenuated total reflectance
BO	Born oppenheimer
BN	Boron nitride
BN-TiO_2	Titanium dioxide nanoparticles doped boron nitride
BSA	Bovine serum albumin
CA	Continuous assessment
CE	Capillary electrophoresis
CE	Counter electrode
C-SPE	Carbon screen printed electrode
CFE	Carbon felts electrode
CV	Cyclic voltammetry
CS	Chitosan

DPV	Differential pulsed voltammetry
DC	Direct current
DLS	Dynamic light scattering
DFT	Density functional theory
DFF	Dreiding force field
EDC	N-ethyl-N-(3-dimethylaminopropyl carbodimide
EIS	Electrochemical impedance spectroscopy
ELISA	Enzyme linked immunosorbent assays
FFF	Field flow fractionation
FF	Force field
FDA	Food and drug administration
FAO	Food and agriculture organization
GC	Gas chromatography
GC-MS	Gas chromatography mass spectroscopy
GPU	Graphic processing unit
GO	Graphene oxide
HF	Hartree Fock
HOMO	Highest occupied molecular orbital
HPLC	High performance liquid chromatography
HRTEM	High resolution transmission electron microscope

IARC	International agency research on cancer
LC	Liquid chromatography
LC-MS	Liquid chromatography mass spectroscopy
LOD	Limit of detection
LSV	Linear sweep voltammetry
LUMO	Lowest unoccupied molecular orbital
MC	Monte Carlo
MD	Molecular docking
MD	Molecular dynamic
MS	Materials studio
NMR	Nuclear magnetic resonance
NPV	Normal pulse voltammetry
NHS	N-hydroxysuccinimide
OTA	Ochratoxin A
PdNPs	Palladium nanoparticles
PdNPs-BN	Palladium nanoparticles grown on boron nitride film
PBS	Phosphate-buffered saline
PL	Photoluminescence
PDI	Polydispersity index
RC	Resistor capacitor

RE	Reference electrode
RSD	Relative standard deviation
rGO	Reduced graphene oxide
SA	South Africa
SCF	Self consistent field
SEM	Scanning electron microscope
SPR	Surface plasmon resonance
TEM	Transmission electron microscope
TLC	Thin layer chromatography
UFF	Universal force field
WE	Working electrode
WHO	World Health Organisation

LIST OF PUBLICATION AND CONFERENCE

Published

Kwanele Kunene, Matthieu Weber, Myalowenkosi Sabela, Damien Voiry, Suvardhan Kanchi, Krishna Bisetty**,** Mikhael Bechelany, Highly-efficient electrochemical label-free immunosensor for the detection of ochratoxin A in coffee samples, Sensors and Actuators B: Chemical, 305 (2020) 127438.

Kwanele Kunene, Myalowenkosi Sabela, Suvardhan Kanchi, Mikhael Bechelany, Krishna Bisetty, Functionalized Electrochemical Aptasensor for Sensing of Ochratoxin A in Cereals Supported by *in silico* Adsorption Studies. ACS Food Science & Technology, 2021, XXXX, XXX, XXX-XXX.

Under review

Kwanele Kunene, Syreina Sayegh, Matthieu Weber, Myalowenkosi Sabela, Damien Voiry, Igor Iatsunskyi, Emerson Coy, Suvardhan Kanchi, Krishna Bisetty, Mikhael Bechelany, Electrochemical immunosensor for detection of Aflatoxin B_1 in wine using Pd nanoparticles supported on boron nitride coated carbon felt electrode: The tool to wine industries. Biosensors and Bioelectronics, Submitted 24 August 2021

Conference

Kwanele Kunene, Myalowenkosi Sabela, Suvardhan Kanchi, Mikhael Bechelany, Krishna Bisetty, **Green Synthesis of Silver Nanoparticles using Amadumbe Extract**: Gold Workshop in Occitanie, Montpellier, France from 04-05th December 2019 in ENSCM.

CHAPTER 1: INTRODUCTION

This chapter provides a brief overview of ochratoxin A (OTA) and aflatoxin B_1 (AFB_1), as they are the most toxic mycotoxins and widely present in different food commodities. The various methods used for the detection of OTA and AFB_1 are discussed in this chapter. The aim and objectives and a brief outline of the thesis is presented in this chapter.

1.1 Background and Problem Statement

Mycotoxins are secondary metabolites produced by *Aspergillus* fungal species such as *Penecillium, Fusarium,* and *Trichoderma* that contaminate food around the world, with developing countries as the most affected (Mupunga *et al.* 2014; Tola and Kebede 2016; Zahra *et al.* 2019). They are named after the mould that produces them. For example, aflatoxins are produced by Aspergillus, while fumonisins are produced by Fusarium (Nleya, Adetunji and Mwanza 2018). Over 300 mycotoxins have been reported in the literature (Zain 2011), however aflatoxins, zearalenone, trichothecenes, fumonisins, and ochratoxins are the most toxicologically important mycotoxins. These mycotoxins possess hepatotoxic, carcinogenic, mutagenic, and teratogenic properties, as well as the ability to delay growth in both humans and animals, affecting production (Mupunga *et al.* 2014; Santos *et al.* 2019; Agriopoulou, Stamatelopoulou and Varzakas 2020c). Mycotoxins can be found as toxic compounds in feed and food, such as cereals, legumes, wine, coffee, and milk, as well as vegetables and fruits with high moisture and nutrient content (Carballo *et al.* 2018; Li *et al.* 2018; Arrúa *et al.* 2019; Dong *et al.* 2019; Kunene *et al.* 2020; Tebele *et al.* 2020). Due to their high toxicity, mycotoxins are among the most serious public health issues. Research on mycotoxins has been carried out extensively to assess their prevalence and extent in various food entities (Berthiller *et al.* 2018).

The analysis of mycotoxins in food is a critical practice for ensuring food safety and controlling health hazards posed by infected foods. Numerous detection methods for mycotoxins have been developed, chromatographic methods such as, TLC (thin layer chromatography), GC (gas chromatography) with Mass spectrometer, LC (liquid chromatography) and HPLC (high performance liquid chromatography) as the most commonly used (Casoni *et al.* 2017; Ji *et al.* 2017; Hidalgo-Ruiz *et al.* 2019; Narváez *et al.*

2020). These techniques produce reliable results, but they are time-consuming and entail extensive preparation steps. Alternative methods with high sensitivity and simplicity are therefore urgently desirable.

In order to meet these expectations, novel biosensor strategies using the aptamer and the antibodies as the bio recognition element coupled with nanostructured materials were proposed. The nanostructured materials used include silver nanoparticles (AgNPs), palladium nanoparticles (PdNPs), palladium grown on boron nitride (PdNPs-BN) and titanium nanoparticles doped with boron nitride BN-TiO_2. Although these methods, are based on different concepts and they, provide a desirable property of a good biosensor (such as sensitivity, rapidity, and so on), a thorough understanding of how they work is still needed. New, well-described and tested methods for rapid mycotoxins analysis have been developed in response to increased uncertainty in the food industry and competition within companies. The detection of different mycotoxins in food matrixes has been reported in the literature as depicted in **Table 1-1**.

Table 1-1: Biosensors for detection of OTA and AFB_1 in different food matrixes.

Biosensor	**Analyte**	**Food matrix**	**Reference**
Aptasensor	AFB_1	Wine	(Geleta, Zhao and Wang 2018a)
Aptasensor	AFB_1	Beer	(Wang, Li and Zhao 2019)
Aptasensor	AFB_1	Rice cereal	(Guo *et al.* 2014)
Aptasensor	OTA	Grain	(Zhang *et al.* 2018b)
Aptasensor	OTA	Coffee	(Liu *et al.* 2016)
Aptasensor	OTA	Rice	(Zhang *et al.* 2016a)
Immunosensor	AFB_1	Peanut	(Azri *et al.* 2018)
Immunosensor	AFB_1	Olive oil	(Yu *et al.* 2015)
Immunosensor	AFB_1	Rice	(Xu *et al.* 2014)
Immunosensor	AFB_1	Corn	(Zhang *et al.* 2016c)
Immunosensor	OTA	Coffee	(Kunene *et al.* 2020)
Immunosensor	OTA	Wine	(Prieto-Simón *et al.* 2008)
Immunosensor	OTA	Malt	(Sun *et al.* 2020)
Immunosensor	OTA	Wheat	(Ren *et al.* 2018b)

The main goal of this study is to fabricate biosensors for the detection of naturally occurring secondary metabolites, especially aflatoxin B_1 (AFB_1) and ochratoxin A (OTA), with high sensitivity and specificity, rapid, and inexpensive.

These analytes were selected for this study because they the most found mycotoxins in food and dairy products. The main aim was to fabricate biosensors that will be applied to detect these mycotoxins in different food samples.

1.2 Aim and Objectives

Aim:

This study is aimed at developing novel and selective aptasensors and immunosensor for the detection of mycotoxins (OTA and aflatoxins AFB_1) in food samples.

1.3 Objectives of the study:

- ✓ To synthesize silver and palladium nanoparticles (AgNPs, PdNPs), palladium nanoparticles grown on the thin layer of boron nitride (PdNPs-BN), titanium dioxide decorated boron nitride nanoparticles (BN-TiO_2) and graphene oxide (GO) using green synthesis (amadumbe extract), atomic layer deposition (ALD) and modified Hummer's methods.
- ✓ To characterize the synthesized nanoparticles using UV-Visible spectroscopy (UV-Vis), photoluminescence (PL), high-resolution transmission electron microscopy (HR-TEM), atomic force microscopy (AFM), liquid chromatography mass spectroscopy (LC-MS), scanning electron microscopy (SEM), attenuated total reflectance (ATR), dynamic light scattering (DLS), field-flow fractionation (FFF), electrochemical techniques such as cyclic voltammetry (CV) and electrochemical impedance spectroscopy (EIS).
- ✓ To develop an electrochemical aptasensor and immunosensor for ochratoxin (OTA) and aflatoxins (AFB_1) by immobilizing the selective aptamer or antibody onto the surface of carbon screen printed electrode (C-SPE) and carbon felts electrode (CFE) modified with nanostructured composite.
- ✓ To optimise the aptasensor/immunosensor parameters (sensitivity and selectivity) and investigate the electrochemical behaviour of mycotoxins on a bare and modified electrode (designed sensors) using the nanostructures.
- ✓ To quantify mycotoxins in different food samples using the developed aptasensor/immunosensor.

- ✓ To validate the experimental method using Monte Carlo (MC) adsorption studies to predict the binding sites or active sequences for mycotoxin targeted molecules and to assess the intermolecular interactions of the fabricated surfaces.
- ✓ To identify the oxidation/reduction sites with electron density maps by HOMO-LUMO calculations based on the implementation of density functional theory (DFT) calculations.

The thesis is divided into six chapters. Following the introduction, further chapters of the thesis are outlined below:

Chapter 2: This chapter describes the literature review of the study including a discussion of the different mycotoxin's occurrences, its toxicity and their detection using different analytical techniques. Additionally, the electrochemical immunosensor and aptasensors for the detection of mycotoxins in food samples and the synthesis of different nanoparticles are presented.

Chapter 3: This chapter deals with the theoretical principles underpinning the instruments used for experimental work. A brief overview of the theoretical aspects of the computational studies is presented. Furthermore, the equations in relation to the operation of the techniques are presented. Special attention is given to the DFT, and molecular docking as implemented within the computational methods.

Chapter 4: A description of the materials and methods used in the design of the experimental and computational study is presented in this chapter. This chapter describes the method used for the synthesis of different nanoparticles and the fabrication of aptasensor/immunosensor for the detection of ochratoxin A (OTA) and aflatoxin B_1 (AFB_1). It also gives an idea of the general procedure for the analysis of mycotoxins content in real food samples like Weet-Bix, coffee, wine, and yoghurt. For the computational work, focuses on DFT, MC adsorption studies and MD simulations.

Chapter 5: This chapter deals with the results and discussion reported in a case-study format.

Case Study 1: deals with the development of an aptasensor for the detection of OTA in Weet-Bix.

Case Study 2: an aptasensor developed for the determination of AFB_1 in yoghurt.

Case Study 3: deals with the development of an immunosensor for the detection of OTA in coffee.

Case Study 4: an immunosensor developed for the detection of AFB_1 in wine.

Chapter 6: The chapter deals with the overall summary and concluding remarks including future directions of this study.

References: This comprises a list of references used in this thesis.

1.4 Structure of the project

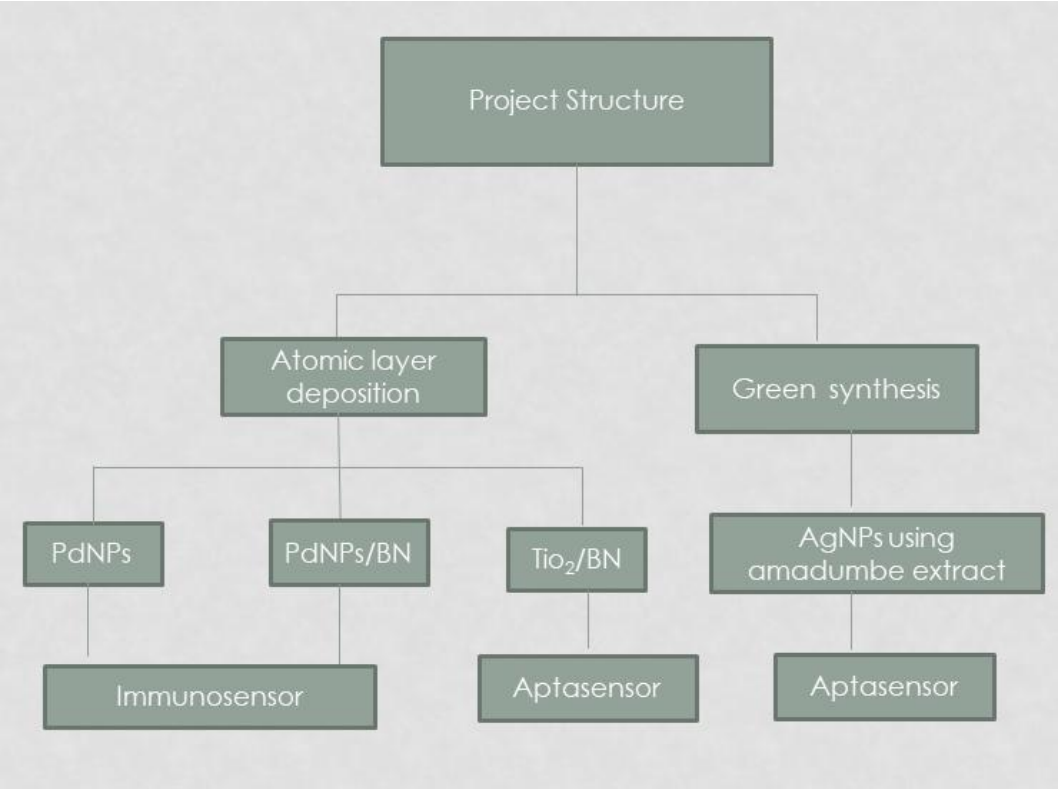

CHAPTER 2: LITERATURE REVIEW

This chapter presents an overview of the literature review of the study including a discussion of the different mycotoxin's occurrences, its toxicity and their detection using different analytical techniques. Additionally, the immunosensors and aptasensors for the detection of mycotoxins in food samples are presented, including the synthesis of different nanoparticles.

2.1 Ochratoxins

Ochratoxins are secondary metabolites that are produced by a fungal species of *Aspergillus* and *Penicillium* (Heussner and Bingle 2015; Fadlalla *et al.* 2020). The major *Penicillium* species capable of producing OTA are *P. nordicum* and *P. verrucosum* are often associated with temperate climates (El Khoury and Atoui 2010; Gil-Serna *et al.* 2018). The most toxic compound in the ochratoxin group is ochratoxin A (OTA), L-phenylalanine-*N*-[(5-chloro-3,4-dihydro-8-hydroxy-3-methyl-1-oxo-1*H*-2-benzopyrane-7-yl)carbonyl]-(*R*)-isocoumarin which is a structurally chlorinated isocoumarin compound, connected by a peptide bound to phenylalanine (**Figure 2-1**A) (Chen *et al.* 2018a; Gil-Serna *et al.* 2018). Merwe and co-workers described Ochratoxin A (OTA), after isolating a new toxic metabolite from Aspergillus ochraceus (Van der Merwe *et al.* 1965). There are a few metabolites that are similar to OTA, but they are not as significant as OTA. This includes, Ochratoxin B (OTB), the dechloro analog of OTA, and ochratoxin C (OTC), its ethyl ester, the isocoumaric derivative of OTA. These metabolites are slightly different from each other in their chemical structures and toxic potential. The general structure of these different metabolites is shown in **Figure 2-1**B, and the characteristic composition of each is shown in **Table 2-1**.

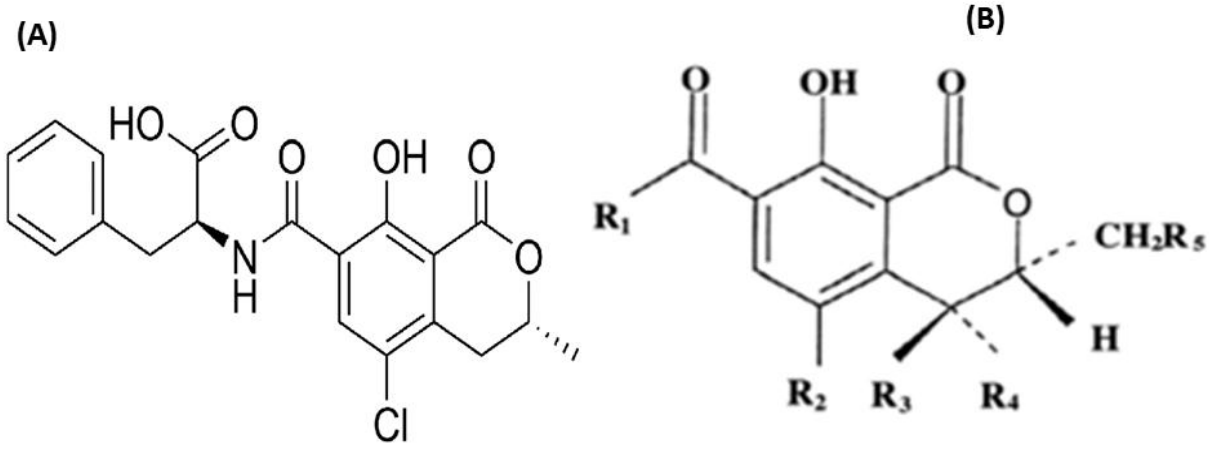

Figure 2-1: (A) Chemical structure of ochratoxin A and (B) Natural and synthetic forms of ochratoxins (Heussner and Bingle 2015; VALENTINA et al. 2016).

Table 2-1: Characteristic composition of the metabolites of ochratoxin A.

Ochratoxins	**R1**	**R2**	**R3**	**R4**	**R5**
Ochratoxin A	Phenylalanine	Cl	H	H	H
Ochratoxin B	Phenylalanine	H	H	H	H
Ochratoxin C	Ethyl-ester, phenylalanine	Cl	H	H	H

2.1.1 Properties of Ochratoxin A (OTA)

OTA is a weak organic acid with a pKa values of 3.2 for carboxyl group and 7.9 for hydroxyl group 7.1 (Kholová *et al.* 2020) with a molecular formula of $C_{20}H_{18}ClNO_6$, CAS number 303-47-9 and a molar mass of 403.8 g mol^{-1}. This crystalline structure is colorless at room temperature and displays an intense green and blue fluorescence under ultraviolet light in acidic and alkaline conditions respectively (Vieira, Cunha and Casal 2015). OTA is soluble in polar organic solvents (alcohols, ketones, chloroform) at acidic and neutral pH, slightly soluble in water, insoluble in petroleum ethers, and insoluble in saturated hydrocarbons.

When crystallized from benzene as a solvent, it has a melting point of about 90 °C. OTA is volatile in humid conditions, but stable when stored in ethanoic solutions in the dark. OTA is very stable in most food processing conditions, as a result after food products have been infected, completely extracting of this molecule is extremely difficult, which is then a safety barrier regarding food product.

2.1.2 Worldwide regulations of Ochratoxin A in products

OTA is subjected to national and international regulations due to its high toxicity in nature. In the late 1970s the OTA toxicity was less evident compared to the 1990s. The real discussion about the regulation level of OTA was carried out to place it to national or international level. More than sixty countries respected the legal regulation of OTA, however only eleven countries managed to set the allowed limits of OTA in different food products (Van Egmond 1991). Those countries includes Brazil, Czechoslovakia, Denmark, France, Greece, Hungary, Israel, Netherlands, Romania, Sweden, and the United Kingdom (Malir *et al.* 2016). The Food and Agriculture Organization (FAO) together with Dutch Foreign Service (DFS) conducted a global survey on the legal regulation limits on OTA in different food and feed (Malir *et al.* 2016) (**Table 2-2**). OTA is a common toxin found in a range of food product such as cereals, coffee, alcoholic beverages, fruits, and spices (Heshmati *et al.* 2017; Sun *et al.* 2017b; Arrúa *et al.* 2019; Kunene *et al.* 2020; Zareshahrabadi *et al.* 2020). According to a European survey, cereals account for 44% of total adult OTA exposure, followed by 15% of other foods, 10% wine, 9% coffee, 7% beer, 5% cacao, 4% dried fruits, 3% meat, and 3% spices (Heussner and Bingle 2015). In general, OTA contamination levels in European food commodities are low (ng kg^1 to g kg^1), but individual batches may have higher levels. Despite the fact that steps are taken to keep OTA levels low in food, contamination appears to be inevitable (Postupolski *et al.* 2019; Mehri *et al.* 2020). Furthermore, much higher contamination levels can occur in other countries where food screening is uncommon and old-fashioned storage and transportation conditions are still in use.

Table 2-2: OTA in different food product and countries.

Country	**Food**	**Limits**	**Reference**
Morocco	Cereal	3 ng/g	(Tabarani, Zinedine and Bouchriti 2020)
Iran	Baby food cereals	1 µg/kg	(Khoshnamvand *et al.* 2019)
Cameroon	Coffee beans	5 μg/kg	(Nganou *et al.* 2020)
Turkey	Grapes	2 µg/kg	(YURDAKUL *et al.* 2019)
United States	Wine	2 µg/L	(De Jesus *et al.* 2018)
Argentina	Apple Juice	2.0 mg/kg	(Oteiza *et al.* 2017)
United States	Wheat	1 µg/g	(Yu, Mikiashvili and Liang 2019)

2.1.3 Occurrence of Ochratoxin A in coffee and cereal

Coffee is one of the complicated matrix (Benites *et al.* 2017). The toxigenic fungi contaminate coffee beans during the production steps, especially washing, fermentation, and drying (Oliveira *et al.* 2019). The microorganisms contaminate the coffee beans during the primary contacts with soil, this result in the formation of malfunctioning, black and sour grains (Taniwaki *et al.* 2014). Some fungal species cause the grain defects that results in the production of mycotoxin such as OTA (de Almeida *et al.* 2019). The main fungi that produced OTA in coffee include *A. ochraceus*, *Aspergillus westerdijkiae*, *A. niger* and *Aspergillus carbonarius* (de Almeida *et al.* 2019; da Silva *et al.* 2020; das Neves *et al.* 2021). However, coffee can be polluted with other fungal species, such as *A. steynii, A.* and *A. sclerotiorum* (Gil-Serna *et al.* 2014). Oliveira and co-workers, reveal that the temperature and the time used to roast coffee does not destroys OTA completely (Oliveira *et al.* 2019). The temperature and water activity (a_w) are both accountable for the growth and production of ochratoxin A (OTA) by *Aspergillus* species in coffee (das Neves *et al.* 2021). When OTA contaminates the coffee beans, it remains in the roasted coffee in higher levels that those permitted by legislation (Oliveira *et al.* 2019). Cereal and cereal-based products are one of the significant source of energy, minerals and vitamins worldwide (Pereira, Fernandes and

Cunha 2014; Baniwal *et al.* 2021). Different mycotoxins contaminate these products as a results of grain infection by fungi, or during the harvest season or during storage (Pitt, Taniwaki and Cole 2013). The level of mycotoxins contamination is caused by various factors such as insufficient storage conditions, moisture, temperature, insect damage, and drought (Marin *et al.* 2013; Jeyaramraja, Meenakshi and Woldesenbet 2018; Khodaei, Javanmardi and Khaneghah 2020). The concentration of mycotoxins that is present in the cereal-based product is associated with some factors such as water activity, production managements, and temperature (Reyneri 2006; Kamika and Tekere 2016; Rastegar *et al.* 2017). A good agriculture practices (GAP) plays a significant role in the reduction of mycotoxins contamination (Rubert *et al.* 2013; Serrano *et al.* 2013). During the food production, different mycotoxins are present resulting in the reduction of contamination (Vaclavikova *et al.* 2013). Nonetheless, the cereal and cereal-based products contaminated with mycotoxins has a great risk to both human and animal health (da Rocha *et al.* 2014; Campagnollo *et al.* 2016; Amirahmadi *et al.* 2018).

2.1.4 Toxicity effect of ochratoxin (OTA)

Intensive research have been carried out to investigate the toxicological profile of OTA by various authors (Mally 2012; Doi and Uetsuka 2014; Limonciel and Jennings 2014; Vettorazzi, González-Peñas and de Cerain 2014; Wu, Groopman and Pestka 2014; Damiano *et al.* 2021). These studies revealed that OTA has a nephrotoxic, hepatotoxic, neurotoxic, carcinogenic, teratogenic and immunotoxic affects both in animals and human health. OTA toxicity depends on the gender, topographical location, season, the species, and the cellular type of the examined animals (Malir *et al.* 2013; Leitão 2019). There are limited studies of OTA in humans compared to animals. The carcinogenicity of OTA in humans was discovered by the International Agency for Research on Cancer in 1993, and identified OTA as a possible human carcinogen (Group 2B) (Organization and Cancer 1993). The chronic exposure at low OTA doses has a severe effect compared to acute exposure at high doses (Malir *et al.* 2016). The kidney is one of the targeted organs by OTA. The low concentration of OTA presents in the renal cell is considered as a modulator of cellular signaling, because it interacts with a specific cellular key target and these results in the alterations of cell function and re-programming of the cells (Leitão 2019). OTA concentrations stimulate apoptosis in culture cells, while necrosis has small role in cellular death (Leitão 2019). Schwerdt and co-

workers finding shows that low OTA concentrations exposures for extended days led to cell hypertrophy and affect the proximal tubule cells (Schwerdt *et al.* 2007). They also find out that its causes the Balkan endemic nephropathy (BEN) in humans (Schwerdt *et al.* 2007). OTA exposure results in the liver damage and depends on both the period and dose of exposure. Additionally, the oxidative stress is the factor that increases the hepatotoxicity of OTA in humans (Damiano *et al.* 2021).

2.1.5 Detection methods of ochratoxins

Mycotoxins are chemically stable toxins, OTA has the ability to endure harsh environments such as cooking in high temperature, or long period storage at ambient condition. These features make it essential to prevent the formation of OTA itself as a preventative measure. The various physicochemical properties of mycotoxins make it unfeasible to develop good technique to detect all mycotoxins endangering public health. OTA is toxic even in a very low concentration, examining this toxin usually requires extremely sensitive techniques with skilled technicians, that can be able to handle OTA test in a variety of food matrixes. For future applications, simple detection methods with non-scientific personnel will be devotedly pursued, which should offer a route for rapid and on-site detections, preventing contaminated grains from spreading to secondary products or to consumers. The development of a cost-effective OTA method should be selective, and sensitive towards regulation levels. One of the desirable features for field monitoring entails a fast and portable technique. Various methods for the detection of OTA particularly in food matrixes have been reported in the literature (Zhang *et al.* 2017b; Jiang *et al.* 2018; Rojas, Qu and He 2021). The traditional and powerful methods like high performance liquid chromatography (HPLC), gas chromatography (GC), thin layer chromatography (TLC), and electrochemical are applied for the detection of OTA in different samples.

2.1.5.1 High performance liquid chromatography (HPLC)

HPLC is one of the analytical techniques generally used to detect OTA in food matrices. These techniques can be coupled with different detectors such as mass-spectrometry and fluorescence (Asadi 2018; Alsharif *et al.* 2019). It is difficult to detect OTA in food matrices using HPLC due to the presence of the countless interfering components along with the low concentration of OTA in these samples. These interferences can be removed by introducing proper sample preparation steps prior to the analysis with HPLC. The common pretreatment method such as liquid–liquid extraction (LLE) and liquid-phase micro extraction (LPME), solid phase extraction (SPE), cloud point extraction (CPE), homogeneous liquid–liquid extraction (HLLE), solid-phase micro extraction (SPME), liquid-phase micro extraction (LPME), dispersive liquid–liquid micro extraction (DLLME) and dispersive liquid–liquid micro extraction based on solidification of a floating organic drop (DLLME-SFO) are applied for this purpose (Zhu *et al.* 2016; Andrade and Lanças 2017; Arroyo-Manzanares *et al.* 2018; Wu *et al.* 2018; Alsharif *et al.* 2019; Huang *et al.* 2020; Mottaghianpour, Nazari and Hosseini 2021; Taşpınar *et al.* 2021).

2.1.5.2 Gas chromatography (GC)

GC is a technique commonly used in the investigation of volatile compounds in foods matrixes due to its high chromatographic resolution, sensitivity, and accuracy. It primarily depends on differential splitting of analytes between the two phases of sample analysis. The chemical composition of the sample distribute themselves between the stationary phase and mobile phase. The mass spectrometer (MS), electron capture detector (ECD), and flame ionization detector (FID) are common detectors that are used for the analysis of mycotoxins (Debevere *et al.* 2019; Zhang *et al.* 2019b; Agriopoulou, Stamatelopoulou and Varzakas 2020a). These detectors have been used to detect different OTA in different matrixes as show in **Table 2-3**. This technique is sensitive and selective to most of the mycotoxins, but it requires the mycotoxins to be derivatized in order to be volatile so that they can be detected (Singh and Mehta 2020). The disadvantages of using GC for the detection of mycotoxins includes the degradation of sample during heating, (GC uses high temperatures), high risks of contamination, and vaporisation during injection time (Turner, Subrahmanyam and Piletsky 2009; Singh and Mehta 2020).

Table 2-3: Different detectors applied to detect OTA in different food matrixes.

Matrix	**Detector**	**Reference**
Wine	MS	(Zhang *et al.* 2019b)
Alcohol	MS	(Zhang *et al.* 2017a)
Meat	ECD	(Amelin, Karaseva and Tretyakov 2013)
Cereal	MS	(Olsson *et al.* 2002)
Oil	FID	(Schlösser and Prange 2019)
Wine	FID	(de Andrade Santiago *et al.* 2018)
Essential oil	FID	(Puvača *et al.* 2019)

MS: mass spectrometer, ECD electron capture detector, FID flame ionization detector

2.1.5.3 Thin layer chromatography (TLC)

Thin layer chromatography (TLC) has been well-known as a suitable separation technique for the detection of mycotoxins that can screen a huge number of samples efficiently. This common technique for the analysis of mycotoxins applied both quantitative and semi-quantitative determinations (Turner, Subrahmanyam and Piletsky 2009). TLC requires the cleanup procedures, and depends on the properties and the nature of the toxin (Agriopoulou, Stamatelopoulou and Varzakas 2020b). Different clean up procedures includes silica gel, solid phase extraction (SPE), immunoaffinity column clean-up (IAC), and supercritical fluid extraction (SFE) (Huertas-Pérez *et al.* 2017; Irakli, Skendi and Papageorgiou 2017; Thipe *et al.* 2020). Atumo reported that TLC is rapid and efficient compared to adaptable HPLC, for the detection of OTA (Atumo 2020). Few research have been steered regarding the use of TLC for the detection of OTA compared to other chromatographic techniques. This method required large amounts of solvent, complicated procedures, and it is not automatic, though, it feasible to detect a range of samples with minimizing the cost factor.

2.1.5.4 Electrochemical biosensors

The use of electrochemical biosensor in the food industry can contribute into the reduction of mycotoxins. This technique is rapid, simple, low cost sample analysis, portable, and precised (Hoyos-Arbeláez, Vázquez and Contreras-Calderón 2017; Karimi- Maleh *et al.* 2020). Kunene and co-workers recently fabricated the immunosensors for detection of ochratoxin A (OTA) in coffee (Kunene *et al.* 2020). Different recognition elements such as enzymes, antibodies, and aptamers are commonly used for the detection of OTA in different food matrixes (Cheng *et al.* 2017; Zhang *et al.* 2018d; Hou *et al.* 2019). Nanomaterials such as graphene, nanotubes, and nanoparticles have been confirmed to enhance the sensitivity of the biosensor (Kaur *et al.* 2019; Abera *et al.* 2020; Kunene *et al.* 2020). These biocompatible materials are categorized by their unique physical and chemical attributes, such as high surface area and electrochemical stability (Huang *et al.* 2018).

2.2 Aflatoxins

Aflatoxins (AFs) are the family of poisonous metabolites that are produced by a certain fungal species found in food and feeds (Coppock, Christian and Jacobsen 2018). AFs were first discovered as Turkey X disease in 1960 (Patel *et al.* 2015).These epidemic results in the fatal death of more than 100,000 turkeys in England, because they were feed with the exported groundnut meal from Brazil which was contaminated with a toxins (Butler and Barnes 1963). It was then discovered that the cause of these fatal death were due to the metabolites of *Aspergillus flavus*, which were then called aflatoxins (*A.flavustoxins*) (Rushing and Selim 2019). AFs are produced by two main fungi species of *Aspergillus flavus* and *Aspergillus parasiticus*, found mainly in warm and humid environments worldwide (Tiwari *et al.* 2017a; Gizachew *et al.* 2019). There are different factors that influence the production of aflatoxins by these fungal species, which include temperature, insect damage, the ability of the crop to adapts into the environment, and agricultural strategies (Khlangwiset, Shephard and Wu 2011; Mannaa and Kim 2017; Tai *et al.* 2020). Aflatoxins can also be produced by these fungal species during storage, shipping, and processing (Khlangwiset, Shephard and Wu 2011). These fungi species are found mainly in food commodities, mostly in grapes, maize, oil seeds, and dairy products worldwide (Altun *et al.* 2017; Kos *et al.* 2018; Heshmati *et al.* 2019; Ting *et al.* 2020). Literature reveals that they are 20 derivatives and more than 10

structures of AFs that has been identified (Xing *et al.* 2017; Zhang *et al.* 2020a). Aflatoxin B_1, B_2, G_1, G_2 M_1 and M_2 (shown in **Figure 2-2**) are the different types of aflatoxins that has been reported in the literature, and classified according to their fluorescence emission in UV light (B-blue and G-green) (Hernández-Meléndez *et al.* 2018). These aflatoxins have been listed as Class I carcinogens by the World Health Organization (WHO) (Guo *et al.* 2017; Xing *et al.* 2017; Xue *et al.* 2019b). Previous report conducted by different authors has describe that these toxins have carcinogenic, mutagenic, teratogenic, and immunosuppressive effect on both animals and humans (Wang *et al.* 2018; Omotayo *et al.* 2019; Asghar, Ahmed and Asghar 2020; Ahmed and Asghar 2021). Among them, aflatoxins B_1 (AFB_1) is one of the most poisonous mycotoxins because, it contaminates food even at low concentrations.

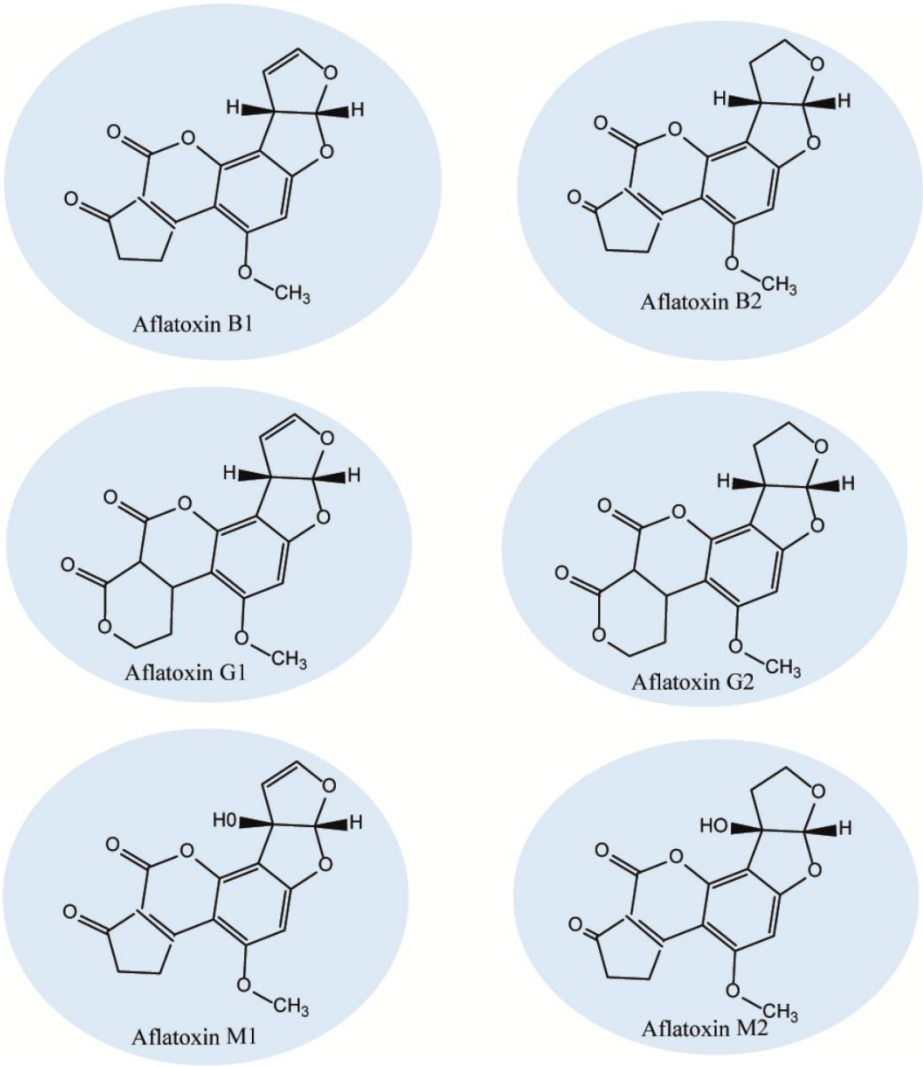

Figure 2-2: Chemical structures of Aflatoxins (Nazhand *et al.* 2020).

2.2.1 Chemical properties of aflatoxin B_1 (AFB_1)

Aflatoxins are a group of compounds that are classified as difuranocoumarins, which are highly substituted coumarin derivatives comprising a joined dihydrofurofuran moiety (Marchese *et al.* 2018). AFB_1 contains a cyclopentenone ring bonded to the lactone ring of the coumarin structure **(Figure 2-2**). When AFB_1 is exposed to UV light its emits a strong fluorescence emission in the blue region (Khan *et al.* 2021). The chemical structure of AFB_1 is similar to that of AFM_1, with a low molecular weight of 312.28 g mol^{-1} and the molecular formula of $C_7H_{12}O_6$. It is sparingly soluble in water, insoluble in non-polar solvents and soluble in polar solvents (Marchese *et al.* 2018; Liu *et al.* 2020c). It is also thermal stable even at high temperatures and protect them from being thermal degraded during food production (Ndagijimana, Shahbaz and Sun 2020).

2.2.2 Principal Activation Pathways of AFB_1

To understand the mechanism in which aflatoxins utilize their toxic effect, it is essential to know how they are metabolized. The investigation on the mechanism of the toxicity of AFB_1 has been carried out to propose a scientific method that can be used for prevention and regulation measures. AFB_1 is basically metabolized within the liver upon the activity of the microsomal mixed function oxidase (MFO) enzyme that belongs to the large group of CYP450. The interaction of oxidase with AFB_1 results in the conversion of AFB_1 into the reactive 8,9-epoxide, with an exo and endo stereoisomers, which is reported to be a poisonous species accountable for AFB_1 genotoxic properties (Marchese *et al.* 2018). The interaction between the exo-8,9-epoxide and DNA results in the formation of 8,9-dihydro-8-(N7-guanyl)-9-hydroxy-AFB_1 (AFB_1-N7-Gua) adduct, hence causing a DNA mutations (Zhuang *et al.* 2016; Rushing and Selim 2017; Benkerroum 2020).The previous report reveals that the induction of oxidative stress (OS) is due to the high effect of AFB_1 on cell function (Ayala, Muñoz and Argüelles 2014; Benkerroum 2020). **Figure 2-3** shows the different toxicity mechanisms of AFB_1.

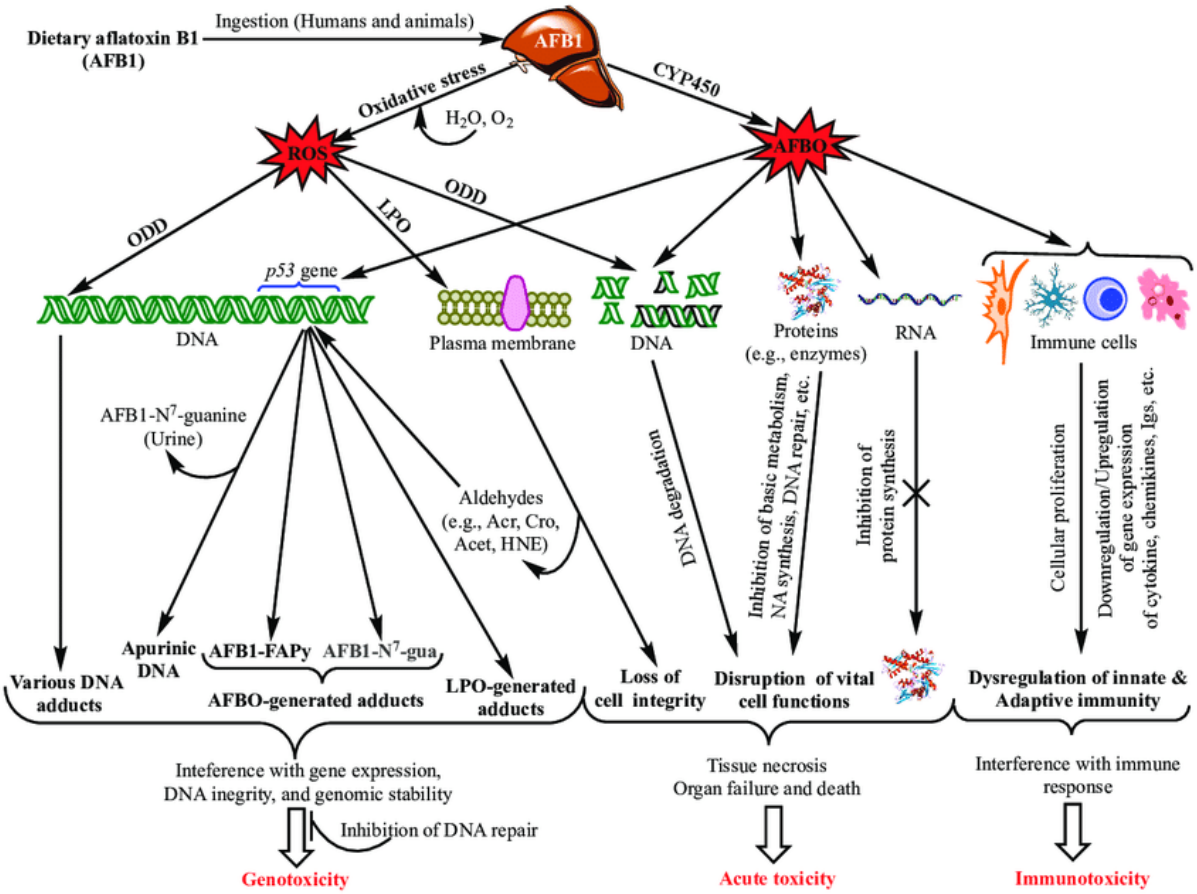

Figure 2-3: Main aflatoxin B_1 toxicity mechanisms mediated by the oxidative stress and AFB_1-exo-8,9 epoxide (Benkerroum 2020).

2.2.3 Aflatoxin B_1 related diseases

Chronic diseases such as cancer are caused by the repeated exposure to aflatoxin even at low concentration. Literature reveals that the dietary intake and exposure to aflatoxins causes cancer of different organs such as, liver, kidney, pancreas, bladder, lung, esophagus, and intestines (Abdulrazzaq *et al.* 2017; Xue *et al.* 2019a; Zhou *et al.* 2019; Owumi *et al.* 2020; Lu *et al.* 2021b).The exposure to aflatoxins causes a variety of other diseases, comprises of immunosuppression, teratogenicity, mutagenicity, cytotoxicity, and estrogenic effect in both animal and humans (Klvana and Bren 2019). Aflatoxins also interferes with the micronutrients, proteins and metabolic enzymes and result in the nutritional disorders such as kwashiorkor (Turner 2013; Rushing and Selim 2019). When animals and feeds are exposed to aflatoxins, it results in the reduction of production and reproduction, increases diseases, and reduces crop produce during harvesting time (Joint, Organization and Additives 2017). Regardless of the insidious properties of aflatoxin related diseases, their effect on public well-

being worldwide is more serious and more expensive. However, the aflatoxin outbreak can simultaneously trigger hundreds of deaths, prevent or hinder analysis of suspect crops/foods, for example clear mold growth and aflatoxin levels if they exceed regulatory standards. Therefore, different countries have set a maximum standard concentration of aflatoxins that have to be present in food and feed to sustain the human health. The acceptable value of aflatoxin in human intake depends on the food type (Mahato *et al.* 2019). **Table 2-4** shows different countries with food type and their maximum concentration range.

Table 2-4: Different countries showing maximum permissible level of AFB_1 in different food.

Country	**Food**	**Maximum limits (µg kg^{-1})**	**References**
Algeria	Spices	10	(Azzoune *et al.* 2015)
Egypt	Peanuts	5 - 10	(Abdel-Rahman *et al.* 2021)
Hungary	Wheat flour	2	(Varga, Fodor and Soros 2021)
China	Peanut oil	20	(Qi *et al.* 2019)
Zimbabwe	Maize	5	(Murashiki *et al.* 2017)
Kenya	Fish	5	(Marijani *et al.* 2020)

2.2.4 Occurrence of aflatoxins B_1 in alcoholic beverages and in dairy product

Aflatoxin B_1 (AFB_1) is one of the widely known mycotoxins and its generally found in numerous fermented foodstuffs and in alcoholic beverages (Shukla *et al.* 2017). The aflatoxin present in the food additives or from malted barley may be transmitted from the polluted grains into alcohol during the brewing process (Shukla *et al.* 2017). The fungal pathogens are the one that are responsible for the occurrence of AFB_1 in wine. These fungal pathogens can grow on grapes during the crushing and grape juice production, and as a result they passed over into the wine (Wang *et al.* 2015a). Since aflatoxins are thermally stable at high temperature, they remain in the alcohol during the brewing process, and pasteurization, but

are effectively eliminated during distillation (Ioi *et al.* 2017; Seyedjafarri 2021).There is more focus on the elimination of AFB_1 contamination in wine during brewing process using pre and post-harvest methods (Anitha *et al.* 2019). Goud and co-workers reveals that alcohol beverages such as beer and wine can be contaminates by AFB_1 (Goud *et al.* 2016b). Milk is one of the most important nutritious food that contains various nutrients that are essential in human diet (Iqbal *et al.* 2015). Aflatoxin B_1 (AFB_1) is one of the most toxins that is found in the cattle feed due to the inappropriate cropping and storage conditions (Intanoo *et al.* 2018). Lactating cows that consume AFB_1-contaminated feed generate aflatoxin M_1 (AFM_1), the hydroxylated metabolite of AFB_1 (Xiong *et al.* 2015; Xiong *et al.* 2018). The formation of AFM_1 occurs in the liver and resulted in the secretion of milk (Kara and Ince 2014). Literature reveals that there is a linear relationship between the quantity of AFM_1 in milk and AFB_1 present in the feed that was consumed by animals (Dragacci *et al.* 1995; Jalili and Scotter 2015; Gizachew *et al.* 2016). Milk is a valuable liquid that loose it quality or spoils if not processed (Amenu *et al.* 2019). There are several ways of processing milk; however the effects of processing and storage are of great concern due to the contamination of AFB_1 (Mohammadi 2011). The existence of aflatoxin M_1 (AFM_1) in milk and dairy products is an significant concern, particularly in the well developed countries (Campagnollo *et al.* 2016).

2.2.5 Preventative approaches of aflatoxin B_1

The contamination of food product with AFB_1 is inevitable. The contamination percentage can be significantly reduced by taking certain safety measures such as pre-harvest and post-harvest. Temperature, moisture content, soil condition and nutrient composition of food on aflatoxin contamination and insect activity during storage are the factors that enhances the production of *A. flavus* and *A. parasiticus* contamination (Achaglinkame, Opoku and Amagloh 2017; Mousavi Khaneghah *et al.* 2018). To reduce the risk of crop spoilage by AFB_1, one of the best practices is to dry the harvested crop (Zorlugenç *et al.* 2008; Kang'ethe *et al.* 2017). Mousavi Khaneghah and co-workers proposed a summary on the prevention methods for the formation of AFB_1 during and after harvesting period (Mousavi Khaneghah *et al.* 2018) (**Figure 2-4**). The hazard analysis critical control point (HACCP) are applied to prevents and reduce the aflatoxins spoilage in agricultural products (Gil *et al.* 2016).

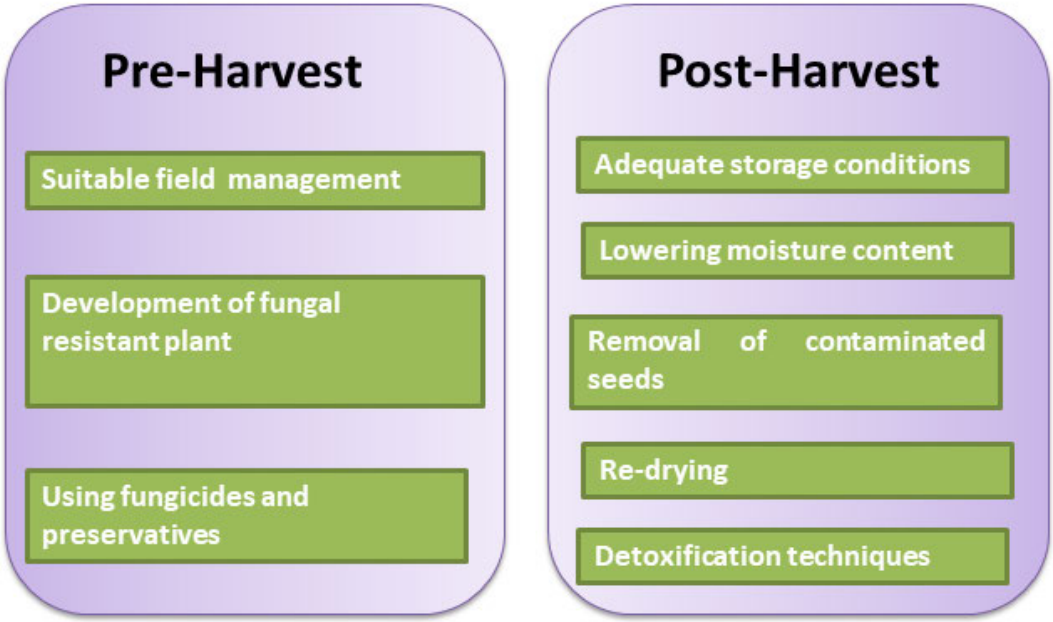

Figure 2-4: Summary of the propose prevention methods of aflatoxin formation in field and postharvest (Mousavi Khaneghah *et al.* 2018).

2.2.6 Detection methods of aflatoxin B_1

The widespread presence of mycotoxins in food and feed presents a significant threat to both human and animal health world-wide due to their wide range of toxicological properties. The European Commission (EC), the US Food and Drug Administration (FDA), the World Health Organization (WHO), and the Food and Agriculture Organization (FAO) are examples of national and international institutions/organizations that set up the regulation limits. This organization have acknowledged the potential risks of mycotoxins, and they have set up the regulatory limits for major classes and selected individual molecules (Hickert *et al.* 2015; Zhang *et al.* 2016b). Since AFB_1 is the widely distributed mycotoxins, controlling it in everyday products has become a top priority for researchers around the world to protect people and reduce economic losses. The analytical technique for detection of AFB_1 has been improved over the last century. However, due to the wide variety of chemical structures and concentration levels in various types of commodities, a common standard technique for all AFB_1 analysis and/or detection is unlikely. Therefore, most modern analytical methods require additional steps such as extraction, clean-up, and separation prior detection. Those measures are important (despite the time constraints). Different analytical techniques used

and reported in literature for the detection of AFB_1 include chromatographic (Coskun *et al.* 2018), ultra violet absorption (Hassan 2018), florescence (Aklaku, Sowley and Ofosu 2020), and electrochemical methods (Karapetis, Nikolelis and Hianik 2018; Li *et al.* 2020c).

2.2.6.1 Liquid chromatography-tandem mass spectrometry (LC-TMS)

(LC-TMS) is one of the powerful approaches used for the quantification of aflatoxin B_1, as reported in literature by several authors (Qi *et al.* 2017; Deng, Su and Wang 2018; Dong *et al.* 2018; Pereira, Cunha and Fernandes 2020), coupled with different LC-MS interfaces such as atmospheric pressure chemical ionization (APCI), atmospheric pressure photo-ionization (APPI), and electrospray ionization (ESI) interfaces (Laaniste, Leito and Kruve 2019; Cortese *et al.* 2020). The LC-TMS technique combines the separating power of liquid chromatography with the highly sensitive and selective mass analysis capability of triple quadrupole mass spectrometry, ion trap, and time of flight analyzers (TOF) as detectors (Du *et al.* 2018; Hidalgo-Ruiz *et al.* 2019; Tolosa *et al.* 2019). The triple quadrupole mass spectrometry are generally used as detectors due to its selectivity, which allows the simultaneously detection of mycotoxins with a reduced sample clean up procedure (AlFaris *et al.* 2020). Detection of aflatoxins simultaneously in different food products using LC-TMS has been reported in the literature by several authors (Liu *et al.* 2017b; Ren *et al.* 2018a; Saha *et al.* 2018; Campone *et al.* 2020).

2.2.6.2 High performance liquid chromatography (HPLC)

HPLC is one of the well-known and rapid approach used for the quantification of aflatoxins, coupled with different detectors such as UV absorption, fluorescence, mass spectrometry, and photodiode array (Singh and Mehta 2020; Arroyo-Manzanares *et al.* 2021; Mottaghianpour, Nazari and Hosseini 2021), amongst these, the fluorescence detector is generally used. The mobile phase and the stationary phase are both in liquid phase. In HPLC, the separation is based on the distribution of analyte between stationary and mobile phases. The HPLC methods comprises of two types including normal phase and a reversed phase. The reverse phase is the most commonly used method in detection of aflatoxins because it is sensitive compared to normal phase (Moldoveanu and David 2016; Zheng *et al.* 2016).

2.2.6.3 Thin layer chromatography (TLC)

TLC is one of the generally used chromatographic techniques for the detection of aflatoxins. It separates, identifies and assesses the purity of the aflatoxins (Cheng *et al.* 2019). TLC comprises of a stationary phase, which can be a glass, metal or a plastic plate and a mobile phase which is normally a liquid solvent (Sherma 2017; Malik and Bhushan 2018). Different liquid solvents has been used in the literature by several authors (Ciura *et al.* 2017; Danciu, Hosu and Cimpoiu 2018; Sarker *et al.* 2018; Anh 2019).The stationary phase is used to hold the sample, while the chromatographic plates are retained in a solvent reservoir vertically where it moves (Mahfuz *et al.* 2018). The thin layer chromatography combined with surface-enhanced Raman spectroscopy (TLC-SERS) was used for the screening of AFB_1 in peanuts and the detection limit was $1.5x10^{-6}$ M (Qu *et al.* 2018). Recently Pradhan and Ananthanarayan fabricated the high-performance thin-layer chromatography (HPTLC) for detection of AFB_1 in dried chilies (Pradhan and Ananthanarayan 2020).This technique is rapid and sensitive, but in few occasions gives incorrect results due to the solvent ratio that causes by humidity and temperature (Mahfuz *et al.* 2018).

2.2.6.4 Ultraviolet absorption

This technique is generally applied in the detection of aflatoxins (AFs) because they have a molar absorptivity of 20,000 cm^2/mol and displays an absorption around 223 to 362 nm (Lalah, Omwoma and Orony 2019; Singh and Mehta 2020). The ultraviolet is not sensitive to detect AFs in trace levels and only applicable to micro molar ranges. However the sensitivity can be enhanced by extraction and cleanup procedure (Singh and Mehta 2020).

2.2.6.5 Electrochemical methods

The above-mentioned techniques are sensitive and rapid, but they entail the use of the classy expensive instrument, time-consuming, require complex pre-treatment, and trained persons to operate (Abnous *et al.* 2017; Bhardwaj, Pandey and Sumana 2019; Wu *et al.* 2019). Amongst these presented detection techniques, electrochemical methods have been greatly favored due to its ease of operation, portability, outstanding sensitivity, automation,

short analysis time, low power consumption, cost-effective instrumentation and reliability to detect toxic compounds in the foodstuff (Chauhan *et al.* 2016; Bhardwaj, Pandey and Sumana 2019; Chen *et al.* 2020b; Shi *et al.* 2020).

2.3 Biosensors

Biosensors are generally portable analytical devices that are based on the incorporation of recognition element with the transducer in order to detect chemical and biological species (Labib, Sargent and Kelley 2016). A biosensor generally comprises of four parts which includes analyte (toxins, human sample, bacteria), bio-recognition element (enzymes, antibody, aptamers and etc.), signal transducer (electrochemical, optical, magnetic, thermal, piezoelectric and colorimetric) and signal amplifier (Labib, Sargent and Kelley 2016; Soleymani and Li 2017; Sanati *et al.* 2019) as shown in **Figure 2-5**. Biosensors has several applications in agricultural monitoring, health and medicine, and military applications (Wang, Zhou and Li 2017; Pohanka 2018; Griesche and Baeumner 2020).

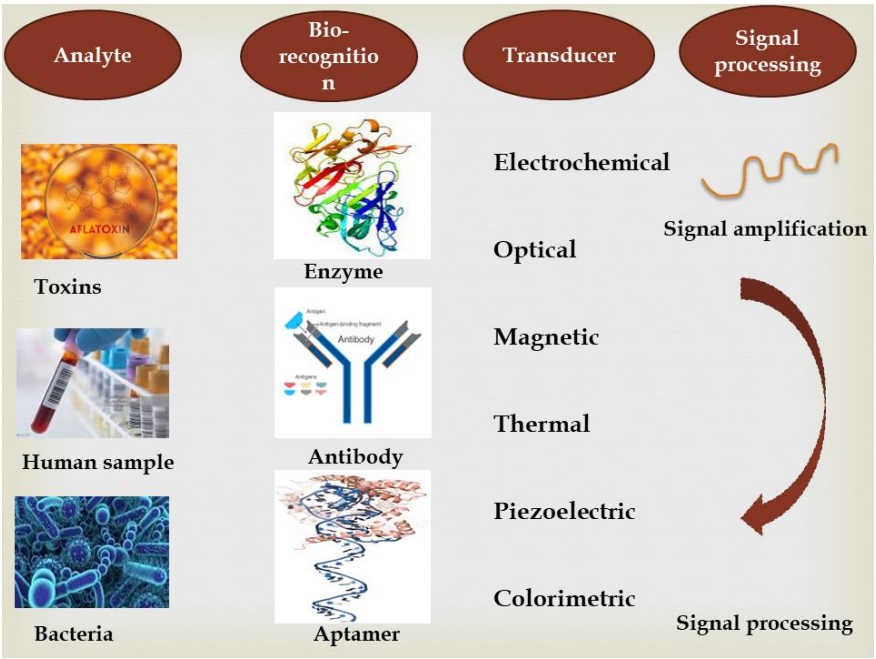

Figure 2-5: Features of a biosensor.

2.3.1 Classification of the biosensors

Biosensors are categorized into two main groups based on their bio-recognition, this includes the catalytic-based and affinity-based biosensors (Labib, Sargent and Kelley 2016; Hashemi Goradel *et al.* 2018). The catalytic-based biosensors are commonly involve the use of catalyst such as glucose oxidase (GOx) for detection of biological species (Cui 2017), while the affinity-based biosensors are based on using antibodies, protein receptors and aptamers as bio-recognition elements (Tu *et al.* 2020). The affinity based biosensors has received a great attention in the analysis of various toxins that might be present in food products, owing to their extraordinary properties such as sensitivity, specificity and reliability (Azri *et al.* 2018; Kunene *et al.* 2020).

2.4.1.1 Catalytic-based biosensors (CBBs)

The CBBs are generally based on the catalytic reaction on a catalyst surface with a redox–active target molecule. The catalytic reaction includes inorganic materials, enzymes, microorganisms, tissues, etc. (Mahshid *et al.* 2016; Sanati *et al.* 2019). The electrochemical analyzer monitors the response of the consumption of the target molecule. The CBBs are simple, rapid, and can be used several times (Mulchandani 2011).

Enzymatic electrochemical biosensors (EEBs)

One of the common receptors that are used on the enzymatic electrochemical biosensors (EEBs) is the enzymes. The formation of the complex occurs when the enzyme binds with the analyte in the enzyme-active and thus results in the conversion of the analyte into products (Nguyen *et al.* 2019) (**Figure 2-6**). During the conversion, the analyte consumption is monitored on the transducer. The selection of the enzymes is based on the specificity of the analyte. For example, acetylcholinesterase (AChE) for aflatoxin B_1 (AFB_1) (Chrouda *et al.* 2020), horseradish peroxidase (HRP) for ochratoxin A (OTA) (Lu *et al.* 2021a) and alkaline phosphatase for aflatoxin M_1 (AFM_1) (Karczmarczyk, Baeumner and Feller 2017). Enzymes are used in affinity-based biosensors to enhances the electrochemical signal (Liu *et al.* 2017a; You *et al.* 2020).

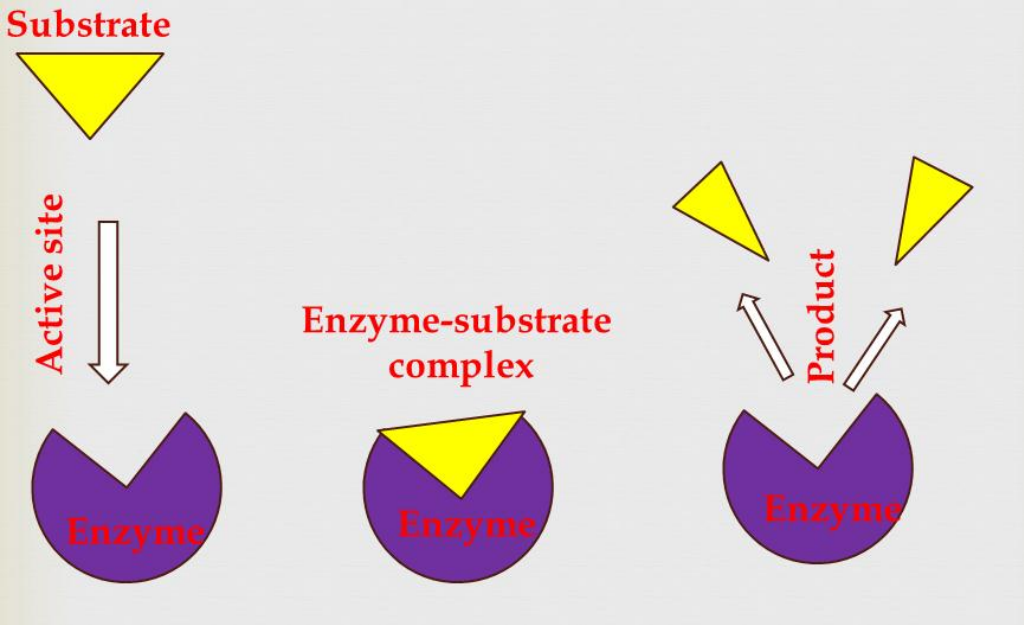

Figure 2-6: Schematic design of the enzymatic reaction on catalytic-based biosensors.

2.4.1.2 Affinity-based biosensors (ABBs)

The affinity-based biosensors (ABBs) imitate a biological event by the interactions of the target analyte with a bio-recognition element such as proteins, antibodies, synthetic DNAs, and aptamers (Victorious *et al.* 2019; Antiochia 2021). The interaction between the target analyte and the bio-recognition element results are transferred to a signal by linking to a transducer (Sanati *et al.* 2019).They have a range of applications in the environmental monitoring, agricultural sector and medical sector (Suresh *et al.* 2018; Pérez-Fernández *et al.* 2019; Khoshbin, Housaindokht and Verdian 2020). **Figure 2-7** displays the different types of ABBs, which are characterized according to their bio-recognition elements.

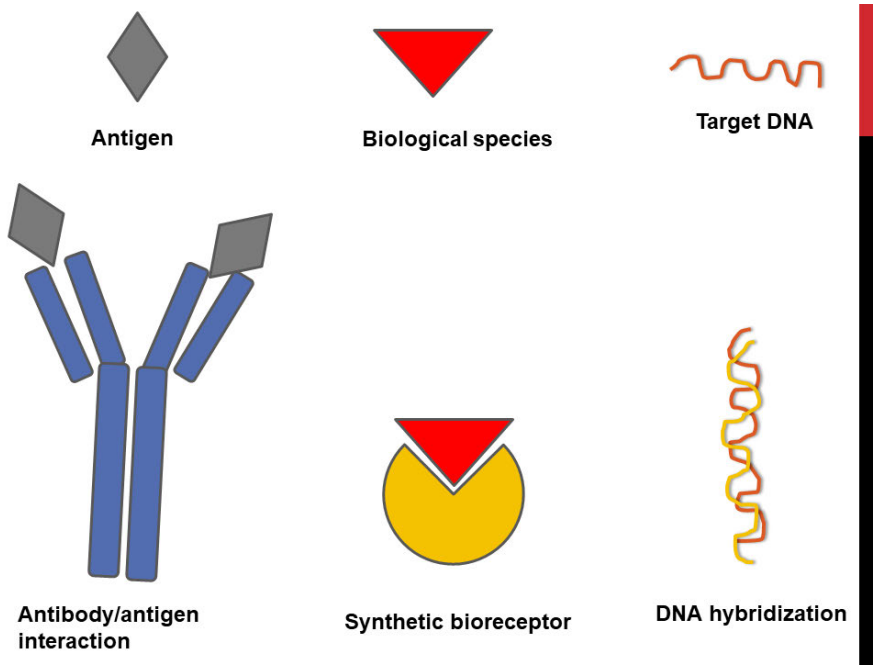

Figure 2-7: Types of ABBs showing the different bio-recognition elements.

(i) Immunosensors antibody-based biosensors

The immune system produces the protein called immunoglobulin, which is also known as antibody, in order to responds to the presence of the foreign species called antigen (Augustine *et al.* 2020; Zahid *et al.* 2020). The antibodies comprises of the antigen-binding sites that binds the antigens by the monovalent interactions with relatively high affinity (Kafil *et al.* 2020; Orlandi *et al.* 2020) (**Figure 2-8**). The interaction between the antibody and the antigen is the most significant parameter in immunosensors.

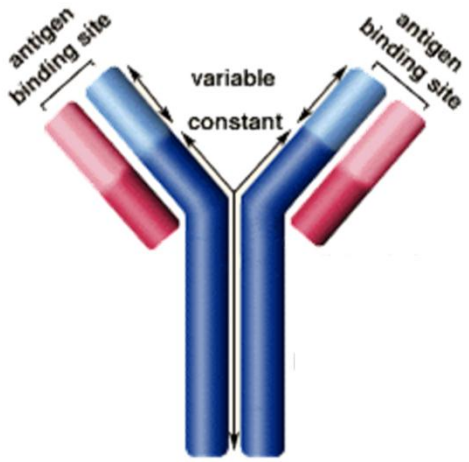

Figure 2-8: Structure of the antibody.

The immunosensor are classified into two groups like labeled (sandwich type) (**Figure 2-9**) and non-labeled (label free) (**Figure 2-9**), which is further categorized as competitive and noncompetitive based on the detection strategy (Wang *et al.* 2017a; Filik and Avan 2019).

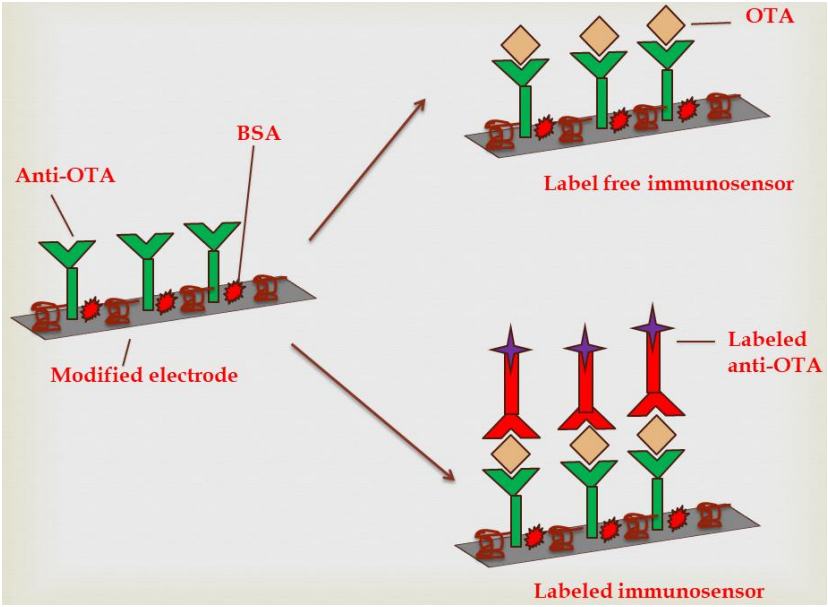

Figure 2-9: Schematic presentation of the label-free and labeled immunosensor.

(a) Label-free immunosensor

In the case of label-free (non-labeled), the label is not required to monitor the binding event. They have a better accuracy compared to labeled methods. The main advantages of the label-free immunosensor is that it is user-friendliness, inexpensive, rapid and uses small amount of the reagents (Rizwan *et al.* 2018; Chanarsa, Jakmunee and Ounnunkad 2021). Although these immunosensors are simple to fabricate and rapid, the non-competitive protocol is preferential over the competitive one. However, the non-competitive suffer from false positive error caused by the nonspecific binding. In a label free non-competitive immunosensor, the interaction of immobilized antibodies and analyte is read out by the transducer. The transducer and mode of detection play the important role for obtaining the enhanced sensitivity of the label free immunosensor. The sensitivity of the electrochemical immunosensor can be improved by incorporating with nanomaterials.

(b) Labeled Immunosensor

Labeled immunosensor also called as sandwich-type immunosensor (**Figure 2-9**) is commonly used for the selective and sensitive examination of cancer antigens. In the sandwich type the target antigen binds with a supplementary antibodies first before binding to the secondary labeled antibody (Filik and Avan 2019). The labeled immunosensor are stable, rapid, simple instrumentation and sensitive (Yang *et al.* 2018b; Zhang, Li and Ma 2018). The formation of the antibody-antigen (Ab-Ag) complex in the immunoelectrode surface effect the availability of ions from supporting electrolyte that are embedded into the sensing layers, and results in the hindrance of electron transfer (Zhang, Li and Ma 2018). So far, different nanostructures such as graphene, metal oxide nanomaterials, and noble metal nanoparticles have been used to enhance the sensitivity of the sandwich-type immunosensors and immunoassays (Tabrizi *et al.* 2019; Zhang *et al.* 2019a; Song *et al.* 2021).

(ii) Aptasensors/aptamer-based biosensors

Aptamers are single-strand DNAs or RNAs that are derived by an *in vitro* molecular evolution method known as systematic evolution of ligands by exponential enrichment (SELEX) (Pang *et al.* 2018; Adachi and Nakamura 2019). SELEX experiments are performed against various target molecules, such as small compounds, proteins, nanoparticles, or living cells with high affinity and specificity (Cataldo, Leuzzi and Alfinito 2018; Fechter *et al.*

2019). Aptamers are very stable even at high temperature because they regain their active conformation even after denaturation (Wu *et al.* 2015; Cataldo, Leuzzi and Alfinito 2018). Aptamers have advantages over antibodies due to their smaller size, manageable synthetic procedure, and ease of modification by a variety of molecules (Duan *et al.* 2016; Ding *et al.* 2017).These make aptamers interesting candidates for biosensing, with excellent specifications for diagnostic applications. Aptamer-based biosensors also called aptamers. Aptasensors are categories as labeled and label-free aptasensor (Saberi, Rezaei and Ensafi 2019). In a labeled aptasensor, different labels such as nanoparticles, fluorescent dye, magnetic metal organic frameworks (mMOFs), and horseradish peroxidase are used (Chen *et al.* 2018c; Luo *et al.* 2019; Taib *et al.* 2020; He and Dong 2021). The label is usually attached to the target molecule; the transducer measures the label activity. The detection are often attained through the transducer either in "signal on" or "signal off" form, depending on the format of the assay (Hitabatuma, Tuyishime and Komera 2017). In the "signal on" format, target detection is based on the signal enhanced after the interaction with target. While the "signal off" refers to reduction of signal due to the formation of target-aptamer complex (Pilehvar *et al.* 2014). In the label-free aptasensor, there are no labels that are used as redox markers and the transducer measures the interaction between the aptamer and target analyte (Dong *et al.* 2020). The label-free aptasensors are simple, rapid, and cheap compared to labeled aptasensor (Li *et al.* 2019; Lopa *et al.* 2019).

Factors affecting aptamer affinity

The aptamer affinity is one of the most significant parameters when fabricating the aptasensor. One of the most factors that affect the aptamer affinity includes the existence of divalent cation and the effect of pH (Li *et al.* 2015; Jiao *et al.* 2017). The binding of the target analyte to the DNA aptamers depends on the presence of divalent cations. The negatively charged DNA forms a coordination complex with the target analyte (Wang *et al.* 2019).The effect of pH also affect the binding affinity. The basic pH results in the high affinity, while the acidic pH results in the decrease of binding because the acidic pH hinders the complex formation.

2.4 Nanomaterials

Nanomaterials (NMs) are materials that has a size ranging from 1 to 100 nm (Khan, Saeed and Khan 2019). They have different shapes, sizes and applications (Chen *et al.* 2018b; Singh, Goyal and Devlal 2018). NMs are mostly used to enhance the performance of the biosensor (Kumar *et al.* 2019). They are classified according to their dimension such as; zero dimension (0D), one dimension (1D), two dimension (2D) and three dimension (3D) (Saleh 2020).The 0 Ds NMs have all their dimensions smaller than 100 nm, like; quantum dots (QDs), hollow sphere, and metal NMs. In 1Ds NMs, one dimension is smaller than 100 nm whereas the other two dimensions are in nanoscale like: nanowires, nanofibers, and nanorods. The 2Ds NMs, one dimension is in nanoscale like; ribbon, plates and sheets, and triangles. The 3Ds NMs, has all the dimension beyond 100 nm like; stars, corns, dumbbells, flowers, boxes, cubes (Asghari *et al.* 2016; Shiau *et al.* 2018; Saleh 2020). They are also classified as noble metal nanomaterials (gold, silver, palladium, and platinum nanoparticles) and metal oxide nanomaterials (titanium oxide, zinc oxide and copper oxide) (Ding *et al.* 2018; Nabila and Kannabiran 2018; Lv *et al.* 2021; Sharma *et al.* 2021).

2.4.1 Noble nanoparticles (NNPs)

Noble metals are used to form a group of nanoparticles, called noble nanoparticles (NNPs). These NNPs are inert (resistant to oxidation/corrosion) and have unique physical and optical properties. NNPs comprises of gold (Au), silver (Ag), platinum (Pt), palladium (Pd), are generally involved in electrochemical sensor and biosensor applications platforms due to their extraordinary size and shape, physical, chemical, and electrochemical properties (Smith and Gambhir 2017; Pan *et al.* 2020). NNPs have countless applications because they are more stable compared to other metal nanoparticles. These applications include catalysts, antibiotics, cancer diagnosis, drug delivery, and biosensor (Davidson *et al.* 2018; Sengupta *et al.* 2018; Fazio, Ridolfo and Neri 2019; John *et al.* 2021).

2.4.1.1 Silver nanoparticles (AgNPs)

Silver nanoparticles (AgNPs) have been broadly studied owing to it superior physical, chemical, and biological properties, and their size, shape, composition, crystallinity, and structure of AgNPs (Desireddy *et al.* 2013; Syafiuddin *et al.* 2017; Lee and Jun 2019). AgNPs has interesting material properties, inexpensive and an abundance natural resource, however the silver-based nanomaterials has a restricted applications because of their instability in oxygen-containing liquids (Wang *et al.* 2015b). The size, distribution, and morphological shape influences the physical, optical, and catalytic properties of AgNPs (Raza *et al.* 2016) and the surface properties can be improved using reducing agents and stabilizers such as sodium alginate (SA), corn starch, and sodium citrate (Chen *et al.* 2020a; Wang *et al.* 2021). Previous report shows that different size of AgNPs has different applications (Kumar and Poornachandra 2015; Francis *et al.* 2017; Hembram *et al.* 2018).

(i) AgNPs in sensor application

Silver nanoparticles (AgNPs) has numerous applications in the field of agriculture, sensors, etc. (**Figure 2-10**) due to its extraordinary properties. AgNPs has attracted a great attention in the sensor application due to their unique physical and chemical properties (Gilroy *et al.* 2016). Jiang and co-workers have developed a rapid and selective chemiluminescence method for the detection of multiple mycotoxins using AgNPs modified glass chip. Compared with the poor signal at the unmodified glass chip, the chemiluminescence response of AFB_1 and OTA at the AgNPs-modified glass chip was significantly enhanced. A wide linear range from 0.001 to 1 ng mL^{-1} and a low detection limit of 0.44 and 0.83 pg mL^{-1} for AFB_1 and OTA respective was attained using this modified electrode (Jiang *et al.* 2020). A sensitive and simple surface enhanced Raman spectroscopy (SERS) method was developed for the determination of tartrazine in food. A modified paper with AgNPs was constructed to study the Raman synergistic response behavior of tartrazine. AgNPs displayed the outstanding electrocatalytic activity in the oxidation of tartrazine. AgNPs greatly enhanced the determination of tartrazine (Liu *et al.* 2020b). The electrochemical behavior and detection of cholesterol at AgNPs modified GCE was carried out by Nantaphol and co-workers. AgNPs enhances the sensitivity of detection of cholesterol. This method had the advantages such as ultra sensitivity, rapid response and excellent reproducibility (Nantaphol, Chailapakul and Siangproh 2015). Tagad and co-workers

developed an optical fiber sensor for the determination of hydrogen peroxide at AgNPs modified GCE. The linear concentration range attained for this fabricated electrode was in the range of 0.01 to 1 mM with a detection limit of 0.01 mM (Tagad *et al.* 2013). Elavarasi and co-workers have developed AgNPs modified glassy carbon electrode for the colorimetric detection of chromium. The modified electrode exhibited high sensitivity towards chromium (Elavarasi *et al.* 2014).

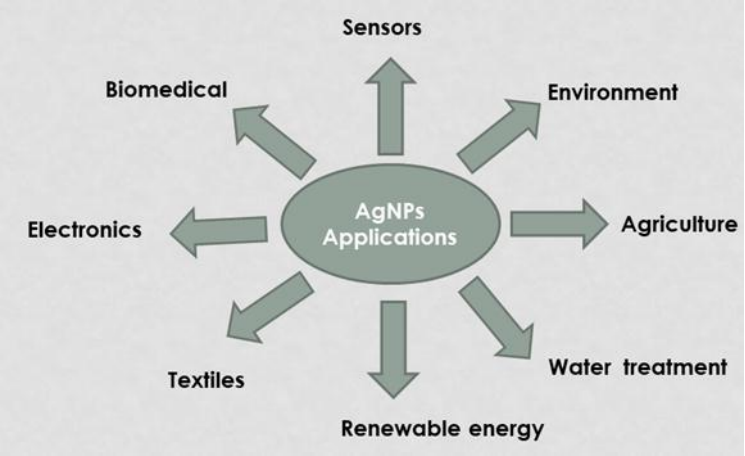

Figure 2-10: Various applications of AgNPs.

2.4.1.2 Palladium nanoparticles (PdNPs)

Palladium (Pd) is one of the very valuable noble metal with extraordinary catalytic, mechanical, and electroanalytical properties. Pd nano-based structures have been attracted great attention due to their outstanding properties, such as high thermal stability, chemical stability, photocatalytic activity, electronic properties, optical properties, and inexpensive (Chen and Ostrom 2015; Saldan *et al.* 2015). Different methods are applied for the synthesis of PdNPs with variety of size and shape as shown in **Table 2-5**. PdNPs has the wide application in coupling reaction, hydrogenation of unsaturated olefins, alcohol oxidation, activation for electrode metal deposition, fuel cells, and sensors (Elhage, Lanterna and Scaiano 2018; Quan *et al.* 2018; Cai *et al.* 2019; Yao *et al.* 2019; Kulikov *et al.* 2020; Kunene *et al.* 2020).

Table 2-5: Different methods applied for the synthesis of PdNPs.

Methods of synthesis	**Size (nm)**	**Shape**	**Reference**
Atomic layer deposition	6.0	-	(Kunene *et al.* 2020)
Green synthesis	4.8	Spherical	(Kora and Rastogi 2018)
Hydrothermal	3.1	Spherical	(Shirman *et al.* 2021)
Ultra-sonication	3.9	Spherical	(Şen *et al.* 2018)
Micro-wave	20 - 40	-	(Elazab, Sadek and El-Idreesy 2018)

PdNPs in sensors application

The outstanding properties of PdNPs such as electronic properties and excellent electrocatalytic property make it a good candidate in sensor applications (Baghayeri *et al.* 2019; Eswaran *et al.* 2019). Numerous studies have been conducted using PdNPs in sensor application for detecting different analyte as depicted in **Table 2-6**. Li and co-workers fabricated an electrochemical aptasensor for detection of aflatoxin M_1 (AFM_1).

Table 2-6: PdNPs sensors for detection of different analyte.

Electrode	**Analyte**	**Linear range (ng mL^{-1})**	**LOD (ng mL^{-1})**	**Reference**
Apt/PdNPs	AFM_1	0.01- 0.15	0.002	(Li *et al.* 2017)
Anti-OTA/PdNPs	OTA	0.5 - 20	0.096	(Kunene *et al.* 2020)
PILs/PdNPs	ZEA	0.03 - 35	0.010	(Afzali and Fathirad 2016)
PdNPs/CPM	4-NP	0.3 - 15	0.07	(Veerakumar *et al.* 2014)
PdNPs/ITO	DA	17 -177	NR	(Thiagarajan, Yang and Chen 2009)

Aptamer (Apt); palladium nanoparticles (PdNPs); aflatoxin M_1 (AFM_1), ochratoxin A (OTA); zearalenone (ZEA); polymeric ionic liquids (PILs); 4-nitrophenol (4-NP); Carbon porous material (CPM); dopamine (DA); Indium Tin Oxide (ITO)

2.4.2 Metal oxide nanoparticles (MONPs)

Metal oxide nanoparticles (MONPs) are made of purely metal precursors. These nanoparticles play a major role in countless fields like physics, chemistry, and material sciences. The metal precursors can form a wide range of oxide compounds such as cerium oxide (CeO_2), copper oxide (CuO), iron oxide (Fe_2O_3), cobalt oxide (Co_3O_4), manganese oxide (MnO_2), zinc oxide (ZnO), titanium oxide (TiO_2), tin oxide (SnO_2), cadmium oxide (CdO), etc. They improve the selectivity and sensitivity of the sensors due to its reduced dimension, high surface area, and the specific facet exposure (Galstyan *et al.* 2016; Kannan *et al.* 2016; Leung and Xuan 2016; Lan *et al.* 2017). MONPs have been extensively used in environmental industry for sensing countless analytes or toxins due to their strong electrocatalytic activity, relatively inexpensive, and high organic capture ability.

2.4.2.1 Titanium dioxide nanoparticles (TiO_2 NPs)

Titanium dioxide nanoparticles (TiO_2 NPs) are one of the widely synthesized semiconductor nanoparticles worldwide due to its fascinating properties (Keller *et al.* 2013). The attractive physical and chemical structure of TiO_2 depends on the crystal phase, size, and shape of particles. TiO_2 generally occurs in three crystalline states: anatase, rutile and brookite as presented in **Figure 2-11**. These crystalline structures have different band gap, the band gap for rutile, brookite and anatase is as follows: 3.0, 3.13 and 3.2 eV respectively and these bands define the photocatalytic performance of TiO_2 (Jahdi *et al.* 2020; Rosado *et al.* 2020). TiO_2 is widely used due to its wide band gap, outstanding chemical stability, ecofriendly, and inexpensive (Navale *et al.* 2018; Patil *et al.* 2019).

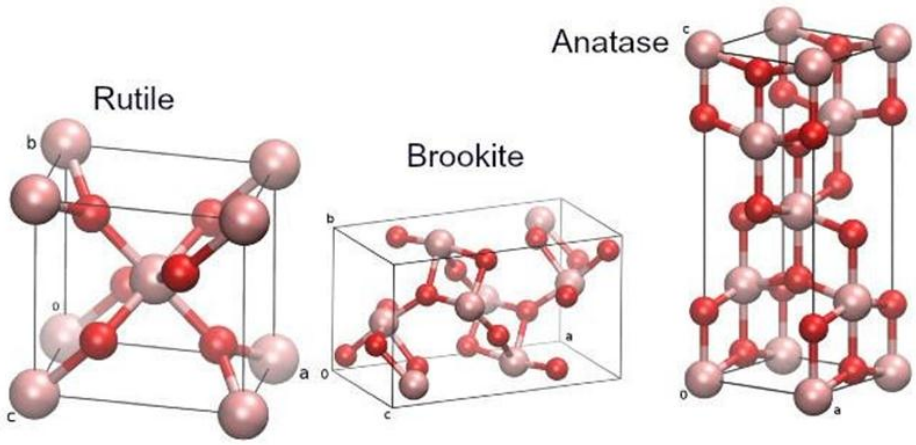

Figure 2-11: Different crystalline structure of TiO_2 **(**Pelaez *et al.* 2012**)**.

Various method has been applied for the synthesis of TiO_2 (**Figure 2-12**), and they are explained in detail under silver nanoparticles. Among these synthesis method ALD is one of the best method for the synthesis of TiO_2 because its allows the thickness control of the materials, exceptional conformality, and high aspect ratio (Graniel *et al.* 2018a).

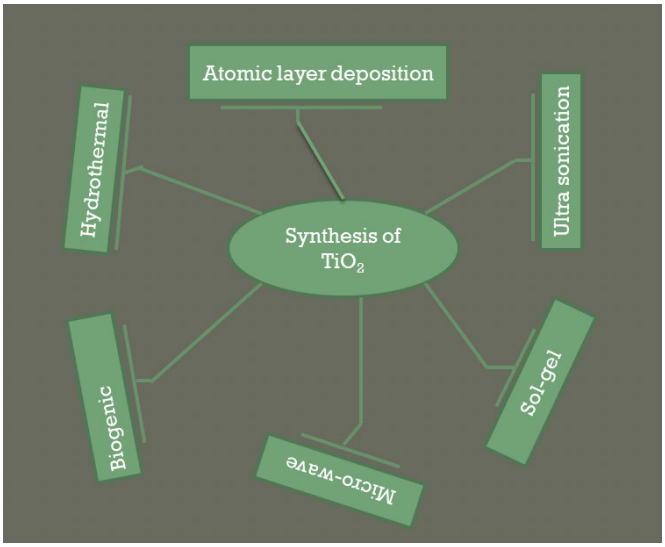

Figure 2-12: Synthesis methods of TiO_2.

TiO_2 is white pigment that is generally integrated into countless consumable products, such as food additives, toothpaste, and medications. It has attracted a great attention to various fields such as catalysis, photo catalysis, food, and sensors, due of its fascinating properties. Then, doped TiO_2 are good candidates in the performance of these applications. The incorporation of dopant in the TiO_2 lattice narrows the band gap and these results in the enhancement of electrocatalytic effect, adsorption capacity, photocatalytic activity, and reduces the photo generated electron and proton recombination (Khan *et al.* 2014; Boningari *et al.* 2018; Shetti *et al.* 2019). Different dopants such as transition metals, polymers, nitrides, etc. has been used to improve the capability of TiO_2 NPs (Yang *et al.* 2017; Hashim and Hamad 2018; Kawrani *et al.* 2020). Amongst the different dopants nitrides especially, boron nitride has been considered as an operative candidate to modify the TiO_2 lattice owing to its high surface area, which enables its attaching into the TiO_2 lattice. Furthermore, due to high available active sites, and rapid electron transfer properties make it a desirable material in sensor applications (Ferrari, Rowley-Neale and Banks 2020). Intensive research has been carried out using semi-conductor nanoparticles TiO_2 in sensor application **Table 2-7**.

Table 2-7: Different sensor using TiO_2.

Material	Method	Linear range (ng mL^{-1})	LOD (ng mL^{-1})	References
TiO_2	Flourescence	0.1–10	15.4	(Liu *et al.* 2018a)
TiO_2	Flourescence	0.01–10	1.48	(Liu *et al.* 2018a)
TiO_2	Flourescence	0.001–10	2.1×10^{-4}	(Liu *et al.* 2018a)
TiO_2	Colorimetric	0.177 – 0.001	3.1×10^{-4}	(Gökdere *et al.* 2019)
TiO_2	Electrochemical	10 – 80	10	(Zhang *et al.* 2016d)
TiO_2	Electrochemical	$5.0\times10^{-4} – 4.5\times10^{-3}$	1.73×10^{3}	(Hoffmann *et al.* 2008)
TiO_2	Photo electrochemical	0.01 – 100	0.0074	(Sun *et al.* 2017a)

2.4.3 Methods of nanomaterials synthesis

The synthesis of NMs is achieved by using chemical or green (biological) methods. The chemical method involves the top-down and bottom-up method which aids in attaining different sizes, morphology, and shapes of NMs. The top-down method includes co-precipitation, biosynthesis, hydrothermal, chemical vapour deposition (CVD), sol-gel, physical vapor deposition (PVD), spray drying, microwave synthesis, spray pyrolysis, and atomic layer deposition (Ghassan, Mijan and Taufiq-Yap 2020; Mokhena *et al.* 2020; Vaseghi and Nematollahzadeh 2020). While bottom-up include mechanical milling, nanolithography, laser ablation, sputtering, and electrospinning (Vaseghi and Nematollahzadeh 2020). In top-down method bulk materials have been reduced to nanomaterials, and in case of bottom-up method, the nanomaterials are synthesized from elementary level.

2.5.3.1 Chemical methods

(i) Hydrothermal method

The term, hydrothermal was discovered during the 19th century by the British geologists when they simulated the hydrothermal conditions to examine the arrangement of certain minerals and rocks. Hydrothermal methods has been applied for the synthesis of single crystal growth, oxides, superionic conductors, and magnetic materials powder (Rane *et al.* 2018; Yang and Park 2019). Hydrothermal method refers to the use of an aqueous solution in a sealed reaction vessel to generate a high-temperature, high-pressure reaction environment by heating the reaction system and pressurizing it. The advantages of the hydrothermal method are convenient operation, easy synthesis process, and manageable particle size (Rane *et al.* 2018). However, it consumes more energy, need costly autoclaves, and impossible to observe the reaction process (Burova *et al.* 2019).

(ii) Ultrasound method

Ultrasound is one of the significant tools for the synthesis of nanoparticles. It is based on the radiation of liquid with ultrasonic irradiation to form the ultrasonic cavitation. This ultrasonic cavitation generates different physical and chemical effect, such as high temperature, pressure, and cooling rate, which offers a special environment for chemical reactions under extreme conditions. The advantages of using ultrasound include the use of ambient temperature and rapidity with controlled morphologies (Moghtada, Shahrouzianfar and Ashiri 2017). But it is very difficult to scale up and requires high energy supply (Rane *et al.* 2018).

(iii) Sol-gel method

Sol–gel method is one of the typical approaches used to synthesize high-quality nanoparticles and oxide composites. This approach has the ability to controls the morphology and composition properties of the synthesized materials (Zheng and Boccaccini 2017). The sol–gel method typically comprises of five steps; hydrolysis, condensation, aging, drying and calcination (Parashar, Shukla and Singh 2020) as presented in **Figure 2-13**. In step 1(hydrolysis), the precursor undergoes the hydrolysis reaction in the presence of water or organic solvents. The organic solvents can be ethanol, methanol, and propanol (Ivanova,

Kareth and Petermann 2018). Zheng and Boccaccini reveals that acidic or basic environment affects the properties of the synthesized materials (Zheng and Boccaccini 2017). Step 2 (condensation) involves the elimination of water molecule or organic solvents with the formation of metal oxide linkage. Condensation occurs by means of olation and oxolation. Step 3 (aging process), the structure and properties of the gel changes while the condensation continues, this results in the decrease of porosity and increase of particle thickness (Parashar, Shukla and Singh 2020). Step 4 (drying), the resulted material is dried using different drying methods such as atmospheric/thermal drying, supercritical drying, and freeze-drying (Parashar, Shukla and Singh 2020).Temperature and relative humidity (RH) are the most important parameters in this step. The heating of sol in high temperature causes the densification and result in the removal of pore in the gel that has low surface area and shrinkage of gel (Niederberger and Pinna 2009; Parashar, Shukla and Singh 2020). The RH affects the stability and the performance of the synthesized nanomaterial. The nanomaterial that are dried at low RH are stable compared to those dried at high (RH) (Parashar, Shukla and Singh 2020).The last step (calcination), involves the calcination of the synthesized sample in order to remove residues and water. The calcination temperature plays a significant role in controlling the diameter pores and the density of the material.

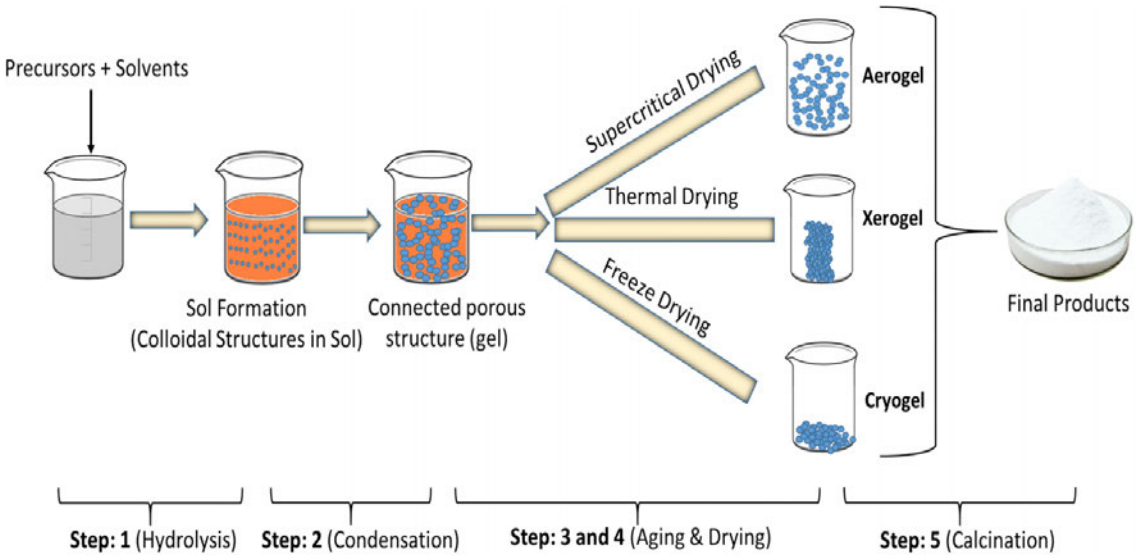

Figure 2-13: Different steps that are involved in the sol-gel process (Parashar, Shukla and Singh 2020).

(iv) Micro-wave methods

Micro-wave (MW) synthesis is one of the widely used methods for the synthesis of various nanoparticles with a controlled size distribution (Sharma *et al.* 2017a). MW method is based on preparing the mixture with the reducing agent under nitrogen atmospheric condition, and then the prepared mixture is then heated in the MW to get the mono dispersed nanoparticles. Different reducing agent such as glucose, hydrazine hydrate, and ethylene glycol are used (Iskandar *et al.* 2017; Bafana *et al.* 2018; Schütz *et al.* 2018). MV is normally employed for the preparation of trimetallics nanoparticles.

(v) Atomic layer deposition (ALD)

ALD was first discovered in 1960s by the Russian scientist and was known as molecular layering (ML) (Malygin *et al.* 2015). Afterwards, in 1970s the Finland scientists Suntola and Antson has developed the Atomic Layer Epitaxy (ALE) to deposits ZnS for electroluminescent displays (Suntola and Antson 1977; Yan *et al.* 2017). Within the following decades and up until today, the method is then referred as ALD. ALD is gas phase technique that is used for the preparation of thin film materials with conformality and excellent control over the thickness (Zhang *et al.* 2020b). This technique is based on exposing the substrate to vapor phase precursors and allows the sequential deposition of thin films in a layer-by-layer manner. The typical ALD method comprises of numerous ALD cycles with each ALD cycle consist of four representative steps, as illustrated schematically in **Figure 2-14**. In step 1, the first precursor reacts with the functional groups that are present in the substrate in a self-terminating way. Step 2, the excess of the first precursor and the vaporous by-products are purged out from the system using nitrogen or argon gas. Step 3, the second precursor reacts with the adsorbed molecules on the surface in a self-terminating way. Step 4, which is the final step, involves the removal of the unreacted precursor and the by-products in the system by purging again. This results in the deposition of a one monolayer film on the substrate surface. The preferred thickness is attained by the repetition of cycles. A wide range of materials such as oxides, nitrides, sulfides, and pure elements are prepared by ALD (Johnson, Hultqvist and Bent 2014; Lu *et al.* 2017; Weber *et al.* 2017; Ho *et al.* 2018; Ansari *et al.* 2019). These features have made ALD an appropriate technique for many applications such as energy conversion, water splitting, water purification, encapsulation, membranes,

solar cells, and batteries (Ahmed *et al.* 2017; Bachmann 2017; Shang *et al.* 2017; Feng *et al.* 2018; Yang *et al.* 2018a; Lee *et al.* 2019a; Seo *et al.* 2019; Masurkar *et al.* 2021).

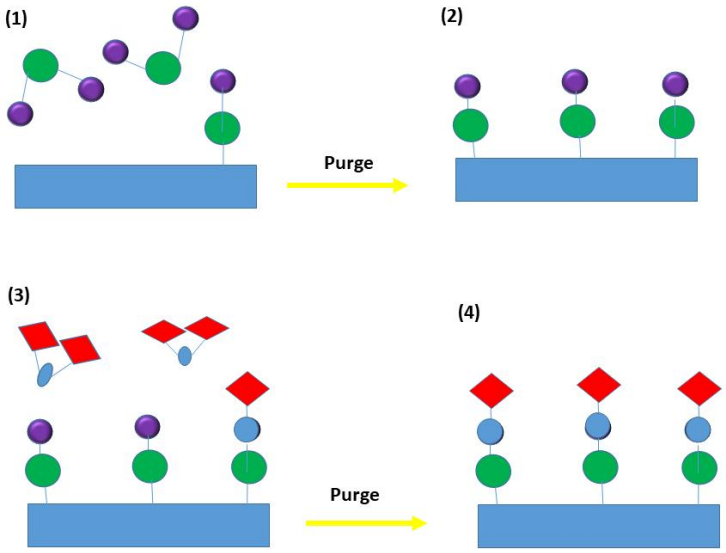

Figure 2-14: Schematic illustration of one ALD cycle process.

2.5.3.2 Green methods

The green methods also called as biogenic synthesis which is one of a promising substitute to traditional methods for the synthesis of nanoparticles. Green synthesis is an environmentally friendly approach that exploits biological sources such as plants, fungi, and virus for the synthesis of nanoparticles (**Figure 2-15**). Green approach offers a nontoxic, low-cost, and consistent manner for the synthesis of nanoparticles with variety in size, shape, morphology, and physicochemical properties. It is an attractive approach that allows the synthesis in aqueous environment with minimum expenses and low energy requirement, and can be easily scaled up to higher level (Dhuper, Panda and Nayak 2012).

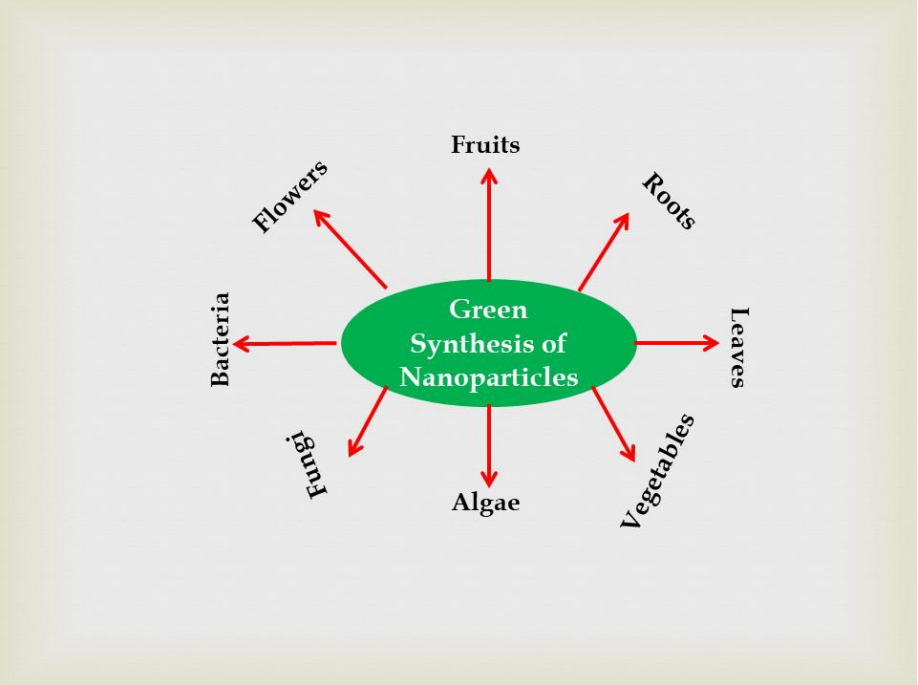

Figure 2-15: Different types of sources applied for the synthesis of metal nanoparticles.

Several studies have been carried for the synthesis of different metal nanoparticles using different biological sources as shown in **Table 2-8.** Different sources yield to different shape and size due to the biomolecules that are present in that source.

Table 2-8: Different sources applied for the synthesis of metal nanoparticles.

Source	Nanomaterials	Shape	Size(nm)	Application	Reference
Bacteria	AgNPs	Spherical	10 - 30	Antimicrobial	(Jo *et al.* 2016)
Bacteria	AuNPs	Flower	30 - 100	Antimicrobial	(Al-Akraa *et al.* 2017)
Fruits	CuNPs	-	20	Antimicrobial	(Shende *et al.* 2015)
Leaves	FeNPs	Hexagonal	21	Antibacterial	(Naseem and Farrukh 2015)
Roots	AgNPs	Spherical	10 - 30	Antibacterial	(Singh *et al.* 2016)
Algae	PdNPs	Spherical	10 – 20	Adsorbent	(Sayadi *et al.* 2018)

2.4.4 Boron nitride (BN)

BN is a chemical compound formed from equal numbers of boron (B) and nitrogen (N) atoms (**Figure 2-16**). BN was first synthesized in 1842 by using molten boric acid (H_3BO_3) and potassium cyanide (KCN) (Balmain 1842). BN has a similar structure to carbon and it's usually exists in four crystal-like forms comprising of graphite-like hexagonal BN (h-BN), diamond-like cubic BN (c-BN), rhombohedral BN (r-BN), and wurtzite BN (w-BN). These structures differs in hybridization B-N bonds (h-BN and r-BN are sp^2 hybridized while c-BN and w-BN are sp^3 hybridized) and in terms of density (h-BN and r-BN are dense while c-BN and w-BN are low-density phase) (Yu *et al.* 2018).

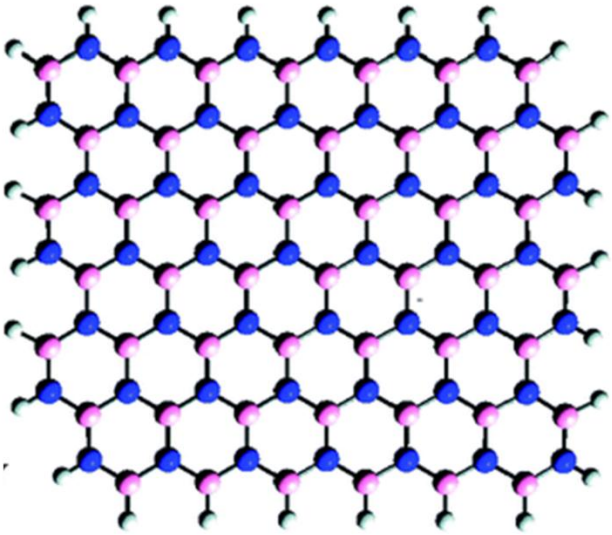

Figure 2-16: Horizontal structure diagram of h-BN. Blue, represent nitrogen atoms and pink represent boron atoms, respectively (Wang, Ma and Sun 2017).

A great attention has focused on h-BN due to it similarities to graphite, normally known as "white" graphite (Zeng *et al.* 2010). Ever since then, a massive study has been carried out for the synthesis of several BN nanostructures such as nanotubes, nanoribbons, nanowires, graphene-like…etc. (Khan *et al.* 2017; Ji *et al.* 2018; Shtansky, Firestein and Golberg 2018). BN has demonstrated outstanding properties such as high specific surface area (SSA), electrical insulation, wide energy band gap, and chemical inertness (Yu *et al.* 2018). These outstanding properties make BN a promising materials for sensor applications (Babar, Murat and Schwingenschlögl 2020). In the past few years, BN was found to be a promising candidate for support of metal atoms or nanoparticles and as the dopant, due to its fascinating properties such as high surface areas, low toxicity, and catalytic properties (Deng *et al.* 2019a; Liu *et al.* 2020a). Countless studies have been carried out using BN as a support and dopant as shown in **Table 2-9**.

Table 2-9: Different methods and application of BN.

Material	**Synthesis Method**	**Application**	**References**
Pd/BNNS	Precipitation	Hydrogenation	(Sun *et al.* 2016)
CuCo/BNNS	Impregnation process	Hydrolysis	(Yang *et al.* 2019)
Ni/BN	Impregnation process	Catalyst	(Cao *et al.* 2018)
Pd/BN	Atomic layer deposition	Sensor	(Weber *et al.* 2019b)
Ce/Tb-doped BN	Pyrolysis	Anti-counterfeiting	(Jung, Song and Kim 2019)
Sm-doped BNNTs	Thermal chemical vapour deposition	Medical therapy	(da Silva *et al.* 2018)
Ti-doped BNNTs	Computational	Adsorption	(Mananghaya 2019)
Ti-doped BNNTs	Computational	Sensor	(Al-Khaza'leh, Almahmoud and Talla 2020)

2.4.5 Graphene oxide (GO)

Carbonic materials consist of carbon atoms which is the fundamental parts of all allotropic carbonic materials. The allotropes of carbon include graphite, diamond, BC8, graphene, fullerene, etc. (**Figure 2-17**). Carbon is regarded as a versatile material element because it is not heavy and can adopt a range of structures with diverse bonding possibilities that lead to carbon allotropes exhibiting distinct properties.

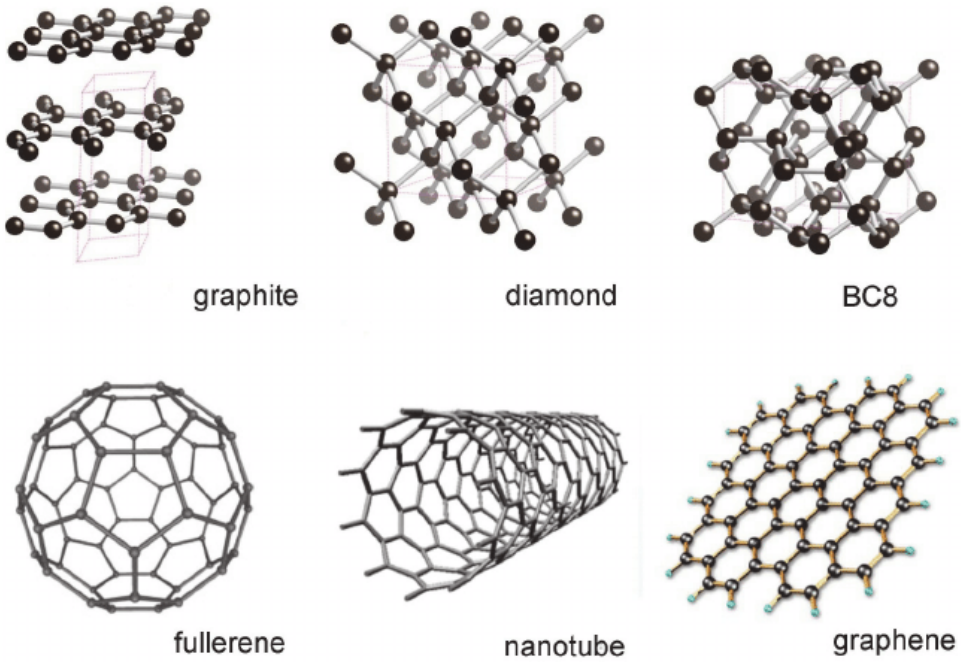

Figure 2-17: Allotropes of carbon (Giubileo *et al.* 2018).

Graphene is one of the well-known carbonic materials, alongside with its derivatives graphene oxide (GO) and reduced graphene oxide (rGO) (**Figure 2-18**). Graphene was theoretically predicted years ago as a two-dimensional (2D) crystal made of a basal monolayer of sp^2 hybridized carbon atoms disposed in hexagonal packing (Wallace 1947), but was only first produced in 2004 by Novoselov and co-workers (Novoselov *et al.* 2004). GO is a constituent of several other carbonic materials such as fullerene buckyballs, carbon nanotubes or 3D graphite (Tarcan *et al.* 2020). The π bonds that are present in graphene structure results in the remarkable mechanical properties, and extraordinary electrical properties (Lee *et al.* 2019b; Zhao *et al.* 2020). Among these derivatives of graphene, reduced graphene oxide (rGO) is preferred due to it conductivity, and easy to be synthesized from GO. rGO can be attained by eliminating of oxygen functional groups from GO using various approaches such as thermal reduction, photo reduction, electrochemical reduction, microwave reduction, solvothermal reduction, and chemical reduction. The advantages and disadvantages of the above approaches are summarized in **Table 2-10**. rGO has a wide range of application (**Figure 2-19**) due to its astonishing graphene-like properties.

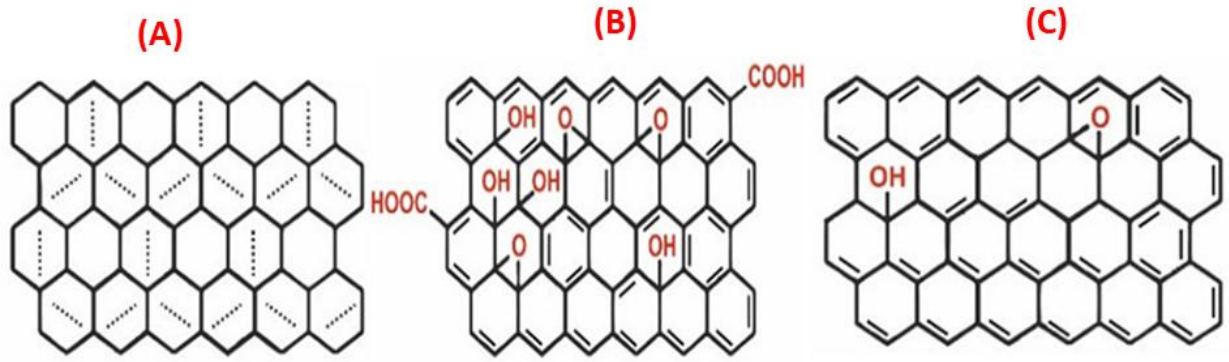

Figure 2-18: (A) Graphene (B) GO derivatives (C) and rGO (Tadyszak, Wychowaniec and Litowczenko 2018).

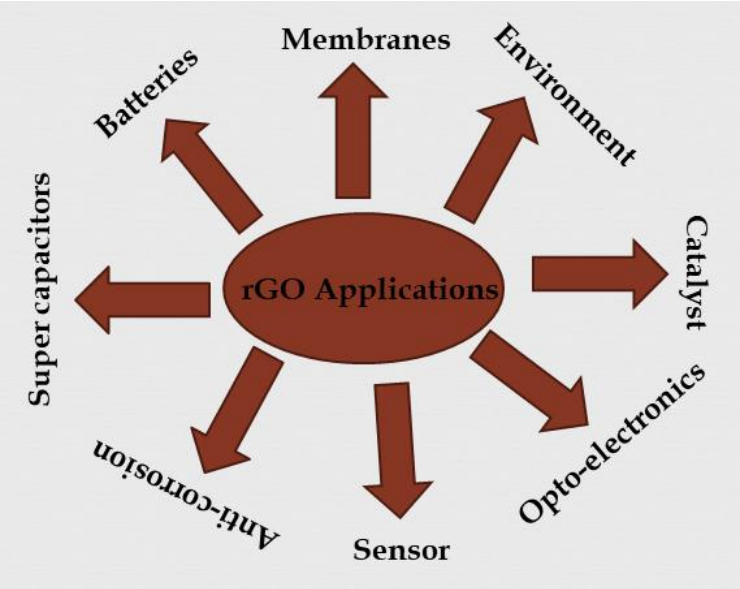

Figure 2-19: Application of rGO.

Table 2-10: Advantages and disadvantages of reduction approach used in the production of reduced graphene oxide.

Method	**Advantages**	**Disadvantages**
Thermal reduction	High reduction degree. Environmentally friendly Non expensive	Small and wrinkly rGO sheets Release of CO_2 causes structural damage
Photo reduction	Under UV Visible irradiation Easily oxygen reduction More removal of epoxy groups	Complex technique
Chemical reduction	High reduction degree Cheap High amount of reduction agent	Non environment friendlily
Solvothermal reduction	Quick Effective	Extreme thickness causes the breaking of rGO sheets
Microwave reduction	Quick reduction	Expensive technique
Electrochemical reduction	Removal of oxygen groups facilitated by electrolytes Longer rGO sheets	More defective rGO sheets

Reduced graphene oxide in sensors

Sensors are technological device that are used to detect toxins substances that are present in food samples. The detection of molecules, elements and atoms at low concentrations is essential, to monitor the safety of both human and animal health, therefore a highly sensitive sensors need to be developed. Sensors have attracted a great attention due to their sensitivity and selectivity. rGO is a good candidate for fabrication of sensors due to it extraordinary properties such as electrical, excellent thermal conductivity as well as high chemical stability and large specific surface areas (Sharma *et al.* 2017b; Shafiei *et al.* 2018). **Table 2-11** summarizes the reported sensors using rGO; it is normally incorporated with nanomaterials in order to enhance the sensitivity of the fabricated sensor.

Table 2-11: Sensors for detecting different analyte using rGO.

Electrodes	**Analyte detected**	**LOD (ng mL^{-1})**	**Reference**
rGO/Fe_3O_4	AFM_1	3.8	(Zhang *et al.* 2021)
rGO/AuNPs/PPy	AFB_1 DON	4.2 8.6	(Lu *et al.* 2016)
rGO/MoS_2/PANI@AuNPs	AFB_1	1.0×10^{-6}	(Geleta, Zhao and Wang 2018a)
rGO/Au NPs	OTA	3.4×10^{-4}	(Alhamoud *et al.* 2021)
rGO/Fe_3O_4/PPy	OTA	0.04	(Liaqat *et al.* 2021)
rGO/ZrO_2	OTA	0.079	(Gupta *et al.* 2017c)
rGO/Ni/PtNPs	AFB_1	0.70	(Molinero- Fernández *et al.* 2018)

CHAPTER 3: THEORETICAL PRINCIPLES

This chapter focuses on the theoretical principles underpinning the instruments used for the experimental work in this study. A brief overview of the relevant theoretical aspects implemented in the computational work is presented. Furthermore, the equations in relation to the operation of the techniques are presented. Special attention is given to the DFT, and molecular docking as implemented within the computational methods.

3.1 Experimental techniques

The various electrochemical techniques such as cyclic voltammetry (CV), linear sweep voltammetry (LSV), differential pulse voltammetry (DPV) and electrochemical impedance spectroscopy (EIS) are discussed below.

3.1.1 Voltammetric techniques

Voltammetry is one of the electrochemical techniques in which the current potential behavior is measured at an electrode surface. The variation of potential causes the oxidation and reduction of the electroactive species at the electrode surface, and the resultant current is proportional to the concentration of the electrochemical species. The three-electrode system is generally used, in which it comprises a working electrode (WE), where the electrochemical driven and chemical reactions occur. The reference electrode (RE) maintains the potential of the WE and counter electrode (CE), known as an auxiliary electrode transfers current to the electrodes. The voltammetric method is based on measuring the current flowing over the working electrode that is immersed in a buffer solution comprising the electro-active species. The measured current depends on the concentration of the analyte in the working electrode surface, and this is best defined by the combination of Faraday's Law and Fick's first law of diffusion: (Ismail, Oluleye and Oluwafemi 2017).

$$i_d = nFAD_0\left(\frac{\delta C_0}{\delta x}\right) \tag{3.1}$$

Where i_d is the diffusional-limited current, A is the electrode surface, D_0 is the diffusion coefficient of the analyte and $(\delta Co/\delta x)_0$ is the concentration gradient at the electrode surface.

3.1.1.1 Cyclic Voltammetry (CV)

CV is a significant and commonly used electroanalytical method in numerous area of science. It is generally applied for the investigation of redox reaction, understanding response of the reaction intermediates and attaining the stability of the reaction product (Elgrishi *et al.* 2018). This method depends on varying the applied potential at a working electrode (WE) in both forward and reversed scan while observing the current. The cyclic voltammogram displayed in **Figure 3-1** shows the applied potential (E) on the x-axis and the current (i) on the y-axis. The peak potentials (E_{pc}, E_{pa}) and peak currents (I_{pc}, I_{pa}) of the cathodic and anodic peaks respectively are the most significant parameters in a cyclic voltammogram as depicted in **Figure 3-1**. Understanding of the US and IUPAC conventions is necessary in the interpretation of CV data. The potential axis gives a hint of the convention used, as show in **Figure 3-2**A-B. According to the US convention, the potential is scanned from high potential to low potential (**Figure 3-2**A), while in the IUPAC convention, the potential is scanned from the low potential to high potential (**Figure 3-2**B). In the US convention, the reduction and oxidation peak current is at the top and bottom accordingly and vice versa for IUPAC convention. The equilibrium of the reaction is best defined by the Nernst equation. The Nernst equation describe the relationship between the electrochemical cell potential (E) to the standard potential of a species (E^0) and the relation activities of the oxidized (Ox) and reduced (Red) analyte on the equilibrium system (Noble 2017; Elgrishi *et al.* 2018).

$$E = E^0 + \frac{RT}{nF} In \frac{(Ox)}{(Red)} \tag{3.2}$$

In the equation, F is Faraday, R is the universal gas constant, n is the number of electrons, and T is the temperature. The peak potential separation between anodic and cathodic potential is used to confirm the reduction process (reversible and irreversible reaction). The fast electron transfer results in the reversible reaction and the peak separation is calculated by using the equation below:

$$\Delta E_p = E_{pa} - E_{pc} = 2.303/nF \tag{3.3}$$

where, E_{pc} and E_{pa} are assigned to the cathodic and anodic peak potential respectively, n is the number of electrons and F is the faraday constant. The reversible redox reaction at 25 °C with n electrons ΔE_p should be 0.0592/n V or about 60 mV for one electron. It is difficult to achieve this value due to cell resistance. The slow electron transfer results in the irreversible

redox reaction with $\Delta E_p > 0.0592/n$ V or greater than 70 mV for a one-electron reaction. In a reversible reaction, a concentration that is related to peak current is calculated by the Randles-Sevick expression (at 25 ^oC):

$$I_p = 2.69 \times 10^5 n^{3/2} A D^{1/2} C_O v^{1/2} \quad (3.4)$$

where I_p is the peak current, A is the electrode area, D is the diffusion coefficient, C_0 is the concentration and υ is the scan rate.

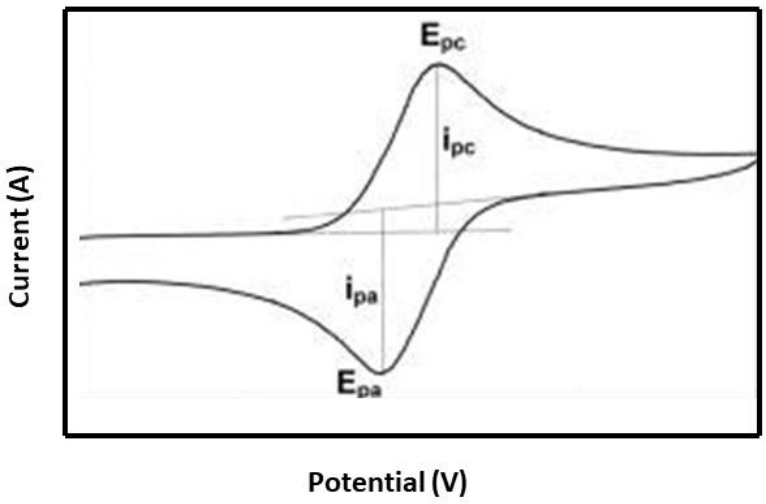

Figure 3-1: Shape of a cyclic voltammogram (Kunene 2018).

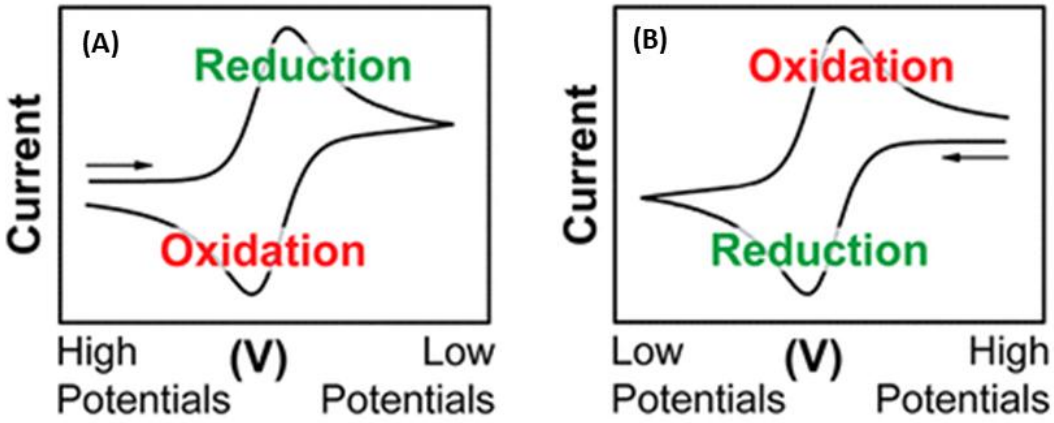

Figure 3-2: CVs for (A) US and (B) IUPAC convention (Elgrishi *et al.* 2018).

3.1.1.2 Linear sweep voltammetry

Linear sweep voltammetry (LSV) is one of the most simplest voltammetric method, where by the potential is stepped with digital potentiostat from one voltage to another at a specified scan rate (**Figure 3-3**A and B) (Borrill, Reily and Macpherson 2019). LSV is useful in evaluating the voltammetric behavior of the modified electrode surface because it comprises both the faradaic and non-faradaic current.

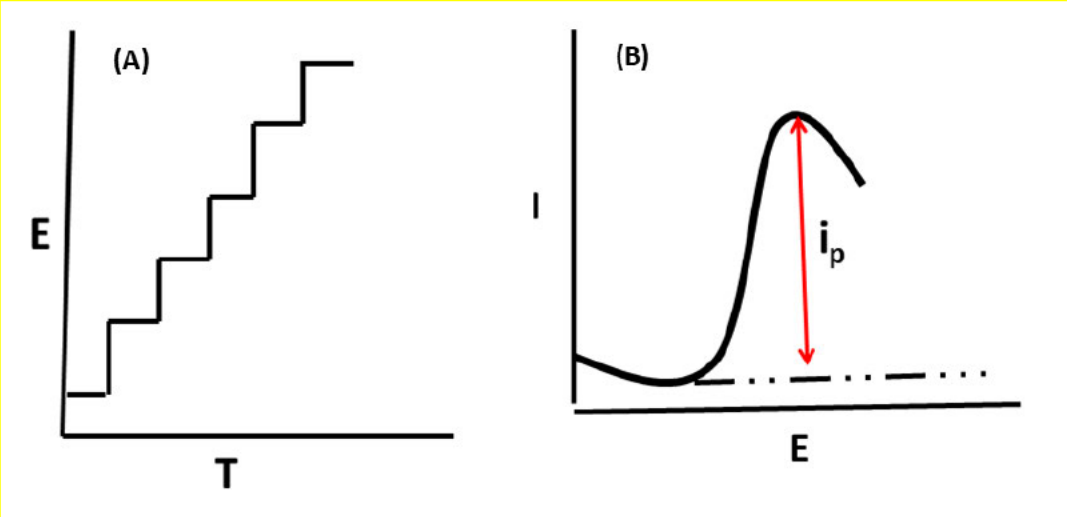

Figure 3-3: (A) The relationship between the change in potential and time (B) The digital LSV current peak.

3.1.1.3 Pulse voltammetric methods

Barker and Jenkin were the first scientists that introduced the pulse voltammetric techniques, they intended to lower the detection limits of voltammetric measurements (Inam, Demir and Uslu 2020). These techniques can be able to measure low concentration levels because their performance is improved. The traditional polarography has been replaced by the contemporary pulse techniques in the laboratory. The pulse techniques are based on a sampled current/potential-step experiment. A sequence of such potential steps, each lasting approximately 50 milliseconds, is applied to the working electrode. After a sudden change in potential, the load current drops rapidly (exponentially) to a negligible value, while the Faraday current drops more slowly. Therefore, by measuring the current at the end of the life of the pulse, an effective discrimination of the load current is achieved. The excitation

waveform and the current sampling regime differentiate the pulse voltammetric techniques as follows:

Differential Pulse Voltammetry (DPV)

Differential pulse voltammetry (DPV) is a technique in which the pulse in the fixed-magnitude is superimposed on a linear potential ramp (Scholz 2015). The relationship between the potential and time (potential wave form) is illustrated in **Figure 3-4**A**.** The current response is sampled before the pulse application and at the end of the pulse (**Figure 3-4**A**)**. The current different between the initial and final current is plotted against the applied potential. The pulse length generally takes values between 40 and 60 milliseconds, with the interval pulses varies from 0.5 to 5 s. The sampling of current just before the potential is altered; the quantity of capacitive current is reduced within the current measurement (Hoyos-Arbeláez, Vázquez and Contreras-Calderón 2017).The current response is presented by the voltammogram that present the peak current, in which the height of the peak is directly proportional to the concentration of the analyte according:

$$i_p = \frac{nFAD^{a/2}C}{\sqrt{\pi t_m}}\left(\frac{1-\sigma}{1+\sigma}\right) \qquad (3.5)$$

Where n is the number of transferred electrons, F is the Faraday constant (96485.4 C mol^{-1}), A is the electrode surface area, D is the diffusion coefficient of the analyte, C is the bulk's concentration of the analyte, t_m is the time after application of the pulse at which the current is sampled, $\sigma = \exp[(nF/RT)(\Delta E/2)]$, R is the ideal gas constant (8.314 J mol^{-1} K^{-1}), T is the temperature in Kelvin (Scholz 2015). A differential pulse voltammogram recorded is typified by **Figure 3-4**B

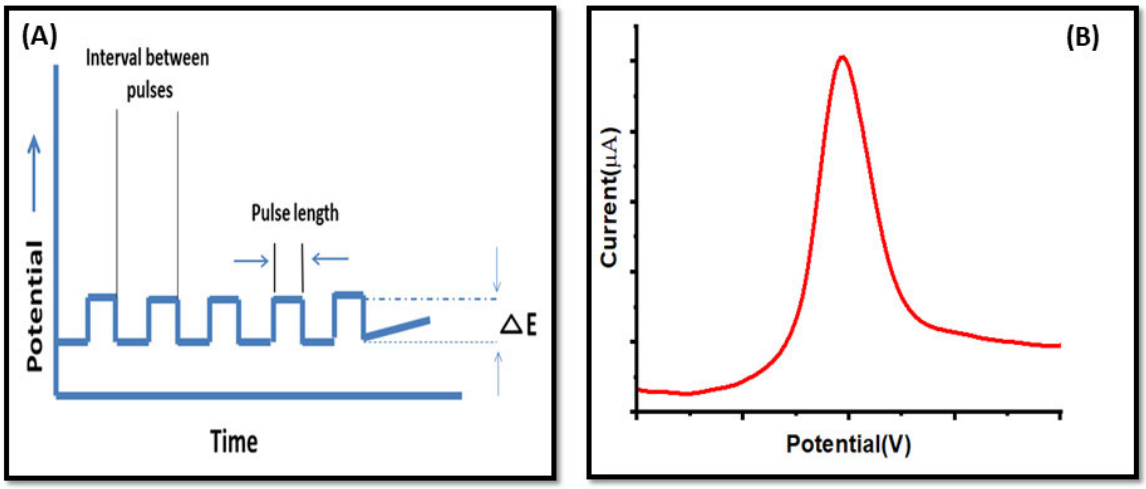

Figure 3-4: Typical (A) differential pulse wave form and (B) voltammogram.

3.1.2 Electrochemical impedance spectroscopy (EIS)

EIS is conducted in order to study the electrochemical behavior of a system, therefore in plays a major role in the electrochemical research. It is the one of the most popular and powerful technique that is extensively applied in numerous applications such as corrosion monitoring, coatings evaluation, semiconductor characterization, and biosensors (Husain, Chakkamalayath and Al-Bahar 2017; Bouferra *et al.* 2019; Khadka *et al.* 2019; Li *et al.* 2020b). In biosensor application it is used in the detection of binding events on the transducer surface (Muñoz, Montes and Baeza 2017). The impedance response is measured at different frequencies range of the imposed alternating voltage and it's separated into real and imaginary components. The attained response between the real and imaginary components is represented by Cole–Cole (Nyquist) plot (**Figure 3-5**). The Cole–Cole plot is normally simulated with an equivalent circuit (**Figure 3-6**) comprises of ohmic resistance (R_s), double layer capacitance (C_{dl}), charge transfer resistance (R_{ct}) and the Warburg impedance element (Z_w), in which the electrolyte solution interphase is virtually structured (Kunene *et al.* 2020). Therefore, EIS can be used for the characterization of the electrode surface.

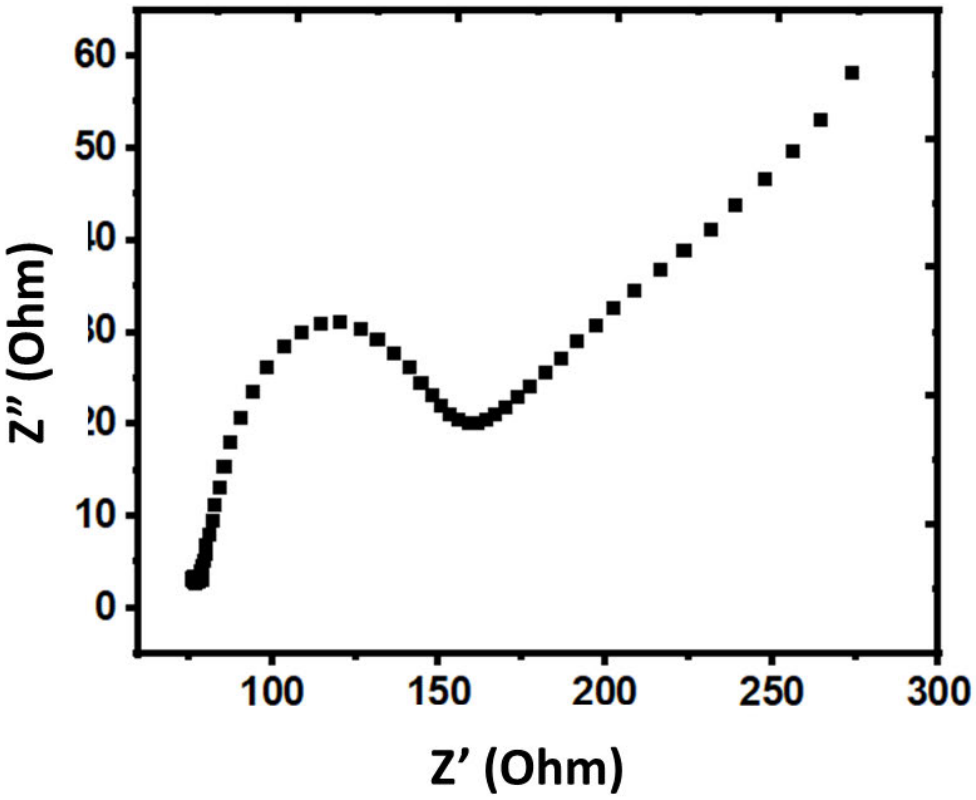

Figure 3-5: Cole-Cole (Nyquist) plot.

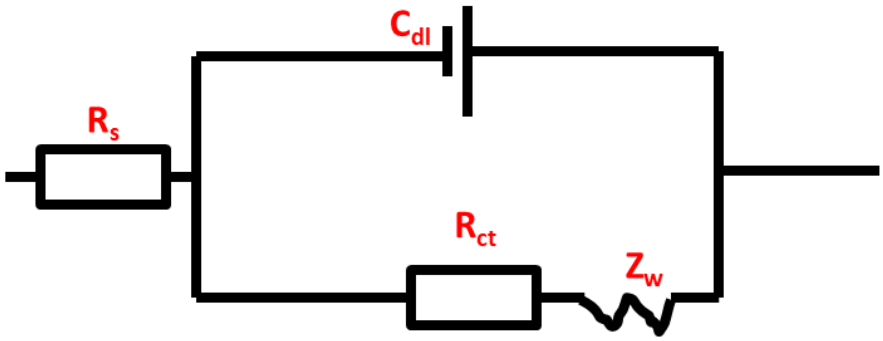

Figure 3-6: Equivalent circuit model.

3.1.3 Experimental set-up and instrumentation

The voltammetric instrumentation set-up is very complex compared to potentiometric techniques. The potentiostat is one of the important requirements for the voltammetric instrumentation, because they monitor the applied potential and regulate the current in the working electrode. The Nobel Prize winners in 1959 Jaroslav Heyrovsky in 1922 develop the voltammetric techniques (Scholz 2011). Electrochemical studies are conducted in an electrolytic cell which consist of working electrode (WE), reference electrode (RE), counter electrode (CE) and an inert salt solution (supporting electrolyte) that aids effective transfer of ions across the electrodes **(Figure 3-7)**. The RE functions controls the capacitance of the working electrode and it's allow the measurement of the potential at the working electrode without passing current through it. WE monitors the oxidation or reduction of a species near the surface of the electrode, while the CE completes the circuit and allow the charge to flow. CE are typically required to avoid passing current through the reference electrode. Otherwise, the potential changes due to the changes in the activity of different species. The electrical circuit through which the current flows is located between the working (indicator) electrode and the auxiliary electrode. The potentiostat drives the three electrodes **(Figure 3-7)** and allows direct control of a computer which displays the measured signal. The digital signal can be converted to a signal using a digital-to-analog converter, and the response, if necessary, re-digitized using an analog-to-digital converter. Control and collection of signal data can be accessibly accomplished with a personal computer through the appropriate interface in the digital potentiostat.

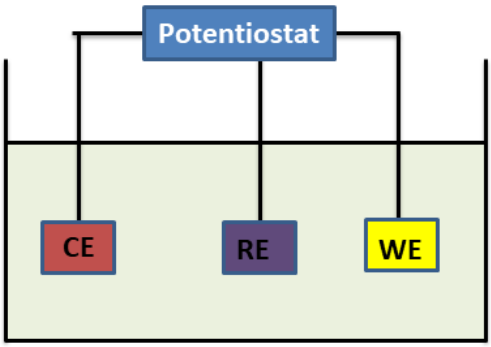

Figure 3-7: Three electrode system.

3.2 Computational methods

Computational methods are applied to attain a better understanding about the interactions between a protein, enzyme, and DNA with ligands (Liu *et al.* 2018c; Zhdanov 2019). The electronic structure can be examined using different methods such as molecular docking (MD) studies (Pagadala, Syed and Tuszynski 2017), density functional theory calculations (DFT) (Reimers *et al.* 2018), molecular dynamic (MD) simulation (Zarringhalam *et al.* 2019), and Monte Carlo simulations (Andersen, Panosetti and Reuter 2019b).

3.2.1 Molecular docking studies

Docking studies are applied for the prediction of the structure of the ligand and estimation of binding strength of the protein (Waszkowycz, Clark and Gancia 2011). Molecular docking studies have attracted a considerable attention in drug discovery as a tool for the prediction of protein because most of the protein structures are predicted experimentally using x-ray crystallography or nuclear magnetic resonance (NMR) spectroscopy. It is possible to perform docking studies on the proteins that has unknown structures using homology-modeled target. The druggability of the compounds and binding affinity of the target are evaluated by the optimization procedure (Pagadala, Syed and Tuszynski 2017). Docking programs employ the algorithm search with protein–protein docking method to predict the binding mode (s) of the ligand to the 3-dimensional protein of interest up until the minimum energy is reached.

3.2.2 Density functional theory (DFT)

DFT was initial discovered in 1964 by Hohenberg and Kohn (Hohenberg and Kohn 1964). DFT studies used in the simulation of adsorption process and in understanding the interaction mechanism of the modified electrode (Obot, Macdonald and Gasem 2015; Ghalkhani, Beheshtian and Salehi 2016). The precision of DFT calculations is based on the choice of functionals that are used. The development and the application of DFT is based on the key principles such as Schrödinger equation, Born-Oppenheimer approximation, Hartree-fock approximation, Hohenberg-Kohn Theorem, and Kohn-Slam equation.

3.2.2.1 Schrödinger equation

The Schrödinger equation is one of the most important mathematical equations and is the foundation of many applications in quantum mechanics. This equation describes the wave function or state function of a system. It is applied in chemical approaches, solving the time independent aids in the description of molecular, atomic, and subatomic systems (Itti and Koch 2001; Lewars 2011). Schrödinger equation has been revised by Kohn and Sham in order to attain the complex electron interactions through an "exchange-correlation" functional, where they concluded by basing approximations of this functional on gas models, but up to date the exact form of this functional is not exactly known (Ziegler *et al.* 2008). The most significant Schrodinger's equation includes the partial differential equations for the wave function (equation 3.6) and a single particle that is moving in the electric field (equation 3.7).

$$íħ\frac{\partial}{\partial t}\,\Psi(r,t) = \hat{H}\,\Psi(r,t) \qquad (3.6)$$

Where i is the imaginary unit, ħ is the Planck constant divided by 2π, *∂*/*∂*t specifies a partial derivative with respect to time t, Ψ is the wave function of the quantum system, and Ĥ is the Hamiltonian operator.

$$íħ\frac{\partial}{\partial t}\,\Psi(r,t) = \left[\frac{-ħ^2}{2\mu}\nabla^2 + V\,(r,t)\right]\Psi(r,t) \qquad (3.7)$$

The second equation applies to a single particle moving in an electric field. Where, μ is the particle's "reduced mass", V is its potential energy, ∇ sup (2) is the Laplacian differential operator.

3.2.2.2 Born-Oppenheimer (BO) approximation

Born-Oppenheimer (BO) approximation is the typical mathematical tool that is used to study the molecular system. This approximation assumes that the wave functions of atomic nuclei and electrons in a molecule can be treated independently, based on the fact that the nuclei are much heavier than the electrons. BO approximation was first discovered in 1927, during the period of quantum mechanics, by Born and Oppenheimer and it still imperative in quantum chemistry. The BO approximation is applied to determine the potential energy by the ab initio electronic structure calculations using the following equation:

$$\Psi = \Psi_e(\mathrm{r},\mathrm{R})\Psi_n(R) \quad (3.8)$$

Where Ψ_e is the electronic wave function, which depends on the electron coordinates r and nuclear coordinates R, and Ψ_n is the nuclear wave function.

3.2.2.3 Hartree-Fock (HF) approximation

HF also known as self-consistent field method (SCF) is one of the uncomplicated approximates theories that are applied in solving the Schrödinger equation. It is based on an approximation of the wave function and the energy of a quantum many-body system in a motionless state. HF approximation regularly presumes that the exact *N*-body wave function of the system can be approximated by a single Slater determinant (in the case where the particles are fermions) or by a single permanent (in the case of bosons) of *N* spin-orbitals. By invoking the variational method, a set of *N*-coupled equations for the *N* spin orbitals can be derived. A solution of these equations yields the Hartree–Fock wave function and energy of the system.

3.2.2.4 Hohenberg-Kohn Theorem

The first Hohenberg–Kohn theorem in DFT, states that the electron density alone can be able to determine the ground state of any property. The electron density functional can accurately determine the exchange and correlation energies such properties molecular structure and chemical reactivity (Rong *et al.* 2020). Then the ground-state energy E as a functional of the ground-state density can be determined using the following equation:

$$E\left[\Psi[n_o]\right] = < \Psi[n_o]\,|\hat{T} + \hat{V} + \hat{U}|\Psi[n_0] > \quad (3.9)$$

Even though the first Hohenberg–Kohn theorem carefully confirms that a functional of the electron density $E[n(0)]$ exists, the theorem says nothing about the actual form of the functional. The second Hohenberg–Kohn theorem describes a valuable property of the functional and states that the electron density that reduces the energy of the overall functional is the true electron density corresponding to the full solutions of the Schrödinger equation (Sholl and Steckel 2009). If the true functional form is known, then the minimization of

energy is carried out by varying the electron density, to find the ground-state electron density. When the ground-state electron density is known, all the molecular properties can be calculated from the electron density.

3.2.2.5 The Kohn-Sham equation

The Kohn-Sham equation is one of the most essential equations of density functional theory. This equation shows that the motion of the interacting electrons can be treated the same as a system of independent particles. The electrons can be considered as if they moved in a common effective local potential. Kohn-Sham method can be applied to calculate the motion of the interacting electrons using the following equation.

$$\left[-\frac{\nabla^2}{2m} + V_{ext}(r) + V_H(r) + V_{xc}(r)\right]\phi_n(r) = \varepsilon_n\phi_n(r) \qquad (3.10)$$

3.2.3 Molecular dynamics simulations

The molecular dynamics (MD) simulation is applied to investigate the structure and thermodynamics of the biomolecules (Chen, Brooks III and Khandogin 2008). The simulations is also applicable to study the physical behavior of the biological macromolecules, and gives the information about the interaction between the protein and ligand (Liu *et al.* 2018b). Simulations understand the biochemical processes and give a dynamic dimension to structural data. MD simulation is generally employed in the drug discovery.

3.2.4 Force fields

A force field (FF) is one of the mathematical expressions that describe the dependency of the energy of a system on the coordinates of its particles. It comprises of an analytical form of the interatomic potential energy, $U = (r_1, r_2, \ldots\ldots, r_n)$. These parameters are classically attained either from *ab initio* or semi-empirical quantum mechanical calculations or by fitting to experimental data such as neutron, x-ray and electron diffraction, NMR, infrared, raman

and neutron spectroscopy, etc. (González 2011). Literature revealed that they are many force fields that are available such as GAFF, AMBER ff94, PRODRGFF, and CGenFF (Zhang *et al.* 2018c; Zhu 2019; Luczkowska *et al.* 2020). These force fields have distinct degrees of complexity and designed to handle different kinds of systems.

3.2.4.1 COMPASS

The COMPASS is one of the force field (FF) that is applied for simulating of various materials such as polymers, cellulose, and carbons (Asche, Behrens and Schneider 2017; Wang *et al.* 2017b; Savin and Mazo 2020).This FF predicts the structural, electrical, thermal, and mechanical properties of the targeted materials (Savin and Mazo 2020). This FF is usually parameterized using *ab initio* and hundreds of molecules as a training set. The parameters precisely identify the frequency spectrum of the atomic vibrations of the materials. However, it failed to describe the frequency spectrum of the target material. The molecular mechanics and dynamic calculation is applied to validate the COMPASS FF parametrization (Asche, Behrens and Schneider 2017).

3.2.4.2 Universal force field (UFF)

The UFF is generally employed in the prediction of structure, calculating bond lengths and angles of the organic molecules (Casewit, Colwell and Rappe 1992). UFF is an all-atom force field that has parameterizations of all atoms present in the periodic table with atomic number lower than 103. The flexibility of UFF makes it suitable to generate a wide spectrum of systems, which has been shown by means of the evaluations of organic molecules, main group compounds, metal complexes, and Metal-Organic Framework (MOFs) (Boyd *et al.* 2017; Lunghi and Sanvito 2019; Song *et al.* 2020). The UFF is different to other force fields because it does not use the partial energies from electrostatic interactions, hence it cannot handle hydrogen bonds therefore XUFF method was then established (Jász *et al.* 2019).

3.2.4.3 DREIDING

DREIDING is a common force field that is applied in several computational chemistry software such as Material Studio and SciMAPS (Sasaki and Yamashita 2021). It is normally useful in structure prediction and dynamic of organic, biological, and main-group inorganic molecules (Deng *et al.* 2019b). The DREIDING force field (DFF) has an explicit van der Waals force term, which can be used to describe hetero-interatomic interactions by the Lorentz–Berthelot mixing rules in biological systems (Deng *et al.* 2019b). Furthermore, it can describe best the hydrogen bond and Coulomb force. These two forces are very significant for the applications in biological systems because several ions occur in biological systems, and the hydrogen bond needs to be considered due to the existence of water and functional groups of organic molecules (Deng *et al.* 2019b). DFF is one of the flexible force fields because it allows the addition of possible combination of atoms and new atoms.

3.2.5 Monte Carlo simulations

The Monte Carlo (MC) simulations is one of the versatile approaches that have gained great attention in computational chemistry. MC simulation is based on the Basin Hopping method for global geometry optimization (Paleico and Behler 2020). It is a common tool that describes a range of phenomena associated with diffusion, structures and properties of materials or equilibrium and non-equilibrium chemistry (Andersen, Panosetti and Reuter 2019). The MC is particularly appropriate to hierarchical multi scale modeling approaches, where information at different levels of accuracy or detail is integrated to provide a more comprehensive description. MC is an important approach to bridge the gap between the microscopic world (elementary processes such as atomistic diffusion jumps or the making and breaking of chemical bonds) and the meso- to macroscopic world (e.g., a diffusion constant or a reaction rate) (Andersen, Panosetti and Reuter 2019).

CHAPTER 4: MATERIALS AND METHODS

This chapter focuses on the materials and research design used in this study. The synthesis and characterization of different nanomaterials along with the fabrication of the electrochemical aptasensor and immunosensor are described here.

4.1 Experimental methods

4.1.1 Reagents and Materials

Ammonia (NH_3) (Air Liquide Paris, France), L-Cysteine (L-Cy), N-hydroxysuccinimide (NHS), N-ethyl-N-(3-dimethylaminopropylcarbodimide (EDC), aflatoxin B1 (AFB_1), ochratoxin A (OTA), ethanol, potassium ferricyanide/ferrocyanide $[Fe(CN)_6]^{3-/4-}$, acetonitrile (ACN), boron tribromide (BBr_3), dipotassium hydrogen phosphate (K_2HPO_4), potassium dihydrogen phosphate (KH_2PO_4), sulphuric acid (H_2SO_4), formaldehyde solution (CH_2O), titanium chloride ($TiCl_4$), bovine serum albumin (BSA), palladium (II) hexafluoroacetylacetonate ($Pd(hfac)_2$ and anti-AFB_1 produced in rabbit were purchased from Sigma Aldrich France. Graphite powder, silver nitrate ($AgNO_3$), chitosan (CS), potassium manganite (VII) ($KMnO_4$), sodium nitrate ($NaNO_3$), monosodium phosphate (NaH_2PO_4) and disodium phosphate (Na_2HPO_4) were purchased from Sigma-Aldrich, Durban, SA. Hydrogen peroxide (H_2O_2) (30%, w/w), hydrochloric acid (HCl) (37%, v/v) were purchased from Laboratory supplies (Pty) LTD, Durban, SA. Phosphate buffered saline tablet (PBS). The red wine was obtained from the local supermarket in Montpellier, France. Nescafe (NES, Vevey, Switzerland) obtained from a local supermarket. Amadumbe (*Colocasia esculenta*) and Weet-Bix were collected from the local market, Durban. Monoclonal antibody anti-ochratoxin A (anti-OTA) (Catalog #: ICP9948, 250 μg mL^{-1} in PBS 50% glycerol) was obtained from Immune Chem Pharmaceutical Incl (Canada). The oligonucleotides related to OTA and AFB_1 were provided by WhiteSci, Whitehead Scientific (Pty) Ltd (Durban, SA), and Sigma Aldrich France respectively. The sequence of oligonucleotides related to OTA and AFB_1 was as follows:

5′-GATCGGGTGTGGGTGGCGTAAAGGGAGCATCGGACA-3′, 5′-thionine (Zhang, Xu and Qiang 2020), 5′-GTT GGG CAC GTG TTG TCT CTC TGT GTC TCG TGC CCT TCG CTA GGC CC-3′, 5-NH_2-$(CH2)_6$ (Kong *et al.* 2018). The selected aptasensor sequence was then synthesized by WhiteSci, Whitehead Scientific (Pty) Ltd (Durban, SA)

Sigma Aldrich France respectively. Ultrapure water (Mill-Q, Millipore, 18.2 M Ω resistivity) was used for the entire experiments.

4.1.2 Instrumentation

The electrochemical measurements such differential pulse voltammetry (DPV), cyclic voltammetry (CV), linear sweep voltammetry (LSV) and electrochemical impedance spectroscopies (EIS) were performed at room temperature (~25.0 °C) using different electrochemical techniques. A portable combined bipotentiostat/galvanostat and spectrometer with light source called SPELEC VIS-NIR Instrument (350-1050 nm) (Metrohm DropSens, Durban, SA) which is controlled with the SPELEC software, a SP-150 EC-LAB electrochemistry chemical workstation (VSP Potentiostat from BioLogic Science Instruments, France) and a Solartron 1286 electrochemical interface (TICS International Ltd., UK),was used for electrochemical measurements. The three-electrode configuration comprising of a working electrode (WE), a counter electrode (CE) and a reference electrode (RE) was used in this study. The electrodes were designed on the ceramic substrate by Metrohm DropSens, Durban, SA. The strip's general dimensions: 3.4 x 1.0 x 0.05 cm, and the WE diameter was 4 mm with the 0.11 cm^2. Carbon felts (CF) MGL 190, fuel cell earth (10 Draper St. Unit 32 Woburn, MA, MA 01801 www.Fuelearth.com) were also used as the electrodes using a three electrode system: modified carbon felt (CF, 3.5 cm length, 0.7 cm width and 0.3 cm thickness) as a working electrode, a graphite rod as the auxiliary electrode and Ag/AgCl as the reference electrode. The modified CF electrodes were characterized by scanning electron microscopy (SEM, Hitachi S-4800) and Transmission electron microscopy (TEM, JEOL 2200FS (200 kV), The contact angle (CA) measurements were conducted on a homemade contact angle setup. During measurement, a drop of deionized water was deposited over the electrode surface and the angle of the liquid surface with contact surface was observed at the solid-liquid interface. Attenuated total reflectance (ATR) spectra were collected using iS50 ATR Thermo scientific spectrophotometer. Atomic Force Microscope (AFM, Veeco Nanoscope Dimension 3100) was used for the morphological characterization of the fabricated immunosensor. The UV–Vis spectrophotometer Cary UV 50, from Varian, was used to investigate the optical properties of graphene oxide and reduced graphene oxide. All spectra were recorded from 200 to 800 nm. The ATR spectra were recorded in the range 200-4000 cm^{-1} on a Cary 630 FTIR Spectrometer (Agilent Technologies, Johannesburg, SA).

An oven (model PF 200, ProLab oven, Pretoria, SA) that can go up to 250 °C was used for drying purposes was employed in this study. A 781 pH/Ion Meter (Metrohm DropSens, Durban, SA) was used for all the pH optimization measurements.

The Dynamic light scattering (DLS) measurements were conducted in the Zetasizer (Nano ZS, Malvern Instruments Ltd, UK) AF4-MALS (AF2000 Multiflow, Postnova Analytics) was used to measure the diameter of the nanomaterials. spICP-MS spectrometer (PerkinElmer, NexION 2000) was used to determine the particle size. Photoluminescence studies were evaluated by using eclipse Flourescence spectrophotometer (Agilent technologies). Waters Quattro Micro LC/MS-MS, Quattro Miro API by Waters Alliance was used to identify the biomolecules that are present in the amadumbe extract. X-ray Photoelectron Spectroscopy (XPS) (ESCALAB 250 Thermo Electron) with Al-Ka (1486.6 eV), where the binding energies were calibrated using carbon (C 1s = 284.4 eV), was used to determine the chemical composition of the grown nanomaterials. The Zeta potential was measured using Litesizer 500, particle analyser Anton Paar instrument, Germany.

4.1.3 Pre-treatment of carbon screen printed electrode (C-SPE) and carbon felts electrode (CFE)

The C-SPEs were first activated by applying a fixed current of 3 μA for 2 min in 0.1 M H_2SO_4 solution and then, rinsed thoroughly with MilliQ-water and 0.1 M PBS, pH 7.0 (Rivas *et al.* 2015). The pre-treatment of CF was carried out in order to improve the hydrophobic nature of CF to hydrophilic by following the method that was reported in literature (Kosimaningrum *et al.* 2017). To eliminate the impurities that might be present on the carbon felts (CF) surface, CF were first ultra-sonicated in ethanol for 2 h, washed with water and dried in an oven at 70 °C for overnight. The cleaned CF was then electrochemically pretreated in 1 M H_2SO_4 by cyclic voltammetry (CV) from 0 to 1.5 V versus Ag/AgCl for 30 cycles at 20.0 m Vs^{-1}. Then, the samples were thoroughly washed with water until a neutral pH was recorded, and finally dried in the oven at 70 °C for overnight.

4.1.4 Preparation of working solutions

Different working solutions were prepared in distilled water, or otherwise stated.

4.1.4.1 Preparation of phosphate buffer solution

0.1 M phosphate buffer solution (PBS) was prepared by dissolving dipotassium hydrogen phosphate (K_2HPO_4) and potassium dihydrogen phosphate (KH_2PO) in the separate volumetric flask in Millipore water. Different pH (6.0, 6.5, 7.0, 7.5 and 8.0) was then prepared by mixing certain volume of mono and di-hydrogen phosphate solutions (see **Table 4-1**). The PBS was kept in refrigerator at 4 °C for not more than 2 weeks.

Table 4-1: Preparation of PBS at pH ranging from 6 – 8.

pH	**Volume of K_2HPO_4 (mL)**	**Volume of KH_2PO_4 (mL)**
6.0	6.60	43.40
6.5	13.90	36.10
7.0	30.75	19.25
7.5	40.10	9.90
8.0	47.00	3.00

4.1.4.2 Preparation of 5 mM $[Fe(CN)_6]^{3-/4-}$

The 5 mM $[Fe(CN)_6]^{3-/4-}$ in 0.1 M KCl solution was prepared by dissolving ferricyanide $[Fe(CN)_6]^{3-}$ and ferrocyanide $[Fe(CN)_6]^{4-}$ salt respectively in volumetric flask that contains a 0.1 M KCl solution.

4.1.4.3 Preparation of OTA and AFB_1 stock solution

The stock solution of AFB_1 and OTA was prepared in phosphate buffer (0.1 M, pH 7.5) with 10% methanol and stored at 20 °C. Different concentrations of OTA and AFB_1 was then prepared from the stock solution using standard dilution method in a PBS.

4.1.5 Synthesis of nanostructures

Different nanostructures were synthesized using different methods. Silver nanoparticles (AgNPs) was synthesized by a green method, palladium nanoparticles (PdNPs), palladium nanoparticles supported on boron nitride (PdNPs-BN) and titanium doped boron nitride nanoparticles (BN-TiO_2) were synthesized by atomic layer deposition (ALD). Graphene oxide (GO) and reduced graphene oxide (rGO) were synthesized by a modified hummers method.

4.1.5.1 Synthesis of AgNPs by Green method

The biogenic synthesis of AgNPs was conducted according to the method reported previously (Tamileswari *et al.* 2015). Amadumbe (*Colocasia esculenta*) were collected at the local market, South Africa, Durban and stored at 4 °C before use. Amadumbe were thoroughly washed with tap water, followed with deionized distilled water, and cut into small pieces. To obtain the aqueous extract, 5.0 g of amadumbe pieces were boiled in 100 mL deionized water for 40 min and allowed to cool at room temperature. After cooling it was filtered through No.1 Whatmann filter paper. The filtrate was then used as the reducing agent for the synthesis of AgNPs by adding 4.0 mL to 8.0 mL of 1 mM aqueous of $AgNO_3$: the mixture was then stirred at 150 rpm at 80 °C for 30 min (**Scheme 4-1**). The reduction of Ag^+ to Ag^0 was observed at 30 min by a colour change from colorless to brown and it was monitored by UV-Visible spectroscopy.

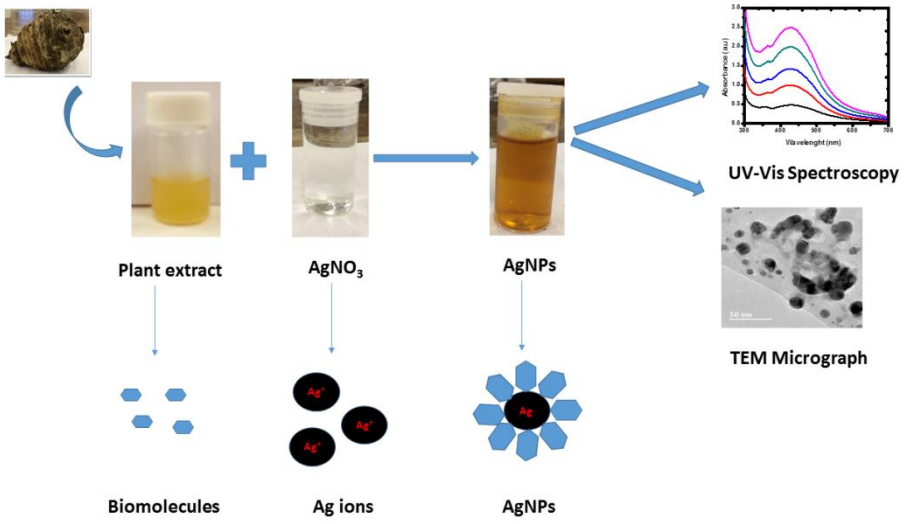

Scheme 4-1: Synthesis of AgNPs by the green chemistry method.

4.1.5.2 Synthesis of palladium nanoparticles (PdNPs) by atomic layer deposition (ALD)

The synthesis of PdNPs was achieved by applying different ALD cycles (100, 200 and 300) on the carbon felt (CF) electrode supported using a low-pressure hot-wall (home-built) ALD reactor, which has been described previously (Graniel *et al.* 2018b; Weber *et al.* 2019a). Briefly, the typical ALD cycle consisted of 5s pulse of palladium (II) hexafluoroacetylacetonate $Pd(hfac)_2$, 15 s exposure, and 10 s purge, followed by a 1 s pulse of formalin, 15 s exposure and 60 s purge with argon (**Scheme 4-2**).

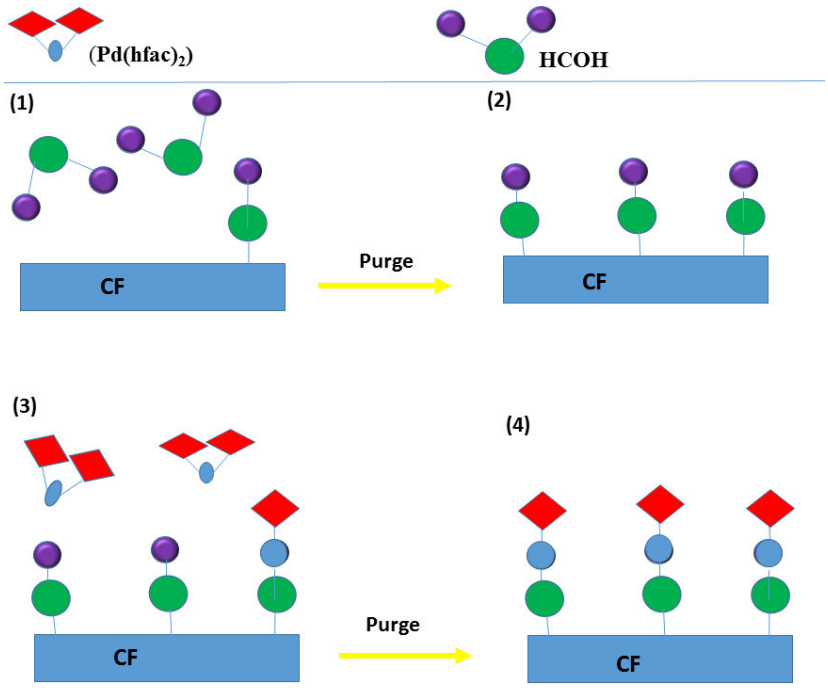

Scheme 4-2: Schematic representation of PdNPs synthesis by atomic layer deposition (ALD) using carbon felt as the substrate.

4.1.5.3 Synthesis of palladium nanoparticles on boron nitride (PdNPs-BN) by atomic layer deposition (ALD)

The home made ALD reactor was used for the deposition of boron nitride (BN) and palladium nanoparticles (PdNPs) onto the surface of CF. This low pressure ALD reactor has been reported in the literature (Weber *et al.* 2019d).The deposition of BN onto the CF was carried out using the method that was reported by Weber and co-workers (Weber *et al.* 2019c). The boron nitride (BN) process is based on boron tribromide (BBr_3) and ammonia (NH_3) as precursor and co-reactant, respectively. In order to avoid the condensation, the precursor and the co-reactant lines are directly connected to the reactor through gate valves and heated at 100 °C. The temperature of the chamber was set at 750 °C. The typical ALD cycle consists of 0.1 s pulse of BBr_3, 5 s of exposure, and 15 s purge followed by a 3 s pulse of NH_3, 5 s exposure and 15 s purge with argon (Ar). The as-fabricated samples of BN are referred to as CF/BN. The deposition of PdNPs on the surface of CF/BN was carried out following our recent work (Kunene *et al.* 2020). Briefly, 200 ALD cycles was then deposited on the CF/BN using low-pressure hot-wall (home-built) ALD reactor. The deposition of PdNPs on the CF/BN surface was carried out using a Pd precursor palladium (II) hexafluoroacetylacetonate ($Pd(hfac)_2$) and co-reactant, formalin (HCOH), and argon as the

carrier gas. The exposure conditions for the Pd and formalin were as follows, 5 s pulse, 15 s of gas exposure and 1 s pulse, 15 s of gas exposure.

4.1.5.4 Synthesis of titanium nanoparticles doped boron nitride (BN-TiO_2) by atomic layer deposition (ALD)

The homemade ALD reactor was used for the deposition of titanium nanoparticles (TiO_2) onto the carbon felt (CF) surface. The TiO_2 process is based on titanium chloride ($TiCl_4$) (0.5 s exposure) and water (H_2O) (0.5 s exposure) as precursor at 200 °C. In order to deposit BN over TiO_2, the ALD technique was applied. The ALD of BN thin film was deposited using tribromide (BBr_3) and ammonia (NH_3) as precursor and co-reactant respectively. To avoid the condensation between BBr_3 and NH_3, the reactor was heated at 100 °C, while the deposition chamber was set at 750 °C. The sequential step of the ALD cycle consisted of a 0.1 s pulse of BBr_3, 5 s exposures, and 15 s purge, followed by a 3 s pulse of NH_3, 5 s exposure and 15 s purge with argon. Different ALD cycle (10, 25, 50 and 100) were deposited over TiO_2 to get the optimum ALD cycle. Deposition of NH_3, BBr_3 onto TiO_2 were also carried out using the same ALD procedure. The only difference is that we use BBr_3 without NH_3 and NH_3 without BBr_3 alone as precursors. After all the procedures, a result in the four sets (i) CF/TiO_2, (ii) CF/ BN-TiO_2, (iii) CF/BBr_3-TiO_2 and CF/NH_3-TiO_2.

4.1.5.5 Synthesis of GO and rGO by modified Hummers methods

Graphene oxide (GO) was synthesized from natural graphite according to the modified Hummers' method (Guerrero-Contreras and Caballero-Briones 2015; Zaaba *et al.* 2017). The $KMnO_4$ and $NaNO_3$ were used to oxidize graphite in the concentrated H_2SO_4. Primarily, 1.2 g of graphite powder and 2.0 g of $NaNO_3$ were added in 50 mL of concentrated H_2SO_4. The reaction mixture stirred in the ice bath for 2 h, sustaining the temperature ranges from 0−6 °C, thereafter 6.0 g of $KMnO_4$ was gently added to the reaction mixture. The reaction was constantly stirred for 2 h, then removed in the ice bath and stirred at 30 °C for 2 h and the reaction mixture turns into a brownish paste. 100 mL of water was thereafter added into the reaction in order to weaken the paste followed by the addition of 8.0 mL of H_2O_2 which resulted to a colour change from brownish to golden yellow. The visual marker was an indication of the formation of GO. The resulted mixture was centrifuged, washed with 8%

HCl, then deionized water for numerous times. The residue was then dried in the oven at 60 °C for 12 h and crushed into fine powder. The reduced graphene oxide (rGO) was attained by using the existing method with slight modifications using chitosan as a reducing agent (Ye *et al.* 2015). The reduction of GO was carried out by adding 1.0 mL of GO suspension into 10.0 mL of chitosan (10.0 mg mL^{-1} in 1.0% acetic acid) under vigorously stirring. The reaction was allowed to react at 90 °C for 9 h, in which GO was reduced. The resulted product was dried at 40 °C for 48 h in order to obtain a powdered rGO.

4.1.6 Fabrication of the electrochemical sensors

Prior to the fabrication of electrochemical sensors C-SPE and CFE used as substrates, were pre-treated in order to increase their hydrophilic and electrochemical properties. Two different bio-receptor, the aptamer and the antibody was used for the fabrication of the electrochemical sensor.

4.1.6.1 Fabrication of C-SPE/rGO/AgNPs/Apt/BSA for detection of OTA

The fabrication process of aptasensor is presented in **Scheme 4-3**. The activated C-SPE was first coated by casting 10.0 μL of rGO/AgNPs solution and dried at 37.0 °C for 1 h. Then 10.0 mL of 3.0 μM Apt was dropped on top of the rGO/AgNPs and dried at 24.0 °C for 3.0 h. After 3.0 h the electrode was then washed with phosphate buffer (0.1 M, pH 7.0) to remove the unabsorbed Apt on the electrode surface. After rinsing, the electrode was further incubated with 1.0% BSA solution for 20 min to completely block the unbound sites of the C-SPE surface. The resultant OTA aptamer denoted as C-SPE/rGO/AgNPs/Apt/BSA and used directly as aptasensor or stored dry at 4.0 °C when not in use.

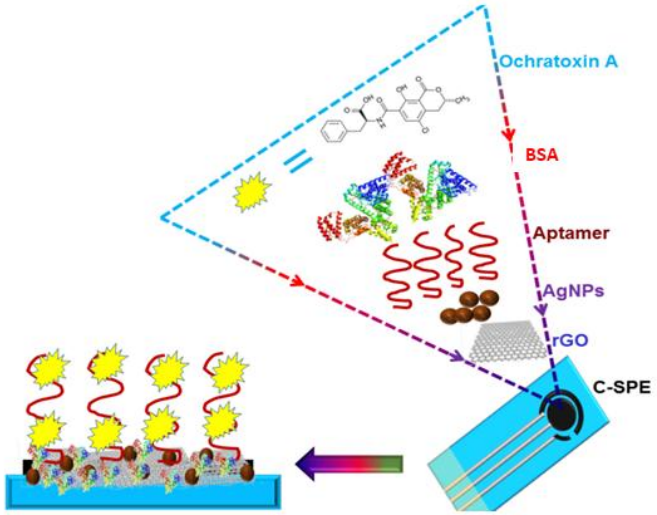

Scheme 4-3: Illustration of electrochemical aptasensor for the detection of OTA.

4.1.6.2 Fabrication of CF/BN-TiO_2/Apt/BSA for detection of AFB_1

In a first step, 2 µM of activated aptamer was immobilized onto CF/BN-TiO_2 electrode and allowed to dry at 25 °C for 2 h, after which it was washed with PBS to remove the unbounded or excess Apt from the electrode surface. Secondly, 10 µL of BSA (0.1%) was spread over CF BN-TiO_2/Apt surface, to block any non-specific active sites on the electrode (**Scheme 4-4**). The fabricated CF/BN-TiO_2/Apt/BSA was kept at 4 °C when not in use.

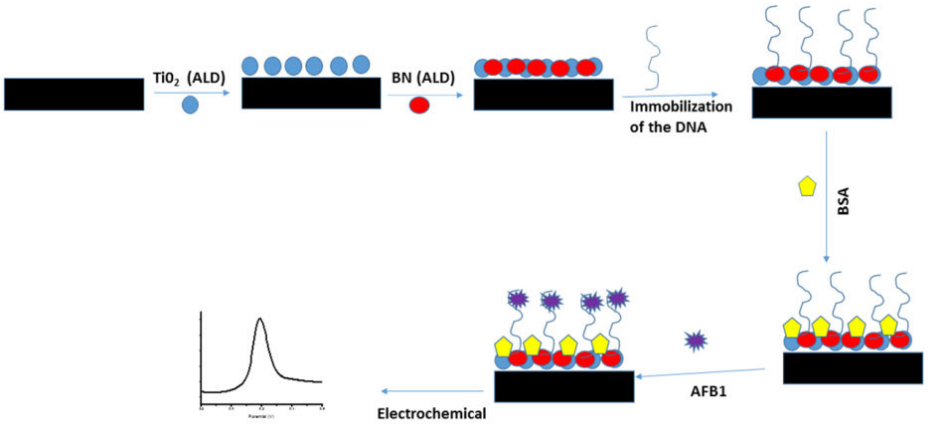

Scheme 4-4: Fabrication of Aptasensor for AFB_1.

4.1.6.3 Fabrication of CF/PdNPs/anti-OTA/BSA for detection of OTA

A fresh stock solution of anti-OTA (1.0 µg mL^{-1}) was prepared in phosphate buffer saline solution (PBS) presenting a pH value of 7.4. The anti-OTA solution was mixed with 0.4 M EDC and 0.1 M NHS in the ratio of 4:1:1 and kept at 4 °C for 30 min, to activate the carboxyl groups in fragment crystallizable (Fc) region of anti-OTA (Gupta *et al.* 2017c). Thereafter, the anti-OTA was ready for the two steps immobilization process onto the surface of CF/PdNPs. In a first step, 10 µL of anti-OTA with EDC-NHS was spread over the CF/PdNPs electrode and incubated at 4 °C for 6 h, after which it was washed with PBS to remove the unbounded or excess anti-OTA from the electrode surface. Secondly, 10 µL of BSA (0.1%) was spread over CF/PdNPs/anti-OTA immunoelectrode surface, to block any non-specific active sites on the electrode (**Scheme 4-5**). The fabricated CF/PdNPs/anti-OTA/BSA immunoelectrode was kept at 4.0 °C when not in use.

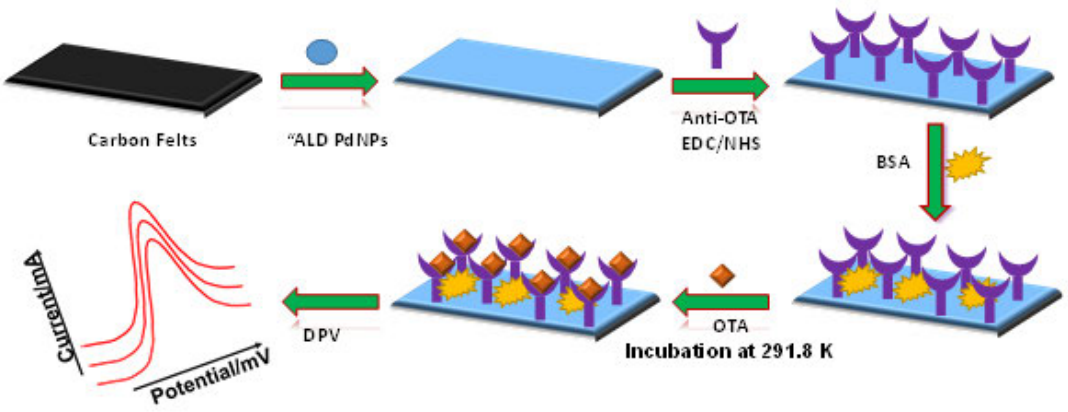

Scheme 4-5: Schematic representation for the preparation of CF/PdNPs/anti-OTA/BSA immunoelectrode.

4.1.6.4 Fabrication of CF/PdNPs-BN/L-Cys/anti-AFB_1/BSA for detection of AFB_1

Scheme 4-6 shows the fabrication process of the electrochemical immunosensor for the determination of AFB_1 in wine. First, the CF/PdNPs-BN electrode was immersed in 10 $mmoL^{-1}$ L-cysteine solution at room temperature (RT) for overnight in order to form a Cys/NP thiolate bond. The electrode was thereafter washed with PBS to remove any unbound L-Cys molecules. Subsequently, 20 µL of 0.4 mol L^{-1} EDC and 0.1 mol L^{-1} NHS in 1:3 volume ratio was dropped on the CF/PdNPs-BN/L-Cys for 50 min at room temperature (RT)

in order to convert the terminal carboxylic to active NHS ester (Tran *et al.* 2019). After that, the modified electrode was rinsed with PBS, 20 µL of 1.0 µg mL^{-1} anti-AFB_1 solution (prepared in PBS at pH of 7.5 was spread over CF/PdNPs-BN/L-Cys electrode surface and incubated for 2 h at 4 °C to give CF/PdNPs-BN/L-Cys/anti-AFB_1 electrode. The electrode (CF/PdNPs-BN/L-Cys/anti-AFB_1) was then rinsed with PBS to remove excess anti-AFB_1 on the modified electrode surface. In order to block the non-active site, 10 µL BSA (10%, m/v) was dropped on the CF/PdNPs-BN/L-Cys/anti-AFB_1 electrode and kept in RT for 20 min, when not in use they are stored in the freeze (4 °C).

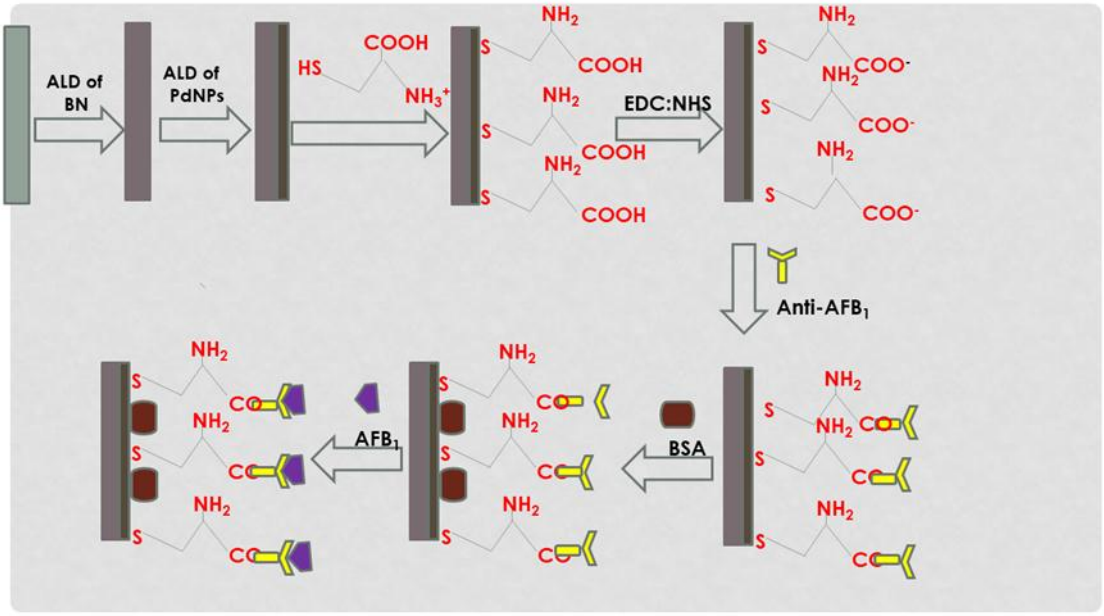

Scheme 4-6: The schematic representation of the electrochemical immunosensor fabrication procedure for the detection of AFB_1 in wine.

4.1.7 Electrochemical measurement of mycotoxins (OTA and AFB_1)

4.1.7.1 Electrochemical measurement of OTA with C-SPE/rGO/AgNPs/Apt/BSA

Electrochemical experiments were performed in a 10 mL electrochemical cell. Cyclic voltammetry (CV) and differential pulse voltammetry (DPV) measurements were carried out in a redox probe 5 mM $[Fe(CN)_6]^{3-/4-}$ containing 0.1 M PBS (pH 7.0) at room temperature. Different concentrations of OTA (0.002 to 0.016 mg L^{-1}) were incubated in the redox probe for 20 min.

4.1.7.2 Electrochemical measurement of AFB_1 with CF/BN-TiO_2/Apt/BSA

The response to target analyte AFB_1 in a solution that contains 5 mM $[Fe(CN)_6]^{3-/4-}$ in 20 mL, 0.1 M PBS (pH 7.5) was studied using DPV. The responses of different stock solution (2.5 to 20 ng mL^{-1}) of AFB_1 on CF/BN-TiO_2/Apt/BSA were recorded after the addition of the appropriate analyte stock solution. All electrochemical experiments were carried out at 25 °C.

4.1.7.3 Electrochemical measurement of OTA with CF/PdNPs/anti-OTA/BSA

For the OTA measurements, 10 µL of OTA standards with different concentrations ranging from 0.5 to 20 ng mL^{-1} in PBS was pipetted onto the surface of the CF/PdNPs/anti-OTA/BSA immunoelectrode and allowed to stand for 40 min at room temperature. DPV was used for the quantification of OTA and the measurements were conducted using a 5 mM $[Fe(CN)_6]^{3-/4-}$ prepared in PBS (pH 7.0). The EIS measurement was performed in 1 M KCl solution containing 5 mM $[Fe(CN)_6]^{3-/4-}$ with AC frequency from 0.1 to 10^5 Hz at the potential of the 0.2 V.

4.1.7.4 Electrochemical measurement of AFB_1 with CF/PdNPs-BN/L-Cys/anti-AFB_1/BSA

The bio-recognition experiment was carried out by dipping CF/PdNPs-BN/L-Cys/anti-AFB_1/BSA in the cell that contains 20 mL of 5 mM $[Fe(CN)_6]^{3-/4-}$ prepared in 0.1 M PBS (pH 7.5). Then 10 µL AFB_1 of different concentrations (1.0, 2.0, 4.0, 6.0, 8.0 and 10 ng mL^{-1}) were added on the cell and incubated for 30 min. Linear sweep voltammetry (LSV) was used for the quantification of OTA. The electrochemical impedance spectroscopy (EIS) data were recorded in the frequency range from 0.1 Hz to 10 kHz at the potential of the 0.6 V.

4.1.8 Preparation of real sample

Different food samples such as coffee, wine, Weet-Bix, and yoghurt were prepared using different procedures.

4.1.8.1 Preparation of coffee sample

The stock solution of the coffee sample (1.0 mg mL^{-1}) was prepared by ultrasonicating a mixture of 10 mL of PBS and 10 mg of coffee for 2 h. 1.0 mL of the prepared stock solution was spiked with different concentrations of OTA ranging from 0.5 to 20 ng mL^{-1} and kept at 4 °C until further use.

4.1.8.2 Preparation of wine sample

The red wine sample was prepared following the reported procedure by Goud and co-workers (Goud *et al.* 2016a). Initially, the wine samples were mixed with PBS and acetonitrile (ACN) in 1:3:1 v/v ratio (wine: PBS: ACN), sonicated for 1 h centrifuged at 5000 rpm and filtered using micro filters. 20 ng mL^{-1} of AFB_1 was added to the mixture that contains wine: PBS: ACN, this mixture was then used to prepare AFB_1 spiked wine sample of (2.0, 4.0, and 6.0 ng mL^{-1}).

4.1.8.3 Preparation of Weet-Bix sample

Weet-Bix sample was prepared by following the procedure reported by He and co-workers (He *et al.* 2012). The sample was finely grounded, and then 4.0 g of the finely grounded sample was mixed with 10 mL methanol–PBS (60:40, v/v), extracted for 5 min and filtered. The filtrate in methanol was spiked with different concentration of OTA.

4.1.8.4 Preparation of yoghurt sample

2.0 g of yogurt sample was diluted with 8.0 mL of 0.1 M PBS buffer (pH 7.5). The solution was then centrifuged for 10 min at RT to remove the upper fat layer. The resulted filtrate was then spiked with different concentration of AFB_1.

4.2 Computational studies

4.2.1 Construction of the nanostructures

All the studied nanoclusters were built using Materials Studio (MS) BIOVIA (Ulicny and Kozar 2018). Geometry optimizations of the nanomaterials were performed with the Forcite module as implemented in the MS software. Forcite in the MS software is a classical molecular mechanics tool, designed to perform a range of tasks including fast energy calculations and geometry optimizations for single molecules as well as periodic systems. A detailed knowledge of surface interactions plays a key role in the design of many materials and processes. An important first step in the preparation of a model of molecules adsorbed onto the surface is to ensure that the geometries are fully optimized. Among the different steps involved in the modelling approach are; the construction of the surface from the pure crystal, the addition of the molecules near the surface, the selection of an appropriate force field to study the nanomaterial interaction, followed by initial calculations of the energy and geometry optimization.

4.2.2 Molecular construction of the aptamer sequence

The approach consists of four main steps, building the ssDNA secondary structure from the sequence using M-fold, constructing refined equivalent 3D ssRNA models using Chimera, translating the 3D ssRNA models into ssDNA models using VMD, and refining the 3D ssDNA structures using VMD (Jeddi and Saiz 2017). The BSA (PDB code: 4F5S) structure was extracted from the protein database into MS to predict the interaction with the aptamer sequences. The aptamer-BSA interaction was explored using discovery Studio visualizer.

4.2.3 Adsorption Studies by Monte Carlo Simulations

Monte Carlo (MC) adsorption studies were applied to search for the lowest energy configurations of adsorbates on the surface of selected substrates as the temperature is gradually decreased. The Adsorption Locator (AL) module as implemented in the MS software was used as a preparatory and screening tool with the force-field method to obtain a

ranking of the energies for each generated configuration, thereby indicating the preferred adsorption sites. Possible adsorption configurations were identified by carrying out Monte Carlo searches of the configurational space of the substrate–adsorbate conformations to mimic the electrochemical layer-by-layer strategy of different scheme (Ulicny and Kozar 2018; Naidoo *et al.* 2020).

4.2.4 DFT Calculations

Density functional theory (DFT) calculations on the 3D structure are geometrically optimized at the B3LYP level using the 6–311+G basis sets of Gaussian 09 (Frisch *et al.* 2016). The global minimum for the optimized geometry was further confirmed by a frequency calculation. The energy differences (ΔE) between the highest occupied molecular orbital (HOMO) and the lowest unoccupied molecular orbital (LUMO) are an important parameter which defines the chemical activity of any compound, with the smaller value indicating a stronger tendency to donate electrons.

CHAPTER 5: RESULTS AND DISCUSSION

This chapter focuses on the results and discussion based in the form of 4 Case Studies:

5.1 Case Study 1: Aptasensor for the detection of OTA in Weet-Bix

In this section the results for the fabricated aptasensor for the detection of OTA are presented. The fabrication and characterization of the synthesized nanocomposites are outlined. In addition, the results of the fabricated aptasensor in relation to the determination of OTA in Weet-Bix cereal samples are presented. Also outlined in this chapter is the accompanying computational studies which aim to supplement and correlate the experimental data.

5.1.1 Experimental

5.1.1.1 Optimization of different parameters for the biogenic synthesis of AgNPs by amadumbe extracts

In order to attain optimum condition for AgNPs formation, various parameters have to be optimised. The formation of AgNPs was monitored by UV-Vis spectroscopy. The reduction of Ag^{+} to Ag^{0} using amadumbe extract was evidenced by the visual colour change of solution from colourless to brown, resulted in the formation of AgNPs as shown on **Figure 5-1**A. The biogenic synthesis of AgNPs display a brown colour due to SPR bands at 428 nm, similar results were reported in literature (Veisi, Azizi and Mohammadi 2018; Sneharani, Prabhudev and Sachin 2019). Jin and co-workers reported that the particles size depends on the absorption peak, broader peaks shows the large particles and narrow peaks shows small particles (Umadevi, Shalini and Bindhu 2012), while the absorption intensity indicates the number of nanoparticles formed (Ahmad *et al.* 2013). This criterion was used for the selection of best parameter for the biogenic synthesis of AgNPs. Different parameters such as the boiling time of amadumbe extract, extract amount, silver nitrate concentration and the reaction time was optimised. In general, the intensity of the SPR peak changes with the change in other variables.

The intensity increases with the increase in the boiling time of the extract to 40 min as illustrated in **Figure 5-1**B. Beyond the 40 min of boiling time, the intensity decreases because high temperature denatures the biomolecules that are present in the extract.

The effect of volume of the extract was conducted by varying from 1.0 to 5.0 mL, while keeping other parameters constant. The absorption intensity increases with the increase in the volume of the extract until 4.0 mL, however beyond 4.0 mL, there is no significant change in the absorption intensity demonstrating the attainment of the saturation in the bio-reduction of Ag^{+} to Ag^{0} as shown in **Figure 5-2**A. When the volume of the extract is increased, the formation of AgNPs is rapid due to the availability of biomolecules in the reduction of Ag^{+} to Ag^{0} (Rani *et al.* 2020). Additionally, Kathiravan and co-worker demonstrated that the particle size decreases with the increase in the volume of the extract (Kathiravan, Ravi and Ashokkumar 2014). **Figure 5-2**B shows the absorption spectra of AgNPs synthesized at different concentration of $AgNO_3$. The absorption intensity and the intensity of SPR absorption peak increases with the increase of $AgNO_3$ concentration during reaction. This specifies the change of particle size (Tripathy *et al.* 2010), and the absorption of the AgNPs solutions is directly proportional to the concentration of $AgNO_3$. Similar results were reported in the literature showing the increase of AgNPs with the increase of $AgNO_3$ concentration (Ahmed *et al.* 2016b).

The effect of reaction temperature was also optimised by varying temperature from 20 to 80 °C. The formation of AgNPs is temperature dependent phenomenon. **Figure 5-2**D shows that the increase in the reaction temperatures from 20 to 90 °C results in increase in the number of particles until 80 °C. Beyond 80 °C, there is no significant change in the absorption. Elbagory and co-workers demonstrated that the higher temperature facilitates the synthesis of smaller particles (Elbagory *et al.* 2017).

The effect of reaction time on the biogenic synthesis of AgNPs was also optimised by varying from 10 to 60 min as depicted in **Figure 5-2**C. With the increase in the reaction time, number of particles increases until 30 min. Beyond 30 min, the intensity in the absorption peak is negligible. Therefore, it was obvious that all the parameters certainly contributed to the formation of AgNPs. Then, the optimum conditions for biogenic synthesis of AgNPs by amadumbe extract was 40 min of boiling time of the extract, 4.0 mL extract volume, 1 mM of $AgNO_3$ concentration, reaction temperature and time of 80 °C and 30 min, respectively.

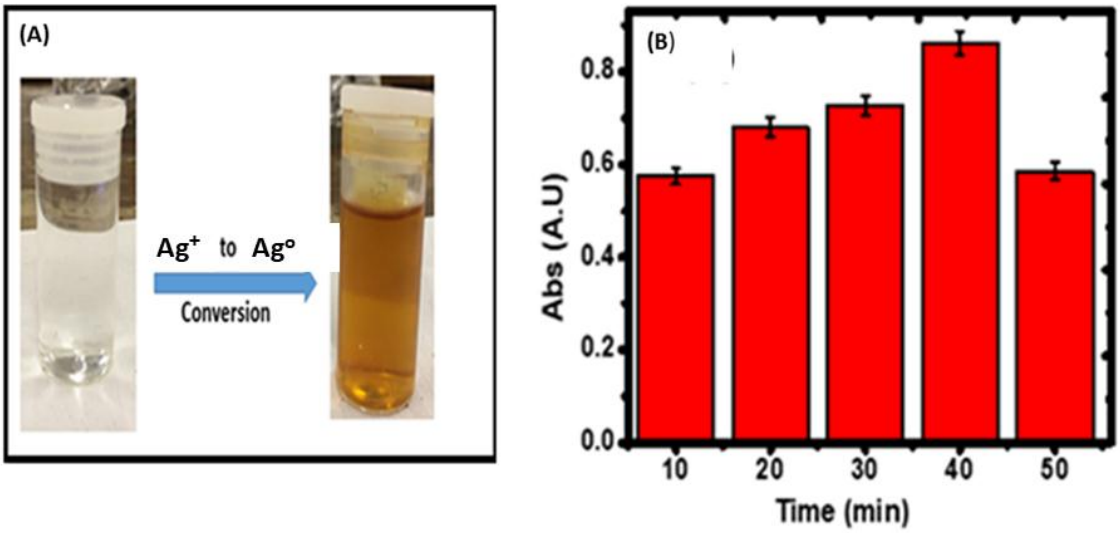

Figure 5-1: (A) The reduction of AgNPs and (B) Effect of extract boiling time on absorbance.

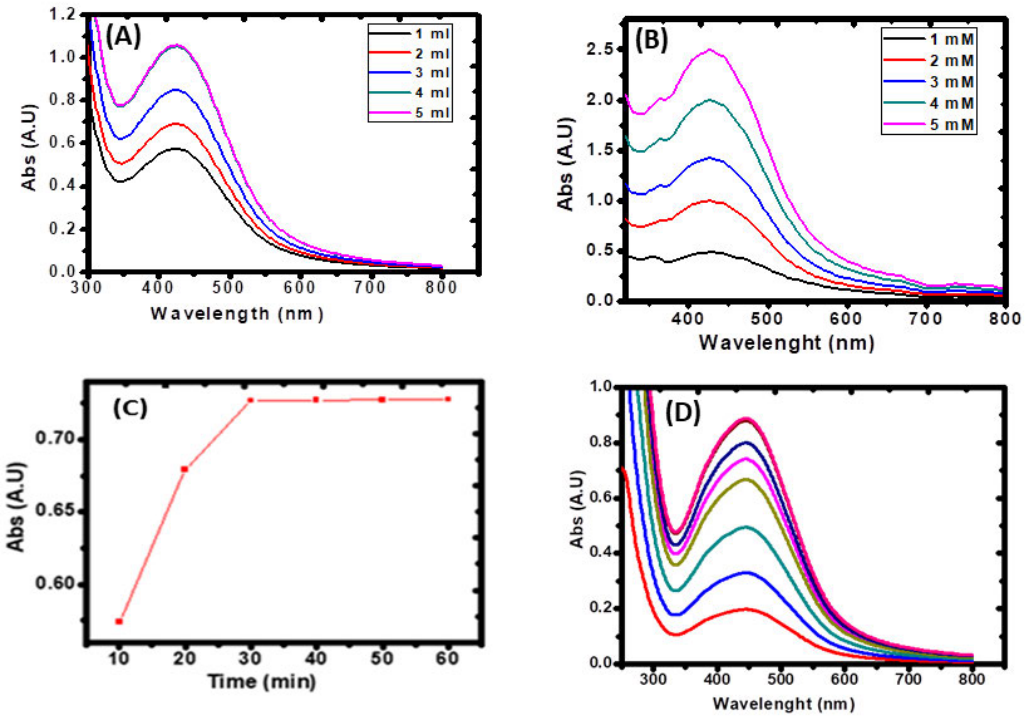

Figure 5-2: The effect of (A) extract amount, (B) $AgNO_3$ concentration, (C) reaction time, and (D) reaction temperature.

5.1.1.2 Spectroscopic characterization of amadumbe extract and AgNPs

(i) UV-visible analysis

The reduction of silver ions (Ag^{+}) by amadumbe extract was analysed by UV-Vis spectroscopy. **Figure 5-3** shows the UV-Visible spectra of (i) amadumbe extract and (ii) AgNPs under the optimized conditions. The surface plasmon resonance (SPR) absorption band at 428 nm is observed, which is lower than that obtained by several researchers (Kathiravan, Ravi and Ashokkumar 2014; Ahmed *et al.* 2016b).This shows that the synthesized AgNPs are spherical in shape.

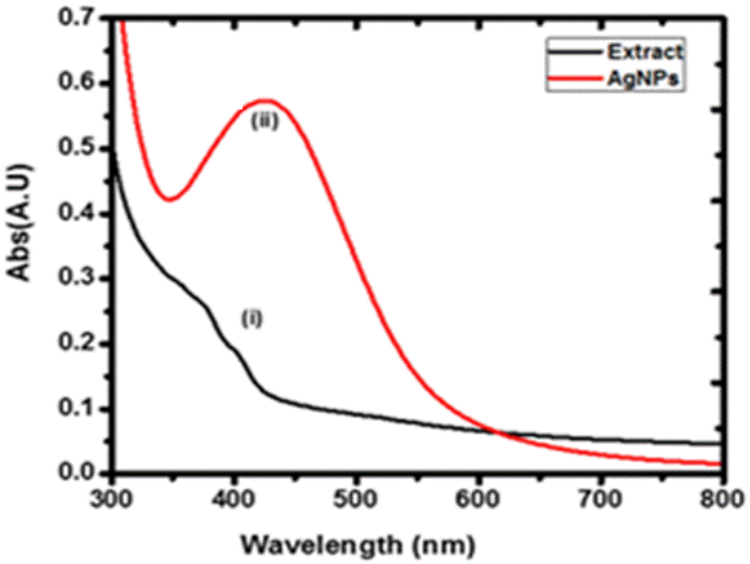

Figure 5-3: UV-Vis spectroscopy of (i) the extract (ii) AgNPs.

(ii) High resolution transmission electron microscope (HRTEM)

The size, shape and morphology of AgNPs were identified by HRTEM. **Figure 5-4**A reveals a spherical shape and well dispersed AgNPs ranging from 8 to 25 nm with an average size of 17 nm. Veisi and co-workers reported a spherical shape of AgNPs, when they used plant extract as a reducing agent (Veisi, Azizi and Mohammadi 2018). **Figure 5-4**B shows that the particles are spherical and highly crystallized; this is confirmed by the uniform lattice fringes. The lattice spacing of 0.23 nm corresponds to (111) planes of silver.

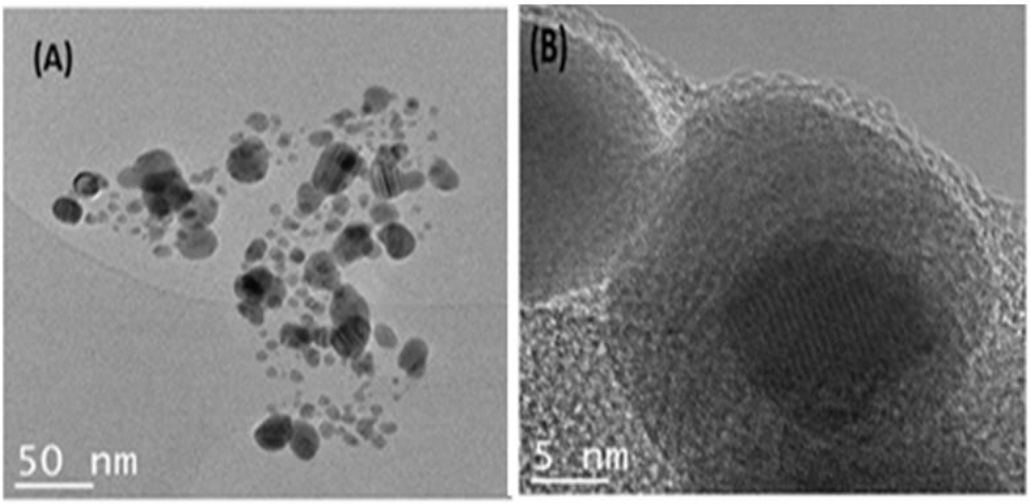

Figure 5-4: (A) HR-TEM image of AgNPs synthesized by green methods and (B) Selected area electron diffraction SAED pattern.

(iii) Attenuated total reflectance (ATR)

Figure 5-5A shows the ATR spectrum of (i) amadumbe extract and (ii) AgNPs. The obtained spectrum of amadumbe extract displayed vibrational bands at 3213, 2984, and 1684 cm^{-1} which are attributed to O-H, aliphatic C-H and C=O stretching of flavonoids/phenolic groups, respectively. The C-O and C=O stretching observed at 1172 and 1537 cm^{-1} indicates the presence of esters, alcohols, ketones, and carboxylic acids. These results showed that amadumbe extracts have metabolites such as terpenoids that has different functional groups of alcohols, ketones, ester and carboxylic acids. In **Figure 5-5**A(ii), the broad peaks at 3312 and 1634 cm^{-1} corresponding to -OH and –C=C were noticed. The disappearance of peaks at 2984, 1537 and 1172 cm^{-1} assigned to C-H, C-O and C=O respectively which were present in FTIR spectrum of extract was also observed in the synthesized AgNPs spectrum **Figure 5-5**A(ii). This suggests that, the functional group such as alcohols and flavonoids/phenolic groups, are interacted with $AgNO_3$ acted as a reducing agents and are responsible in the formation of AgNPs (Veisi, Azizi and Mohammadi 2018). However, the LC-MS analysis further confirmed that (2S)-4-methyl-2-[[1-[(2S)-4-methyl-2-[(2-methylpropan-2-yl) oxycarbonylamino] pentanoyl] piperidine-4-carbonyl] amino] pentanoate is one of the major metabolites present in the extract. Similar result was reported by Sharma and co-workers in the synthesis of AgNPs using Myristica fragrans seed extract (Sharma *et al.* 2014).

(iv) Dynamic light scattering (DLS), Inductively Coupled Plasma Spectroscopy (spICP-MS) and Flow Field Flow Fractionation (AF4)

The hydrodynamic diameter is the size that is measured by DLS technique. The size includes the metallic core of the nanoparticle, the stabilizers and the thickness of the solvation shell, moving along with the particle (Aziz *et al.* 2014). The DLS results revealed a non-homogeneous AgNPs with two average particle size in the range of 108 ± 0.5 to 555 ±1.5 nm. The polydispersity index (PDI) of AgNPs was observed to be 0.677; this shows that these particles are polydispersed with a PDI scale ranges from 0 to 1 (less than 0.3 being monodisperse and more than 0.3 being polydispersed). Notably, the particle size was significantly larger compared to the spICP-MS and the HRTEM results. DLS has large particle size because the total size includes the coating material and surfactants layer attached to the particle (Banerjee and Nath 2015). The spICP-MS was used to determine the size of the nanoparticles at low concentration. The internal calibration with isotope dilution was used to determine the size of AgNPs. The spICP-MS results (**Figure 5-5**B) for the synthesized AgNPs indicate an average core diameter of 60 nm. The fractogram in **Figure 5-5**C represents the particle size distribution of AgNPs by AF4-MALS, under the optimised parameters indicating a clear separation from the void peak. The diameter of the particles (D_{geo}) for the elution time ranging from 10 to 25 min, results in an average geometric diameter of 45 nm.

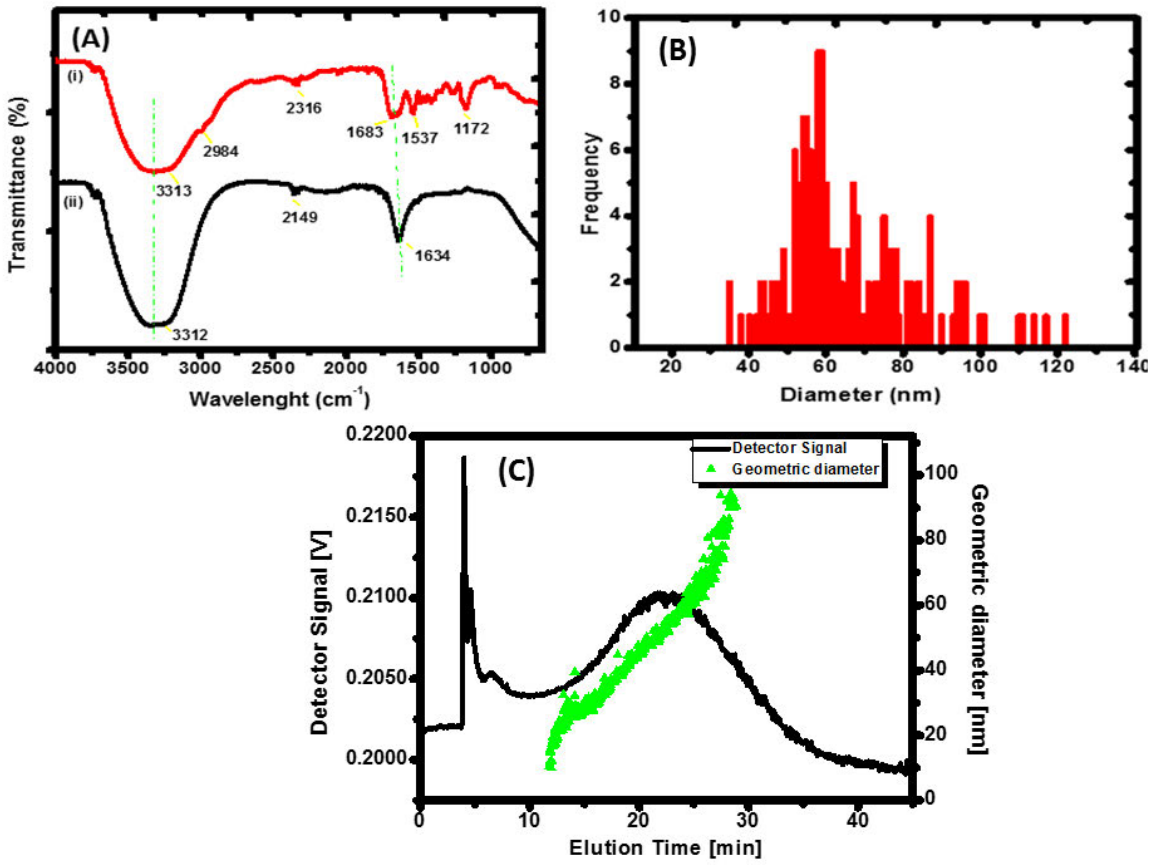

Figure 5-5: (A) AT-R spectrum of (i) the extract (ii) AgNPs, (B) Particle size distribution obtained from spICP-MS, and (C) AF4-MALS fractogram of AgNPs.

(v) Photoluminescence (PL)

Previous reports show that AgNPs exhibit a visible photoluminescence (Xu *et al.* 2006; Ahmed *et al.* 2016b).The PL of the synthesized AgNPs by amadumbe extract was studied via fluorescence emission spectroscopy as shown in **Figure 5-6**A. AgNPs were dispersed in deionised water and the PL emission spectra was recorded in the excitation wavelength at 300 nm. AgNPs display two luminescent emission at 320 nm and 459 nm, the biological and antioxidants that are found in the extract cause the emission at 320 nm (Khalil, Ismail and El-Magdoub 2012). Similar PL spectra with a band around 450 nm were reported by Verma and Mehata when synthesising AgNPs using Neem leaves (Verma and Mehata 2016).

(vi) Liquid chromatography mass spectroscopy (LC-MS)

LC-MS was used to investigate and identify the biomolecules that were present on the amadumbe extract. LC-MS analysis showed that the amadumbe extract contains four major compounds. The compounds were 3-(Carboxyoxy)-2-methyl-6-(3-methylbutyl)-5-(2-methyl-2-propanyl)-(2-methyl-2-propanyl)phenolate**,**4-(2-Hydroxy-2-phenyl-3,5,6,7,8,9-hexahydroimidazo[1,2-a]azepin-4ium-1-yl)-1,5-dimethyl-2-phenylpyrazol-3-one,2-(6-{1-ethyl-4-[4-(1H-pyrrol-2-ylcarbonyl)-2,3,3a,4,5,7a-hexahydro-1H-inden-5-yl]-1,3-butadienyl}-5-methyltetrahydro-2H-pyran-2-yl)propanoate and (2*S*)-4-methyl-2-[[1-[(2*S*)-4-methyl-2-[(2-methylpropan-2-pentanoyl]piperidine-4-carbonyl]amino]pentanoate and the corresponding chemical shift peaks of the spectrum were shown in **Figure 5-6**B. The predominant compounds of amadumbe extract were: 2-(6-{1-ethyl-4-[4-(1H-pyrrol-2-ylcarbonyl)-2,3,3a,4,5,7a-hexahydro-1H-inden-5-yl]-1,3-butadienyl}-5-methyltetrahydro-2H-pyran-2-yl) propanoate (R_t = 12.87 min) at m/z = 464.3 and (2*S*)-4-methyl-2-[[1-[(2*S*)-4-methyl-2-[(2-methylpropan-2-pentanoyl]piperidine-4-carbonyl]amino]pentanoate (R_t = 13.10 min at m/z 454.3).

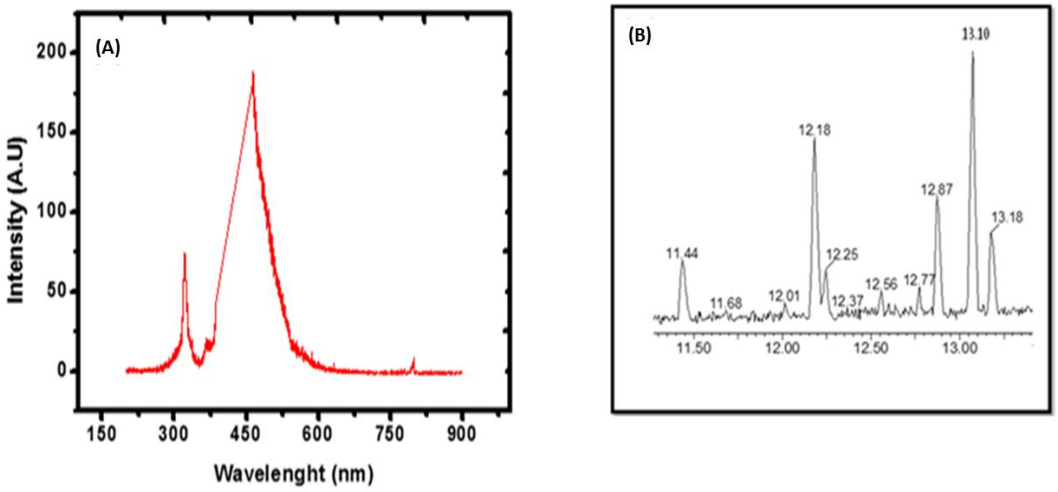

Figure 5-6: (A) Photoluminescence spectrum of AgNPs and (B) LC-MS spectrum of amadumbe extracts.

(vii) Zeta potential

Zeta Potential (ZP) is one of the important parameter that is used to measure the stability of the synthesized nanoparticles. The synthesized AgNPs demonstrate a ZP of –19.04 mV. A similar result has been reported in the literature (Balashanmugam *et al.* 2016; Paosen *et al.* 2017; Das and Bhuyan 2019). The negative ZP demonstrates the stability of the synthesized AgNPs which is due to electrostatic repulsion.

5.1.1.3 Electrochemical Characterization of AgNPs by Cyclic Voltammetry (CV)

Cyclic voltammetry (CV) was used to characterize the synthesized AgNPs modified C-SP electrode. **Figure 5-7** shows the CV voltammogram of the bare C-SPE (i) and AgNPs/C-SPE (ii) in the 0.1M KCl solution containing 1 mM $[Fe(CN)_6]^{3-/4-}$. A well-defined redox peak was observed for the C-SPE (curve i), this quasi-reversible redox peak was attributed to the transformation between $[Fe(CN)_6]^{4-}$ and $[Fe(CN)_6]^{3-}$. The anodic peak appearing 0.27 V and cathodic peak at 0.03 V, with the anodic current of 12.74 µA was observed on C-SPE. However, AgNPs/C-SPE (curve ii) shows two anodic peaks appearing at 0.10 and 0.24 V and one cathodic peak at 0.12 V and the anodic current of 17.69 µA. The increase of anodic current confirms successful deposition of AgNPs onto the C-SPE substrate which accelerated the rate of electron transfer between analyte and working electrode. The increased transfer rate is ascribed to high surface area and improved catalytic activity of the electrode. The anodic peak at 0.10 V is the peak position of Ag. Saw and co-workers reported the anodic peak current of Ag at 0.15 V (Saw *et al.* 2016). These results confirmed the presence of AgNPs and their participation in the redox reaction on the electrode surface.

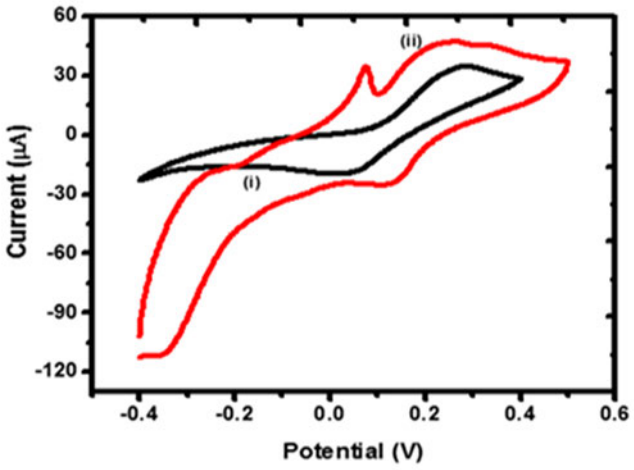

Figure 5-7: Cyclic voltammogram of (i) C-SPE and (ii) C-SPE/AgNPs in 0.1 M KCl containing 1 mM $[Fe(CN)_6]^{3-/4-}$ at a scan rate of 50 mVs^{-1}.

5.1.1.4 Spectroscopic characterization of GO and rGO

(i) UV-Visible analysis

The UV-Visible was also used for the characterization of GO and rGO synthesized by the modified Hummers methods. A distinct absorption band for GO was observed at 238 nm with a shoulder absorption band at 298 nm (**Figure 5-8**). These bands are associated with the π→π* aromatic (C=C) and n→π* (C=O) transitions, respectively. Similar results were reported in literature (Krishna *et al.* 2014; Emiru and Ayele 2017; Hidayah *et al.* 2017). The absorption band of rGO red shifted to 265 nm depicting an accumulation of electrons and the removal of some functional groups on the GO surface (Roy *et al.* 2016; Emiru and Ayele 2017; Gebreegziabher *et al.* 2019). The removal of oxygen and the C=O groups from GO results in the disappearance of the shoulder peak at 298 nm (Gebreegziabher *et al.* 2019).

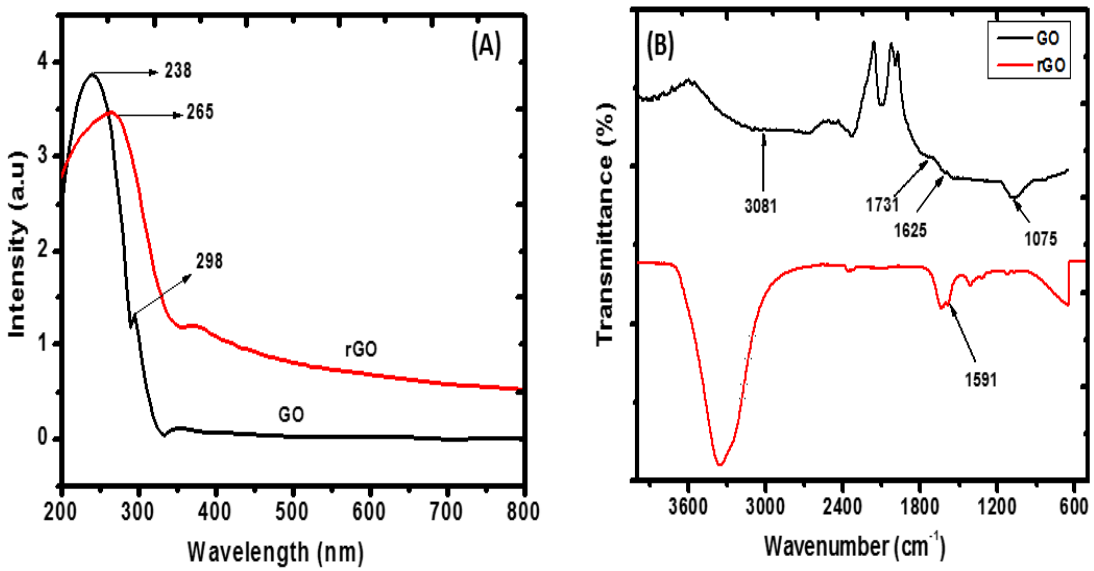

Figure 5-8: (A) UV-Visible spectra and (B) ATR spectra of GO and rGO.

(ii) ATR

ATR spectroscopy was used to identify the functional groups that are present in the synthesized carbonaceous material. Numerous oxygen-containing functional groups were detected on the corresponding bands. The ATR spectrum of GO and rGO as shown in **Figure 5-8**B. An intense peak at 3081, 1731, 1625, and 1075 cm^{-1} in the GO spectrum corresponds to O–H groups of the adsorbed water molecules between GO sheets, this reveals the hydrophilic characteristic of GO, C=O stretching, aromatic C=C vibrations, and alkoxy C–O stretching vibration, respectively (Xu *et al.* 2015; Husnah *et al.* 2017; Iskandar *et al.* 2017; Malas *et al.* 2017). The peak at 1731 cm^{-1} present in GO spectrum was absent in rGO spectrum, suggesting the elimination of oxygen-containing functional groups, such as C=O and C-O bonds (Gülercan, Gergin and Sarac 2018; Thangavel *et al.* 2018).The intense peak at 1591 cm^{-1} indicates the restoration of the sp^2 carbon networks (Johra and Jung 2015).

5.1.1.5 Electrochemical characterization of C-SPE/GO and C-SPE/rGO using cyclic voltammetry (CV)

Carbon containing compounds have diverse electrochemical properties because of their different structures. Their structure, morphology and electrochemical reactivity can predict in various carbon containing compounds with their electrochemical behaviour. The electrochemical conductivity of a carbon containing compounds were evaluated using a redox couple $[Fe(CN)_6]^{3-/4-}$ by monitoring the oxidation and reduction peak current. **Figure 5-9** shows the voltammogram of C-SPE/GO and C-SPE/rGO. Greater electrochemical response was observed on rGO (41.22 µA) modified screen printed electrode compared to GO (about 2 times higher than GO). This is due to the sp^2 hybridization of carbon atom that is present on the rGO structure. GO displayed a low peak current (20.13 µA) which could be due to a low electrical conductivity resulting from the functional groups that are present in the GO structure which causes a separation in the conjugated electronic structure of the graphene (Sreenivasan and Berry 2013).

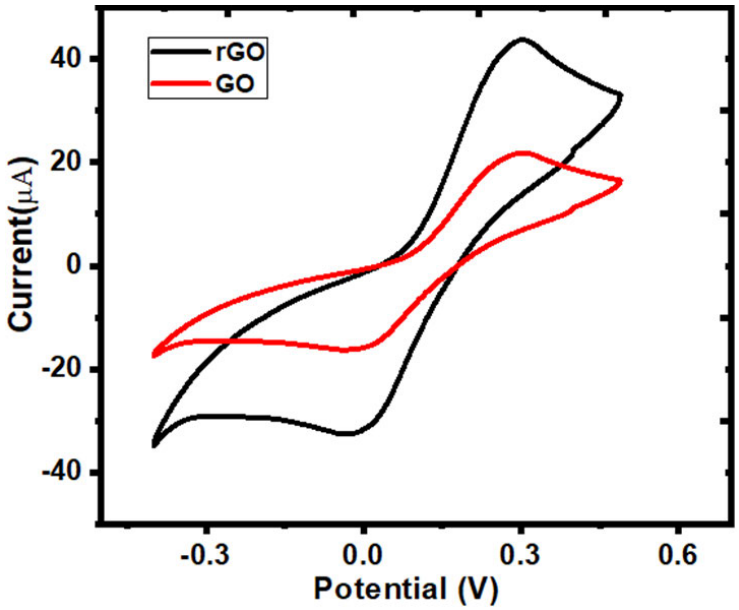

Figure 5-9: Cyclic voltammogram of C-SPE/GO and C-SPE/rGO in 0.1 M KCl and 1 mM $[Fe(CN)_6]^{3-/4-}$ at a scan rate of 50 mVs^{-1}.

5.1.1.6 Optimization and characterization of the C-SPE/rGO/AgNPs/Apt/BSA

In order to attain the greater detection performance of the electrochemical aptasensor, different parameters such as rGO concentration, the ratio between rGO: AgNPs, BSA incubation time, aptamer concentration and incubation time were examined. These results were expressed by the differences in the peak current responses using DPV (ΔI_p), measured before and after incubated with OTA. The fabricated aptasensor was then characterized using different techniques.

(i) Effect of rGO concentration

The loading amount of rGO on the surface of the electrode had major effect on the analytical behaviour of the sensor. The amount of rGO on the modified electrode depended on the concentration of rGO. Different concentration of rGO was prepared using different amounts of rGO (5, 10, 15, 20, 25, 30, 35, 40 mg) in 50 mL of deionised water. **Figure 5-10**A shows that the amount of rGO deposited on the C-SPE/rGO/AgNPs/Apt/BSA increased with increasing concentration of rGO, this provides much more surface area for immobilization of aptamer. The current increases with an increase of rGO from 0.1 to 0.5 mg mL^{-1}. When the concentration was more than 0.5 mg mL^{-1}, the effective area of C-SPE/rGO/AgNPs/Apt/BSA is reduced because of excessive rGO deposited on the electrode surface results in the decrease of peak current. Therefore, 0.5 mg mL^{-1} of rGO was applied in the experiments.

(ii) Effect of rGO and AgNPs ratio

The amount of AgNPs loaded on to the rGO was also studied as shown in **Figure 5-10**B. This was carried out by preparing different ratio of rGO (0.5 mg mL^{-1}) and AgNPs (1 mM). Different ratio of rGO: AgNPs (1:1, 1:2, 1:3, 1:4, 1:5, and 1:6) has been studied. The gradual increase of peak current with increasing AgNPs ratio in the different of 1:1, 1:2, 1:3, results in the large amount of AgNPs with good electroactivity were deposited on the modified electrode. The peak current reaches its maximum in the ratio of 1:3 but decreases at ratio greater than 1:3 because of decreased surface area probably caused by increase in amount of, AgNPs deposited on the electrode. Hence, only a small amount of aptamers could be immobilized on the electrode. The ratio of 1:3 was used in the experiments.

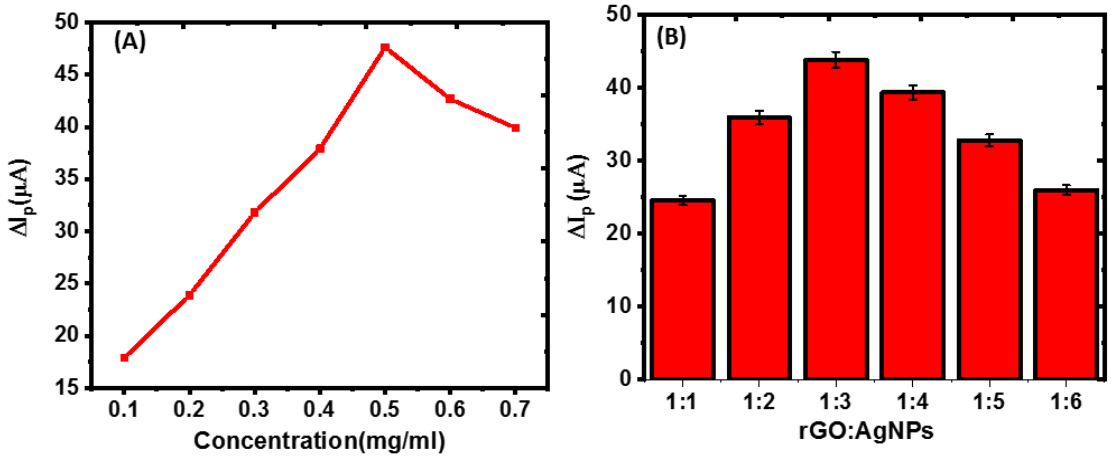

Figure 5-10: Effect of (A) rGO concentration and (B) the ratio of rGO: AgNPs.

(iii) BSA incubation time

To avoid the non-specific adsorption on the electrode, the blocking reagent BSA was used. The effect of incubation time of the BSA (5, 10, 15, 20, 25, and 30 min) was investigated on the modified electrode. **Figure 5-11**A shows that the current increases with the increase of incubation time from 5 to 20 min, then beyond 20 min no noticeable current differences were observed. Thus, the incubation time was kept at 20 min at 24 °C.

(iv) Optimization of the Aptamer concentration

Aptamer immobilization is one of the most significant and essential factors for fabrication of the aptasensor. Literature reveal that higher aptamer concentration decreases the detection value and lower concentration results in the weak signals (Mishra *et al.* 2016; Zejli, Goud and Marty 2019).The effect of the aptamer concentration was studied by modifying the C-SPE using different concentration of the aptamer (1, 2, 3, 4, 5 and 6 µM) as shown in **Figure 5-11**B. The current response increases from 1 to 3 µM and reached a maximum of 37.5 µA at 3 µM. The current response decreases beyond 3 µM, due to the excess aptamer immobilized on the electrode surface might hinder the interfacial electron transfer. Thus, 3 µM was used for the entire experiments.

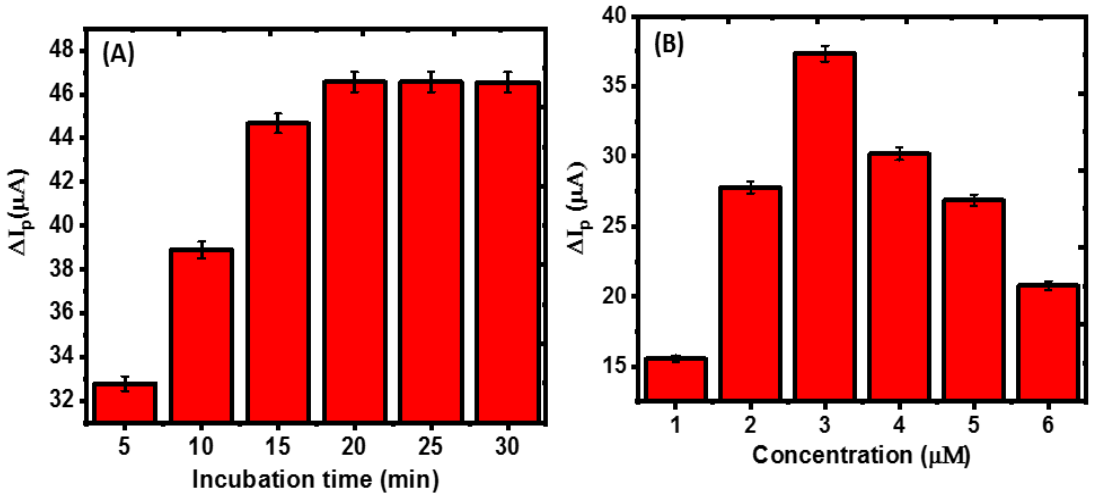

Figure 5-11: Effect of BSA (A) incubation time and (B) aptamer concentration.

(v) Effect of incubation time of the Aptamer

In order to attain the maximum current signals from the analysed sample, the incubation time of the aptamer was optimized. Different incubation time ranging from 1 to 6 h was investigated. **Figure 5-12**A shows that the current increases with increase in the incubation time and reach the maximum ΔI_p at 3 h of incubation. Beyond 3 h the current decreases, because long incubation causes the partial hybridization of the aptamer. Then, 3 h was determined as the optimum incubation time for the aptamer to be combined on the surface of C-SPE.

(vi) Effect of incubation temperature

Incubation temperature plays an important role when fabricating the aptasensor. **Figure 5-12**B shows that ΔI_p increases with the increase of incubation temperature up to 24 °C and further increase in the temperature, ΔI_p gradually decreases. Peng and co-workers reveals that high incubation temperature causes the aptamer to decompose (Peng *et al*. 2019). Therefore, 24 °C of the incubation time was used for the entire experiment.

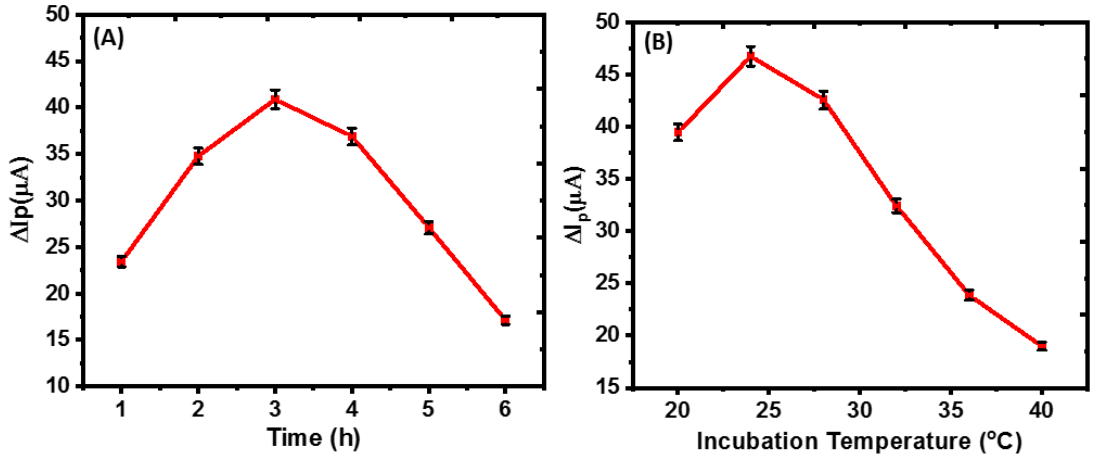

Figure 5-12: Effect of the incubation (A) time and (B) the temperature of the aptamer.

5.1.1.7 Structural and morphological characterization of C-SPE/rGO/AgNPs/Apt/BSA

(i) ATR

ATR spectroscopy was studied to determine the functional groups that are present in the fabrication steps of the aptasensor as shown in **Figure 5-13**A. The ATR spectra of C-SPE/rGO/AgNPs shown in (curve i) is similar to that of rGO (**Figure 5-8**B), but there is a weak intensity with a minor blue shift from 1585 to 1591 cm^{-1}, arising from the large presence of AgNPs (Yuan and Gurunathan 2017). After the immobilization of the aptamer onto the electrode surface (curve ii), the C=O peak at 1645 cm^{-1} was observed, this confirmed the formation of metal-DNA aptamer bonding on the electrode surface (Bagheri *et al.* 2021). The incubation of the blocking agent, BSA, on the electrode surface resulted in the secondary amide peak at 1532 cm^{-1}, indeed confirming the adsorption of BSA onto the electrode surface.

(ii) Raman spectroscopy

The Raman spectroscopy was used to characterize rGO before and after AgNPs was absorbed on the electrode surface as shown in **Figure 5-13**. The graphite spectrum is characterized by the G-band and D-bands. These two bands are attributed to the disorder in the C-C bonds and the in-plane vibration bonds respectively (Gurunathan *et al.* 2019).The two characteristic D and G bands around 1320 cm^{-1} and 1586 cm^{-1} were observed on the rGO

spectra before AgNPs modification. The D band provides information of the breathing mode of the k-point, while the G band relates to the tangential stretching mode of the E_{2g} phonon of the sp^2 carbon atoms (Jorio 2012). After the AgNPs were decorated onto the rGO, the intensity of D and G bands observed at 1327 cm^{-1} and 1574 cm^{-1} respectively were then enhanced (curve (ii)) because of the surface enhanced Raman scattering of nanoparticles.

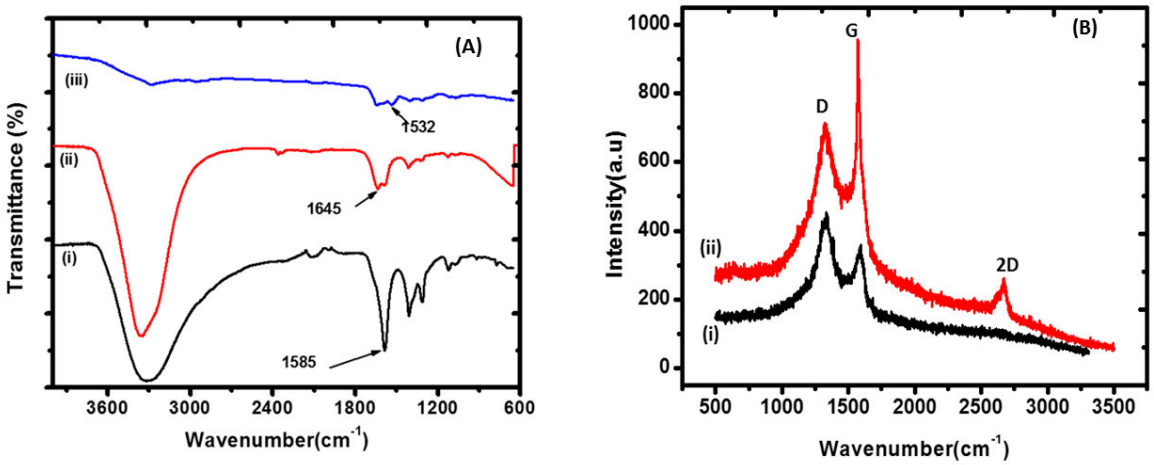

Figure 5-13: (A) ATR spectrum of (i) C-SPE/rGO/AgNPs, (ii) C-SPE/rGO/AgNPs/Apt and (iii) C-SPE/rGO/AgNPs/Apt/BSA and (B) Raman spectra of (i) rGO and (ii) rGO/AgNPs.

5.1.1.8 Electrochemical characterization of the C-SPE/rGO/AgNPs/Apt/BSA by Cyclic voltammetry (CV)

CV is the useful technique in evaluating the electrochemical behaviour of the modified electrodes. **Figure 5-14**A shows the cyclic voltammograms attained at the fabricated aptasensor in 1 mM $[Fe(CN)_6]^{3-/4-}$ prepared in a 0.1 M PBS at pH 7. The bare C-SPE (curve i) displayed a well-defined redox peak which corresponds to the reversible redox reaction of $[Fe(CN)_6]^{3-/4-}$. After deposition of rGO/AgNPs composite (C-SPE/rGO/AgNPs (curve ii)), a notable increase in the redox peak current was witnessed, due to the presence of improved conductivity properties of rGO and AgNPs. The rGO/AgNPs composite promoted an electron transfer because of the increased surface area. The oxygen groups in GO provided a selective interface for the deposition of AgNPs. The π-π stacking interaction present in rGO accelerated the electron transfer and AgNPs conductivity (Aydogdu and Pekyardimci 2020). After immobilization of the aptamer (C-SPE/rGO/AgNPs/Apt (curve iii)), a decrease in the

redox peak suggests that the presence of the aptamer on the electrode surface hinders the electron transfer (Liu *et al.* 2012). The peak current decrease further on immobilization of BSA (C-SPE/rGO/AgNPs/Apt/BSA (curve iv)) due to the blocking of the non-specific binding sites of the aptasensor, demonstrating a successful immobilization onto the electrode surface. The observed shifts of the anodic and cathodic peak potential (E_{pa}) towards the left and right accordingly as shown in **Figure 5-14**B, indicates an efficient mass transfer between the modified electrodes (Bojang and Wu 2020).

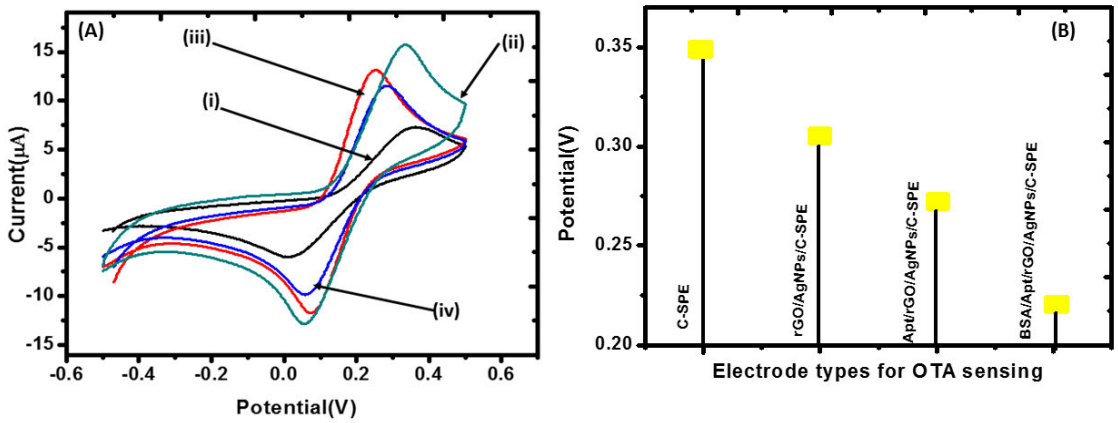

Figure 5-14: (A) Comparative cyclic voltammograms of (i) bare C-SPE, (ii) C-SPE/rGO/AgNPs, (iii) C-SPE/rGO/AgNPs/Apt and (iv) C-SPE/rGO/AgNPs/Apt/BSA in 1 mM $[Fe(CN)_6]^{3-/4-}$ and 0.1 M PBS (pH 7.0) at a scan rate of 20 mVs^{-1} and (B) Dependence of the peak potential shift at different electrode types.

5.1.1.9 Optimization of analytical parameters for C-SPE/rGO/AgNPs/Apt/BSA

(i) Effect of pH

pH value is another significant factor that affects the response of the sensor. Su and co-workers previously reported that an acidic and basic environment could damage the negatively-charged aptamer and therefore affects the interaction between the aptamer and their targets (Su *et al.* 2013). The effect of pH on the current response of the C-SPE/rGO/AgNPs/Apt/BSA towards OTA was evaluated at pH 4 to 8 (**Figure 5-15**A). The current response towards OTA increases until it reaches pH 7 and decreased beyond 7. This result confirms that the aptasensor performance is pH dependent; hence all the electrochemical measurements were conducted at pH 7 to ensure that the fabricated aptasensor functions at its maximum sensitivity.

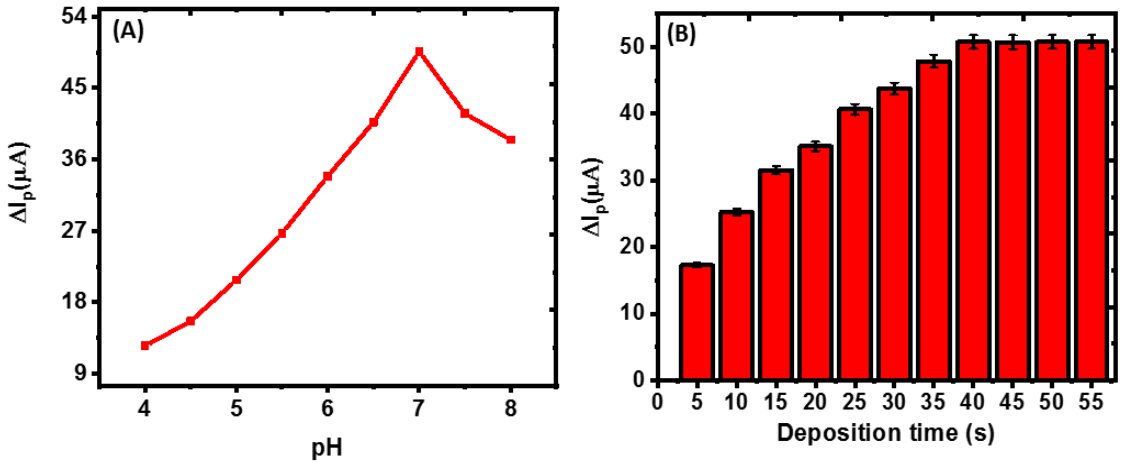

Figure 5-15: Effect of (A) pH and (B) Deposition time on the peak currents of C-SPE/rGO/AgNPs/Apt/BSA.

(ii) Effect of deposition time

The effect of deposition time was carried out by the investigation of various deposition times from 5 to 55 s. The current response increases with increase of deposition time from 5 to 40 s with maximum peak current at 40 s (**Figure 5-15**B). Beyond 40 s, the peak current decreased gradually because the nanocomposite on the electrode peeled off from the electrode, resulting in the lower peak currents. Therefore, 40 s was used as the optimized deposition time in all experiments.

(iii) Investigation of effect of the scan rates on C-SPE/rGO/AgNPs/Apt/BSA

In order to determine the type of electrochemical reaction at the fabricated aptasensor, the effect of scan rate on OTA redox reaction was studied. **Figure 5-16**A shows that the peak current increases with increase of scan rate (10 to 100 mVs^{-1}). The increase of scan rate causes the shifting of anodic peak potential towards more positive potential. This proposes that the mechanism of the fabricated aptasensor is a quasi-reversible electron transfer (Nazari *et al.* 2019). The square root of scan rate ($v^{1/2}$) versus anodic and cathodic peak current plot displayed a linear relationship as shown in **Figure 5-16**B, and the equation can be expressed as ipa (μA) = $19.612v^{1/2}$–18.776, R^2 = 0.996, ipc (μA) = $-15.529v^{1/2}$ +1.886, R^2 = 0.988, indicating a quasi-reversible mechanism and diffusion controlled process. Additional studies were conducted to confirm that the electrode reaction was diffusion controlled. A relationship between log of scan rates versus log of anodic and cathodic peak current was found to be

linear, (log ipa (µA) = 0.534log *v* + 1.064, R^2 = 0.997) (**Figure 5-16**C),with a slope, 0.534 which is close to a theoretical slope value of 0.5 for a diffusion controlled process (Muhammad *et al.* 2016).

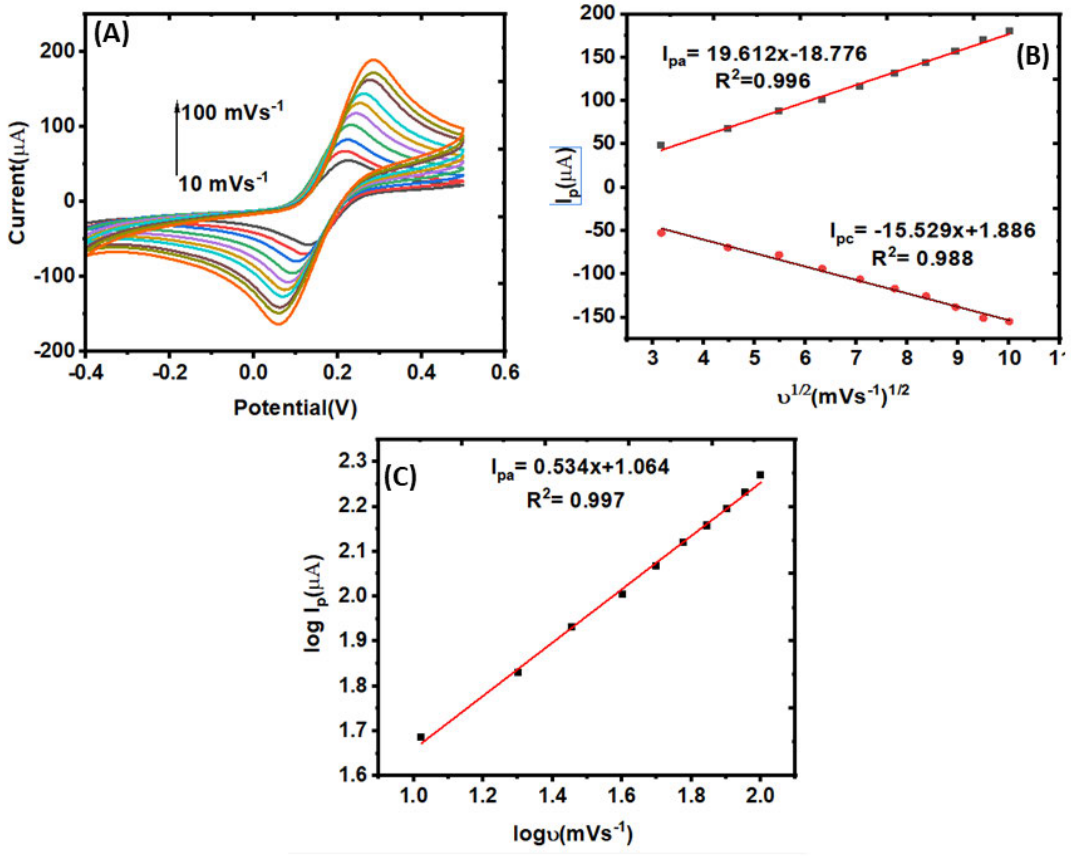

Figure 5-16: (A) Effect of scan rates (10 to 100 mVs^{-1}) (B) Plot of peak current vs. square root of scan rate, and (C) Plot of logarithm of peak current vs. logarithm of scan rate.

(iv) Effect of recognition time

Figure 5-17 represents the analytical performance of the aptasensor towards OTA with recognition time of aptamer. The current response increased with increase in the recognition time from 5 to 20 min and decreases with recognition time greater than 20 min, suggesting a complete biorecognition reaction. Hence, 20 min of recognition time was chosen.

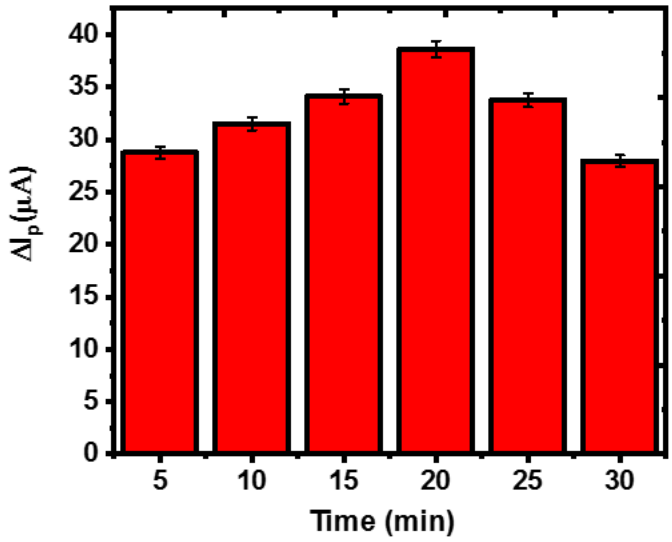

Figure 5-17: Effect of OTA recognition time at pH 7 and 40 s deposition time.

5.1.10 Electrochemical behaviour of OTA at C-SPE/rGO/AgNPs/Apt/BSA

(i) Analytical performance of C-SPE/rGO/AgNPs/Apt/BSA

The analytical performance of the fabricated aptasensor was examined by assessing the DPV current response of the aptasensor incubated with OTA concentrations ranging from 0.002 to 0.016 mg L^{-1}. **Figure 5-18**A shows a significant decrease in the peak current with the increase of OTA concentration. This shows that the aptamer was folded and the formation of OTA-Apt complexes on the sensing interface causes inhibition of electron transfer of the redox probe $[Fe(CN)_6]^{3-/4-}$ (Fan *et al.* 2019). A linear relationship between the current change (ΔI_p) and the OTA concentrations results in the equation of $\Delta I = -22.916[OTA] + 43.056$ with a correlation coefficient of 0.997 (**Figure 5-18**B). The limit of detection (LOD) of 7×10^{-4} mg L^{-1} was achieved based on three times the standard deviation of blank measurement ($3S_{blank}/m$) (Gu *et al.* 2019), where S_{blank} and m demonstrate the signal of blank sample and the slope, respectively. The obtained LOD was lower compared with the previous studies (Lv *et al.* 2016; Costantini *et al.* 2019). These results show that a fabricated aptasensor displayed the highly sensitivity towards the determination of OTA.

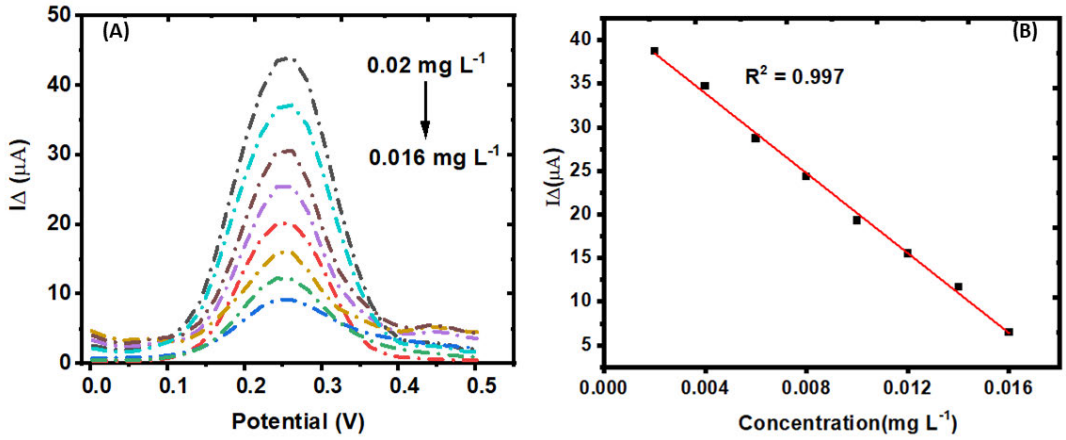

Figure 5-18: (A) The DPV response of C-SPE/rGO/AgNPs/Apt/BSA in 1 mM $[Fe(CN)_6]^{3-/4-}$ after incubation with different concentrations of OTA from (0.002 - 0.016 mg L^{-1}); and (B) The linear calibration curve of (ΔI_p) with OTA concentrations.

(ii) The application of the fabricated aptasensor to wheat sample (Weet-Bix)

The fabricated C-SPE/rGO/AgNPs/Apt/BSA was applied in practical analytical applications by determining OTA in wheat sample (Weet-Bix). Different concentration of OTA in spiked Weet-Bix samples was investigated using DPV. **Table 5-1** shows the recovery range of 94.00 -106.25% with the RSD ranging from 1.09 to 2.50%. This implied that the fabricated aptasensor has a promising feature for sensing of OTA in real samples.

Table 5-1: The detection of OTA in the spiked wheat sample.

OTA added (mg L^{-1})	**OTA Founded (mg L^{-1})**	**Recovery (%)**	**±RSD (n=3)**
2.0	1.88	94.00	2.04
8.0	8.50	106.25	2.50
12.0	11.89	99.08	1.09

(iii) Reproducibility and stability of C-SPE/rGO/AgNPs/Apt/BSA

The reproducibility of the fabricated aptasensor was studied by incubation of 0.002 mg L^{-1} OTA in six independent modified electrodes (aptasensors). A relative standard deviation (RSD) of 3.5% (**Figure 5-19**A) was obtained for six successive measurements, demonstrating a good reproducibility of the fabricated aptasensor and its suitability for OTA detection. The stability of the fabricated aptasensor was evaluated for 20 days with measurements recorded at intervals of 5-days. The aptasensor was stored in a refrigerator when not in use. The initial current response decreased to 87.8% (**Figure 5-19**B) on the 20th day, signifying an acceptable stability of the developed aptasensor.

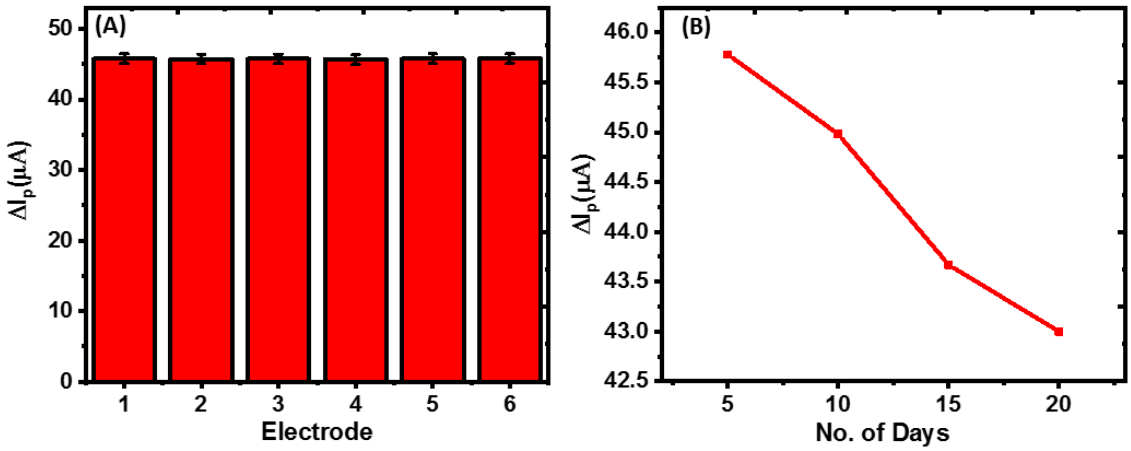

Figure 5-19: (A) The reproducibility, and (B) The stability of C-SPE/rGO/AgNPs/Apt/BSA.

(iv) Interference study of C-SPE/rGO/AgNPs/Apt/BSA

To evaluate the specificity of the proposed aptasensor in response to OTA in the presence of AFB_1, the fabricated aptasensor was incubated in a mixture of 0.002 mg L^{-1} and 0.01 mg L^{-1} of OTA and AFB_1, respectively. **Figure 5-20** shows a major current response when the aptasensor was incubated with 0.002 mg L^{-1} of OTA and the mixture, while the incubation of 0.01 mg L^{-1} AFB_1 showed a negligible DPV signal, indicating that the fabricated aptasensor is highly specific towards OTA.

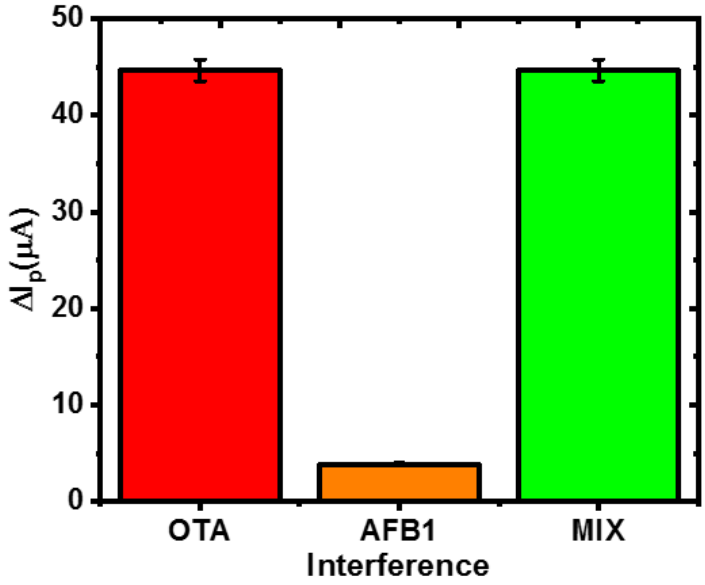

Figure 5-20: Interference test for the fabricated aptasensor.

5.1.2 Computational Studies

5.1.2.1 Monte Carlo Adsorption Studies

In this section, the adsorption energies of the adsorbate-substrate system for the layers was measured to mimic the electrochemical layers (**Scheme 4-3**), based on the Monte Carlo simulation protocol. The total adsorption energies for the minimized structures based on the adsorption locator (AL) algorithm is presented in **Table 5-2**.

Table 5-2: The adsorption energy distributions C-SPE/rGO/AgNPs/Apt/BSA.

Structure	Optimized 3-D structures	Adsorption energy kcal/mol
C-SPE/rGO	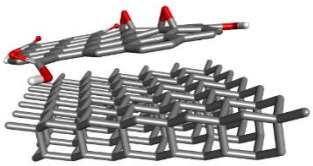	**-1.136 x 10^4**
C-SPE/rGO/AgNPs	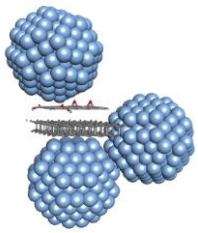	**-3.176 x 10^3**
C-SPE/rGO/AgNPs/Apt	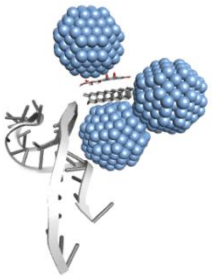	**-1.237 x 10^4**
C-SPE/rGO/AgNPs/Apt/BSA	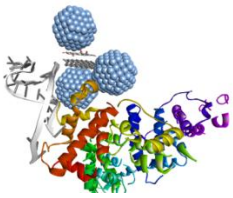	**-198.222**
C-SPE/rGO/AgNPs/Apt/BSA-OTA	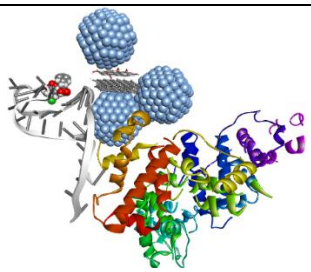	**-394.620**

The negative adsorption energies calculated, signifies stabilization and an exothermic adsorption process (Arya *et al.* 2018; Putri *et al.* 2019). The more negative energy indicates a stronger adsorption between the adsorbate-substrate system. Our results clearly indicate that the presence of the aptamer greatly contributes to the stabilization of the C-SPE/rGO/AgNPs nanocomposite. An increase in the peak current observed at E_{pa} = + 0.3V as shown in **Figure 5-7** (iii). However, the adsorption energy decreased significantly after the immobilization of BSA which is further validated by a decrease in the peak current (**Figure 5-7** (iv)), due to blocking of the non-specific binding sites of the aptasensor. There was an increase in adsorption energy when OTA interacted with the C-SPE/rGO/AgNPs/Apt/BSA. This is a significant result which demonstrates the existence of a good bio-molecular interaction between OTA and the aptamer complex. This prompted a further investigation to understand the electron transfer capabilities of OTA, computed at the density functional theory (DFT) level as discussed below.

5.1.2.2 HOMO-LUMO calculations

The highest occupied molecular orbital (HOMO) is a molecular orbital of the highest energy that is possessed by electrons and has the capability to donate electrons. The lowest unoccupied molecular orbital (LUMO) is the molecular orbital of the lowest energy that is unoccupied by electrons, suggesting the space to acquire the donated electrons (Kavitha, Sundaraganesan and Sebastian 2010). **Figure 5-21**A-B demonstrates the HOMO-LUMO plots obtained at the DFT level of theory. The calculated energy values of HOMO and LUMO are -0.25402 and -0.08793 eV, respectively. The value of the HOMO-LUMO energy gap is -4.519 eV as displayed in **Figure 5-21**.

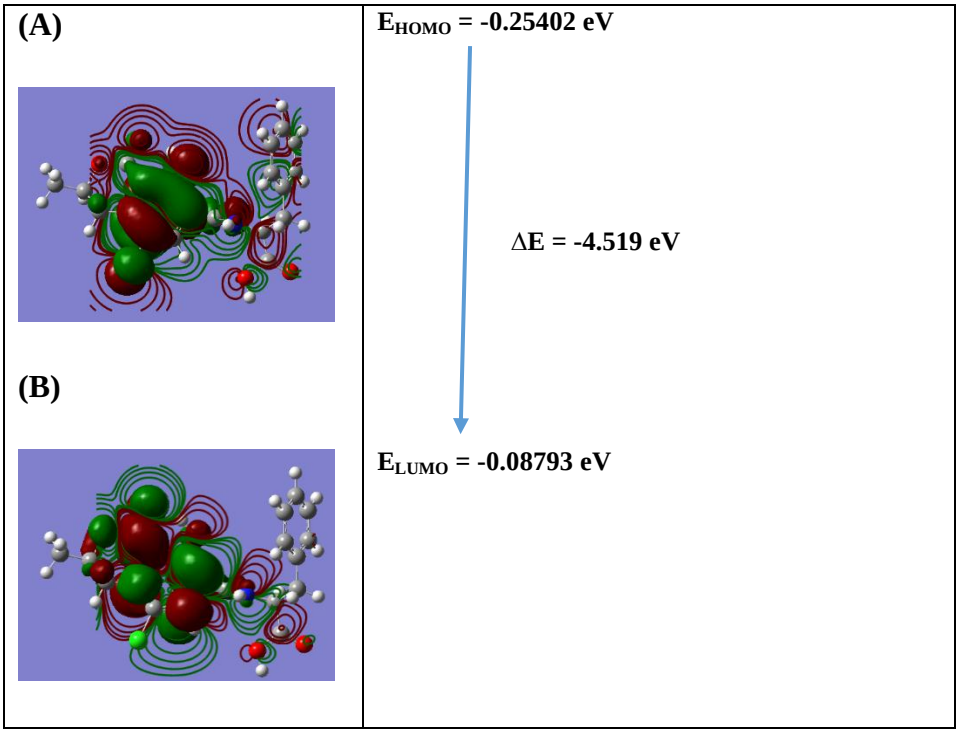

Figure 5-21: (A) HOMO and (B) LUMO Plots for OTA calculated at the DFT level. The red coloured lobes indicate the negative charge and green coloured lobes indicates a positive charge.

According to **Figure 5-21**, the less tightly held electrons which are present in highest occupied molecular orbitals (HOMO) are situated around the oxygen atoms in chlorophenolic group containing a dihydroisocoumarin rings. The spatial location of the lowest unoccupied molecular orbitals (LUMO) is similar except they are located around the carbon atoms in chlorophenolic group containing a dihydroisocoumarin rings. The obtained results show that ester carbonyl group will be the easiest route to the addition of electrons in the molecule.

5.1.3 Conclusion

In this study, a sensitive and efficient electrochemical aptasensor for the detection of OTA in commercial Weet-Bix samples was developed. The construction of the recognition element and the rGO/AgNPs nanocomposite proved to be cost-effective, easy to use and demonstrated good sensitivity towards the detection of OTA. Furthermore, the techniques that were used for the investigation of particle morphology and size characterization provides a complementary information. The TEM images confirmed the spherical shape of the synthesized AgNPs. The mean diameter for the particle size distribution of AgNPs was

evaluated to be 60 nm by the spICP-MS. With the proposed aptasensor, the concentrations range was improved from 0.002 to 0.016 mg L^{-1} with an LOD of 7 $\times 10^{-4}$ mg L^{-1}. In addition, the presence of AFB_1 did not show any significant changes in the current. The proposed aptasensor was successfully applied to the analysis of spiked Weet-Bix samples. A good recovery was obtained with an acceptable range (94.00 to 106.25%). From a computational perspective, this study also presented structural insights into the interaction between the biomolecules at the nanostructure interface by exploring the modification of the C-SPE/rGO/AgNPs/Apt/BSA as a substrate and OTA, an absorbent. The computational studies correlate well with the electrochemical studies with regards to the adsorption energy and the current response of the modification steps of the aptasensor. Our results demonstrate that the proposed aptasensor based on the disposable C-SPE is a promising platform for the on-site detection of OTA in the Weet-Bix samples.

5.2 Case Study 2: Aptasensor for detection of AFB_1 in yoghurt

The second case study deals with the fabrication of an electrochemical aptasensor for the detection of aflatoxin B_1 (AFB_1) at BN-TiO_2/Apt/BSA modified CF electrode. The experimental parameters optimized for an indirect electrochemical method for the determination of AFB_1 are presented. In addition, the results of the fabricated aptasensor in relation to the determination of AFB_1 in yoghurt samples are presented.

5.2.2 Experimental

5.2.1.1 Synthesis of BN-TiO_2 by atomic layer deposition (ALD)

Optimization of different parameters for the electrochemical detection of AFB_1 at BN-TiO_2 modified electrode is discussed. ALD is one of the techniques used to synthesize nanomaterials that have different diameters and achieved by varying the number of cycles. The numbers of cycle have different applications. So, the effect of number of cycle is one of the most important parameter when synthesizing nanoparticle using ALD. The effect of number of cycle was studied by varying the cycles.

(i) Effect of TiO_2 cycle number

Different number of ALD cycle was then optimized in order to get the required thickness. This was carried out by depositing different ALD cycles (10, 20, 40, 60 and 100) onto carbon felts electrode (CFE) in order to understand the electro catalytic properties. The cycle number is proportional to the diameter of the thickness. **Figure 5-22**A show that the increase of cycle number from 10 to 100 results in the increase of the diameter thickness (from 1.0 to 10 nm). The electro catalytic properties of the synthesized nanoparticles were investigated using a redox probe maker 5 mM $[Fe(CN)_6]^{3-/4-}$ in a 0.1 M KCl solution. According to **Figure 5-22**B increase in number of cycles from 10 to 40 resulted in the increase of current signal but decreases beyond cycle number 40. The current increase is due to the short distance between the substrate and the nanoparticles which make it easy for the electrons of the redox probe to migrate through the substrate and the nanoparticles. These results indicate the improvement in the electron transfer process. The thinner diameter entails the higher surface area, which means more active site (Ballai *et al.* 2021). However, the

current decreases because the substrate is too thick, resulting in the obstruction of electrons flow. Therefore, the ALD cycle of 40 was used for the entire experiments.

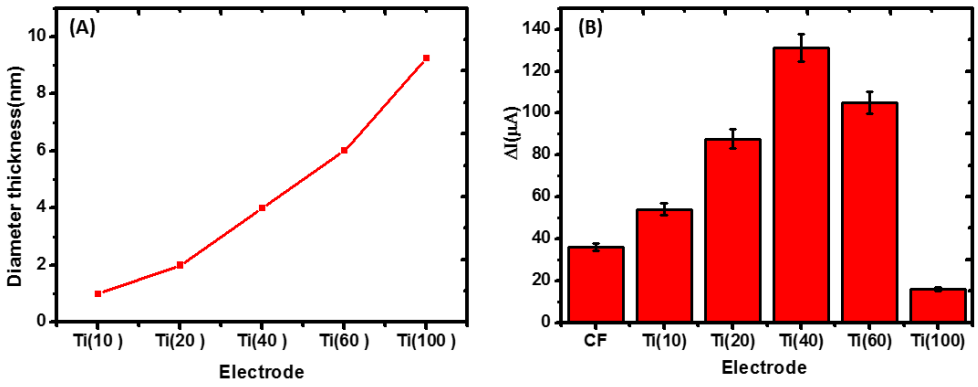

Figure 5-22: (A) The relationship between the cycle number and the diameter and (B) The effect of cycle number.

(ii) Effect of doping

Different doping agents (boron nitride (BN), ammonia (NH_3) and boron tribromide (BBr_3) has yielded different electro-calytic properties. Different doping agent (25 cycle) was then deposited onto the electrode that has been deposited with 40 cycle of TiO_2 in order to enhance the sensitivity of the fabricated electrode. The electro-catalytic properties of each doping agent were then investigated on a redox probe. The low current was observed when the electrode was doped with NH_3 and BBr_3 (**Figure 5-23**A). The electrode that has been doped with BN resulted in the highest current signal compared to NH_3 and BBr_3, this suggest that BN enhanced the sensitivity of electrode. Therefore, BN was used as the best dopant.

(iii) Effect of BN cycle number

Different BN cycle numbers (10, 25, 50 and 100) were then deposited onto the TiO_2. The current increases from cycle 10 to 25, then decreases from 50 to 100 (**Figure 5-23**B). The current increases with decrease in the diameter of the nanocomposite, resulting in the free transfer of electrons, however the decrease of current signal is due to hindrance of electrons due to the thickness of the electrode. Therefore, cycle number 25 was used as the optimum for the entire experiments.

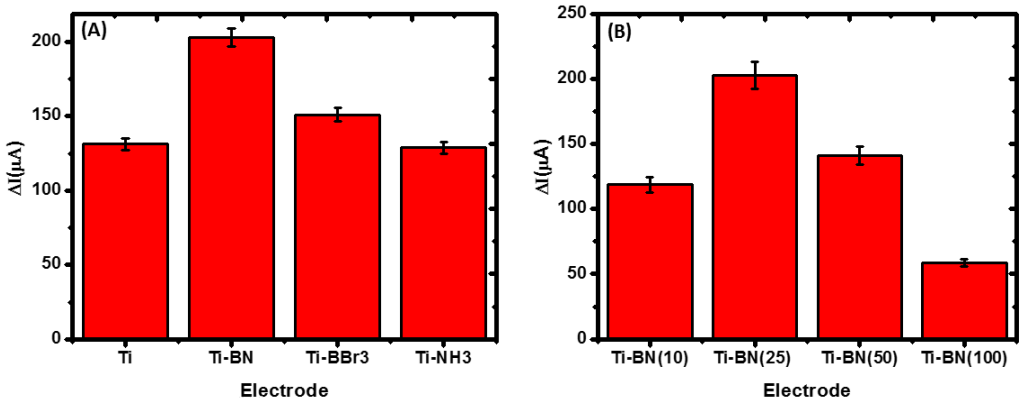

Figure 5-23: Effect of (A) doping agents and (B) BN cycle number.

5.2.1.2 Characterization of BN-TiO_2

The characterization of BN-TiO_2 was carried out using ATR, XRD, and Raman spectroscopy. The above-mentioned techniques did not show any characteristic of TiO_2 or BN due to a tiny layer that was deposited on the electrode. However, transmission electron microscopy (TEM) and scanning electron microscopy-energy dispersive X-ray (SEM-EDX) confirmed the synthesis of BN-TiO_2.

(i) Transmission electron microscopy (TEM) study

The transmission electron microscopic studies were conducted to investigate the morphology of the BN-TiO_2 composites that has been prepared using ALD. The TEM images of TiO_2/CF reveal the amorphous TiO_2 surface, and it was uniformly distributed on the carbon felt support as seen in **Figure 5-24**A. After 40 cycles of ALD, approximately 4–8 nm thickness of TiO_2 layer was synthesized as depicted in **Figure 5-24**B. The ALD deposition of BN onto TiO_2 (40 cycle), shows a notable morphology change, the BN layer was then imbedded on the amorphous structure of TiO_2. **Figure 5-24**D-F shows the TEM/EDS elemental mapping images of the BN-TiO_2 composite. These images show that Ti, C and O elements were scattered over the entire area of the sample. However, B and N were not detected because EDS is not a sensitive to light elements.

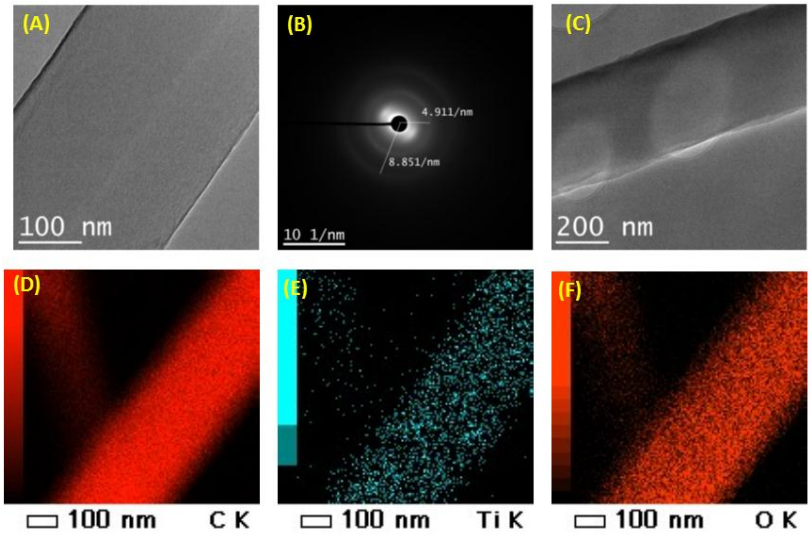

Figure 5-24: (A) TEM images of TiO_2, (B) Electron diffractogram, (C) and BN-TiO_2 samples obtained by ALD and, (D- F) EDS elemental mapping of BN-TiO_2.

(ii) SEM-EDX analysis

SEM-EDX technique was used to understand the differences in morphology and elemental composition of the synthesized BN-TiO_2 nanocomposite. The EDX analysis focuses on different area of the sample and the corresponding peaks were shown in **Figure 5-25**A-B. Both BN and TiO_2 were observed in the synthesized composite in the EDX spectrum. The spectra revealed the presence of Ti, B, N, O, and C. However, Ti, B, and N peaks were not very prominent, owing to the tiny layer of Ti and the low doping levels of N and B during the synthesis. Spectrum A revealed that the BN-TiO_2 nanocomposite contains Ti (21.92%), B (9.83%), O (16.02%), and N (11.76%), while spectrum B comprises of Ti (11.75%), B (8.53%), O (9.64%), and N (9.28%). Details of the EDX spectra of the BN-TiO_2 nanocomposite values measured in atomic and weight % are listed in **Table 5-3**.

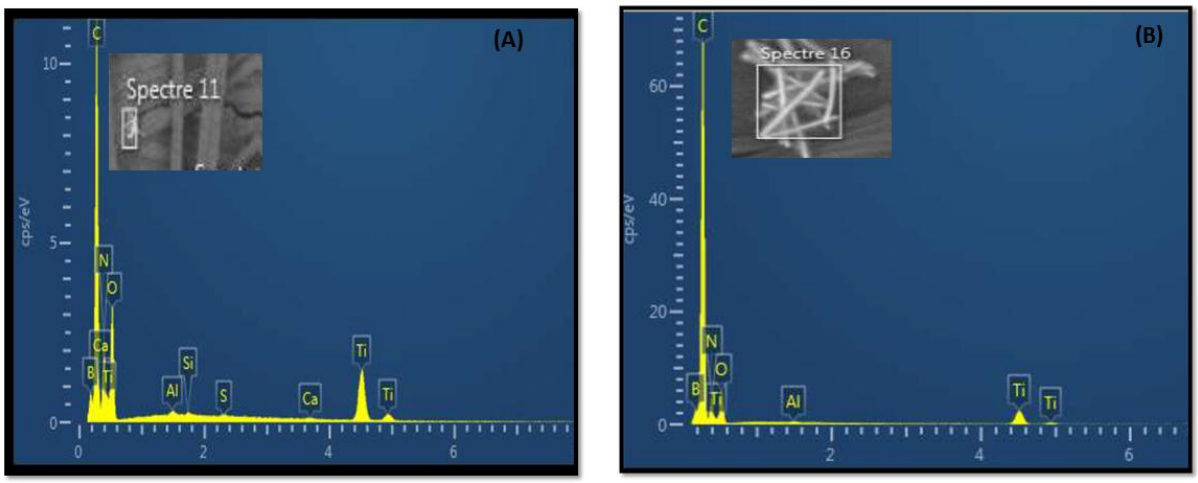

Figure 5-25: (A-B) SEM-EDX spectrum of BN-TiO_2 nanocomposite.

Table 5-3: EDX weight and atomic ratio of BN-TiO_2 nanocomposite using two spectrums focused two distinct areas.

BN-TiO_2 nanocomposite	**Ti**		**B**		**N**		**O**	
	Weight %	**Atomic %**	**Weight %**	**Atomic%**	**Weight %**	**Atomic %**	**Weight %**	**Atomic %**
Spectrum A	21.92	7.01	9.83	13.93	11.76	12.86	16.02	15.92
Spectrum B	11.75	3.33	8.53	10.72	9.28	9.00	9.64	8.19

5.2.1.3 Optimization of parameters for the fabrication of CF/BN-TiO_2/Apt/BSA

(i) Effect of aptamer concentration

The concentration of the aptamer immobilized on the surface of the electrode influences the density and the morphology of the fabricated aptasensor layer. For the best sensor efficiency, a dense layer with few defects must be fabricated. Therefore, different aptamer concentrations from 1 to 5 µM were optimized for maximum coverage of the

electrode (**Figure 5-26**A). The current increases when the concentration of the aptamer was 1 µM and reaches the maximum at 2 µM, demonstrating that all the adsorption sites on the electrode were fully occupied by the aptamer. The current decreases when the concentration was beyond 2 µM. This is due to sterical hindrances of the electrode; the electrode is too crowded for the optimal binding conformation. Therefore 2 µM was chosen as the optimum, and then it was used for the entire experiments.

(ii) Effect of activation time

In order to get a maximum sensitivity, the activation time between the cross-linker and the aptamer should be allowed to reach the equilibrium. The cross-linker and the aptamer were incubated at different time (10, 20, 30, 40, 50 and 60 min). **Figure 5-26**B shows that the current signals were amplified rapidly as the activation time increased and reached the maximum at 30 min, and then the current remains approximately constant which could be attributed to the electrode saturation. For this reason, the activation time of 30 min was set for the entire experiments.

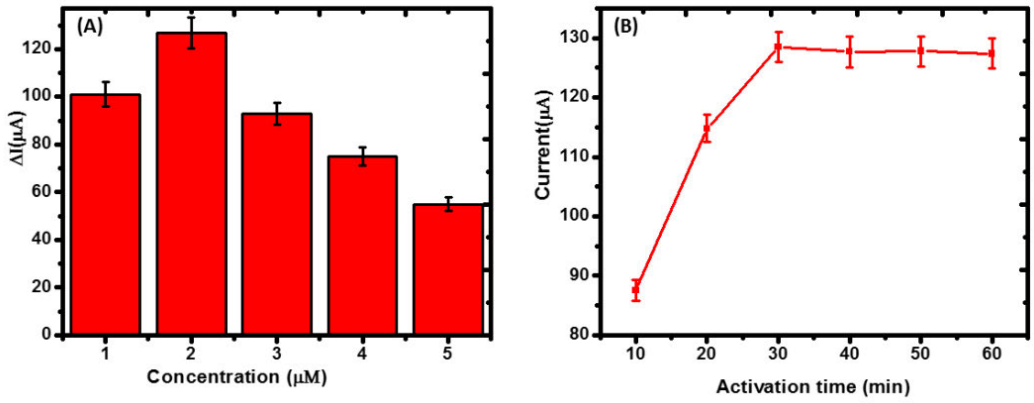

Figure 5-26: The effect of (A) Aptamer concentration and (B) activation time.

(iii) Effect of incubation temperature

The incubation temperature is one of the most important parameter when fabricating the aptasensor. The effect of incubation temperature on the current signals was examined by incubating the aptasensor at different temperature (4.0, 25, 37 and 55 °C) as presented in

Figure 5-26A. The peak current signals increase with increase of incubation temperature and reach maximum at 25 °C and, decreases with the increase of incubation temperature above 25 °C, due to the decomposition of aptamer at higher incubation temperature. Therefore, the incubation temperature at 25 °C was chosen as the optimum and used for the rest of the studies.

(iv) Effect of aptamer incubation time

The incubation time of the aptamer on the modified CF surface was optimized because it is a significant variable that affects the efficiency of the aptasensor. The effect of incubation time was evaluated with different incubating time from 1 to 5 h while monitoring the current signal (**Figure 5-26**B). The current signal rose steeply with the increase of incubation time from 1 to 2 h and then decreases after 2 h, indicating an occurrence of aptamer saturation on the electrode surface. The increase of incubation time for more than 2 h results in the decrease of current signal, due to the saturation of reactive sites that leads to the excessive aggregation of the aptamer (Maghsoudi *et al.* 2020).Thus, the incubation time was kept at 2 h for the entire studies.

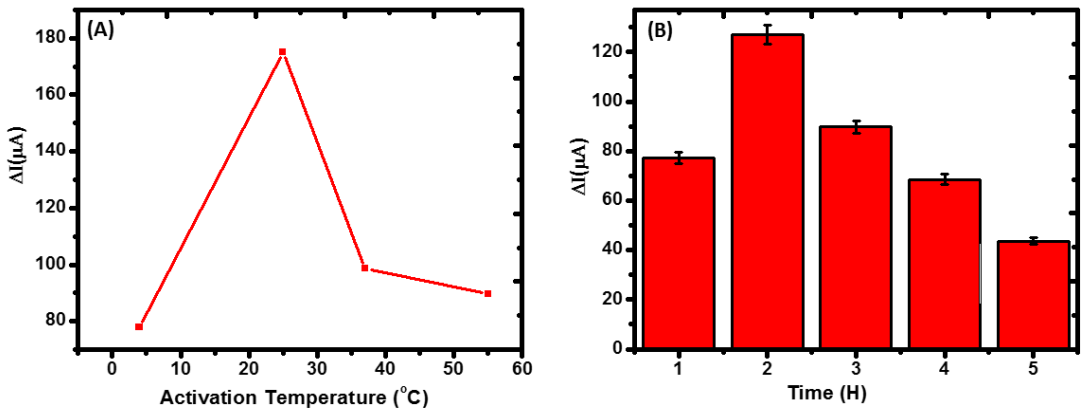

Figure 5-27: Effect of aptamer incubation (A) temperature and (B) time.

(v) Effect of cross linker and aptamer ratio

In order to improve the activation process, the effect of cross-linker and the aptamer ratio was optimized. The aptamer solution (2 µM) was mixed with cross-linker 0.4 M EDC

and 0.1 M NHS in the different ratios (1:1:1, 2:1:1, 3:1:1, 4:1:1, and 5:1:1) and kept at 25 °C for 30 min. The current signal increases with the increase of the ratio up to 2:1:1 and then decreases (**Figure 5-28**). This indicates that most of the carboxylic groups are not activated by the cross-linker. Therefore, the ratio of 2:1:1 was used for the entire experiments.

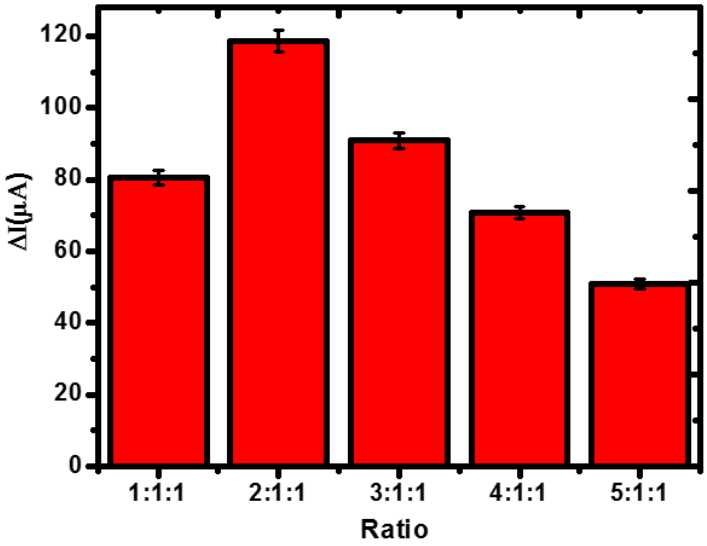

Figure 5-28: Effect of cross-linker and aptamer ratio.

5.2.1.4 Electrochemical characterization of CF/BN-TiO_2/Apt/BSA

Cyclic voltammetry (CV) technique was used to investigate the different steps of the aptasensor fabrication (as indicated in **Figure 5-29**). A bare CF (curve i) shows a well-defined redox with the peak current I_{pa} = 7.32 µA, which is attributed to the high electron transfer efficiency between $[Fe(CN)_6]^{3-/4-}$ in solution and electrode surface. The drastic increase of peak current (I_{pa} = 13.58 µA) was observed after the modification of CF with TiO_2 (curve ii), due to its high catalytic activity and large surface area (Li *et al.* 2020a). A further increase of peak current occurred (I_{pa} = 18.67 µA) when BN was introduced on CF/TiO_2 (curve iii) due to the increased electroactive surface area and the good conductivity of the BN-TiO_2 composite, which stimulates the electron transfer between the electrolyte and the electrode (Singh *et al.* 2017). The immobilization of aptamer onto BN-TiO_2 (curve iv) results in the decrease of anodic peak current (I_{pa} = 14.43 µA). Similar results has been reported in the literature (Wang, Li and Zhao 2019; Han *et al.* 2020). This may be due to the

negatively charged aptamer which repel anionic redox probe, $[Fe(CN)_6]^{3-/4-}$, therefore the electron-transfer resistance increases (Geleta, Zhao and Wang 2018b; Wang, Li and Zhao 2019). When BSA (curve v) was covalently attached onto the CF/BN-TiO_2/Apt surface, a major decrease in the anodic peak current (I_{pa} = 11.56 µA) was observed, due to the low conductivity of proteins (Han *et al.* 2020). The CV results confirmed that the electrochemical aptasensor was successfully fabricated.

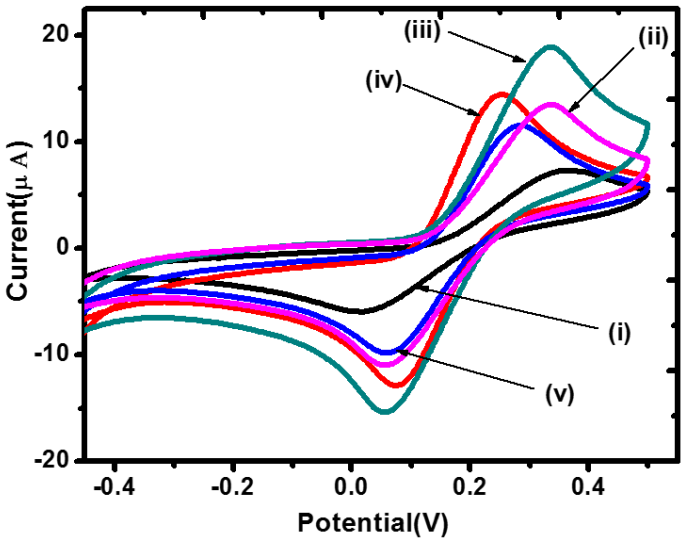

Figure 5-29: Cyclic voltammograms obtained from different electrodes: (i) bare CF; (ii) CF/TiO_2; (ii) CF/BN-TiO_2; (iii) CF/BN-TiO_2/Apt; (iv) CF/BN-TiO_2/Apt/BSA in 5 mM $[Fe(CN)_6]^{3-/4-}$ containing PBS (pH 7.5) and 0.1 M KCl solution (scan rate of 20 mVs^{-1}).

5.2.1.5 Optimization of analytical parameters for CF/BN-TiO_2/Apt/BSA

(i) Effect of pH

pH is one of the critical contributing factors that affect the aptasensor performance. The effect of pH was optimized by preparing different buffers with pH values ranging from 5 to 8. **Figure 5-30**A show that the current signals increased with the increase of pH from 5 to 7.5 and decreases at pH 8.0. The maximum current signal was attained at pH 7.5. This shows that highly acidic or alkaline environment denatures the activity of the immobilized aptamer or it affects the interaction between aptamers and their targets (Su *et al.* 2013). In addition, it suggests that the aptamer maintains its activity at neutral conditions. Therefore pH 7.5 was

selected for the determination of AFB_1, similar to physiological bio-fluid levels (Chung *et al.* 2020).

(ii) Effect of incubation time

Incubation time plays a significant role on the performance of the proposed aptasensor. The impact of AFB_1 incubation time with the novel aptasensor was studied. The current response of CF/BN-TiO_2/Apt/BSA in the presence of AFB_1 at different time (10 to 60 min) was evaluated (**Figure 5-30**B). The current signals increased significantly with the prolongation in AFB_1 incubation time and reached a plateau at an incubation time of 30 min. So, the incubation time of 30 min for AFB_1 was chosen as the optimal incubation time in further experiments.

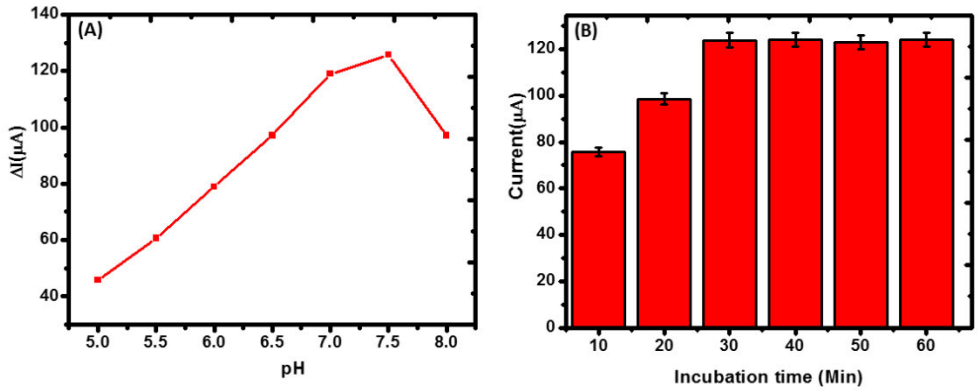

Figure 5-30: Effect of (A) pH and (B) AFB_1 incubation time.

(iii) Effect of scan rates

The effect of scan rate was carried out to verify the reaction process (diffusion or adsorption process) that occurred on the electrode surface. **Figure 5-31**A shows the CV voltammograms at different scan rates (5 to 35 mVs^{-1}) using CF/BN-TiO_2/Apt/BSA in the 5 mM $[Fe(CN)_6]^{3-/4-}$ solution containing 0.1 M PBS of pH 7.5. The increase of scan rate from 5 to 35 mVs^{-1} resulted in the shifting of peak potential towards positive which is due to the formation of the double layer at the electrode surface, showing an irreversible nature of the electroactive molecule (Purushothama *et al.* 2018). A plot of peak current (I_{pa} and I_{pc}) and scan rate (υ) gave a straight line as showed in **Figure 5-31**B, with the linear equation expressed as I_{pa} (μA) = 0.861υ(mVs^{-1}) + 27.905; R^2 = 0.999 and I_{pc} = -0.839υ(mVs^{-1}) -

26.306; R^2 = 0.989.These results confirmed that the electrode reaction is a diffusion controlled process (Ilager *et al.* 2021). A linear correlation between the peak currents (µA) and the square root of scan rate $(mVs^{-1})^{1/2}$ with the equation expressed as $I_{pa}(\mu A) = 7.062\upsilon^{1/2}$ $(mV^{1/2}s^{-1/2})$ +14.518; R^2 = 0.997 and I_{pc} (µA) = $-6.992\upsilon^{1/2}$ $(mV^{1/2}s^{-1/2})$ -12.981; R^2 = 0.999 showed in **Figure 5-31**C also confirmed a diffusion controlled process (Švorc *et al.* 2018; Tajik, Beitollahi and Biparva 2018).

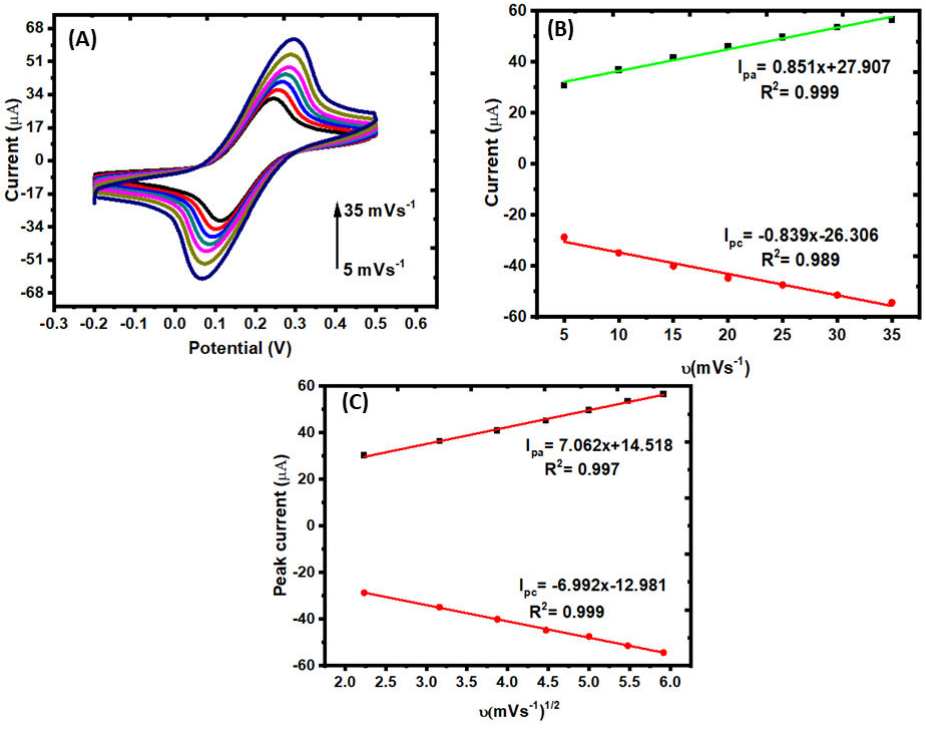

Figure 5-31: (A) Effect of scan rate (5 to 35 mVs^{-1}) on voltammetric behavior of AFB_1 at CF/BN-TiO_2/Apt/BSA. Plot of (B) peak current vs. scan rate, and (C) peak current vs. the square root of the scan rate.

5.2.1.6 Electrochemical behaviour of AFB_1 at CF/BN-TiO_2/Apt/BSA

(i) Quantitative analysis of AFB_1

Under optimal conditions, the analytical performance of the aptasensor was examined by capturing AFB_1 of various concentrations (2.5 to 20 ng mL^{-1}). The DPV curves shows a decrease in the peak current with an increase in the concentration of AFB_1 (**Figure 5-32**A). A good linear relationship was attained between the ΔI and the AFB_1 concentrations in the range of 2.5 ng mL^{-1} to 20 ng mL^{-1}. The regression equation is ΔI = -6.535 [AFB_1] + 187.037 with correlation coefficient of R^2 = 0.997 (**Figure 5-32**B). The limit of detection

(LOD) was found to be 0.002 ng mL^{-1} (LOD = 3σ, σ means standard deviation of blank). The obtained LOD was much lower than that of the reported electrochemical aptasensors for the determination of AFB_1 (Goud *et al.* 2016b; Li *et al.* 2020c). The low detection limits may be attributed to the fact that a large amount of the oligo has been conjugated on the large surface area of BN-TiO_2 composite. The large surfaces area of the nanocomposite increases the interaction between the oligo and the analyte.

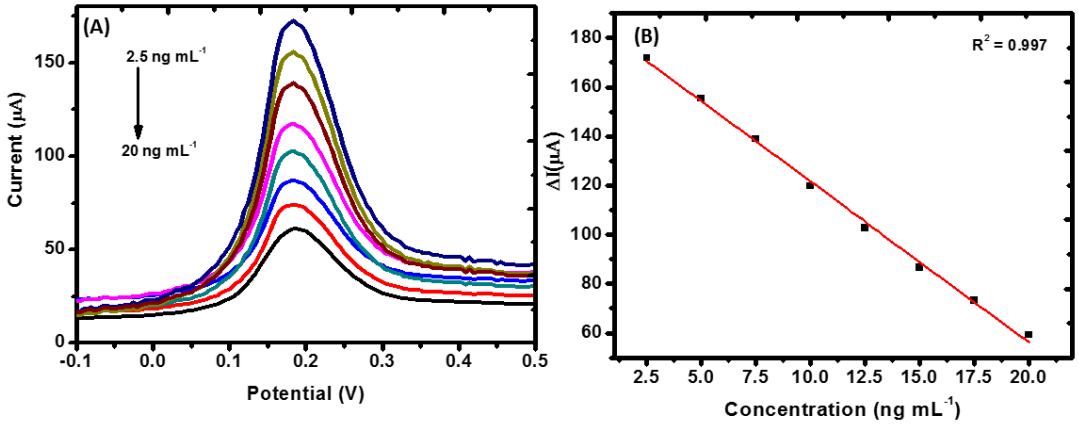

Figure 5-32: (A) DPV response of the aptasensor after incubation with various concentrations (2.5 to 20 ng mL^{-1}) of AFB_1 antigen and (B) Calibration plot of DPV peak current vs. the various AFB_1 concentration.

(ii) Analytical application of designed aptasensor in real sample

To evaluate the performance of fabricated aptasensor, standard addition method was employed to verify the precision. Different concentration of AFB_1 (2.5, 12.50 and 20 ng mL^{-1}) were spiked with yoghurt. The AFB_1 recoveries were 88.00, 104.40 and 99.35%, respectively and the RSD ranging from 2.51 to 4.01% (**Table 5-4**). The real sample analysis showed that the proposed aptasensor has potential applications in practical testing.

Table 5-4: The recovery studies of AFB1 in yoghurt using the fabricated aptasensor.

AFB_1 Added (ng mL^{-1})	**AFB_1 Founded (ng mL^{-1})**	**Recovery (%)**	**±RSD (n=3)**
2.50	2.20	88.00	4.09
12.50	13.50	104.40	2.51
20.00	19.87	99.35	3.31

(iii) Reproducibility and stability of CF/BN-TiO_2/Apt/BSA

Reproducibility of the fabricated aptasensor was studied by fabricating five individual aptasensor using the optimized conditions. Five fabricated aptasensor were tested in identical environment (**Figure 5-33**A). The relative standard deviation (RSD) of the measurement was 4.20%, signifying the precision was reasonably good for AFB_1 detection. The stability was also investigated to assess the storage time of the fabricated aptasensor (**Figure 5-33**B). The well-fabricated aptasensor was stored at 4 °C, and after 15 days, 95.00% of the current signal was retained compared with the initial response, demonstrating the acceptable stability.

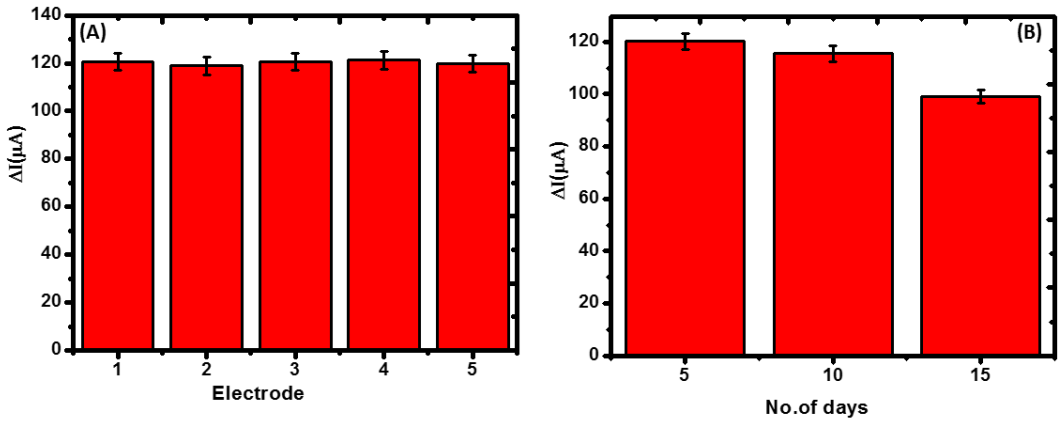

Figure 5-33: (A) Reproducibility of the aptasensor based on five different electrodes incubated with AFB_1 (10 ng mL^{-1}) (D) Long-term stability of the fabricated aptasensor.

(iv) Selectivity study of CF/BN-TiO_2/Apt/BSA

The selectivity of the fabricated aptasensor was examined in the presence of OTA. The DPV response of the aptasensor in presence of 10 ng mL^{-1} AFB_1, 10 ng mL^{-1} OTA and the mixture of AFB_1 and OTA each were recorded and the attained results are shown in **Figure 5-34**. A negligible current signal was observed when detecting OTA compared to AFB_1 detection. Consequently, the current signal of the AFB_1 is almost the similar regardless to the coexistence of OTA. These results proof that the designed aptasensor to be highly selective for AFB_1 detection.

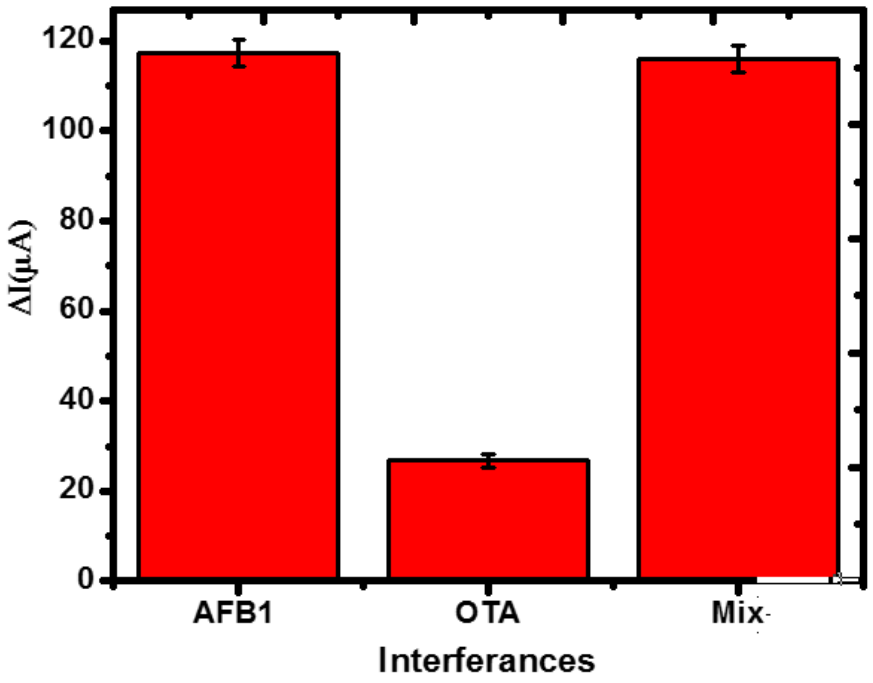

Figure 5-34: Selectivity test of the CF/BN-TiO_2/Apt/BSA for detection of AFB_1.

5.2.3 Conclusion

In the case study, a novel CF/BN-TiO_2/Apt/BSA based electrochemical aptasensor for the detection of AFB_1 was fabricated based on the properties (including the large surface area and good electro-catalytic) of BN-TiO_2 nanocomposites. The developed electrochemical aptasensor displayed a good selectivity, stability, reproducibility, wide linear range from 2.5 to 20 ng mL^{-1} and low detection limits of 0.002 ng mL^{-1}. Furthermore, the recovery studies

in the spiked yoghurt samples suggest acceptable practical feasibility of the fabricated aptasensor. Although the current aptasensor is dedicated on the detection of AFB_1, the CF/BN-TiO_2/Apt/BSA based electrochemical aptasensor can be useful to detect other mycotoxins by using the corresponding aptamer.

5.3 Case Study 3: Immunosensor for detection of Ochratoxin (OTA) in coffee

In this case study, the fabrication and performance of a palladium (PdNPs) modified carbon felt immunosensor for OTA are discussed. Different parameters for the synthesis of PdNPs by atomic layer deposition (ALD) are also discussed. The electrochemical behavior of OTA using cyclic voltammetry (CV) and differential pulse voltammetry (DPV) are presented. The fabricated immunosensor was also successfully applied for the determination of OTA in coffee samples.

5.3.1 Experimental

Synthesis of palladium nanoparticle (PdNPs) by atomic layer deposition (ALD) PdNPs was on the carbon felts (CF) substrate (full procedure on materials and methods chapter 4).

5.3.1.1 Effect of PdNPs cycle number

The PdNPs cycle number was optimized by the deposition of different cycle number (100, 200 and 300) onto the carbon felts electrode (CFE). The electrocatalytic properties of the synthesized PdNPs were examined using a redox probe maker (5 mM $[Fe(CN)_6]^{3-/4-}$) in a 0.1 M KCl solution (**Figure 5-35**A). The current increases from 100 cycles (1.14 µA) to 200 (1.79 µA) due to the availability of more active site on the substrate, easing flow of electrons (Chiappim *et al.* 2016). However, the current decreased at 300 cycles (1.49 µA) due to the thickness of the substrate which obstructed electrons to flow through. These results were in agreement with TEM images. **Figure 5-35(**B-D**)** shows the TEM images of PdNPs as a function of ALD cycles. More NPs were formed on 100 to 200 cycles **(Figure 5-35(**B-C**))**, resulting to the increase of surface area. However, cycle number 300 resulted in the merged NPs, this phenomenal is described as particle coalescence with movement of electrons. Therefore, 200 cycle number of was the best and used for the synthesis of PdNPs.

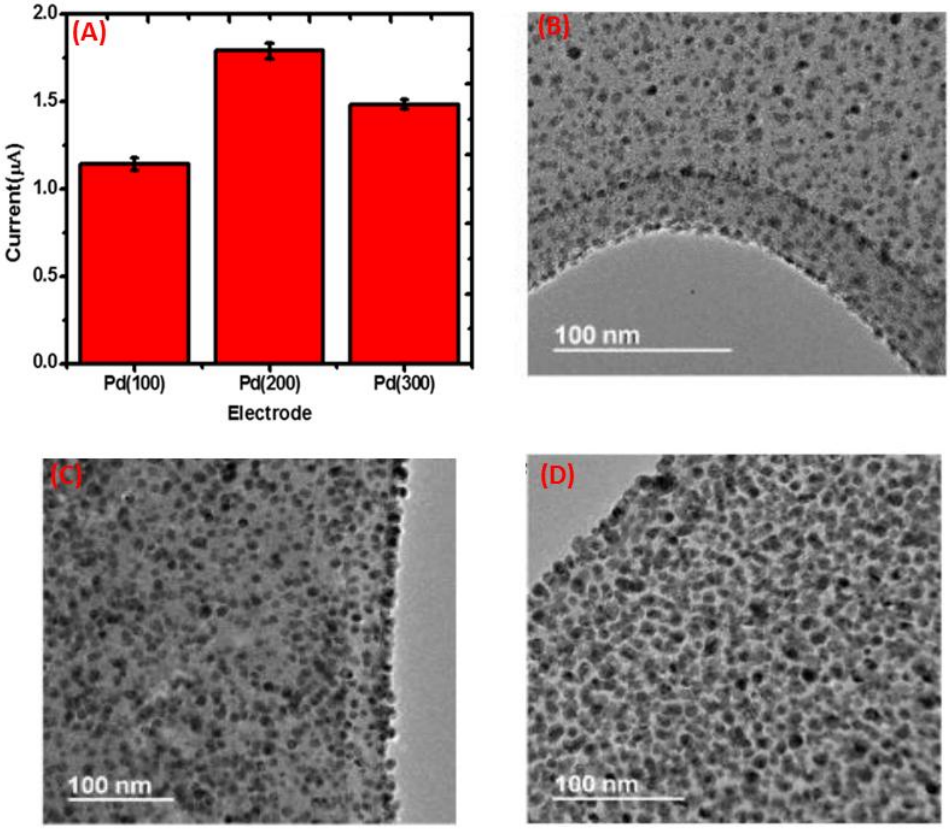

Figure 5-35: (A) The relationship between the number of Pd cycle and current and (B-C) TEM images of PdNPs surface after 100, 200, and 300 ALD deposition respective.

5.3.1.2 Characterisation of PdNPs

Different characterization techniques such as transmission electron microscope (TEM), scanning electron microscope (SEM), and selected area electron diffraction (SAED) were used to characterize the PdNPs.

(i) Scanning electron and transmission electron microscopic (SEM, TEM) characterization.

SEM and TEM were used to study the surface morphology of the fabricated electrodes. SEM micrograph of PdNPs deposited onto CF by ALD over 200 cycles shows the uniform dispersed PdNPs (**Figure 5-36**A). SEM has a limited resolution therefore; TEM was used for further characterization of the PdNPs.The TEM images **(Figure 5-36**B) revealed that the average diameter of PdNPs as 6.0 ± 2 nm which is similar to that reported by Weber and co-workers (4 - 6 nm) (Weber *et al.* 2018).

The crystallinity structure of the PdNPs was then studied by SAED. The SAED pattern showed the highly crystallinity of PdNPs and characteristic diffraction ring of (111), (200), (220), and (311), which corresponds to the lattice planes of fcc palladium, respectively (Kongor *et al.* 2020) (**Figure 5-36**C). Both TEM and SEM images shows that the PdNPs are well-dispersed onto the surface of the carbon substrate with (>70% coverage).

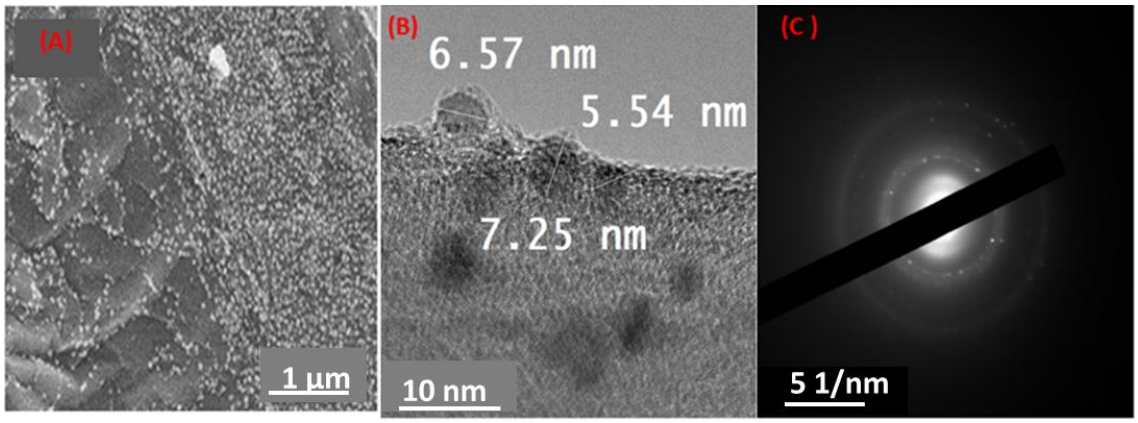

Figure 5-36: (A) SEM images of PdNPs; (B) TEM images of PdNPs and (C) selected area electron diffraction (SAED).

5.3.1.3 Optimization of parameters for the fabrication of CF/PdNPs/anti-OTA/BSA

To attain the greater detection performance of the electrochemical immunosensor, different parameters such as the ratio between EDC: NHS, antibody concentration, incubation time, activation temperature and the activation time of the immunosensor were studied. These results were expressed by the differences in the peak current responses using DPV (ΔI_p), measured before and after incubated with OTA.

(i) Effect of cross linker and antibody ratio

The cross linker was used to activate the carboxyl groups that are present in the anti-OTA. Thus, it is very crucial to optimize the ratio between the cross linker and the antibody in order to improve the activation process. The anti-OTA solution (1 µg mL^{-1}) was mixed with 0.4 M EDC and 0.1 M NHS in the different ratios (1:1:1, 2:1:1, 3:1:1, 4:1:1, 5:1:1, 6:1:1 and 7:1:1) and kept at 4.0 °C for 30 min. The current increases with increase of the ratio from 1:1:1 to 4:1:1 and decreases from ratio 5:1:1 to 7:1:1 (**Figure 5-37**A) suggesting that less cross-linker allowed a great interaction with the antibody which improves the activation process. The

decreased current observed at high ratios, is due to numerous locations of carboxylic that the cross-linker has to interact with. Therefore, the ratio of 4:1:1 was used for the entire experiments.

(ii) Effect of antibody concentration

The concentration of the antibody plays a significant role in the fabrication of the immunosensor. When there is more OTA solution that reacts with the antibody, there will be a less amounts of antibody that will be immobilize on the electrode. Consequently, the electrochemical signal would decrease significantly. So, the effect of anti-OTA antibody concentration on the peak current was also examined. This was conducted by immobilizing four different concentrations of anti-OTA (0.5, 1.0, 5.0 and 10 μg mL^{-1}) onto the PdNPs/CF electrode surface. The electrochemical signal responses of OTA were measured from 0.5 ng mL^{-1} to 2.5 ng mL^{-1} to check the sensitivity of the fabricated immunosensor. **Figure 5-37**B shows a decrease in current with increased OTA concentration in all the four immunosensors. However, different immunosensor fabricated with different anti-OTA yielded a different LOD and R^2 values. The immunosensor with the anti-OTA concentrations of 0.5, 1.0, 5.0 and 10 μg mL^{-1} results in 0.46, 0.25, 0.39 and 0.44 ng mL^{-1} LODs and regression coefficients (R^2) of 0.9651, 0.9982, 0.9857 0.9234 respectively as shown in **Table 5-5**. The results indicated that the low concentration of antibody (1.0 μg mL^{-1}) significantly reduced electrochemical signal and the relatively high concentration (10 μg mL^{-1}) could not obtain enough sensitivity. This is due to the dense electrode surface with an insufficient binding between the antigen and antibody to cause a current change. Therefore, the thicker bioactive layer is the cause of a low performance of the immunosensor. Hence, 1.0 μg mL^{-1} anti-OTA was chosen as the optimal concentration for the further characterization of the immunosensor.

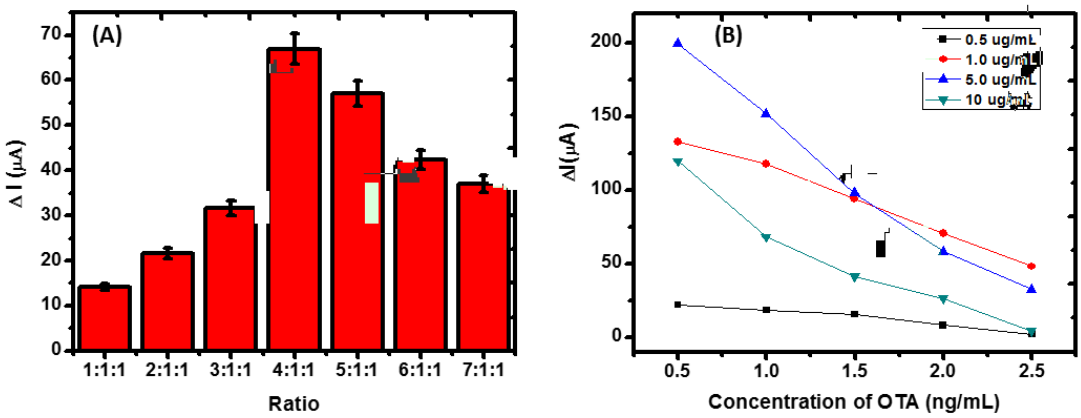

Figure 5-37: (A) Effect of antibody and cross linker ratio and (B) Effect of anti-OTA concentrations.

Table 5-5: Effect of anti-OTA concentrations.

Concentration of antibody (ug mL^{-1})	**LOD**	**LOQ**	**R^2**
0.5	0.46	1.82	0.9651
1.0	0.26	0.75	0.9982
5.0	0.39	1.18	0.9857
10	0.44	1.39	0.9234

(iii) Effect of the incubation time of the antibody

The effect of incubation time of the antibody was carried out by incubating the fabricated electrode at 4 °C at different time from 2 to 8 h while monitoring the current signal. **Figure 5-38**A shows that the current increases with the increase of incubation time up until 6 h with no noticeable current differences after 6 h. This indicates that, the surface saturation occurred beyond 6 h. Also, prolonging the incubation time makes the reaction sufficient and increase the sensitivity of the immunosensor. Thus, the incubation time was kept at 6 h at 4 °C throughout the study.

(iv) Effect of activation time of the antibody

To get a maximum sensitivity, the activation time between the cross-linker and the antibody should be allowed to reach the equilibrium. The cross-linker and the antibody were incubated at 4.0 °C at different time (10, 20, 30, 40 and 50 min). **Figure 5-38**B shows that the peak current increases with the increase of activation time until 30 min, after 30 min there was a negligible current change. Therefore, the activation time was kept at 30 min for the entire experiments.

(v) Effect of activation temperature

The activation temperature is one of the most important parameters when fabricating the immunosensor. The activation was then carried out at different temperature (4.0, 25 and 37 °C). The increase of the activation temperature results in the reduction of the current as shown in **Figure 5-38**C. This shows that high temperatures denature the activity of the antibody and results in the low current signals. The low activation temperature of 4.0 °C has been reported in the literature by numerous researchers (Ma *et al.* 2016; Gupta *et al.* 2017b).

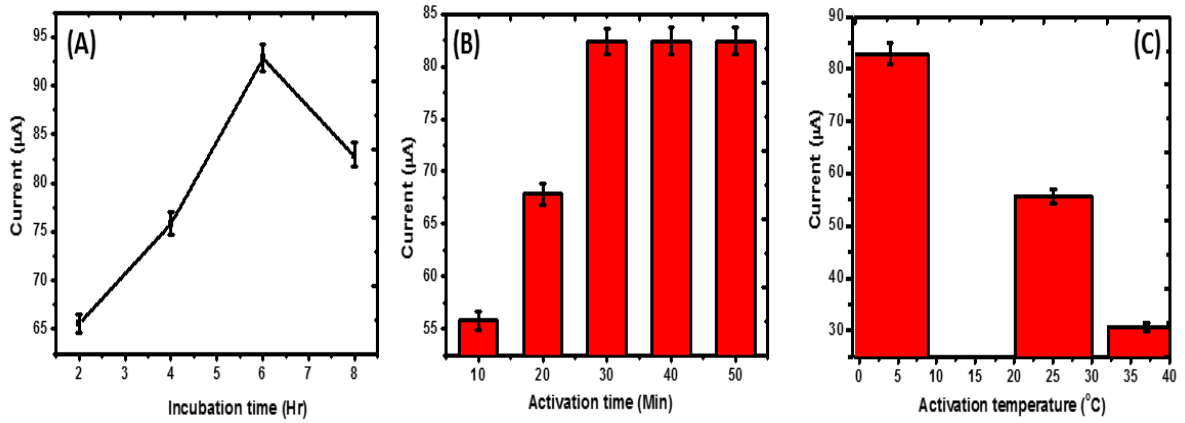

Figure 5-38: Effect of antibody (A) incubation time, (B) activation time, and (C) activation temperature.

5.3.1.4 Structural, morphological, and electrochemical characterization CF/PdNPs/anti-OTA/BSA

Different technique such as scanning electron microscope (SEM), attenuated total reflectance (ATR), cyclic voltammetry (CV) and electrochemical impedance spectroscopy (EIS) were used for the characterization of the immunosensor.

(i) Characterization of the immunosensor by SEM and ATR

The morphology of the fabricated immunosensor was studied by SEM (**Figure 5-39**A-B). After the immobilization of blocking agent BSA onto anti-OTA/PdNPs/CF a smooth surface morphology was obtained as shown in **Figure 5-39**A. The incubation of the mycotoxin OTA onto CF/PdNPs/anti-OTA/BSA results in the rough surface (**Figure 5-39**B), indicating the adsorption of OTA onto the electrode surface. The ATR was used to identify the functional groups present in the immunosensor. Figure 5-40 show the CF/PdNPs/anti-OTA (**Figure 5-40** i) and CF/PdNPs/anti-OTA/BSA (**Figure 5-40** ii) spectra with a characteristic bands of –NH at 1671, $–CH_2$ at 1456 cm^{-1} and 852 cm^{-1} (curve i). These peaks/bands correspond to the deformation of the amide-II bond, the aliphatic moiety of anti-OTA and are due to free $–NH_2$ groups on the electrode surface, respectively. This shows that the antibody was successfully attached onto the electrode surface. Gupta and co-workers reported similar results during the fabrication of an immunosensor (Gupta *et al.* 2017b). The band at 852 cm^{-1} disappeared after the immobilization of BSA (curve ii; CF/PdNPs/anti-OTA/BSA). This confirms that the nonspecific sites that are present on the CF/PdNPs/anti-OTA immunosensor are blocked (Solanki *et al.* 2015b).

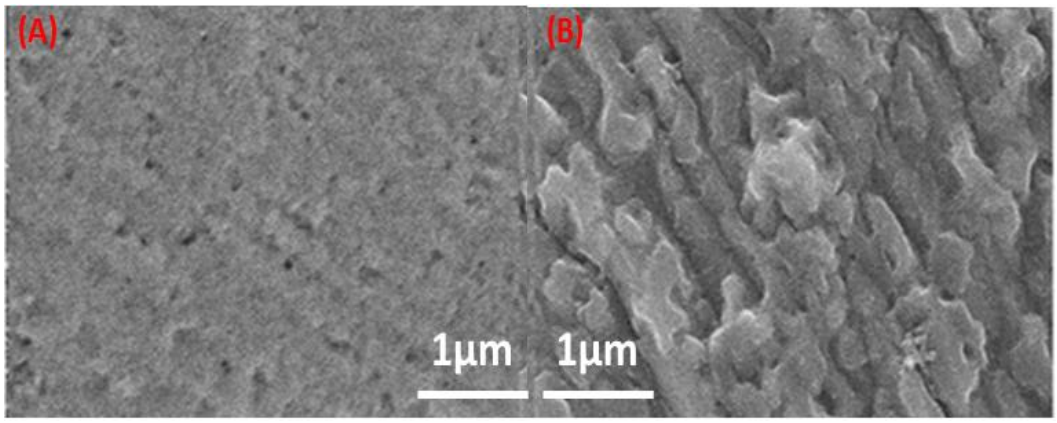

Figure 5-39: (A) SEM images of CF/PdNPs/anti-OTA/BSA and (B) CF/PdNPs/anti-OTA/BSA/OTA.

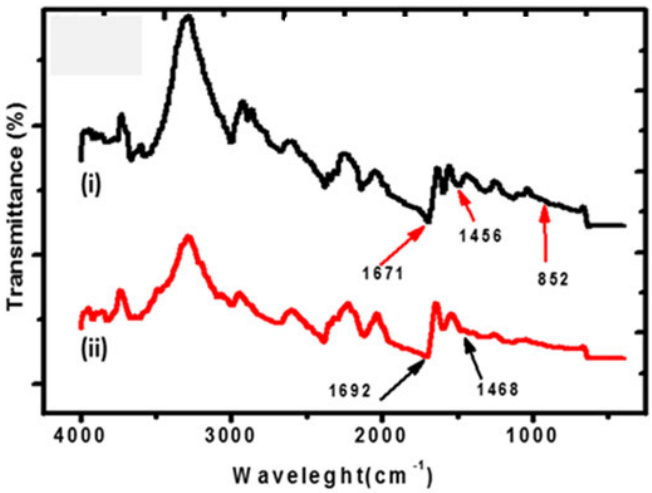

Figure 5-40: The ATR of (i) CF/PdNPs/anti-OTA and (ii) CF/PdNPs/anti-OTA/BSA.

(ii) Characterization of CF/PdNPs/anti-OTA/BSA by cyclic voltammetry (CV)

The behavior of the modified electrode was monitored by CV. **Figure 5-41** shows the CV response obtained using 5.0 mM $[Fe(CN)_6]^{3-/4-}$ in PBS for (i) CF (ii), CF/PdNPs (iii) CF/PdNPs/anti-OTA and (iv) CF/PdNPs/anti-OTA/BSA immunosensors. A pair of well-defined redox peak was observed for the CF (curve i), this quasi-reversible redox peak was attributed to the transformation between $[Fe(CN)_6]^{4-}$ and $[Fe(CN)_6]^{3-}$. The low anodic peak current (I_{pa}) of 0.99 µA for the bare CF electrode exhibits a poor electrochemical response of the CF electrode. The I_{pa} increased to 1.77 µA when CF/PdNPs was coated to the surface (curve ii). These results reveal that deposition of PdNPs onto the CF substrate improves the rate of electron transfer between analyte and working electrode, due to high surface area and

improvement in catalytic activity of the electrode. However, when anti-OTA were immobilized onto the CF/PdNPs electrode the I_{pa} increased to 2.05 µA (curve iii), indicating further enhancement in the sensitivity. This phenomenon is probably due to the fragmented crystalline (Fc) region of the anti-OTA and the amine groups that forms a penetrating path between anti-OTA and electrode (Gupta *et al.* 2017b). The free site amino group of anti-OTA available onto immunosensor surface electrostatically interacts with redox species of electrolyte and facilitates the fast electron diffusion at the electrode. However, for the CF/PdNPs/anti-OTA/BSA electrode the I_{pa} decreased to 1.83 µA (curve iv), this is in agreement with the previous report stating that BSA inhibiting the diffusion of redox species towards the electrode (Ali *et al.* 2014b). Our results confirmed the successful fabrication of the CF/PdNPs/anti-OTA/BSA immunosensor.

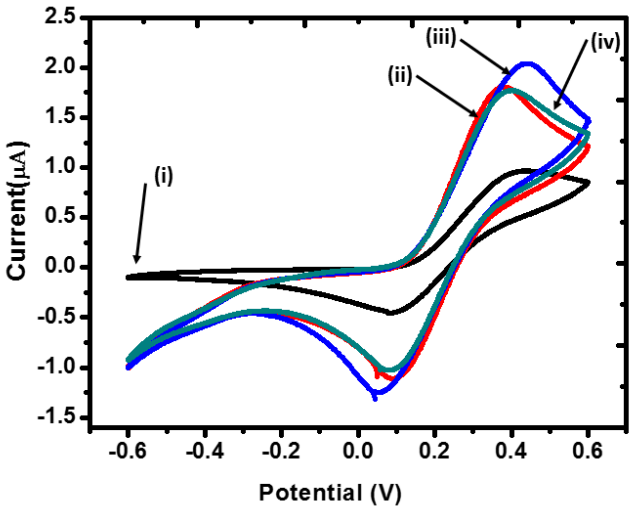

Figure 5-41: CV voltammograms of (i) CF, (ii) CF/PdNPs, (iii) CF/PdNPs/anti-OTA and (iv) CF/PdNPs/anti-OTA/BSA in a 5.0 mM $[Fe(CN)_6]^{3-/4-}$ solution that contains 0.1 M PBS and 0.1 M KCl.

(iii) Characterization of CF/PdNPs/anti-OTA/BSA by electrochemical impedance spectroscopy (EIS)

Electrochemical impedance spectroscopy results are presented using a Nyquist plot of CF with different modification processes using $[Fe(CN)_6]^{3-/4-}$ as the electrolyte. The EIS measurement was performed in 0.1 M KCl containing $[Fe(CN)_6]^{3-/4-}$ with AC frequency from 0.1 to 105 Hz. The EIS spectrum comprises of a semicircle and the linear part as illustrated in **Figure 5-42**A-B. The semicircle diameter represents the electron-transfer resistance (R_{ct}) and reveals the restricted diffusion of the electrolyte through the multilayer

system, directly related to the film permeability. A very small semicircle diameter is observed on CF electrode (**Figure 5-42**A) demonstrating a low charge transfer resistance for the electrochemical process. At low frequency, the linear part (Warburg impedance (W)) is associated with the mass transfer process. After the deposition of PdNPs on the CF, the capacitance increases. **Figure 5-42**B (curve i) shows the modification with PdNPs resulted in the increase of electrochemical active surface area. The amplification of electrochemical signal and the enhancement of the electron transfer rate of the sensor are due to the excellent electro-catalytic activity of PdNPs (Zhang *et al.* 2018a). After immobilization of anti-OTA (curve ii) onto PdNPs/CF electrode, a remarkable decrease of the charge transfers resistance (R_{ct}) is observed. This phenomenon is attributed to the presence of positively charged amino residues on the antibody structure, which facilitates the electrochemical reaction (Radi *et al.* 2009). The increase in electron transfer can also be attributed to the neutralization of surface negative charge upon reaction with EDC/Sulfo-NHS (Conzuelo *et al.* 2012). However, after immobilization of BSA (curve (iii)), both R_{ct} and the capacitance increased, due to the longer path for the electrons to move from the solution to the surface of the electrode. The EIS data in **Figure 5-42**(A-B) were further analyzed by fitting them to the simulation data using the equivalent circuit model shown in **Figure 5-42**B inset. The fitting parameters include the ohmic resistance of the electrolyte solution (R_s), C is the capacitance that arises due to coverage of the electrode surface with BSA, R_{ct} is a charge transfer resistance that is caused by the resistance of electrons between electrode and $[Fe(CN)_6]^{3-/4-}$ redox probe, R is electrolyte resistance in the pore and Q is the CPE arising due to CF surface and Warburg impedance (W). Yang and co-workers reported the similar equivalent circuit on their work, their equivalent fitting has, the interface ohmic resistance (Rd), double layer capacitances (CPEdl) and pore adsorption capacitance (CPEad) (Yang *et al.* 2016). Siddiqui also reported the similar equivalent circuit that has the uncompensated resistance (R_s), capacitance (C), charge transfer resistance (R_{ct}), R is electrolyte resistance in the pore and Q (Siddiqui *et al.* 2012). BSA layer makes the electrode surface more homogenous and generates the capacitance of 0.4×10^{-8} F. Therefore, BSA behaves as an insulator. Moreover, the ohmic resistance (R_s) of CF/PdNPs/anti-OTA/BSA is estimated to be ~8.06 ohms, much lower than that of CF materials (~19.22 ohms) and PdNPs (~10.7 ohms).

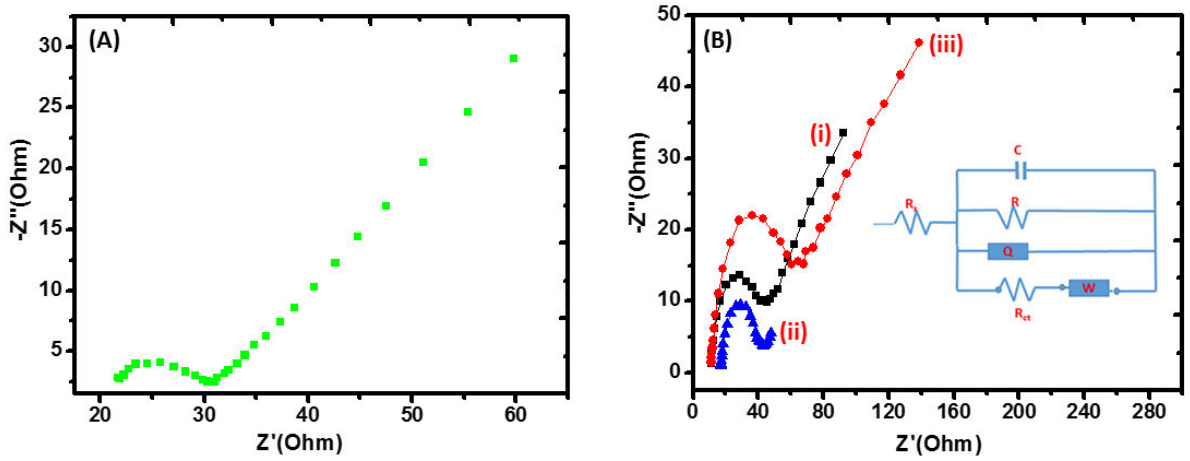

Figure 5-42: (A) Nyquist plots of bare CF electrode and (B) CF/PdNPs (i), CF/PdNPs/anti-OTA (ii) and CF/PdNPs/anti-OTA/BSA (iii) modified electrode in 5.0 mM $[Fe(CN)_6]^{3-/4-}$ solution that contains 0.1 M KCl and 0.1 PBS, pH 7.0.

5.3.1.5 Optimization of analytical parameters for CF/PdNPs/anti-OTA/BSA

To fabricate the immunosensor, the antibody (anti-OTA) was immobilized on the modified carbon felt electrode (CFE) with PdNPs. The fabricated electrode was denoted as CF/PdNPs/anti-OTA/BSA. Several parameter such as pH, scan rate and incubation time were studied.

(i) Effect of pH

The effect of pH is one of the most significant parameter when fabricating an immunosensor, due to the strong influence of the electrolyte on the electrochemical performance. This parameter was examined by observing the current response of the immunosensor in different electrolytes pH range, from pH 6.0 – 8.0. The peak currents response increase from pH 6.0 – 7.0, then gradually decrease beyond pH 7.0 (see **Figure 5-43**A). This shows that biomolecules on the electrode surface performs the best on neutral condition because, the basic or acidic conditions denatures them due to the interaction of H^+ or OH^- ion with amino acid sequence of antibodies (anti-OTA) (Ali *et al.* 2014a; Zhou *et al.* 2015). The optimum peak current was observed at pH 7.0 and therefore it was selected as the optimal pH for the subsequent experiments.

(ii) Effect of incubation time

The immune complex reaction is formed when antibody binds with the antigen. This formation depends on the binding time (incubation time) between the antibody and antigen. Therefore, it's very crucial to optimize the incubation time of the fabricated immunosensor in order to get the optimum incubation time. This was studied by varying the incubation time from 5 to 60 min and measure the current using 1.0 ng mL^{-1} OTA on CF/PdNPs/anti-OTA/BSA. **Figure 5-43**B shows that the current increases with an increase of the interaction time from 5 to 40 min. Beyond 40 min, there was a negligible current change because of the saturation of antibodies. Therefore, the period of 40 min was selected as the optimum interaction time for the immune complex reaction between OTA and anti-OTA.

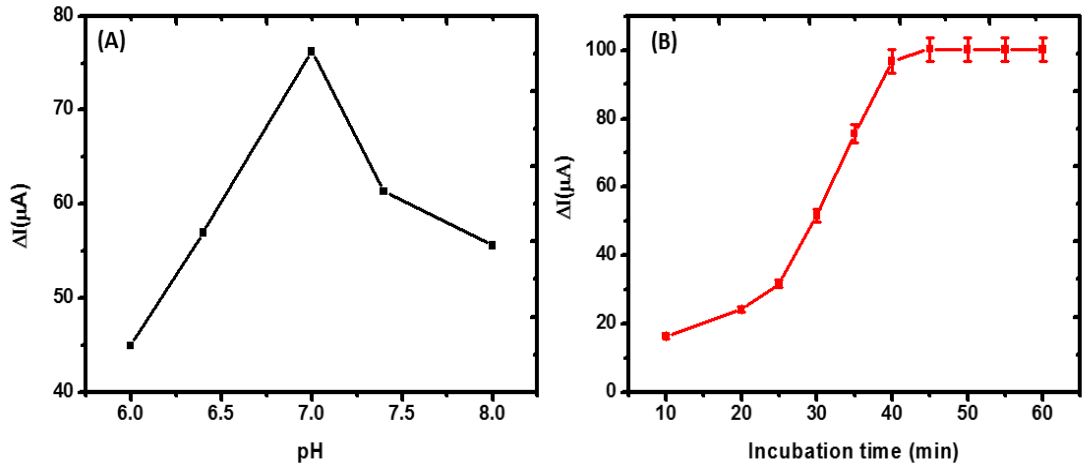

Figure 5-43: Effect of (A) pH and (B) incubation time.

(iii) Effect of scan rates

In order to study the nature of the fabricated immunosensor CF/PdNPs/anti-OTA/BSA, the effect of scan rate was studied by cyclic voltammetry. This was conducted by varying scan rate from 10 - 100 mVs^{-1} (**Figure 5-44**A). The anodic peak current (I_{pa}) and cathodic peak current (I_{pc}) were correlated with scan rates in a range 10 to 100 mVs^{-1}. A linear relationship was observed on both anodic peak current (I_{pa}) and cathodic peak current (I_{pc}) (**Figure 5-44**B), describing the adsorption-controlled process (Solanki *et al.* 2015b), and the equation can be expressed as: $I_{pa}(\mu A) = 1.867\upsilon(mVs^{-1}) - 3.518$; $R^2 = 0.988$, $I_{pc}(\mu A) = -1.140\upsilon(mVs^{-1}) + 8.187$; $R^2 = 0.986$. The nonlinear relationship between peak current (anodic

and cathodic) and square root of scan rate was observed **Figure 5-44**C, this results confirms that it a diffusion controlled process.

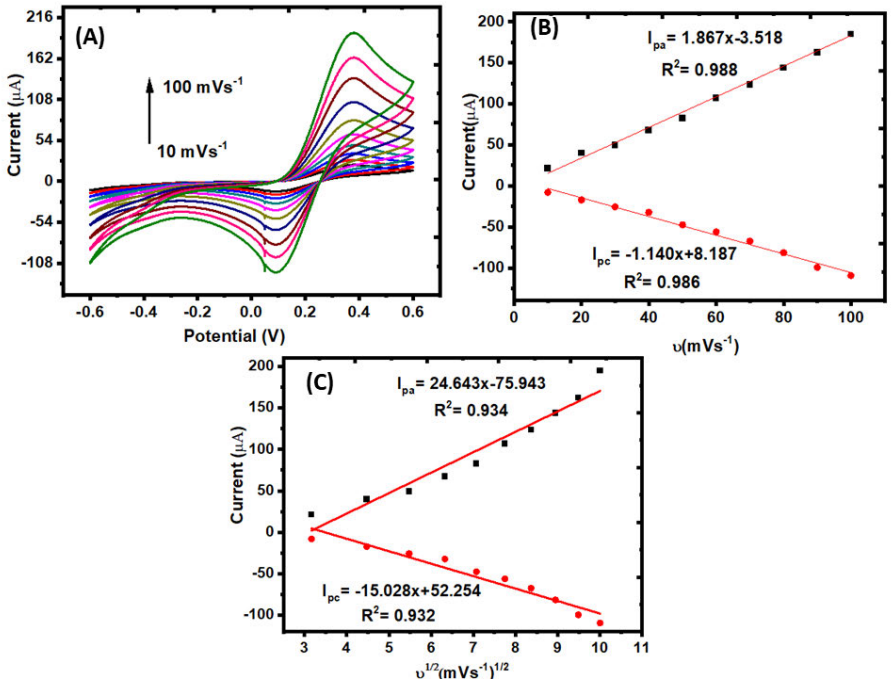

Figure 5-44: (A) Cyclic voltammograms of CF/PdNPs/anti-OTA/BSA at different scan rate (10,20, 30, 40, 50, 60, 70, 80, 90 and 100 mVs^{-1}) in the 5 mM $[Fe(CN)_6]^{3-/4-}$ solution that contains 0.1 M KCl and 0.1 M PBS. (B) The relationship between peak currents (anodic and cathodic) vs. scan rate, and (C) Plot of peak currents (anodic and cathodic) vs. square root of scan rate.

5.3.1.6 Electrochemical behaviour of OTA at CF/PdNPs/anti-OTA/BSA

(i) Quantitative analysis of OTA

The response of the fabricated immunosensor CF/PdNPs/anti-OTA/BSA towards OTA was studied with DPV in concentration range from 0.5 – 20 ng mL^{-1} as depicted in **Figure 5-45**A. The peak current was inversely proportional to the OTA concentrations, displaying the formation of the antigen-antibody complex onto the electrode surface. This was established through the interaction of antigen (OTA) with the antibody (anti-OTA) absorbed onto the CF/PdNPs/anti-OTA/BSA immunosensor which acted as an electron transporting layer (Kaushik *et al.* 2009; Li *et al.* 2011). **Figure 5-45**B shows the calibration curve attained as a function of OTA concentrations. The fabricated immunosensor CF/PdNPs/anti-OTA/BSA responds linearly to the logarithm concentrations of OTA ranging from 0.5 – 20 with LOD of 0.096 ng mL^{-1} (3×se)/m), with the regression equation of Y = -47.909x +

97.620 and a regression coefficient (R^2) of 0.9960. The fabricated CF/PdNPs/anti-OTA/BSA immunosensor have the ability to detect a very low concentration (96 pg mL^{-1}) of OTA as compared to other immunosensors (Malvano *et al.* 2016; Gupta *et al.* 2017a). These results showed that the PdNPs/CF materials provide high surface affinity to bind antibodies.

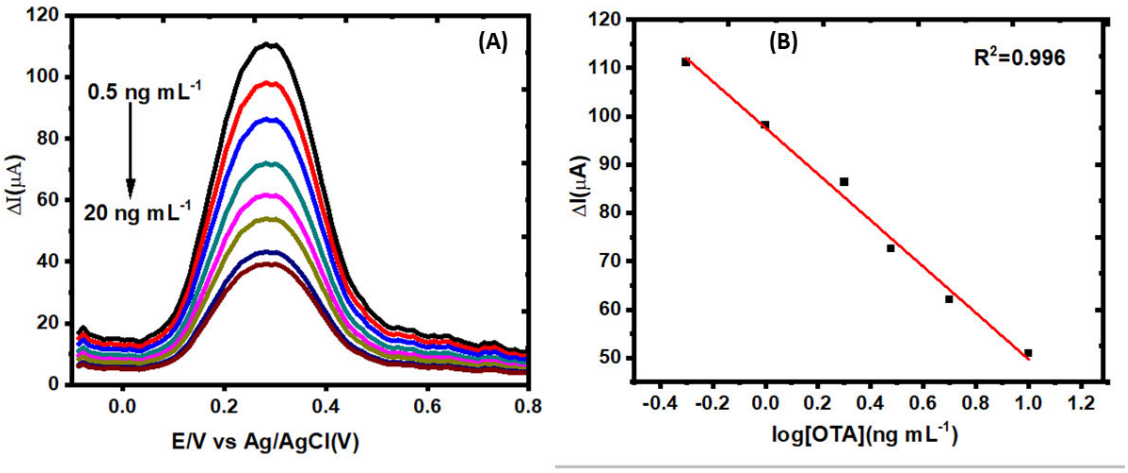

Figure 5-45: (A) DPV response of the immunosensor (CF/PdNPs/anti-OTA/BSA), for 0.5 – 20 ng mL^{-1} in the 5 mM $[Fe(CN)_6]^{3-/4-}$ solution that contains 0.1 M KCl and 0.1 M PBS (pH 7.0) and (B) Calibration plot of OTA detection on the fabricated immunosensor.

(ii) Practical analytical application of the immunosensor studies in real sample

The fabricated immunosensor CF/PdNPs/anti-OTA/BSA was used for the determination of OTA in coffee sample. DPV responses were recorded in the presence of different concentrations of the spiked coffee samples. **Table 5-6** shows the outcomes of the recovery studies for spiked sample in terms of electrochemical current. The DPV response was observed using five concentrations (0.5, 1, 5, 10, 20 ng mL^{-1}), and the recovery was found in the range of 93.20 – 98.90% with the RSD ranging from 1.72 to 2.82%. These results are quite good and suggest that fabricated immunosensor is appropriate to be applied to OTA detection in the food industry.

Table 5-6: Determination of OTA in coffee sample.

Spiked OTA concentration (ng mL^{-1})	**OTA Founded (ng mL^{-1})**	**Recovery (%)**	**RSD (n=3)**
0.5	0.49	97.90	2.82
1.0	0.98	98.90	1.90
5.0	4.65	93.20	2.75
10	9.73	97.30	2.55
20	19.35	96.70	1.72

(iii) Reproducibility and repeatability of CF/PdNPs/anti-OTA/BSA

The reproducibility of CF/PdNPs/anti-OTA/BSA immunosensor was studied by using the inter-assay methods. **Figure 5-46**A shows the DPV of six individual immunosensor that were fabricated independently. The value of the relative standard deviation (RSD) was found to be 5.60%. To estimate the repeatability of the fabricated immunosensor, six successive measurement was carried out on the same modified electrode. The obtained relative standard deviation (RSD) was 1.40% (**Figure 5-46**B) which showed the excellent repeatability of the modified electrode.

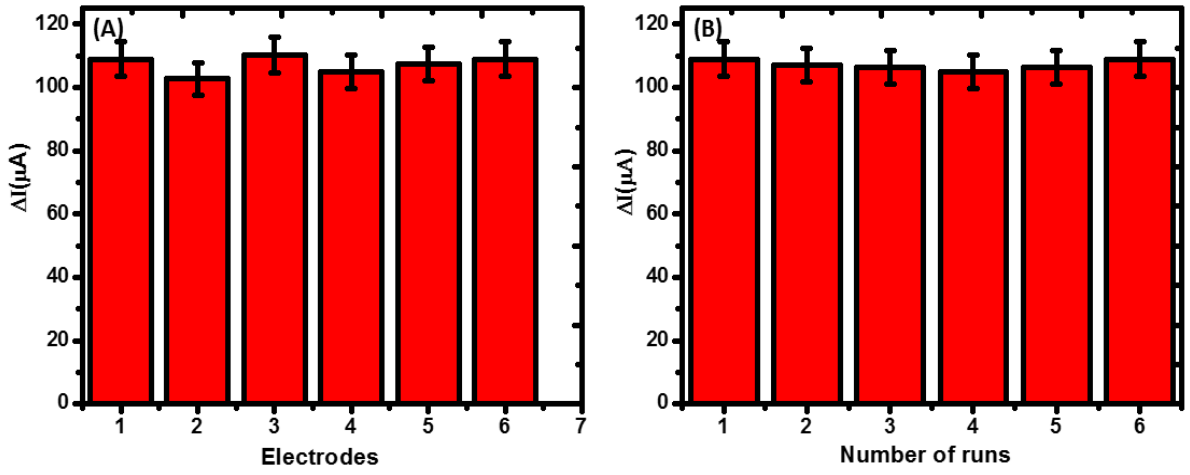

Figure 5-46: (A) Reproducibility and (B) Repeatability of the CF/PdNPs/anti-OTA/BSA immunosensor.

(iv) Stability and interferences study of CF/PdNPs/anti-OTA/BSA

The selectivity of the immunosensor was studied by observing the DPV response of CF/PdNPs/anti-OTA/BSA in the presence of the foreign species. Major interferences such as BSA, Aflatoxin B_1 and L-Trytophan (10 ng mL^{-1}) were mixed with OTA (1 ng mL^{-1}), and the DVP response was evaluated (**Figure 5-47**A). There was a negligible change in the DPV response after the interaction of the immunosensor with the foreign species. This shows that the fabricated immunosensor is highly selective toward OTA detection. The stability of the fabricated immunosensor was studied by monitoring the current on the regular interval of seven days up to three weeks using the optimized parameters. **Figure 5-47**B shows that the immunosensor can be stable up to three weeks, with an insignificant change in current value (99.60%).

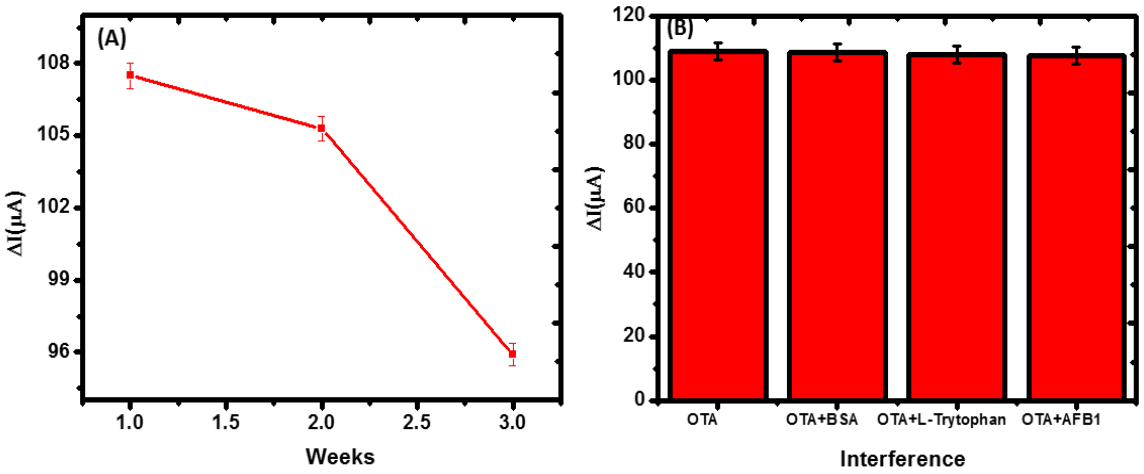

Figure 5-47: (A) Shelf-life of CF/PdNPs/anti-OTA/BSA in weeks and (B) Effect of various interferes on CF/PdNPs/anti-OTA/BSA.

5.3.2 Conclusion

In this study, the fabrication and the characterization of a novel and highly efficient electrochemical immunosensor for the selective detection of OTA is reported. Atomic layer deposition was successfully used as an efficient route to produce highly dispersed PdNPs onto the surface of carbon felt (CF) electrodes, and the BSA and the anti-OTA antibodies were then grafted onto the composite structure via a carbodiimide cross linkage route. Subsequently, the developed immunosensor was used to detect the OTA in coffee samples. The fabricated CF/PdNPs/anti-OTA/BSA immunosensor showed outstanding electrochemical

performances such as a wide detection range of 0.5 - 20 ng mL^{-1} and a LOD of 0.096 ng mL^{-1} for OTA. This study also revealed that the PdNPs accelerated the electron transfer rate at the electrodes due to the large surface area. Additionally, the immobilization of anti-OTA on the surface of the electrodes offers specific intrinsic immuno-recognition, with an improved binding efficiency, wettability property and enhanced selectivity of the sensor. Finally, this study also revealed the stability of the fabricated immunosensor for three weeks and its selectivity towards OTA in the presence of interfering compounds. The results presented in this work open prospects for new sensing routes for molecules of interest in food products.

5.4 Case Study 4: Immunosensor for detection of AFB_1 in wine

This section deals with the fabrication of PdNPs-BN/L-Cys/anti-AFB_1/BSA modified carbon felts (CF) electrochemical immunosensor for the detection of aflatoxin B_1 (AFB_1) in alcoholic sample. The electrochemical behaviour of AFB_1 studied at this modified electrode were characterized using a range of analytical techniques are presented. Also, a discussion on the developed sensor used for the quantification of AFB_1 in wine samples are presented. Also outlined in this section is the accompanying computational studies which aims to supplement and correlate the experimental data

5.4.1 Experimental

5.4.1.1 Synthesize of palladium nanoparticles on the thin layer of boron nitride (PdNPs-BN by atomic layer deposition (ALD)

Palladium nanoparticles (PdNPs) were synthesized on the thin layer of boron nitride (BN) on the carbon felts electrode (CFE) substrate by ALD (full procedure on materials and methods chapter 4). Boron nitride (BN) was synthesized onto the CF to form a thin film by varying the cycle number (10, 25, 50 and 100). According to **Figure 5-48**A, the increase of cycle number from 10 to 100 results in the increase of thickness of the diameter from 1.0 to 10.0 nm. The electrocatalytic properties of the synthesized BN film was examined using a redox probe maker, 5 mM $[Fe(CN)_6]^{3-/4-}$ in a 0.1 M KCl solution. The relationship between a cycle number and current is showed in **Figure 5-48**B. The attained results showed that the current strongly depends on the cycle number. Cycle 10 and 25 with a diameter of 1.0 and 3.0 nm; generate a current of 0.45 and 1.71 µA, respectively. The increase of cycle number (50 and 100) led to the decrease of current; this shows that the thick diameter hinders the flow of electrons on the electrode surface and results in the reduction of current. Cycle 10 generated the highest current of 1.71 µA which was two and thirteen times than that of generated from cycle 50 and 100 respectively; this indicates that the thin diameter allows the electrons to flow freely through the electrode surface. In order to enhance the selectivity and sensitivity of the immunosensor, PdNPs was grown on a thin layer of CF/BN. The 200 cycle of PdNPs was thereafter deposited on the surface of CF/BN following our recent work (Kunene *et al.* 2020), the as-fabricated samples was referred to as CF/PdNPs-BN. The electrochemical behaviours of CF/BN and

CF/PdNPs-BN was investigated. A 2-folds increase of current was recorded at CF/PdNPs-BN compared to CF/BN (**Figure 5-48**C). This confirms the acceleration of electrocalytic properties when PdNPs is intercalated between a carbon surface and BN.

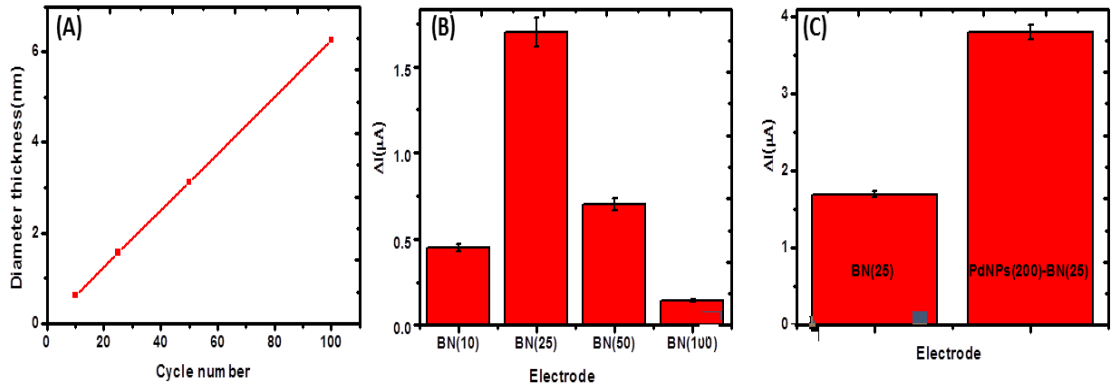

Figure 5-48: (A) The relationship between cycle number and diameter, (B) The effect of BN cycle number, and (C) The relationship between BN and PdNPs-BN.

5.4.1.2 Characterization of PdNPs-BN

Different characterization techniques such as transmissions electron microscope (TEM) and x-ray photoelectron spectroscopy (XPS) were used to characterize the synthesized PdNPs-BN composite.

(i) Transmission electron microscope (TEM) characterization

TEM images of BN deposited on the CFE is shown in **Figure 5-49**A. The smooth surface was observed on both magnification, Nayebi and co-workers reported the similar morphology for BN (Nayebi *et al.* 2020). This smooth surface makes it easier for the nanoparticles to stick together onto the surface. TEM images of the synthesized PdNPs grown on BN support shows a uniform distributed, decorated, and well dispersed PdNPs with the diameter of ~0.23 nm (**Figure 5-49**B). These results demonstrated the proficient catalytic performance of the fabricated sensor (Nayebi *et al.* 2020). The Fast Fourier transform (FFT) shown in **Figure 5-49**C confirms the crystallinity of the dispersed NPs. The EDS elemental map confirmed the existence of the PdNPs in the BN as depicted in **Figure 5-49** (D-F). The elemental map also shows that the Pd element is distributed uniformly across the BN support.

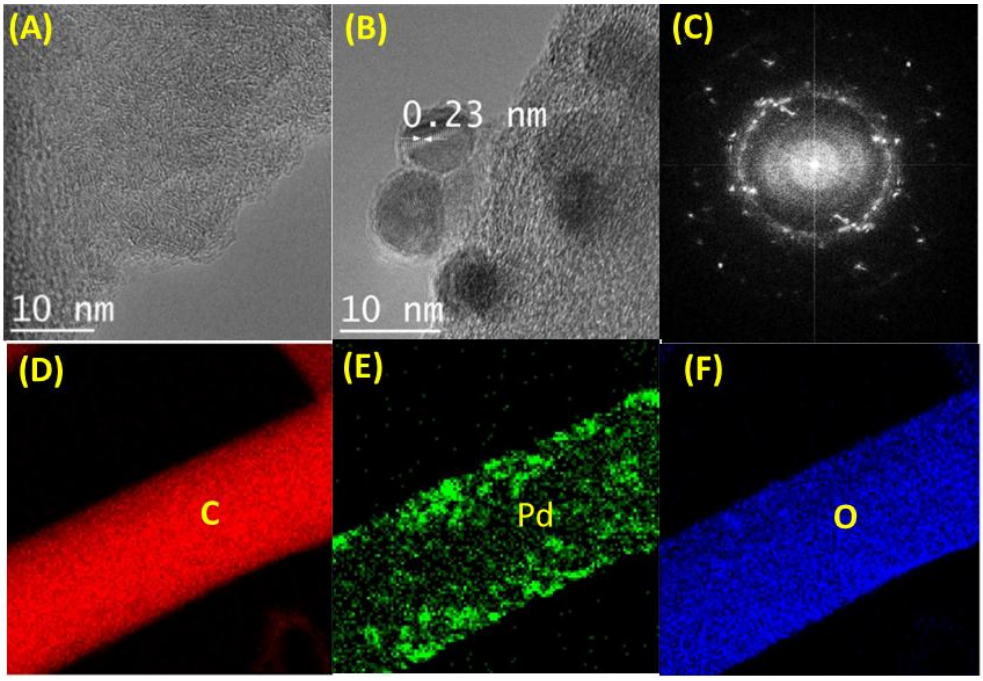

Figure 5-49: (A-B) TEM images of BN and PdNPs-BN respectively, (C) Fast Fourier transform of PdNPs-BN, and (D-F) are the energy-dispersive X-ray spectroscopy (EDS) maps of elements C; Pd and O respectively corresponding to the sample region in (B).

(ii) X-ray photoelectron spectroscopy (XPS) characterization

XPS is a vital method for determining the surface oxidation state as well as the elemental composition of the PdNPs-BN. The survey spectrum of CF/PdNPs-BN presented in **Figure 5-50A,** confirms the presence of C, N, O, B and Pd elements in the PdNPs-BN composite. As shown in **Figure 5-50**B, the Pd 3d3/2 and 3d5/2 binding energies were 340.9 and 335.6 eV, respectively. The deconvoluted peaks are assigned to Pd^0 and PdO_x species, with metal Pd^0 being a major phase. These results are in good agreement with the work published by our colleagues (Weber *et al.* 2019d), the presence of PdO_x species is related to the fact that BN attracts electrons from PdNPs. The fitted B1s spectra give a peak centered at 192.5 eV as shown in **Figure 5-50**C), this peak can be assigned to B−N bonding. For N 1s spectra (**Figure 5-50**D), the initial peak is divided in two major peaks at 398.2 eV and 400.1 eV that correspond to N–O and B–N, respectively. The two intense peaks for O1 s and C1s were also found at binding energies of 532.3 eV and, 284.4eV respectively, as shown in their core-level XPS spectra in **Figure 5-50**E-F, Nayebi and co-workers reported similar results (Nayebi *et al.* 2020).

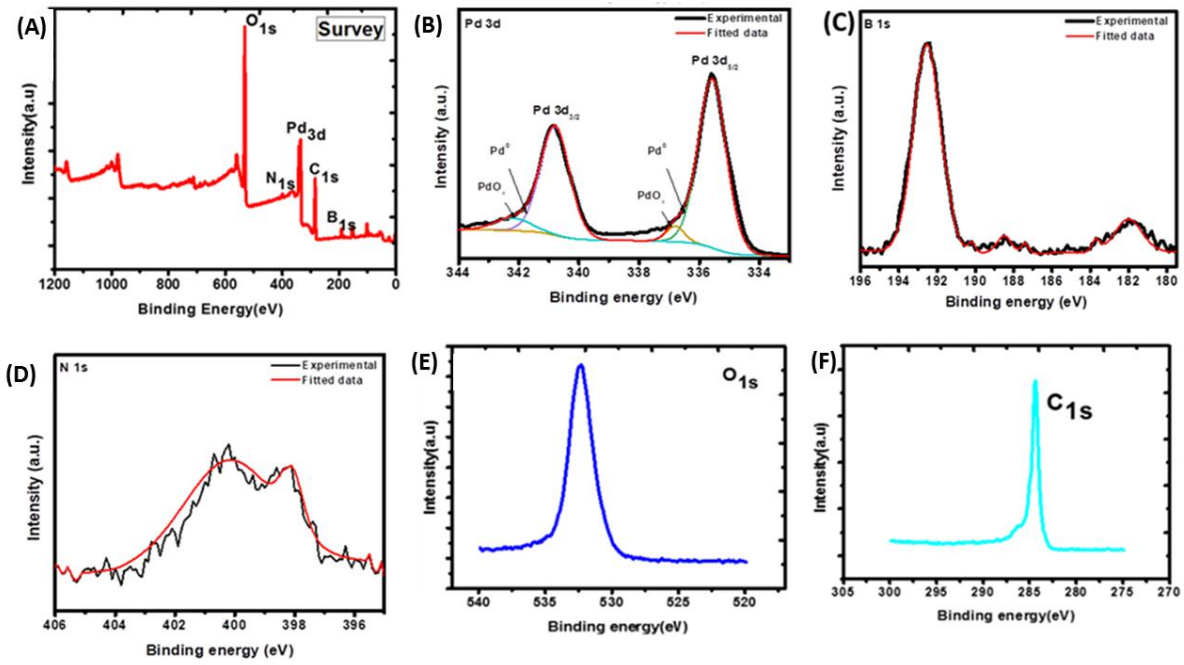

Figure 5-50: (A) Overall XPS Survey spectrum of PdNPs-BN, (B-F) High magnification XPS spectrum of Pd 3d; C1 s ; N1 s; O1 s and B1 s respectively.

5.4.1.3 Optimization of parameters for the fabrication of CF/PdNPs-BN/L-Cys/anti-AFB_1/BSA

(i) Effect of L-cysteine concentration

The concentration of L-cysteine is one of the significant factors in the amplification of the system. Therefore, the relationship between the electrochemical signal and the L-cysteine concentration was investigated. This was carried out by examining different L-cysteine concentration (5.0, 10, 15, 20 and 25 mM) in order to determine the optimum concentration for the electrode modification. **Figure 5-51**A shows that the current increases from 5 to 10 mM, then decreases beyond 15 up until 25 mM. Thus, 10 mM of L-cysteine was used for the entire experiments in order to obtain a highly sensitive immunosensor.

(ii) Effect of anti-AFB_1 concentration

The concentration of the antibodies that is immobilized on the surface of the electrode influences the sensitivity of the sensor due to availability of the binding sites for antigens. Therefore, the effect of anti-AFB_1 concentration was studied by immobilizing four different concentrations of anti-AFB_1 (0.5, 1.0, 5.0 and 10 µg mL^{-1}) onto the surface of the modified

electrode. **Figure 5-51**B shows increase of peak current with the increase of the antibody from 0.5 up to 1.0 µg mL^{-1} which decreases with further increase of anti-AFB_1. This was due to the aggregation of the antibody molecules caused by the overloaded of the support layers (Du *et al.* 2013; Smaniotto *et al.* 2017). Hence, the antibody that is immobilized on the electrode surface has competitors, which can cause the decrease in the peak current. Both the overloading and the competition reduced the number of the available binding site of the antibody to capture AFB_1. This causes the hindrance the electron flow toward the electrode therefore reduces the peak current. The maximum peak current was achieved at concentration of 1.0 µg mL^{-1}, which was then taken as the optimum concentration for further studies.

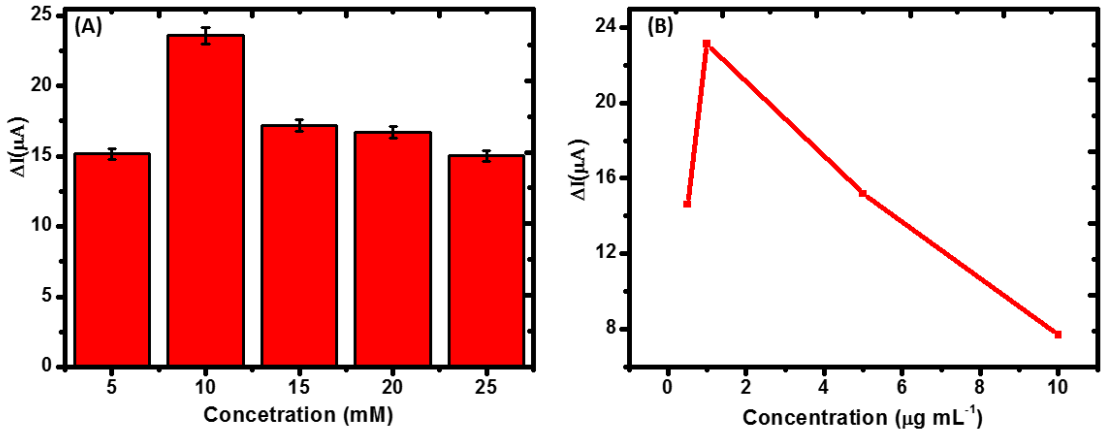

Figure 5-51: (A) Effect of L-Cy concentration and (B) Effect of anti-AFB_1 concentration electrochemical responses of CF/PdNPs-BN/L-Cys-anti-AFB_1/BSA in the presence of using AFB_1. The electrochemical experiments were carried out in 0.1 M KCl containing 0.1 M PBS (pH 7.5) and 5 mM $[Fe(CN)_6]^{3-/4-}$ solution.

(iii) Effect of activation temperature

The activation temperature was carried out by using four different temperatures (4.0, 25, 37 and 55 °C). The current signal increases with increase of activation temperature from 4 to 25 °C and decreases after 25 °C (**Figure 5-52**A). The current decreased is due to unsuitable conformer of anti-AFB_1 and antigen to generate the immunocomplex. High temperatures may cause a permanent denaturation of antigen and the antibody involved in the process (Zhou *et al.* 2015). Therefore, the activation temperature of 25 °C was used allowing the maximum immunoreaction to occur.

(iv) Effect of activation time

Activation time of the L-Cy with the cross-linker is one of the most significant parameter when fabricating the immunosensor. The cross-linker and the L-Cy were incubated at 25 °C at different time (10, 20, 30, 40 50 and 60 min). According to **Figure 5-52**B, conjugation of L-Cy with the cross-linker was favored by increasing time allowed for activation of carboxyl group by the cross-linker up to 50 min. After 50 min the current decrease, this is due to the unfavorable conformation caused by the increase of activation time (Smaniotto *et al.* 2017). Therefore, the activation time was kept at 50 min for the entire experiments.

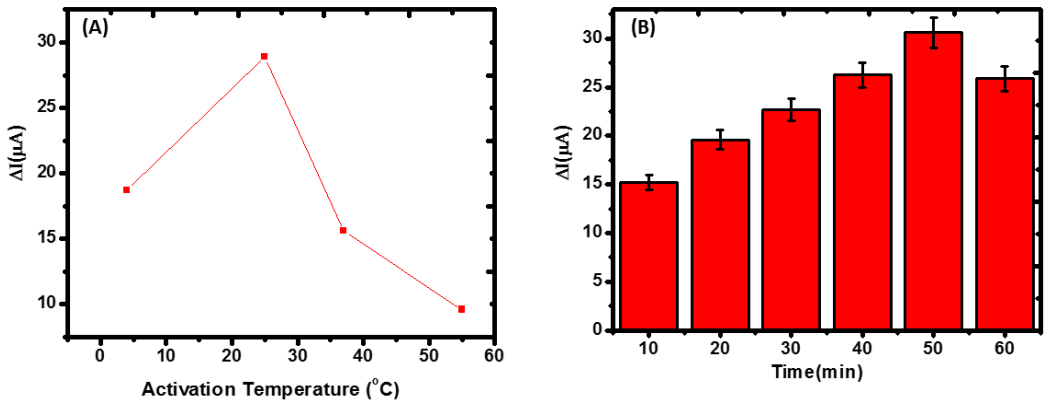

Figure 5-52: Effect of activation (A) temperature and (B) time.

(v) Effect of cross-linker ratio

The effect of cross-linker ratio was also optimized in order to get the optimum. Different ratios of 0.4 M EDC and 0.1 M NHS (1:1, 1:2, 1:3, 1:4 and 1:5) was optimized, while monitoring the current signals. In **Figure 5-53**A, the current responses increased with the increasing ratio from 1:1 to 1:3 then decreases after 1:3. Thus, the ratio (1:3) was chosen for the entire experiment.

(vi) Effect of the incubation time of the antibody

To achieve the sensitivity of the immunosensor, the incubation time of the antibody was then optimized. **Figure 5-53**B shows that when the immunosensor is incubated with 1.0 µg mL^{-1} of anti-AFB_1 at different time from 1 to 6 h. The analytical response rapidly increased and reached the maximum at 2 h but decreased beyond 2 h, indicating the occurrence of

specific binding of anti-AFB_1 to the immunoelectrode. At this point the specifically bound anti-AFB_1 via immunoreaction becomes saturated on the electrode surface, however the non-specific adsorption and desorption of anti-AFB_1 take place from the electrode surface. Therefore, the anti-AFB_1 incubation time of 2 h was used for the entire experiments, since the constant and reliable analytical signals were obtained due to the anti-AFB_1 specific binding.

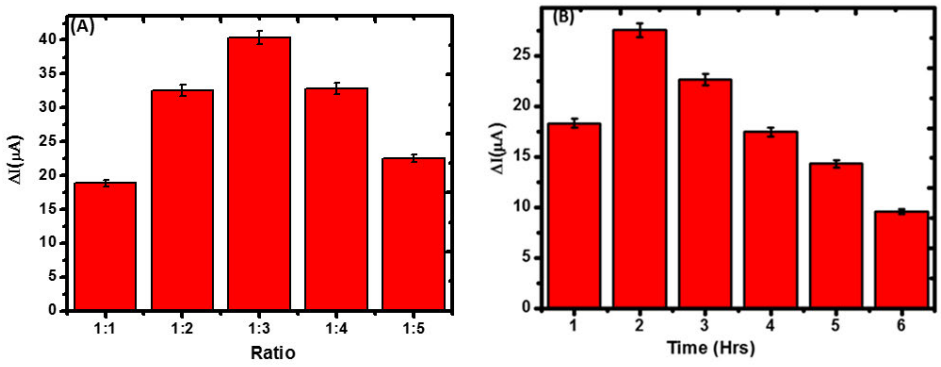

Figure 5-53: The effect of (A) cross-linker ratio and (B) incubation time of the antibody.

5.4.1.4 Structural, morphological, and electrochemical characterization CF/PdNPs-BN/L-Cys/anti-AFB_1/BSA

Different characterization techniques such as atomic force microscope (AFM), (ATR) electrochemical techniques (cyclic voltammetry (CV) and electrochemical impedance spectroscopy (EIS) were used for the characterization of the fabricated immunosensor.

(i) Characterization of the CF/PdNPs-BN/L-Cys/anti-AFB_1/BSA by AFM

AFM was used for the analysis of topographical and morphological of the modified electrode. AFM is one of the most admirable complementary techniques to evaluate the topographical and surface roughness of the proposed immunosensor. The 2D and 3D topographical AFM images of the electrode CF/PdNPs-BN/L-Cys and CF/PdNPs-BN/L-Cys/ anti-AFB_1 attained by static mode are shown in **Figure 5-54**A–B respectively. **Figure 5-54**A displays the topography of the electrode surface after L-Cys modification. The complete and uniform layer of the surface with the absent of aggregates or layer defects was observed with surface roughness (R_z) of 0.6028 µm. When the anti-AFB_1 was immobilized on CF/PdNPs-

BN L-Cys surface more globular looking surface was observed, indicating its protein nature (Simão *et al.* 2016) (**Figure 5-54**B). The surface roughness increases to 1.2552 µm. This demonstrates that the homogeneity of cysteine permitted the antibodies to attach to the functional moiety in a similarly uniform manner (Xue *et al.* 2012). The AFM results revealed that this routine is a proficient mean of immobilizing antibodies to fabricate an immunosensor.

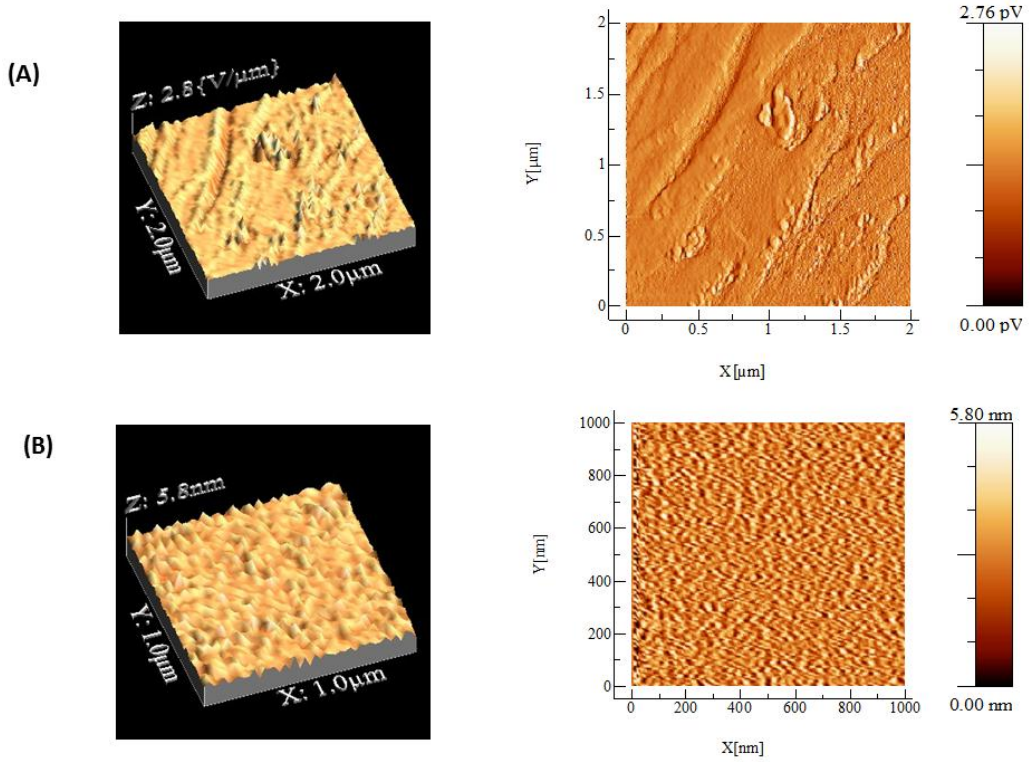

Figure 5-54: (A) Atomic force microscope (AFM) images of CF/PdNPs-BN/L-Cys and (B) CF/PdNPs-BN/L-Cys/anti-AFB_1 using contact mode.

(ii) Characterization of the CF/PdNPs-BN/L-Cys/anti-AFB_1/BSA by ATR

The ATR spectroscopy provides different functional groups that are present in the nanocomposite. The ATR spectra of different nanocomposite that was used on the development of the immunosensor are shown in **Figure 5-55**. When the electrode was modified with a semi essential proteinogenic amino acid L-cysteine (curve i; CF/PdNPs-BN/L-Cys) (**Figure 5-55**). The spectrum shows four characteristic peaks at 1446, 1365 cm^{-1} which corresponds to the asymmetric and symmetric stretching of COO^-, 1528 and 1299 cm^{-1}

are attributed to the bending mode of $–NH_2$ and C-N bend, respectively. Panhwar and co-workers reported similar results (Panhwar *et al.* 2018). This characteristic peak (COO^-, $–NH_2$ and C-N bend) confirms that L-cysteine was successfully modified onto the electrode surface. A very weak thiol group (-SH) peak at 2585 cm^{-1} is present in the spectrum, indicating the presence of L-Cy on the electrode surface (Ahmed *et al.* 2016a). The immobilization of the antibodies resulted to PdNPs-BN/L-Cy (curve ii; CF/PdNPs-BN/L-Cys/anti-AFB_1) with peaks at 3001 cm^{-1}, 1689 cm^{-1} and 866 cm^{-1} assigned to amide bond (N-H) deformation, stretching and $–NH_2$ on the electrode surface groups respectively (Lou *et al.* 2011; Kunene *et al.* 2020). These results show that the antibody is immobilized on the electrode surface. After the incubation of the blocking agent BSA (curve iii; CF/PdNPs-BN/L-Cys/anti-AFB_1/BSA), the $–NH_2$ group disappeared on the spectrum. This confirmed that the nonspecific site present on CF/PdNPs-BN/L-Cys/anti-AFB_1 immunoelectrode are blocked by BSA (Solanki *et al.* 2015a).

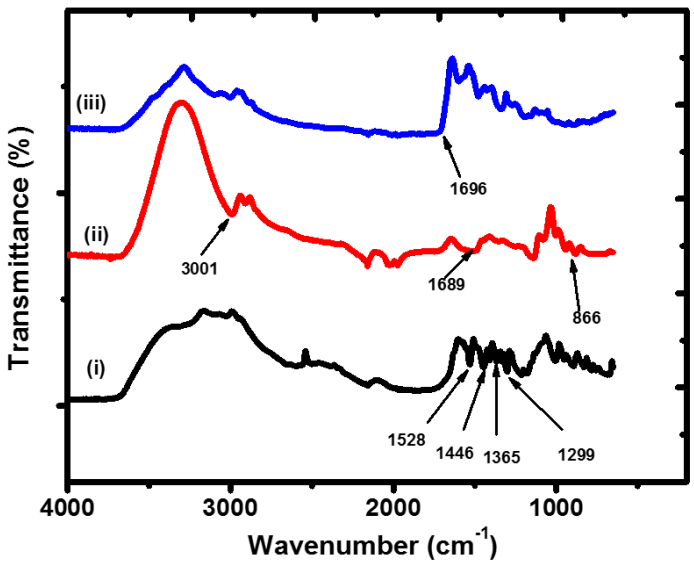

Figure 5-55: ATR spectra of (i) CF/PdNPs-BN/L-Cys, (ii) CF/PdNPs-BN/L-Cys/anti-AFB_1, and (iii) CF/PdNPs-BN/L-Cys/anti-AFB_1/BSA.

(iii) Characterization of CF/PdNPs-BN/L-Cys/anti-AFB$_1$/BSA by cyclic voltammetry (CV)

Cyclic voltammetry (CV) was used to monitor the stepwise fabrication of the immunosensor in the solution that contains 0.1 M KCl and 5 mM $[Fe(CN)_6]^{3-/4-}$ at 20 mVs^{-1} (**Figure 5-56**). The CF/PdNPs-BN (curve i) gave a quasi-reversible electrochemical reaction with a peak potential separation of ~110 mV, and the anodic current (I_{pa}) of 1.45 µA was observed (curve i). The current increases due to the catalytic behavior of BN, which made it easier for the electron transfer to take place. The adsorption of L-Cys on the electrode surface results in the decrease of the I_{pa} to 0.73 µA (curve ii). The L-Cys decreases the resistance of the electrostatic repulsion between the -COOH group of L-Cys and the negative charge of the redox probe $[Fe(CN)_6]^{3-/4-}$ (Hashemi *et al.* 2017). After anti-AFB$_1$ antibodies were immobilized on the modified electrode to produce CF/PdNPs-BN/L-Cys/anti-AFB$_1$, I_{pa} increases to 0.97 µA (curve iii). These results indicate that the anti-AFB$_1$ acts as a mediator activity between PdNPs-BN/ L-Cys and CF electrode, in which the electron tunnelling distance is shorted between the antibodies and the electrode, leading to increase of peak current (Tiwari *et al.* 2017b). The subsequently blocking of nonspecific site with BSA to form CF/PdNPs-BN/L-Cys/anti-AFB$_1$/BSA causes the decrease on I_{pa} to 0.50 µA (curve iv) due to the adsorption of the protein, BSA.

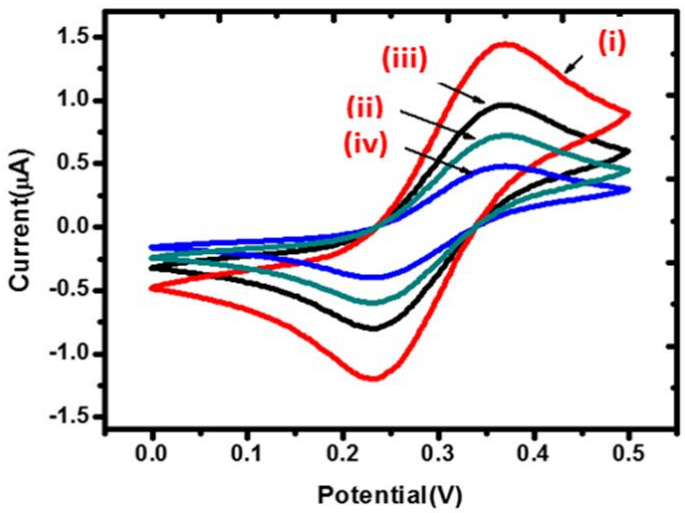

Figure 5-56: Cyclic voltammograms showing the corresponding modification step of (i) CF/PdNPs-BN; (ii) CF/PdNPs-BN/L-Cys; (iii) CF/PdNPs-BN/L-Cys/anti-AFB$_1$; and (iv) CF/PdNPs-BN/L-Cys/anti-AFB$_1$/BSA. Conditions: 0.1 M PBS solution containing 0.1 KCl solution and 5 mM $[Fe(CN)_6]^{3-/4-}$ pH 7.5; scan rate = 20 mVs^{-1}.

(iv) Characterization of CF/PdNPs-BN/L-Cys/anti-AFB_1/BSA by impedance spectroscopy (IES)

Electrochemical impedance spectroscopy (EIS) is one of the most effective tool for investigation of the modified electrode surface (Hashemi *et al.* 2017). The EIS of different electrodes were performed with frequency range from 0.1 Hz to 10 kHz with amplitude of 0.6V. The shape of the impedance spectroscopy comprises of a high frequencies and low frequencies. The high frequencies contain a semicircle, that where the electron transfer processes occur, and the low frequencies contain a linear portion, that where the electrochemical process occurs. The modified Randles circuit (insect **Figure 5-57**) was used for the fitting of the impedance data. The equivalent circuit comprises the ohmic resistance of the electrolyte solution (R_s), double layer capacitance (C_{dl}), charge transfer resistance R_{ct} and the Warburg impedance element (Z_w). Chen and co-workers reveal that R_s and Z_w are not affected by any reaction taking place onto the electrode surface, however C_{dl} and R_{ct} are affected by the insulating features and the electrode interface of the electrode respectively (Chen *et al.* 2015). **Figure 5-57** show the Nyquist plots recorded from different modification steps. The charge transfer resistance R_{ct} and the Warburg impedance element (Z_w) are both parallel with the double layer capacitance (C_{dl}). The modification of the CF with CF/PdNPs-BN (**Figure 5-57**(curve i), results in the R_{ct} of 84 Ω, indicating a high charge transfer, this was due to the excellent electrocatalytic property of the PdNPs and BN. When the L-Cys was assembled onto CF/PdNPs-BN surface, the tremendous increase of R_{ct} was observed at 1200 Ω (curve ii). This shows that L-Cys formed a large barrier to the interfacial charge transfer, which is revealed by increased diameter of the semicircle in the spectrum. Similar results were reported in the literature by Fan and co-workers (Fan *et al.* 2020).When the antibody (anti-AFB_1) was covalently bonded to L-Cys, the R_{ct} of 567 Ω was obtained (curve iii), the decrease of R_{ct} indicates the immobilization of anti-AFB_1 onto the electrode surface. The R_{ct} decreases when BSA is immobilized onto the modified electrode (curve iv), demonstrating that the immunosensor is successfully fabricated. The different R_{ct} confirms that immunosensor were successfully fabricated.

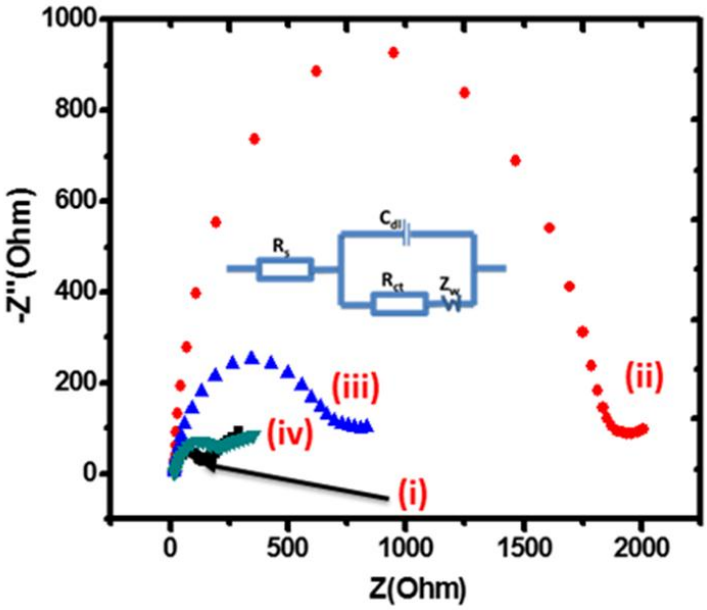

Figure 5-57: Nyquist plot showing the corresponding modification step of (i) PdNPs-BN/CF, (ii) CF/PdNPs-BN/L-Cys, (iii) CF/PdNPs-BN/L-Cys/anti-AFB_1, and (iv) CF/PdNPs-BN/L-Cys/anti-AFB_1/BSA in a 0.1 M PBS (pH 7.5) solution containing 0.1 KCl solution and 5 mM $[Fe(CN)_6]^{3-/4-}$ (insect Randles circuit).

5.4.1.5 Optimization of analytical parameters for CF/PdNPs-BN/L-Cys/anti-AFB_1/BSA

To achieve outstanding analytical capability of the immunosensor, the key parameters such as pH of PBS, incubation time of specific binding to target material and scan rate was optimized.

(i) Effect of pH

The literature reveals that different environmental media with different pH values affects the structure of the antibodies and antigen (Wang *et al.* 2012). Wang and co-workers reported that the immunosensor performs its best at the pHs range of 6.7 - 7.8 (Wang *et al.* 2012). The effect of pH was optimized by preparing solution with different pH values. **Figure 5-58**A shows the peak current of the fabricated immunosensor at pH ranging from 5.5 to 8.5. The peak current increases with the increase of pH up to 7.5 and decreases from pH 8 and 8.5. This shows that highly basic environment denatures the activity and the stability of the immobilized antibodies. Additionally, the safety data sheet acquired from Sigma-Aldrich shows that the pH of anti-AFB_1 is 7.4. This displayed that the antibody maintains its activity and stable combination with the antigen at neutral conditions. Therefore, pH 7.5 was selected as the optimal pH value for the determination of AFB_1.

(ii) Effect of incubation time

Incubation time plays an important on the performance of the proposed immunosensor. The effect of incubation time was studied by varying incubation times from 5 to 40 min. **Figure 5-58**B shows that the peak current increases with the increase of incubation time from 5 to 40 min until it reached a plateau at an incubation time of 30 min. Thus, an incubation time of 30 min was chosen as the optimal incubation time.

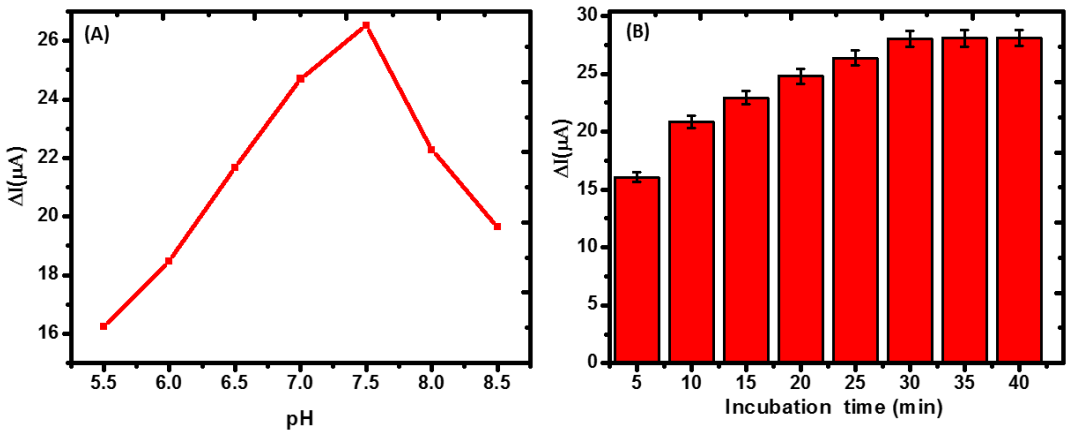

Figure 5-58: Effect of (A) pH (5.5; 6.0; 6.5; 7.0; 7.5; 8.0 and 8.5 and (B) incubation time.

(iii) Effect of scan rates

To reveal the electrochemical reaction mechanism of the developed immunosensor, the effect of the scan rate (ν) at the CF/PdNPs-BN/L-Cys/anti-AFB_1/BSA at different scan rates from 10 to 100 mV s^{-1} was examined by cyclic voltammetry (CV) as displayed in **Figure 5-59**A. The current increased linearly with the scan rate in the redox probe, according to the equation I_{pa} (μA) = 1.882 ν + 35.689 (R^2 = 0.989) suggesting a diffusion-controlled reaction as depicted in **Figure 5-59**B. This was further confirmed by a linear relationship between a square root of scan rate and the anodic current (**Figure 5-59**C). This linear relationship is anticipated by the diffusion-controlled process (Deroco *et al.* 2018; Dettlaff *et al.* 2020).

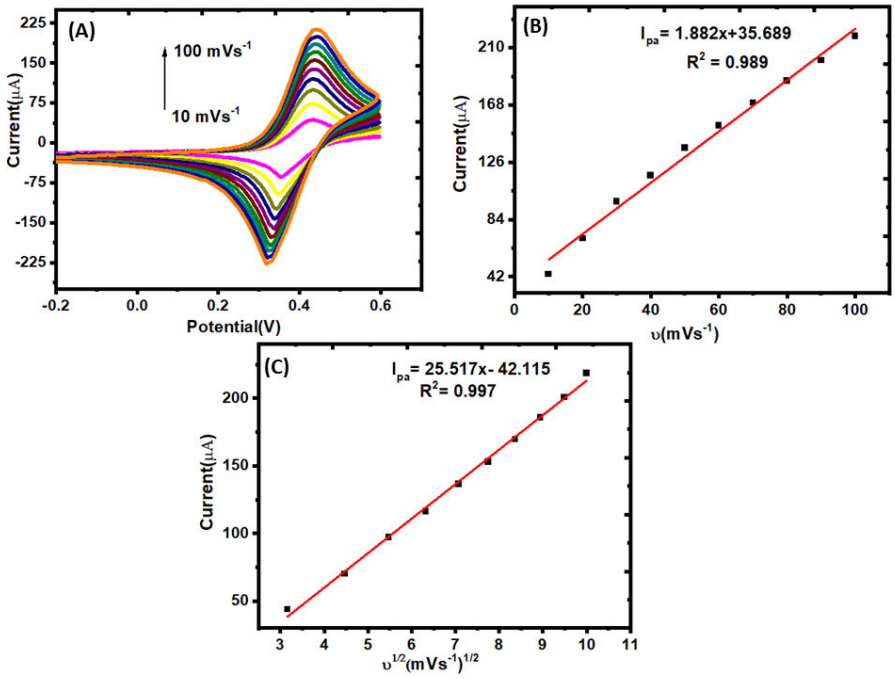

Figure 5-59: (A) The relationship between peak current and scan rate (10 to 100 mVs^{-1}). Graph of anodic peak current (B) vs. scan rate, and (C) vs. square root of the scan rate in 5 mM $[Fe(CN)_6]^{3-/4-}$ solution that contains 0.1 M KCl, 0.1 M PBS (pH 7.5) at CF/PdNPs-BN/L-Cys/anti-AFB_1/BSA.

5.4.1.6 Electrochemical behaviour of AFB_1 at CF/PdNPs-BN/L-Cys/anti-AFB_1/BSA

(i) Quantitative analysis of AFB_1

The performance of the fabricated immunosensor was verified by investigation of AFB_1 standards at different concentration (1.0 to 10 ng mL^{-1}) under the optimized parameters. The LSVs of different concentration of AFB_1 shows a decrease of the peak current with an increase of the AFB_1 concentration as shown in **Figure 5-60**A. The fabricated immunosensor shows that the peak displays a linear relationship with the concentration of AFB_1 ranging from 1.0 to 10 ng mL^{-1}. The linear regression equation was expressed as $Y = -4.775x + 52.482$, $R^2 = 0.9982$, with a limit of detection (LOD) of 0.832 ng mL^{-1} as illustrated in **Figure 5-60**B. The attained LOD is better than that of other electrochemical immunosensors reported in literature (Li *et al.* 2016; Zejli, Goud and Marty 2019). These results were in good alignment with reference range and could be suitable for determination of toxins in alcohol.

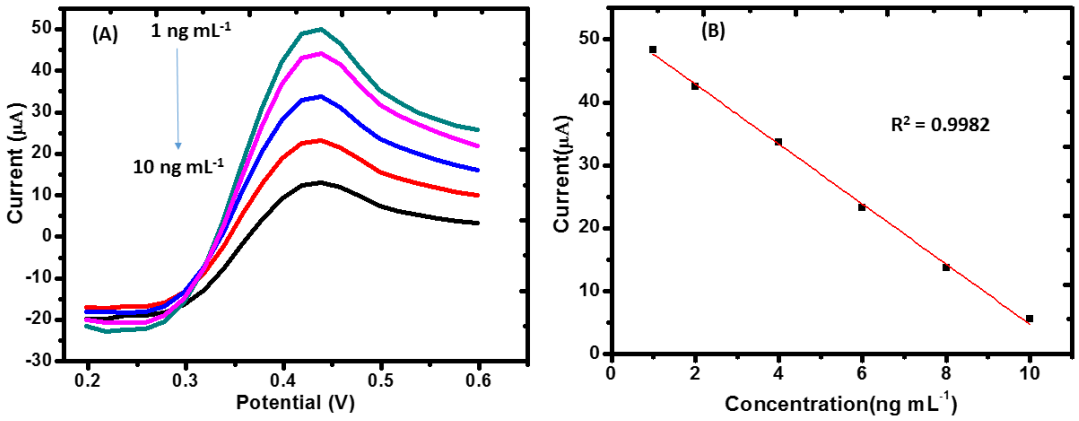

Figure 5-60: (A) LSV response of CF/PdNPs-BN/L-Cys/anti-AFB_1/BSA in different concentrations of AFB_1 ranges from (1.0 - 10 ng mL^{-1}) and (B) The linear calibration curve of AFB_1 concentrations.

(ii) Analysis of contaminated red wine samples

The feasibility of the fabricated immunosensor to detect AFB_1 in wine samples was investigated, by spiking wine with different concentration of AFB_1. The selection of AFB_1 concentration was based on the calibration curve of AFB_1 determination. The fabricated immunosensor was used to test the wine samples that were spiked with known concentration of AFB_1. The attained recovery levels are shown in **Table 5-7**. The fabricated immunosensor displayed good recoveries ranging from 93.00 to 106.00% with RSD ranging from 1.55 to 3.10% signifying the suitability of the fabricated immunosensor for AFB_1 detection in wine samples.

Table 5-7: Quantitative determination of AFB_1 in wine sample.

AFB_1 added (ng mL^{-1})	**AFB_1 Founded (ng mL^{-1})**	**Recovery (%)**	**RSD (n =3)**
2.0	2.12	106.00	1.55
4.0	3.89	97.75	2.30
6.0	5.89	98.17	1.66
8.0	8.34	93.00	3.10

(iii) Reproducibility and stability of CF/PdNPs-BN/L-Cys/anti-AFB_1/BSA

The reproducibility was assessed by the measurements of 6.0 ng mL^{-1} AFB_1, using 6 different electrodes fabricated independently electrode. The RSD was 1.20, demonstrating that a fabricated immunoelectrode possesses a good reproducibility and tolerable precision (**Figure 5-61**A). The stability of the immunosensor was also studied after the storage at 4 °C for three weeks, the peak current of the immunosensor remained at 81.74% of its initial value. These results connotes a good stability of the proposed immunosensor (**Figure 5-61**B).

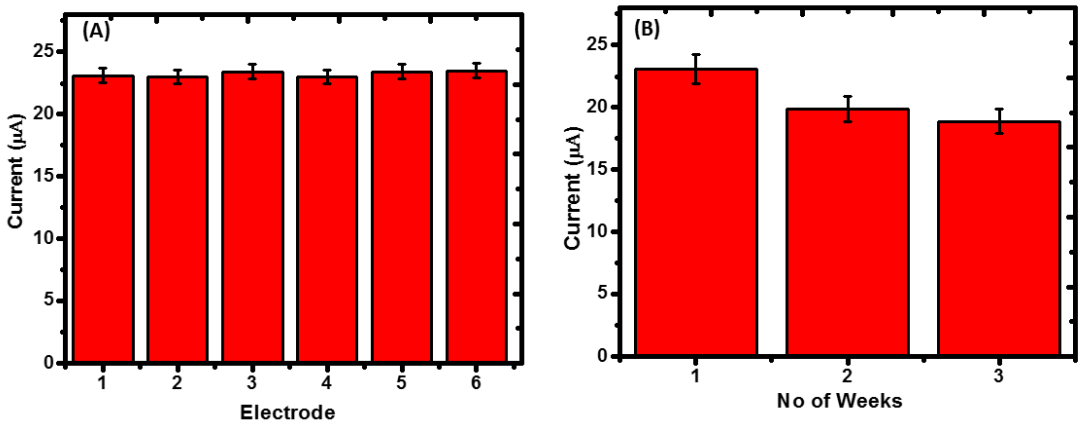

Figure 5-61: (A) The reproducibility and (B) Shelf-lifetime of CF/PdNPs-BN/L-Cys/anti-AFB_1/BSA.

(iv) Interference's study and the precision of CF/PdNPs-BN/L-Cys/anti-AFB_1/BSA

The label-free immunosensor generally suffers from the specificity, which may be instigated from the nonspecific adsorption of foreign compounds on the sensing surface. To check the specificity of the fabricated immunosensor, OTA and AFB_1 at different concentration of 1 and 10 ng mL^{-1} were analysed individually and mixed using the fabricated immunosensor. A negligible peak current was observed when the immunosensor was incubated with OTA and the mixture even at high concentration; however, the noticeable change in peak current was observed on the electrode incubated with AFB_1. These results show that the fabricated immunosensor is only specific to AFB_1 (**Figure 5-62**). The precision of the fabricated immunoelectrode was carried out by assessing consecutive determinations of 6.0 ng mL^{-1} of AFB_1 for 20 times using the same experimental conditions and immunoelectrode. The resulted relative standard deviation (RSD) was 1.50, showing that the fabricated immunosensor can be applicable in the alcoholic industry.

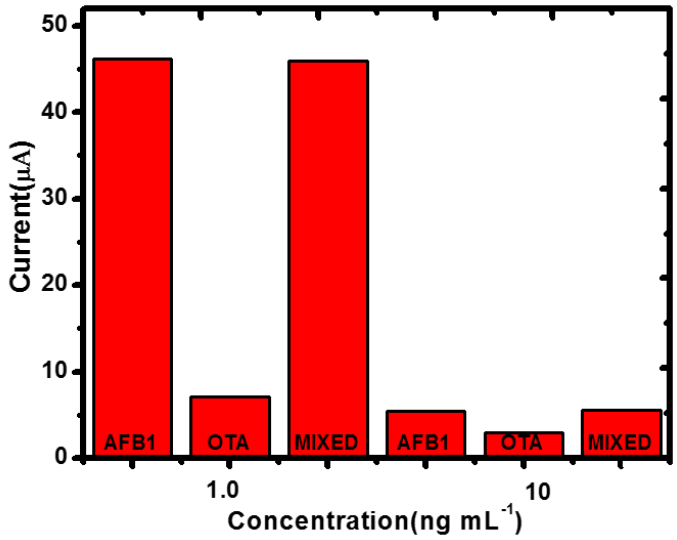

Figure 5-62: The interference study of CF/PdNPs-BN/L-Cys/anti-AFB_1/BSA.

5.4.2 Computational Studies

Figure 5-63A-E shows the variation of the energy values for the minimised structures along with the adsorption energies (**Table 5-8**) based on the adsorption locator (AL). The calculated adsorption energies are all negative, signifies stabilization and an exothermic adsorption process (Harris *et al.* 1997; Brenke *et al.* 2012) with the more negative value indicating stronger adsorption energy. Our results indicate that the adsorption energies increase from **Figure 5-63(**A**) to (**B**)**, demonstrating that the CF/PdNPs/BN nanocomposite is more stabilized than the CF/PdNPs/BN/L-Cys nanocomposite that is attributed to the presence of the cysteine strongly attracted to the electrode surface, in agreement with the amplified electrochemical signals illustrated in **(Figure 5-7(i-ii))**. Further, this also supports the catalytic behaviour of BN, which makes it easier for the electron transfer to take place. The EDC/NHS activation results in a more highly negative adsorption energy observed in **(Figure 5-63C).** Interestingly, a significant decrease in the adsorption energy is observed following the immobilization of the anti-AFB_1 antibodies (**Figure 5-63(D);Table 5-8)** onto the fabricated electrode surface. This is a significant result as it confirms the mediator activity of the anti-AFB_1 between EDC-NHS/PdNPs-BN/L-Cys/EDC/NHS and the CF electrode, results to an increase in peak current as observed in **Figure 5-7(iii)**. Finally, an increase in adsorption energy is observed when AFB_1 was adsorbed onto the composite electrode in the presence of the anti-body and the protein. This result demonstrates that the subsequent

blocking of nonspecific site with BSA to form CF/PdNPs-BN/EDC-NHS/L-Cys/anti-AFB_1/BSA causes the decrease on I_{pa} to 0.50 µA (curve iv).

Table 5-8: Summary of calculated adsorption energies using AL.

Layer	Adsorbate	Substrate	Adsorption energy Kcal/mol
A	PdNPs	CF/BN	-370.46
B	L-Cys	CF/PdNPs/BN	-282.23
C	EDC-NHS	CF/PdNPs/BN/L-Cys	-484.61
D	Anti-AFB_1	CF/PdNPs/BN/L-Cys/EDC-NHS	-1.9×10^{-4}
E	AFB_1	CF/PdNPs/BN/L-Cys/EDC-NHS/BSA	-205.67

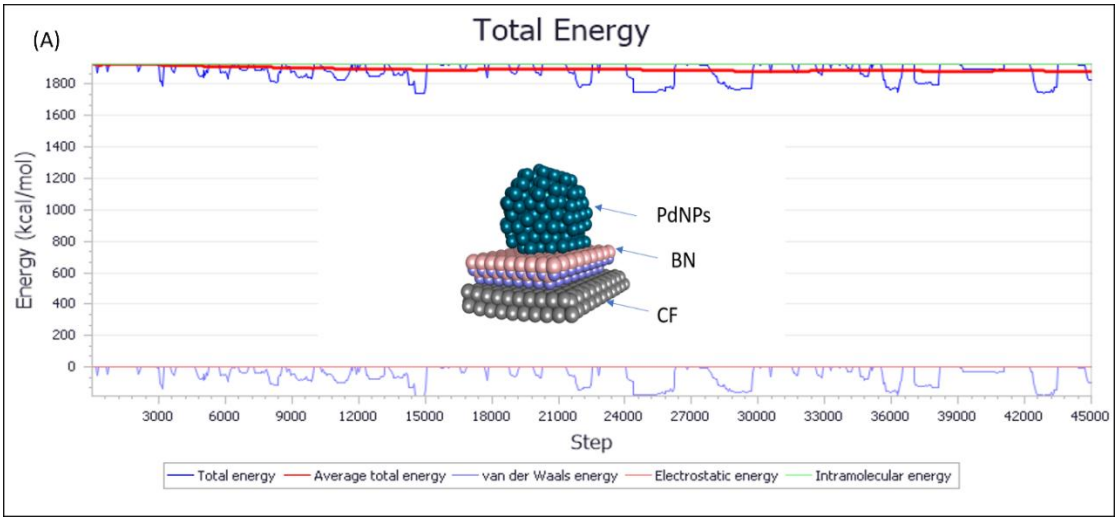
(A)
Total Energy
Energy (kcal/mol)
PdNPs
BN
CF
Step
Total energy
Average total energy
van der Waals energy
Electrostatic energy
Intramolecular energy

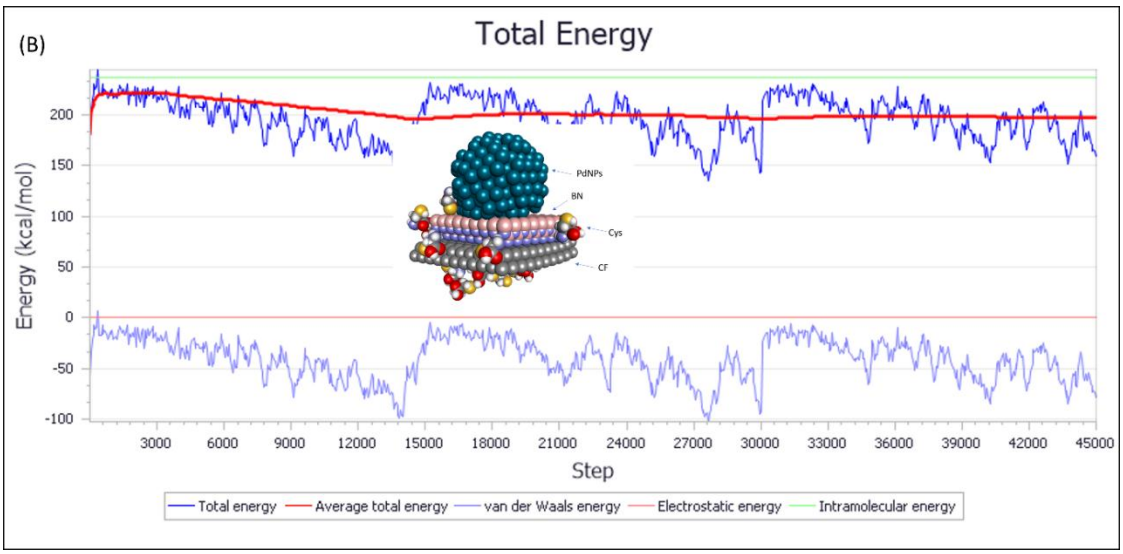
(B)
Total Energy
Energy (kcal/mol)
PdNPs
BN
Cys
CF
Step
Total energy
Average total energy
van der Waals energy
Electrostatic energy
Intramolecular energy

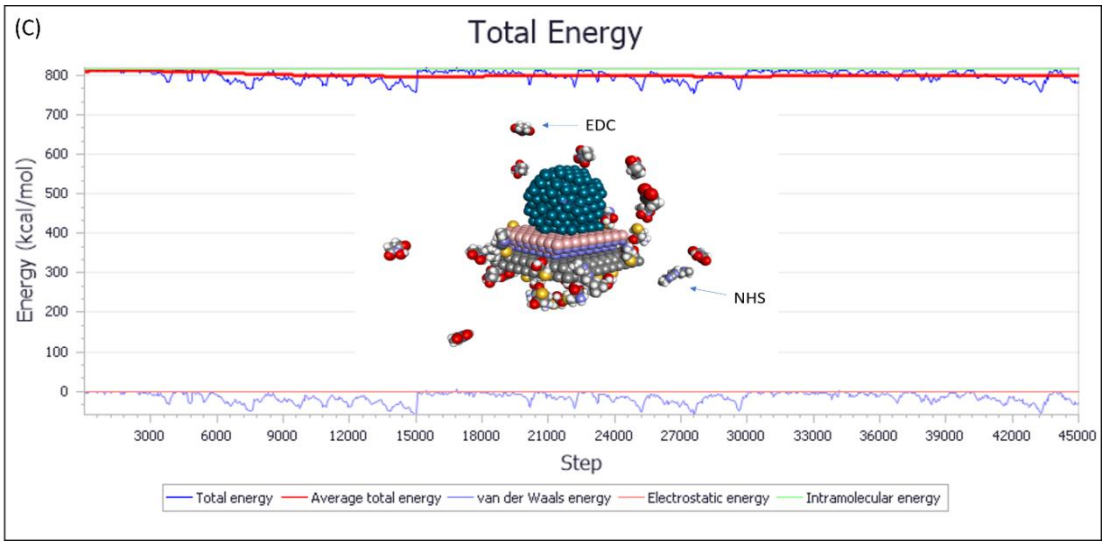
(C)
Total Energy
Energy (kcal/mol)
EDC
NHS
Step
Total energy
Average total energy
van der Waals energy
Electrostatic energy
Intramolecular energy

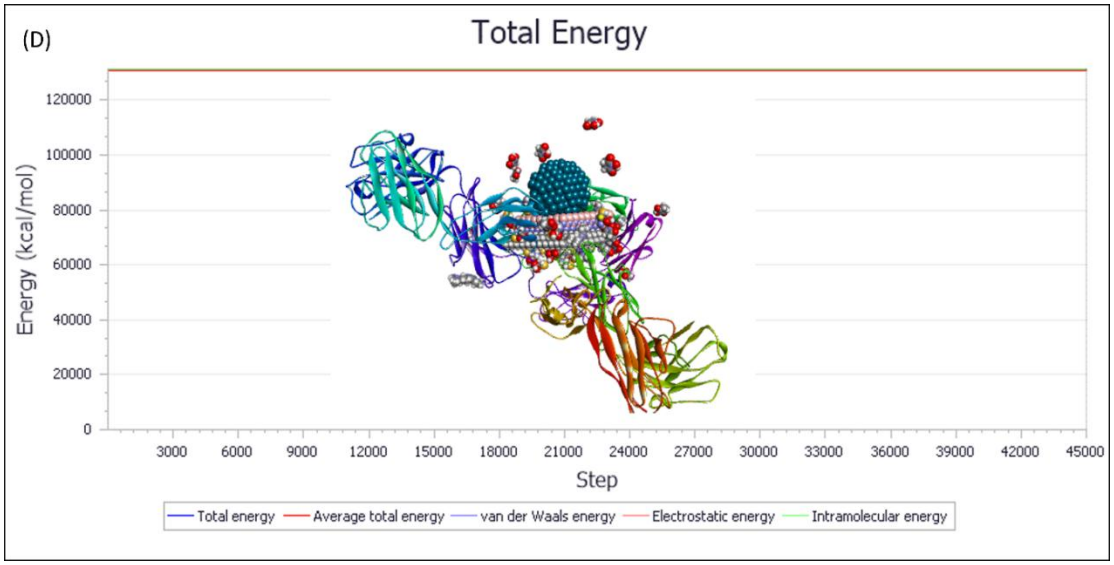

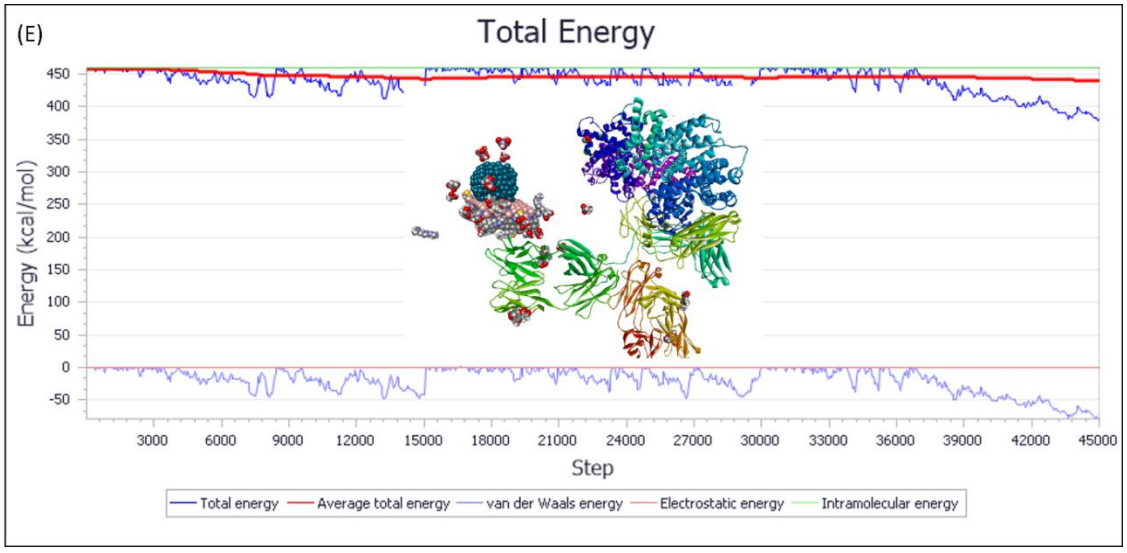

Figure 5-63: Calculated Atomistic total energy distribution for (A) CF/PdNPs-BN, (B) CF/PdNPs-BN/L-Cys, (C) CF/PdNPs-BN/L-Cys/EDC-NHS, (D) CF/PdNPs-BN/L-Cys/EDC-NHS/anti-AFB_1 and (E) CF/PdNPs-BN/L-Cys/EDC-NHS/anti-AFB_1/BSA/AFB_1; The inset refers to minimized structures for (A-E) respectively.

5.4.3 Conclusion

A sensitive, selective, and simple electrochemical immunosensor based on PdNPs/BN/L-Cys for the detection of AFB_1 by integrating with the antibodies signal readout was constructed. The fabricated immunosensor revealed an adequate reproducibility and a high level of specificity and sensitivity for the detection of AFB_1. It also displayed a wide dynamic range from 1.0 to 10 ng mL^{-1} with detection limit of 0.832 ng mL^{-1}. The outstanding performance of the immunosensor is attained by the synergistic effect of the three composed components

in the multifunctional nanocomposite, in which L-Cys provides electroactivity due to its reversibility electrochemical property, PdNPs offers anchor sites for covalent immobilization of antibody and BN renders good electric conductivity as well as rigidity for high stability. Moreover, this study was systematically complimented and validated by computational modelling. The developed method offers a universal strategy for the selective detection of AFB_1 in wine samples, thus holding great promise for a sensitive device with applications in wine safety and screening.

CHAPTER 6: CONCLUSION AND RECOMMENDATIONS

6.1 Concluding Remarks

The aim of this study was to fabricate sensitive electrochemical biosensors for the detection of mycotoxins such as ochratoxin A (OTA) and aflatoxin B_1 (AFB_1) in food samples using two different approaches. The aptasensor and the immunosensor were fabricated using different nanomaterials such as silver nanoparticles (AgNPs), palladium nanoparticles (PdNPs), palladium nanoparticles grown on boron nitride layer (PdNPs-BN) and titanium nanoparticles doped with boron nitride (BN-TiO_2). The nanoparticles enhanced the electrochemical signal while the antibody and the aptamer increase the selectivity of the analytes.

Nanomaterials were successfully synthesized by atomic layer deposition (ALD) and green methods and characterized using different techniques such as UV-vis spectroscopy, high resolution transmission electron microscope (HR-TEM), attenuated total reflectance (ATR), Raman spectroscopy, and dynamic light scattering (DLS).

This study was carried out by using two different approaches: The first approach involves the development of the electrochemical aptasensor for the detection of OTA and AFB_1 by immobilizing the aptamer onto silver nanoparticles (AgNPs) and titanium nanoparticles doped with boron nitride (BN-TiO_2) respectively. Under optimized parameters, the fabricated aptasensors show a linear range of (0.002 - 0.016 mg L^{-1}), (2.5 - 20 ng mL^{-1}) with a limit of detection of 7×10^{-4} mg L^{-1} and 0.002 ng mL^{-1} for the detection of OTA and AFB_1, respectively. The determination of OTA and AFB_1 in cereal and yoghurt samples showed an acceptable average recovery of 99.78 and 97.25%. This result shows that, the fabricated aptasensors are appropriate to be applied for mycotoxins detection in the food industry. The experimental results of the aptasensor for the detection of OTA were in good agreement with computational methods. The second approach involved the fabrication of the electrochemical immunosensor for the detection of OTA and AFB_1 by anchoring the antibody onto palladium nanoparticles (PdNPs) and the growing of palladium nanoparticles on boron nitride (PdNPs-BN) respectively. The fabricated electrochemical immunosensor possessed a high sensitivity towards the detection of OTA and AFB_1. Under the optimized parameters the wide range of (0.5-20 ng mL^{-1}), (1.0 - 10 ng mL^{-1}) with the LOD of 0.096 ng mL^{-1} and 0.832 ng mL^{-1} for

the detection of OTA and AFB_1 were obtained. The detection of coffee and wine in OTA and AFB_1 yielded average recovery of 96.80 and 98.73% accordingly. These showed that the proposed immunosensors has potential applications in practical testing. The experimental results of the fabricated immunosensor for the detection of AFB_1 in wine were in good agreement with computational study. Most desired characteristics of a good biosensor such as high sensitivity, inexpensive, selective, rapid, and simple were attained in this thesis, suggesting proposed approaches significant and very promising tools for prevalent biosensing applications.

6.2 Recommendations for Further work

In regard to the successful detection of mycotoxins on the developed biosensors, the following recommendations for future detection of mycotoxins could be directed towards.

1. More computational studies to be extended to include MD simulations to assess the conformational profile of the nanocomposites of the different fabricated biosensors for a
2. Use of other metal nanomaterials such as gold nanoparticles (AuNPs), aptamer, and antibodies that may perhaps enhance the electrochemical performance of the biosensor.
2. Use of different methods of nanomaterial synthesis for those investigated in this study could also be explored.
3. Use of metal oxide nanoparticles such as zinc oxide nanoparticles (ZnO) with the same aptamer, antibodies and antigens used in this study.

REFERENCES

Abdel-Rahman, G. N., Sultan, Y. Y., Salem, S. H. and Amer, M. M. 2021. Identify the natural levels of mycotoxins in Egyptian roasted peanuts and the destructive effect of gamma radiation. *Journal of Microbiology, Biotechnology and Food Sciences*, 2021: 1174-1177.

Abdulrazzaq, Y. M., Padmanabhan, R., Shafiullah, M., Kochiyil, J. and Bastaki, S. M. 2017. Intrauterine growth restriction and impaired skeletal growth in mouse fetuses following maternal exposure to aflatoxin B1 during early and late organogenesis. *Hamdan Medical Journal*, 212 (5585): 1-16.

Abera, B. D., Shkodra, B., Douaki, A., Ibba, P., Cantarella, G., Petti, L. and Lugli, P. 2020. Single-Walled Carbon Nanotube-Coated Flexible and Soft Screen-Printed Electrochemical Biosensor for Ochratoxin a Detection. In: Proceedings of *2020 IEEE International Symposium on Circuits and Systems (ISCAS)*. IEEE, 1-5.

Abnous, K., Danesh, N. M., Alibolandi, M., Ramezani, M., Emrani, A. S., Zolfaghari, R. and Taghdisi, S. M. 2017. A new amplified π-shape electrochemical aptasensor for ultrasensitive detection of aflatoxin B1. *Biosensors and Bioelectronics*, 94: 374-379.

Achaglinkame, M. A., Opoku, N. and Amagloh, F. K. 2017. Aflatoxin contamination in cereals and legumes to reconsider usage as complementary food ingredients for Ghanaian infants: A review. *Journal of nutrition & intermediary metabolism*, 10: 1-7.

Adachi, T. and Nakamura, Y. 2019. Aptamers: A review of their chemical properties and modifications for therapeutic application. *Molecules*, 24 (23): 4229-4243.

Afzali, D. and Fathirad, F. 2016. Determination of zearalenone with a glassy carbon electrode modified with nanocomposite consisting of palladium nanoparticles and a conductive polymeric ionic liquid. *Microchimica Acta*, 183 (9): 2633-2638.

Agriopoulou, S., Stamatelopoulou, E. and Varzakas, T. 2020a. Advances in analysis and detection of major mycotoxins in foods. *Foods*, 9 (4): 518-541.

Agriopoulou, S., Stamatelopoulou, E. and Varzakas, T. 2020b. Advances in occurrence, importance, and mycotoxin control strategies: Prevention and detoxification in foods. *Foods*, 9 (2): 137-184.

Ahmad, T., Wani, I. A., Manzoor, N., Ahmed, J. and Asiri, A. M. 2013. Biosynthesis, structural characterization and antimicrobial activity of gold and silver nanoparticles. *Colloids and Surfaces B: Biointerfaces*, 107: 227-234.

Ahmed, B., Anjum, D. H., Gogotsi, Y. and Alshareef, H. N. 2017. Atomic layer deposition of SnO2 on MXene for Li-ion battery anodes. *Nano Energy*, 34: 249-256.

Ahmed, F. and Asghar, M. A. 2021. Aflatoxins Occurrence in Spices. In: Abdulra'uf, L. B. ed *Aflatoxins*. London, United Kingdom: IntechOpen. Available: https://www.intechopen.com/online-first/75799 (Accessed 26 Decembar 2020).

Ahmed, K. B. A., Sengan, M., P, S. K. and Veerappan, A. 2016a. Highy selective colorimetric cysteine sensor based on the fotmation of cysteine layer on copper nanoparticles. *Sensors and Actuators B: Chemical*, 233: 431-437.

Ahmed, S., Saifullah, Ahmad, M., Swami, B. L. and Ikram, S. 2016b. Green synthesis of silver nanoparticles using Azadirachta indica aqueous leaf extract. *Journal of radiation research and applied sciences*, 9 (1): 1-7.

Aklaku, E., Sowley, E. and Ofosu, M. 2020. Incidence of fungi and aflatoxin contamination of maize in Tolon-Kumbungu district of Ghana. *African Crop Science Journal*, 28 (2): 195-202.

Al-Akraa, I. M., Mohammad, A. M., El-Deab, M. S. and El-Anadouli, B. E. 2017. Flower-shaped gold nanoparticles: Preparation, characterization, and electrocatalytic application. *Arabian journal of chemistry*, 10 (6): 877-884.

Al-Khaza'leh, K., Almahmoud, E. A. and Talla, J. A. 2020. A novel bionanosensor for dopamine detection based on titanium doped single walled boron nitride nanotube: Density functional theory. *Chinese Journal of Physics*, 68: 204-213.

AlFaris, N. A., Wabaidur, S. M., Alothman, Z. A., Altamimi, J. Z. and Aldayel, T. S. 2020. Fast and efficient immunoaffinity column cleanup and liquid chromatography–tandem mass spectrometry method for the quantitative analysis of aflatoxins in baby food and feeds. *Journal of separation science*, 43 (11): 2079-2087.

Alhamoud, Y., Li, Y., Zhou, H., Al-Wazer, R., Gong, Y., Zhi, S. and Yang, D. 2021. Label-Free and Highly-Sensitive Detection of Ochratoxin A Using One-Pot Synthesized Reduced Graphene Oxide/Gold Nanoparticles-Based Impedimetric Aptasensor. *Biosensors*, 11 (3): 87-99.

Ali, M. A., Kamil Reza, K., Srivastava, S., Agrawal, V. V., John, R. and Malhotra, B. D. 2014a. Lipid–lipid interactions in aminated reduced graphene oxide interface for biosensing application. *Langmuir*, 30 (14): 4192-4201.

Ali, M. A., Reza, K. K., Srivastava, S., Agrawal, V. V., John, R. and Malhotra, B. D. 2014b. Lipid–lipid interactions in aminated reduced graphene oxide interface for biosensing application *Langmuir*, 30: 4192-4201.

Alsharif, A. M. A., Choo, Y.-M., Tan, G. H. and Abdulra'uf, L. B. 2019. Determination of mycotoxins using hollow fiber dispersive liquid–liquid–microextraction (HF-DLLME) prior to high-performance

liquid chromatography–tandem mass spectrometry (HPLC-MS/MS). *Analytical Letters*, 52 (12): 1976-1990.

Altun, S. K., TEMAMOĞULLARI, F., Atasever, M. and Demirci, M. 2017. Determination of Aflatoxin M1 levels in some cheese types and retail yoghurt samples. In: Proceedings of *International Engineering, Science and Education Conference (INESEC) Science Proceeding Book*. Diyarbakir,Turkey, 590-594.

Amelin, V., Karaseva, N. and Tretyakov, A. 2013. Simultaneous determination of trichothecene micotoxins, ochratoxin A, and zearalenone in grain and products of its processing, feed premixes, and meat by gas chromatography. *Journal of Analytical Chemistry*, 68 (1): 61-67.

Amenu, K., Wieland, B., Szonyi, B. and Grace, D. 2019. Milk handling practices and consumption behavior among Borana pastoralists in southern Ethiopia. *Journal of Health, Population and Nutrition*, 38 (1): 1-12.

Amirahmadi, M., Shoeibi, S., Rastegar, H., Elmi, M. and Mousavi Khaneghah, A. 2018. Simultaneous analysis of mycotoxins in corn flour using LC/MS-MS combined with a modified QuEChERS procedure. *Toxin Reviews*, 37 (3): 187-195.

Andersen, M., Panosetti, C. and Reuter, K. 2019. A practical guide to surface kinetic Monte Carlo simulations. *Frontiers in chemistry*, 7: 202-225.

Andrade, M. A. and Lanças, F. M. 2017. Determination of Ochratoxin A in wine by packed in-tube solid phase microextraction followed by high performance liquid chromatography coupled to tandem mass spectrometry. *Journal of chromatography A*, 1493: 41-48.

Anh, H. 2019. HYDROGENIZATION OF SUBSTITUTED NITRO-, AZOBENZENES, THEIR MIXTURE AND SUBSTITUTED NITROAZOBENZEN ON SKELETAL NICKEL IN AQUEOUS 2-PROPANOL SOLUTIONS. *Известия высших учебных заведений. Химия и химическая технология*, 62 (3): 50-56.

Anitha, S., Tsusaka, T. W., Njoroge, S., Kumwenda, N., Kachulu, L., Maruwo, J., Machinjiri, N., Botha, R., Msere, H. W. and Masumba, J. 2019. Knowledge, attitude and practice of Malawian farmers on pre-and post-harvest crop management to mitigate aflatoxin contamination in groundnut, maize and sorghum—implication for behavioral change. *Toxins*, 11 (12): 716-729.

Ansari, M. Z., Parveen, N., Nandi, D. K., Ramesh, R., Ansari, S. A., Cheon, T. and Kim, S.-H. 2019. Enhanced activity of highly conformal and layered tin sulfide (SnS x) prepared by atomic layer deposition (ALD) on 3D metal scaffold towards high performance supercapacitor electrode. *Scientific reports*, 9 (1): 1-15.

Antiochia, R. 2021. Developments in biosensors for CoV detection and future trends. *Biosensors and Bioelectronics*, 173: 112777-112786.

Arroyo-Manzanares, N., Campillo, N., López-García, I. and Viñas, P. 2021. Determination of Aflatoxins by Liquid Chromatography Coupled to High-Resolution Mass Spectrometry. In: Abdulra'uf, L. B. ed. *Aflatoxins*. London, United Kingdom: IntechOpen. Available: https://www.intechopen.com/online-first/75992 (Accessed 11 January 2021).

Arroyo-Manzanares, N., De Ruyck, K., Uka, V., Gámiz-Gracia, L., García-Campaña, A. M., De Saeger, S. and Di Mavungu, J. D. 2018. In-house validation of a rapid and efficient procedure for simultaneous determination of ergot alkaloids and other mycotoxins in wheat and maize. *Analytical and bioanalytical chemistry*, 410 (22): 5567-5581.

Arrúa, A. A., Mendes, J. M., Arrúa, P., Ferreira, F. P., Caballero, G., Cazal, C., Kohli, M. M., Peralta, I., Ulke, G. and Fernández Ríos, D. 2019. Occurrence of deoxynivalenol and ochratoxin A in beers and wines commercialized in Paraguay. *Toxins*, 11 (6): 308-316.

Arya, M., Niklasson, J., Mohsenzadeh, A. and Bolton, K. 2018. A density functional theory study of reactions of relevance to catalytic hydrocarbon synthesis and combustion. *Theoretical Chemistry Accounts*, 137 (11): 1-14.

Asadi, M. 2018. Determination of ochratoxin A in fruit juice by high-performance liquid chromatography after vortex-assisted emulsification microextraction based on solidification of floating organic drop. *Mycotoxin research*, 34 (1): 15-20.

Asche, T. S., Behrens, P. and Schneider, A. M. 2017. Validation of the COMPASS force field for complex inorganic–organic hybrid polymers. *Journal of Sol-Gel Science and Technology*, 81 (1): 195-204.

Asghar, M. A., Ahmed, A. and Asghar, M. A. 2020. Influence of temperature and environmental conditions on aflatoxin contamination in maize collected from different regions of Pakistan during 2016–2019. *Journal of Stored Products Research*, 88: 101637-101642.

Asghari, F., Jahanshiri, Z., Imani, M., Shams-Ghahfarokhi, M. and Razzaghi-Abyaneh, M. 2016. Antifungal nanomaterials: synthesis, properties, and applications. In: *Nanobiomaterials in antimicrobial therapy*. Elsevier, 343-383.

Atumo, S. 2020. A Review of Ochratoxin A Occurrence, Condition for the Formation and Analytical Methods. *International Journal of Agricultural Science and Food Technology*, 6 (2): 180-185.

Augustine, R., Das, S., Hasan, A., Abdul Salam, S., Augustine, P., Dalvi, Y. B., Varghese, R., Primavera, R., Yassine, H. M. and Thakor, A. S. 2020. Rapid antibody-based COVID-19 mass surveillance: relevance, challenges, and prospects in a pandemic and Post-Pandemic world. *Journal of Clinical Medicine*, 9 (10): 3372-3397.

Ayala, A., Muñoz, M. F. and Argüelles, S. 2014. Lipid peroxidation: production, metabolism, and signaling mechanisms of malondialdehyde and 4-hydroxy-2-nonenal. *Oxidative medicine and cellular longevity*, 2014: 360438. Available: https://www.hindawi.com/journals/omcl/2014/360438/ (Accessed 15 October 2020).

Aydogdu, G. and Pekyardimci, S. 2020. An electrochemical sandwich-type aptasensor for determination of lipocalin-2 based on graphene oxide/ polymer composite and gold nanoparticles. *Talanta*, 210: 120666-120674.

Aziz, N., Fatma, T., Varma, A. and Prasad, R. 2014. Biogenic synthesis of silver nanoparticles using Scenedesmus abundans and evaluation of their antibacterial activity. *Journal of Nanoparticles*, 2014: 689419. Available: https://doi.org/10.1155/2014/689419 (Accessed 2 Novembar 2020).

Azri, F. A., Sukor, R., Selamat, J., Abu Bakar, F., Yusof, N. A. and Hajian, R. 2018. Electrochemical immunosensor for detection of aflatoxin B1 based on indirect competitive ELISA. *Toxins*, 10 (5): 196-208.

Azzoune, N., Mokrane, S., Riba, A., Bouras, N., Verheecke, C., Sabaou, N. and Mathieu, F. 2015. Contamination of common spices by aflatoxigenic fungi and aflatoxin B1 in Algeria. *Quality Assurance and Safety of Crops & Foods*, 8 (1): 137-144.

Babar, V., Murat, A. and Schwingenschlögl, U. 2020. Effects of gas adsorption on monolayer Si2BN and implications for sensing applications. *Journal of Physics: Condensed Matter*, 32 (35): 355602-355607.

Bachmann, J. 2017. *Atomic layer deposition in energy conversion applications*. Erlangen,Germany: John Wiley & Sons. Available: https://onlinelibrary.wiley.com/doi/book/10.1002/9783527694822 (Accessed 13 Novembar 2020).

Bafana, A., Kumar, S. V., Temizel-Sekeryan, S., Dahoumane, S. A., Haselbach, L. and Jeffryes, C. S. 2018. Evaluating microwave-synthesized silver nanoparticles from silver nitrate with life cycle assessment techniques. *Science of the Total Environment*, 636: 936-943.

Baghayeri, M., Alinezhad, H., Tarahomi, M., Fayazi, M., Ghanei-Motlagh, M. and Maleki, B. 2019. A non-enzymatic hydrogen peroxide sensor based on dendrimer functionalized magnetic graphene oxide decorated with palladium nanoparticles. *Applied Surface Science*, 478: 87-93.

Bagheri, R., Karimzadeh, F., Kermanpur, A. and Kharaziha, M. 2021. The novel immobilization of G-quadruplex aptamer on Cu deposited surface using electrochemical method. *Materials Letters*, 282: 128703-128706.

Balashanmugam, P., Balakumaran, M., Murugan, R., Dhanapal, K. and Kalaichelvan, P. 2016. Phytogenic synthesis of silver nanoparticles, optimization and evaluation of in vitro antifungal activity against human and plant pathogens. *Microbiological Research*, 192: 52-64.

Ballai, G., Gyenes, T., Haspel, H., Vásárhelyi, L., Szenti, I., Sebők, D., Kónya, Z. and Kukovecz, Á. 2021. Binder-Free Construction of a Methanol Tolerant Pt/TiO2/Carbon Paper Anode by Atomic Layer Deposition. *Catalysts*, 11 (2): 154-163.

Balmain, W. 1842. Bemerkungen über die Bildung von Verbindungen des Bors und Siliciums mit Stickstoff und gewissen Metallen. *Journal für Praktische Chemie*, 27 (1): 422-430.

Banerjee, P. and Nath, D. 2015. A phytochemical approach to synthesize silver nanoparticles for non-toxic biomedical application and study on their antibacterial efficacy. *Nanosci Technol*, 2 (1): 1-14.

Baniwal, P., Mehra, R., Kumar, N., Sharma, S. and Kumar, S. 2021. Cereals: Functional constituents and its health benefits. *Pharma Innov*, 10 (3): 01-07.

Benites, A. J., Fernandes, M., Boleto, A. R., Azevedo, S., Silva, S. and Leitão, A. L. 2017. Occurrence of ochratoxin A in roasted coffee samples commercialized in Portugal. *Food control*, 73: 1223-1228.

Benkerroum, N. 2020. Chronic and acute toxicities of aflatoxins: Mechanisms of action. *International journal of environmental research and public health*, 17 (2): 423-450.

Berthiller, F., Cramer, B., Iha, M., Krska, R., Lattanzio, V., MacDonald, S., Malone, R., Maragos, C., Solfrizzo, M. and Stranska-Zachariasova, M. 2018. Developments in mycotoxin analysis: an update for 2016-2017. *World Mycotoxin Journal*, 11 (1): 5-32.

Bhardwaj, H., Pandey, M. K. and Sumana, G. 2019. Electrochemical Aflatoxin B1 immunosensor based on the use of graphene quantum dots and gold nanoparticles. *Microchimica Acta*, 186 (8): 1-12.

Bojang, A. A. and Wu, H. S. 2020. Characterization of electrode performance in enzymatic biofuel cells using cyclic voltammetry and electrochemical impedance spectroscopy. *Catalysts*, 10 (7): 782-801.

Boningari, T., Inturi, S. N. R., Suidan, M. and Smirniotis, P. G. 2018. Novel one-step synthesis of nitrogen-doped TiO2 by flame aerosol technique for visible-light photocatalysis: effect of synthesis parameters and secondary nitrogen (N) source. *Chemical Engineering Journal*, 350: 324-334.

Borrill, A. J., Reily, N. E. and Macpherson, J. V. 2019. Addressing the practicalities of anodic stripping voltammetry for heavy metal detection: a tutorial review. *Analyst*, 144 (23): 6834-6849.

Bouferra, R., Marín, G., Amhil, S., Wasim, S. and Essaleh, L. 2019. Low temperature electrical impedance spectroscopy characterization of n type CuInSe2 semiconductor compound. *Physica B: Condensed Matter*, 565: 14-17.

Boyd, P. G., Moosavi, S. M., Witman, M. and Smit, B. 2017. Force-field prediction of materials properties in metal-organic frameworks. *The journal of physical chemistry letters*, 8 (2): 357-363.

Brenke, R., Hall, D. R., Chuang, G.-Y., Comeau, S. R., Bohnuud, T., Beglov, D., Schueler-Furman, O., Vajda, S. and Kozakov, D. 2012. Application of asymmetric statistical potentials to antibody–protein docking. *Bioinformatics*, 28 (20): 2608-2614.

Burova, D., Shakhova, I., Morozova, P., Iarchuk, A., Drozhzhin, O. A., Rozova, M. G., Praneetha, S., Murugan, V., Tarascon, J.-M. and Abakumov, A. M. 2019. The rapid microwave-assisted hydrothermal synthesis of NASICON-structured Na 3 V 2 O 2x (PO 4) 2 F 3− 2x (0< x≤ 1) cathode materials for Na-ion batteries. *RSC Advances*, 9 (34): 19429-19440.

Butler, W. and Barnes, J. 1963. Toxic effects of groundnut meal containing aflatoxin to rats and guinea-pigs. *British journal of cancer*, 17 (4): 699-710.

Cai, J., Zhang, M., Sun, Z., Zhang, C., Liang, C., Khan, A., Ning, X., Ge, H., Feng, S.-P. and Li, W.-D. 2019. Highly-facile template-based selective electroless metallization of micro-and nanopatterns for plastic electronics and plasmonics. *Journal of Materials Chemistry C*, 7 (15): 4363-4373.

Campagnollo, F. B., Ganev, K. C., Khaneghah, A. M., Portela, J. B., Cruz, A. G., Granato, D., Corassin, C. H., Oliveira, C. A. F. and Sant'Ana, A. S. 2016. The occurrence and effect of unit operations for dairy products processing on the fate of aflatoxin M1: A review. *Food control*, 68: 310-329.

Campone, L., Rizzo, S., Piccinelli, A. L., Celano, R., Pagano, I., Russo, M., Labra, M. and Rastrelli, L. 2020. Determination of mycotoxins in beer by multi heart-cutting two-dimensional liquid chromatography tandem mass spectrometry method. *Food chemistry*, 318: 126496-126503.

Cao, Y., Maitarad, P., Gao, M., Taketsugu, T., Li, H., Yan, T., Shi, L. and Zhang, D. 2018. Defect-induced efficient dry reforming of methane over two-dimensional Ni/h-boron nitride nanosheet catalysts. *Applied Catalysis B: Environmental*, 238: 51-60.

Carballo, D., Moltó, J., Berrada, H. and Ferrer, E. 2018. Presence of mycotoxins in ready-to-eat food and subsequent risk assessment. *Food and Chemical Toxicology*, 121: 558-565.

Casewit, C., Colwell, K. and Rappe, A. 1992. Application of a universal force field to organic molecules. *Journal of the American chemical society*, 114 (25): 10035-10046.

Casoni, D., Badea, M., Bros, I. and Cobzac, S. C. A. 2017. Investigation on image processing parameters for plate evaluation in TLC analysis of mycotoxins. *Stud. Univ. Babe? Bolyai Chem*, 62: 89-102.

Cataldo, R., Leuzzi, M. and Alfinito, E. 2018. Modelling and development of electrical aptasensors: a short review. *Chemosensors*, 6 (2): 20-33.

Chanarsa, S., Jakmunee, J. and Ounnunkad, K. 2021. A Bifunctional Nanosilver-Reduced Graphene Oxide Nanocomposite for Label-Free Electrochemical Immunosensing. *Frontiers in chemistry*, 9: 631571-631582.

Chauhan, R., Singh, J., Sachdev, T., Basu, T. and Malhotra, B. 2016. Recent advances in mycotoxins detection. *Biosensors and Bioelectronics*, 81: 532-545.

Chen, A. and Ostrom, C. 2015. Palladium-based nanomaterials: synthesis and electrochemical applications. *Chemical reviews*, 115 (21): 11999-12044.

Chen, J., Brooks III, C. L. and Khandogin, J. 2008. Recent advances in implicit solvent-based methods for biomolecular simulations. *Current opinion in structural biology*, 18 (2): 140-148.

Chen, K., Wang, F., Liu, S., Wu, X., Xu, L. and Zhang, D. 2020a. In situ reduction of silver nanoparticles by sodium alginate to obtain silver-loaded composite wound dressing with enhanced mechanical and antimicrobial property. *International journal of biological macromolecules*, 148: 501-509.

Chen, L., Jiang, J., Shen, G. and Yu, R. 2015. A label-free electrochemical impedance immunosensor for the sensitive detection of aflatoxin B_1. *Analytical Methods*, 7 (6): 2354-2359.

Chen, W., Li, C., Zhang, B., Zhou, Z., Shen, Y., Liao, X., Yang, J., Wang, Y., Li, X. and Li, Y. 2018a. Advances in biodetoxification of ochratoxin AA review of the past five decades. *Frontiers in microbiology*, 9: 1386-1396.

Chen, Y., Fan, Z., Zhang, Z., Niu, W., Li, C., Yang, N., Chen, B. and Zhang, H. 2018b. Two-dimensional metal nanomaterials: synthesis, properties, and applications. *Chemical reviews*, 118 (13): 6409-6455.

Chen, Y., Yang, Y., Wang, Y., Peng, Y., Nie, J., Gao, G. and Zhi, J. 2020b. Development of an Escherichia coli-based electrochemical biosensor for mycotoxin toxicity detection. *Bioelectrochemistry*, 133: 107453-107460.

Chen, Z., Lai, G., Liu, S. and Yu, A. 2018c. Ultrasensitive electrochemical aptasensing of kanamycin antibiotic by enzymatic signal amplification with a horseradish peroxidase-functionalized gold nanoprobe. *Sensors and Actuators B: Chemical*, 273: 1762-1767.

Cheng, L., Qu, H., Teng, J., Yao, L., Xue, F. and Chen, W. 2017. Extraordinary tunable dynamic range of electrochemical aptasensor for accurate detection of ochratoxin A in food samples. *Food Science and Human Wellness*, 6 (2): 70-76.

Cheng, S.-C., Bhat, S. M., Lee, C.-W. and Shiea, J. 2019. Simple interface for scanning chemical compounds on developed thin layer chromatography plates using electrospray ionization mass spectrometry. *Analytica chimica acta*, 1049: 1-9.

Chiappim, W., Testoni, G., de Lima, J., Medeiros, H., Pessoa, R. S., Grigorov, K., Vieira, L. and Maciel, H. J. B. J. o. P. 2016. Effect of process temperature and reaction cycle number on atomic layer deposition of TiO 2 thin films using TiCl 4 and H 2 O precursors: correlation between material properties and process environment. 46 (1): 56-69.

Chrouda, A., Zinoubi, K., Soltane, R., Alzahrani, N., Osman, G., Al-Ghamdi, Y. O., Qari, S., Al Mahri, A., Algethami, F. K. and Majdoub, H. 2020. An acetylcholinesterase inhibition-based biosensor for aflatoxin B1 detection using sodium alginate as an immobilization matrix. *Toxins*, 12 (3): 173-184.

Chung, S., Sicklick, J. K., Ray, P. and Hall, D. A. 2020. Development of a Soluble KIT (sKIT) Electrochemical Aptasensor For Cancer Theranostics. *Acs Sensors*, 6 (5): 1971-1979.

Ciura, K., Dziomba, S., Nowakowska, J. and Markuszewski, M. J. 2017. Thin layer chromatography in drug discovery process. *Journal of chromatography A*, 1520: 9-22.

Conzuelo, F., Gamella, M., Campuzano, S., Pinacho, D. G., Reviejo, A. J., Marco, M. P. and Pingarrón, J. M. 2012. Disposable and integrated amperometric immunosensor for direct determination of sulfonamide antibiotics in milk *Biosensors and Bioelectronics*, 36: 81-88.

Coppock, R. W., Christian, R. G. and Jacobsen, B. J. 2018. Aflatoxins. In: *Veterinary toxicology*. Elsevier, 983-994.

Cortese, M., Gigliobianco, M. R., Magnoni, F., Censi, R. and Di Martino, P. D. 2020. Compensate for or minimize matrix effects? Strategies for overcoming matrix effects in liquid chromatography-mass spectrometry technique: a tutorial review. *Molecules*, 25 (13): 3047-3077.

Coskun, E., Jaruga, P., Vartanian, V., Erdem, O., Egner, P. A., Groopman, J. D., Lloyd, R. S. and Dizdaroglu, M. 2018. Aflatoxin-guanine DNA adducts and oxidatively induced DNA damage in aflatoxin-treated mice in vivo as measured by liquid chromatography-tandem mass spectrometry with isotope dilution. *Chemical research in toxicology*, 32 (1): 80-89.

Costantini, F., Lovecchio, N., Ruggi, A., Manetti, C., Nascetti, A., Reverberi, M., de Cesare, G. and Caputo, D. 2019. Fluorescent label-free aptasensor integrated in a lab-on-chip system for the detection of ochratoxin a in beer and wheat. *ACS Applied Bio Materials*, 2 (12): 5880-5887.

Cui, Y. 2017. Electronic materials, devices, and signals in electrochemical sensors. *IEEE Transactions on Electron Devices*, 64 (6): 2467-2477.

da Rocha, M. E. B., Freire, F. d. C. O., Maia, F. E. F., Guedes, M. I. F. and Rondina, D. 2014. Mycotoxins and their effects on human and animal health. *Food control*, 36 (1): 159-165.

da Silva, S. A., Pereira, R. G. F. A., de Azevedo Lira, N., da Glória, E. M., Chalfoun, S. M. and Batista, L. R. 2020. Fungi associated to beans infested with coffee berry borer and the risk of ochratoxin A. *Food control*, 113: 107204-107210.

da Silva, W. M., Ferreira, T. H., de Morais, C. A., Leal, A. S. and Sousa, E. M. B. 2018. Samarium doped boron nitride nanotubes. *Applied Radiation and Isotopes*, 131: 30-35.

Damiano, S., Longobardi, C., Andretta, E., Prisco, F., Piegari, G., Squillacioti, C., Montagnaro, S., Pagnini, F., Badino, P. and Florio, S. 2021. Antioxidative Effects of Curcumin on the Hepatotoxicity Induced by Ochratoxin A in Rats. *Antioxidants*, 10 (1): 125-136.

Danciu, V., Hosu, A. and Cimpoiu, C. 2018. Thin-layer chromatography in spices analysis. *Journal of Liquid Chromatography & Related Technologies*, 41 (6): 282-300.

das Neves, T. T., Brandão, R. M., Barbosa, R. B., das Graças Cardoso, M., Batista, L. R. and Silva, C. F. 2021. Simulation of coffee beans contamination by Aspergillus species under different environmental conditions and the biocontrol effect by Saccharomyces cerevisiae. *LWT*, 148: 111610-111620.

Das, R. K. and Bhuyan, D. 2019. Microwave-mediated green synthesis of gold and silver nanoparticles from fruit peel aqueous extract of Solanum melongena L. and study of antimicrobial property of silver nanoparticles. *Nanotechnology for Environmental Engineering*, 4 (1): 1-6.

Davidson, M., Ji, Y., Leong, G. J., Kovach, N. C., Trewyn, B. G. and Richards, R. M. 2018. Hybrid mesoporous silica/noble-metal nanoparticle materials—synthesis and catalytic applications. *ACS Applied Nano Materials*, 1 (9): 4386-4400.

de Almeida, Â. B., Corrêa, I. P., Furuie, J. L., de Farias Pires, T., do Rocio Dalzoto, P. and Pimentel, I. C. 2019. Inhibition of growth and ochratoxin A production in Aspergillus species by fungi isolated from coffee beans. *Brazilian Journal of Microbiology*, 50 (4): 1091-1098.

de Andrade Santiago, J., das Graças Cardoso, M., Batista, L. R., Santiago, W. D., Passamani, F. R. F., Rodrigues, L. M. A. and Nelson, D. L. 2018. Effect of the essential oils from Melaleuca alternifolia, Melaleuca quinquenervia and Backhousia citriodora on the synthesis of ochratoxin A by Aspergillus niger and Aspergillus carbonarius isolated from tropical wine grapes. *Journal of food science and technology*, 55 (1): 418-423.

De Jesus, C. L., Bartley, A., Welch, A. Z. and Berry, J. P. 2018. High incidence and levels of ochratoxin A in wines sourced from the United States. *Toxins*, 10 (1): 1-12.

Debevere, S., De Baere, S., Haesaert, G., Rychlik, M., Croubels, S. and Fievez, V. 2019. In vitro rumen simulations show a lower disappearance of deoxynivalenol, nivalenol, zearalenone and enniatin B at conditions of rumen acidosis and at dry conditions. In: Proceedings of *41st Mycotoxin workshop*. 61-61.

Deng, C., He, R., Shen, W., Li, M. and Zhang, T. 2019a. A single-atom catalyst of cobalt supported on a defective two-dimensional boron nitride material as a promising electrocatalyst for the oxygen reduction reaction: a DFT study. *Physical Chemistry Chemical Physics*, 21 (13): 6900-6907.

Deng, H., Su, X. and Wang, H. 2018. Simultaneous determination of aflatoxin B1, bisphenol a, and 4-nonylphenol in peanut oils by liquid-liquid extraction combined with solid-phase extraction and ultra-high performance liquid chromatography-tandem mass spectrometry. *Food Analytical Methods*, 11 (5): 1303-1311.

Deng, L., Zhou, N., Tang, S. and Li, Y. 2019b. Improved Dreiding force field for single layer black phosphorus. *Physical Chemistry Chemical Physics*, 21 (30): 16804-16817.

Deroco, P. B., Melo, I. G., Silva, L. S., Eguiluz, K. I., Salazar-Banda, G. R. and Fatibello-Filho, O. 2018. Carbon black supported Au-Pd core-shell nanoparticles within a dihexadecylphosphate film for the development of hydrazine electrochemical sensor. *Sensors and Actuators B: Chemical*, 256: 535-542.

Desireddy, A., Conn, B. E., Guo, J., Yoon, B., Barnett, R. N., Monahan, B. M., Kirschbaum, K., Griffith, W. P., Whetten, R. L. and Landman, U. 2013. Ultrastable silver nanoparticles. *Nature*, 501 (7467): 399-402.

Dettlaff, A., Jakobczyk, P., Ficek, M., Wilk, B., Szala, M., Wojtas, J., Ossowski, T. and Bogdanowicz, R. 2020. Electrochemical determination of nitroaromatic explosives at boron-doped diamond/graphene nanowall electrodes:2, 4 ,6-trinotrotoluene and 2, 4, 6-trinitroanisole in liquid effluents. *Journal of hazardous materials*, 387: 121672-121680.

Dhuper, S., Panda, D. and Nayak, P. 2012. Green synthesis and characterization of zero valent iron nanoparticles from the leaf extract of Mangifera indica. *Nano Trends: J Nanotech App*, 13 (2): 16-22.

Ding, M., Guo, Z., Zhou, L., Fang, X., Zhang, L., Zeng, L., Xie, L. and Zhao, H. 2018. One-dimensional zinc oxide nanomaterials for application in high-performance advanced optoelectronic devices. *Crystals*, 8 (5): 223-251.

Ding, S., Mosher, C., Lee, X. Y., Das, S. R., Cargill, A. A., Tang, X., Chen, B., McLamore, E. S., Gomes, C. and Hostetter, J. M. 2017. Rapid and label-free detection of interferon gamma via an

electrochemical aptasensor comprising a ternary surface monolayer on a gold interdigitated electrode array. *Acs Sensors*, 2 (2): 210-217.

Doi, K. and Uetsuka, K. 2014. Mechanisms of mycotoxin-induced dermal toxicity and tumorigenesis through oxidative stress-related pathways. *Journal of toxicologic pathology*, 27 (1): 1-10.

Dong, H., Xian, Y., Xiao, K., Wu, Y., Zhu, L. and He, J. 2019. Development and comparison of single-step solid phase extraction and QuEChERS clean-up for the analysis of 7 mycotoxins in fruits and vegetables during storage by UHPLC-MS/MS. *Food chemistry*, 274: 471-479.

Dong, X., Yan, X., Li, M., Liu, H., Li, J., Wang, L., Wang, K., Lu, X., Wang, S. and He, B. 2020. Ultrasensitive detection of chloramphenicol using electrochemical aptamer sensor: A mini review. *Electrochemistry Communications*: 106835-106840.

Dong, X., Zou, B., Zhao, X., Liu, S., Xu, W., Huang, T., Zong, Q. and Wang, S. 2018. Rapid qualitative and quantitative analysis of aflatoxin B1 in Pu-erh tea by liquid chromatography-isotope dilution tandem mass spectrometry coupled with the QuEChERS purification method. *Analytical Methods*, 10 (39): 4776-4783.

Dragacci, S., Gleizes, E., Fremy, J. and Candlish, A. 1995. Use of immunoaffinity chromatography as a purification step for the determination of aflatoxin M1 in cheeses. *Food Additives & Contaminants*, 12 (1): 59-65.

Du, L., Wang, S., Huang, J., Chu, C., Li, R., Li, Q., Wang, Q., Hu, Y., Cao, J. and Chen, Y. 2018. Determination of aflatoxin M1 and B1 in milk and jujube by miniaturized solid-phase extraction coupled with ultra high performance liquid chromatography and quadrupole time-of-flight tandem mass spectrometry. *Journal of separation science*, 41 (19): 3677-3685.

Du, S., Qiao, L., Wang, X. and Sun, X. 2013. Fabrication of an electrochemical immunosensor for carbofuran detection based on a nanocomposite film. *Sensors & Transducers*, 149 (2): 156-165.

Duan, N., Wu, S., Dai, S., Gu, H., Hao, L., Ye, H. and Wang, Z. 2016. Advances in aptasensors for the detection of food contaminants. *Analyst*, 141 (13): 3942-3961.

El Khoury, A. and Atoui, A. 2010. Ochratoxin A: general overview and actual molecular status. *Toxins*, 2 (4): 461-493.

Elavarasi, M., Rajeshwari, A., Alex, S. A., Kumar, D. N., Chandrasekaran, N. and Mukherjee, A. 2014. Simple colorimetric sensor for Cr (III) and Cr (VI) speciation using silver nanoparticles as a probe. *Analytical Methods*, 6 (14): 5161-5167.

Elazab, H. A., Sadek, M. and El-Idreesy, T. T. 2018. Microwave-assisted synthesis of palladium nanoparticles supported on copper oxide in aqueous medium as an efficient catalyst for Suzuki cross-coupling reaction. *Adsorption Science & Technology*, 36 (5-6): 1352-1365.

Elbagory, A. M., Meyer, M., Cupido, C. N. and Hussein, A. A. 2017. Inhibition of bacteria associated with wound infection by biocompatible green synthesized gold nanoparticles from South African plant extracts. *Nanomaterials*, 7 (12): 417-438.

Elgrishi, N., Rountree, K. J., McCarthy, B. D., Rountree, E. S., Eisenhart, T. T. and Dempsey, J. L. 2018. A practical beginner's guide to cyclic voltammetry. *Journal of chemical education*, 95 (2): 197-206.

Elhage, A., Lanterna, A. E. and Scaiano, J. C. 2018. Light-induced sonogashira C–C coupling under mild conditions using supported palladium nanoparticles. *ACS Sustainable Chemistry & Engineering*, 6 (2): 1717-1722.

Emiru, T. F. and Ayele, D. W. 2017. Controlled synthesis, characterization and reduction of graphene oxide: A convenient method for large scale production. *Egyptian Journal of Basic and Applied Sciences*, 4 (1): 74-79.

Eswaran, M., Dhanusuraman, R., Tsai, P.-C. and Ponnusamy, V. K. 2019. One-step preparation of graphitic carbon nitride/Polyaniline/Palladium nanoparticles based nanohybrid composite modified electrode for efficient methanol electro-oxidation. *Fuel*, 251: 91-97.

Fadlalla, M. H., Ling, S., Wang, R., Li, X., Yuan, J., Xiao, S., Wang, K., Tang, S., Elsir, H. and Wang, S. 2020. Development of ELISA and Lateral Flow Immunoassays for Ochratoxins (OTA and OTB) Detection Based on Monoclonal Antibody. *Frontiers in cellular and infection microbiology*, 10: 80-89.

Fan, A., Shi, L., Yang, H. and Yang, G. 2020. A Novel Electrochemical Impedance Immunosensor for Aflatoxin B1 Based on L-cysteine Self-Assesmbled on Au Nanoparticles-Porous Nitrogen Doped Graphene Modified Electrode. *Int. J. Electrochem. Sci*, 15: 9669-9682.

Fan, L., Zhang, C., Yan, W., Guo, Y., Shuang, S., Dong, C. and Bi, Y. 2019. Design of a facile and label-free electrochemical aptasensor for detection of atrazine. *Talanta*, 201: 156-164.

Fazio, E., Ridolfo, A. and Neri, G. 2019. Thermally activated noble metal Nanoparticles incorporated in electrospun fiber-based drug delivery systems. *Current Nanomaterials*, 4 (1): 21-31.

Fechter, P., Da Silva, E. C., Mercier, M.-C., Noulet, F., Etienne-Seloum, N., Guenot, D., Lehmann, M., Vauchelles, R., Martin, S. and Lelong-Rebel, I. 2019. RNA Aptamers Targeting Integrin α5β1 as Probes for Cyto-and Histofluorescence in Glioblastoma. *Molecular Therapy-Nucleic Acids*, 17: 63-77.

Feng, M., Liu, Y., Wei, N., Ma, S., Li, Z., Li, H., Chen, S., Liu, J. and Wang, D. 2018. Alumina anchored CQDs/TiO 2 nanorods by atomic layer deposition for efficient photoelectrochemical water splitting under solar light. *Journal of Materials Chemistry A*, 6 (37): 18293-18303.

Ferrari, A. G.-M., Rowley-Neale, S. J. and Banks, C. E. 2020. Recent advances in 2D hexagonal boron nitride (2D-hBN) applied as the basis of electrochemical sensing platforms. *Analytical and bioanalytical chemistry*: 1-10.

Filik, H. and Avan, A. A. 2019. Nanostructures for nonlabeled and labeled electrochemical immunosensors: Simultaneous electrochemical detection of cancer markers: A review. *Talanta*, 205: 120153.

Francis, S., Joseph, S., Koshy, E. P. and Mathew, B. 2017. Green synthesis and characterization of gold and silver nanoparticles using Mussaenda glabrata leaf extract and their environmental applications to dye degradation. *Environmental Science and Pollution Research*, 24 (21): 17347-17357.

Frisch, M. J., Trucks, G. W., Schlegel, H. B., Scuseria, G. E., Robb, M. A., Cheeseman, J. R., Scalmani, G., Barone, V., Petersson, G. A., Nakatsuji, H., Li, X., Caricato, M., Marenich, A. V., Bloino, J., Janesko, B. G., Gomperts, R., Mennucci, B., Hratchian, H. P., Ortiz, J. V., Izmaylov, A. F., Sonnenberg, J. L., Williams, Ding, F., Lipparini, F., Egidi, F., Goings, J., Peng, B., Petrone, A., Henderson, T., Ranasinghe, D., Zakrzewski, V. G., Gao, J., Rega, N., Zheng, G., Liang, W., Hada, M., Ehara, M., Toyota, K., Fukuda, R., Hasegawa, J., Ishida, M., Nakajima, T., Honda, Y., Kitao, O., Nakai, H., Vreven, T., Throssell, K., Montgomery Jr., J. A., Peralta, J. E., Ogliaro, F., Bearpark, M. J., Heyd, J. J., Brothers, E. N., Kudin, K. N., Staroverov, V. N., Keith, T. A., Kobayashi, R., Normand, J., Raghavachari, K., Rendell, A. P., Burant, J. C., Iyengar, S. S., Tomasi, J., Cossi, M., Millam, J. M., Klene, M., Adamo, C., Cammi, R., Ochterski, J. W., Martin, R. L., Morokuma, K., Farkas, O., Foresman, J. B. and Fox, D. J. 2016. Gaussian 16 Rev. C.01 (computer software). Available: https://gaussian.com/citation/ (Accessed 15 June 2020).

Galstyan, V., Comini, E., Kholmanov, I., Ponzoni, A., Sberveglieri, V., Poli, N., Faglia, G. and Sberveglieri, G. 2016. A composite structure based on reduced graphene oxide and metal oxide nanomaterials for chemical sensors. *Beilstein journal of nanotechnology*, 7 (1): 1421-1427.

Gebreegziabher, G., Asemahegne, A., Ayele, D., Dhakshnamoorthy, M. and Kumar, A. 2019. One-step synthesis and characterization of reduced graphene oxide using chemical exfoliation method. *Materials Today Chemistry*, 12: 233-239.

Geleta, G. S., Zhao, Z. and Wang, Z. 2018a. A novel reduced graphene oxide/molybdenum disulfide/polyaniline nanocomposite-based electrochemical aptasensor for detection of aflatoxin B 1. *Analyst*, 143 (7): 1644-1649.

Geleta, G. S., Zhao, Z. and Wang, Z. 2018b. A sensitive electrochemical aptasensor for detection of Aflatoxin B2 based on a polyacrylamide/phytic acid/polydopamine hydrogel modified screen printed carbon electrode. *Analytical Methods*, 10 (38): 4689-4694.

Ghalkhani, M., Beheshtian, J. and Salehi, M. 2016. Electrochemical and DFT study of an anticancer and active anthelmintic drug at carbon nanostructured modified electrode. *Materials Science and Engineering: C*, 69: 1345-1353.

Ghassan, A. A., Mijan, N.-A. and Taufiq-Yap, Y. H. 2020. Nanomaterials: an overview of nanorods synthesis and optimization. *Nanorods and Nanocomposites*: 11.

Gil-Serna, J., Vázquez, C., González-Jaén, M. T. and Patiño, B. 2018. Wine contamination with ochratoxins: A review. *Beverages*, 4 (1): 6-26.

Gil-Serna, J., Vazquez, C., Sandino, F. G., Valle, A. M., Gonzalez-Jaen, M. T. and Patino, B. 2014. Evaluation of growth and ochratoxin A production by Aspergillus steynii and Aspergillus westerdijkiae in green-coffee based medium under different environmental conditions. *Food Research International*, 61: 127-131.

Gil, L., Ruiz, P., Font, G. and Manyes, L. 2016. An overview of the applications of hazards analysis and critical control point (HACCP) system to mycotoxins. *Revista de Toxicología*, 33 (1): 50-55.

Gilroy, K. D., Ruditskiy, A., Peng, H.-C., Qin, D. and Xia, Y. 2016. Bimetallic nanocrystals: syntheses, properties, and applications. *Chemical reviews*, 116 (18): 10414-10472.

Giubileo, F., Di Bartolomeo, A., Iemmo, L., Luongo, G. and Urban, F. 2018. Field emission from carbon nanostructures. *Applied Sciences*, 8 (4): 526-546.

Gizachew, D., Chang, C.-H., Szonyi, B., De La Torre, S. and Ting, W.-t. E. 2019. Aflatoxin B1 (AFB1) production by Aspergillus flavus and Aspergillus parasiticus on ground Nyjer seeds: The effect of water activity and temperature. *International Journal of Food Microbiology*, 296: 8-13.

Gizachew, D., Szonyi, B., Tegegne, A., Hanson, J. and Grace, D. 2016. Aflatoxin contamination of milk and dairy feeds in the Greater Addis Ababa milk shed, Ethiopia. *Food control*, 59: 773-779.

Gökdere, B., Üzer, A., Durmazel, S., Erçağ, E. and Apak, R. 2019. Titanium dioxide nanoparticles–based colorimetric sensors for determination of hydrogen peroxide and triacetone triperoxide (TATP). *Talanta*, 202: 402-410.

González, M. 2011. Force fields and molecular dynamics simulations. *École thématique de la Société Française de la Neutronique*, 12: 169-200.

Goud, K. Y., Catanante, G., Hayat, A., M., S., Gobi, K. V. and Marty, J. L. 2016a. Disposable and portable electrochemical aptasensor for label free detection of aflatoxin B_1 in alcoholic beverages. *Sensors and Actuators B: Chemical*, 235: 466-473.

Goud, K. Y., Catanante, G., Hayat, A., Satyanarayana, M., Gobi, K. V. and Marty, J. L. 2016b. Disposable and portable electrochemical aptasensor for label free detection of aflatoxin B1 in alcoholic beverages. *Sensors and Actuators B: Chemical*, 235: 466-473.

Graniel, O., Weber, M., Balme, S., Miele, P. and Bechelany, M. 2018. Atomic layer deposition for biosensing applications. *Biosensors and Bioelectronics*, 122: 147-159.

Griesche, C. and Baeumner, A. J. 2020. Biosensors to support sustainable agriculture and food safety. *TrAC Trends in Analytical Chemistry*: 115906-115921.

Gu, C., Yang, L., Wang, M., Zhou, N., He, L., Zhang, Z. and Du, M. 2019. A bimetallic (Cu-Co) Prussian Blue analogue loaded with gold nanoparticles for impedimetric aptasensing of ochratoxin A. *Microchimica Acta*, 186 (6): 1-10.

Guerrero-Contreras, J. and Caballero-Briones, F. 2015. Graphene oxide powders with different oxidation degree, prepared by synthesis variations of the Hummers method. *Materials Chemistry and Physics*, 153: 209-220.

Gülercan, D., Gergin, İ. and Sarac, A. S. 2018. Preparation and Electrochemical Performances of graphene oxide/PEDOT and reduced graphene oxide/PEDOT nanofibers and nanocomposites. *Fibers and Polymers*, 19 (10): 2178-2187.

Guo, W., Wu, L., Fan, K., Nie, D., He, W., Yang, J., Zhao, Z. and Han, Z. 2017. Reduced graphene oxide-gold nanoparticle nanoframework as a highly selective separation material for aflatoxins. *Scientific reports*, 7 (1): 1-9.

Guo, X., Wen, F., Zheng, N., Luo, Q., Wang, H., Wang, H., Li, S. and Wang, J. 2014. Development of an ultrasensitive aptasensor for the detection of aflatoxin B1. *Biosensors and Bioelectronics*, 56: 340-344.

Gupta, P. K., Pachauri, N., Khan, Z. H. and Solanki, P. R. 2017a. One pot synthesized zirconia nanoparticles embedded in amino functionalized amorphous carbon for electrochemical immunosensor. *Journal of Electroanalytical Chemistry*, 807: 59-69.

Gupta, P. K., Tiwari, S., Khan, Z. H. and Solanki, P. R. 2017b. Amino acid fuctionalized ZrO 2 nanoparticles decorated reduced graphene oxide based immunosensor. *Journal of Materials Chemistry B*, 5 (10): 2019-2033.

Gupta, P. K., Tiwari, S., Khan, Z. H. and Solanki, P. R. 2017c. Amino acid functionalized ZrO 2 nanoparticles decorated reduced graphene oxide based immunosensor. *Journal of Materials Chemistry B*, 5 (10): 2019-2033.

Gurunathan, S., Arsalan Iqbal, M., Qasim, M., Park, C. H., Yoo, H., Hwang, J. H., Uhm, S. J., Song, H., Park, C. and Do, J. T. 2019. Evaluation of graphene oxide induced cellular toxicity and transcriptome analysis in human embryonic kidney cells. *Nanomaterials*, 9 (7): 969-990.

Han, Z., Tang, Z., Jiang, K., Huang, Q., Meng, J., Nie, D. and Zhao, Z. 2020. Dual-target electrochemical aptasensor based on co-reduced molybdenum disulfide and Au NPs (rMoS2-Au) for multiplex detection of mycotoxins. *Biosensors and Bioelectronics*, 150: 111894-111900.

Harris, L. J., Larson, S. B., Hasel, K. W. and McPherson, A. 1997. Refined structure of an intact IgG2a monoclonal antibody. *Biochemistry*, 36 (7): 1581-1597.

Hashemi Goradel, N., Mirzaei, H., Sahebkar, A., Poursadeghiyan, M., Masoudifar, A., Malekshahi, Z. V. and Negahdari, B. 2018. Biosensors for the detection of environmental and urban pollutions. *Journal of cellular biochemistry*, 119 (1): 207-212.

Hashemi, P., Afkhami, A., Bagheri, H., Amidi, S. and Madrakian, T. 2017. Fabrication of a novel impedimetric sensor based on L-Cysteine/Cu(II) modified gold electrode for sensitive determination of ampyra. *Analytica chimica acta*, 984: 185-192.

Hashim, A. and Hamad, Z. S. 2018. Synthesis, characterization and nanobiological application of (biodegradable polymers-titanium nitride) nanocomposites. *Journal of Bionanoscience*, 12 (4): 504-507.

Hassan, F. F. 2018. Detection of aflatoxin b1 in some canned foods and reduction of toxin by ultraviolet radiation. *Iraqi Journal Of Science*, (58): 2343-2349.

He, B. and Dong, X. 2021. Nb. BbvCI powered DNA walking machine-based Zr-MOFs-labeled electrochemical aptasensor using Pt@ AuNRs/Fe-MOFs/PEI-rGO as electrode modification material for patulin detection. *Chemical Engineering Journal*, 405: 126642-126651.

He, Q.-H., Xu, Y., Wang, D., Kang, M., Huang, Z.-B. and Li, Y.-P. 2012. Simultaneous multiresidue determination of mycotoxins in cereal samples by polyvinylidene fluoride membrane based dot immunoassay. *Food chemistry*, 134 (1): 507-512.

Hembram, K. C., Kumar, R., Kandha, L., Parhi, P. K., Kundu, C. N. and Bindhani, B. K. 2018. Therapeutic prospective of plant-induced silver nanoparticles: application as antimicrobial and anticancer agent. *Artificial cells, nanomedicine, and biotechnology*, 46 (sup3): S38-S51.

Hernández-Meléndez, D., Salas-Téllez, E., Zavala-Franco, A., Téllez, G., Méndez-Albores, A. and Vázquez-Durán, A. 2018. Inhibitory effect of flower-shaped zinc oxide nanostructures on the growth

and aflatoxin production of a highly toxigenic strain of aspergillus flavus link. *Materials*, 11 (8): 1265-1277.

Heshmati, A., Ghadimi, S., Ranjbar, A. and Khaneghah, A. M. 2019. Changes in aflatoxins content during processing of pekmez as a traditional product of grape. *LWT*, 103: 178-185.

Heshmati, A., Zohrevand, T., Khaneghah, A. M., Nejad, A. S. M. and Sant'Ana, A. S. 2017. Co-occurrence of aflatoxins and ochratoxin A in dried fruits in Iran: Dietary exposure risk assessment. *Food and Chemical Toxicology*, 106: 202-208.

Heussner, A. H. and Bingle, L. E. 2015. Comparative ochratoxin toxicity: A review of the available data. *Toxins*, 7 (10): 4253-4282.

Hickert, S., Gerding, J., Ncube, E., Hübner, F., Flett, B., Cramer, B. and Humpf, H.-U. 2015. A new approach using micro HPLC-MS/MS for multi-mycotoxin analysis in maize samples. *Mycotoxin research*, 31 (2): 109-115.

Hidalgo-Ruiz, J. L., Romero-González, R., Vidal, J. L. M. and Frenich, A. G. 2019. A rapid method for the determination of mycotoxins in edible vegetable oils by ultra-high performance liquid chromatography-tandem mass spectrometry. *Food chemistry*, 288: 22-28.

Hidayah, N., Liu, W.-W., Lai, C.-W., Noriman, N., Khe, C.-S., Hashim, U. and Lee, H. C. 2017. Comparison on graphite, graphene oxide and reduced graphene oxide: Synthesis and characterization. In: Proceedings of *AIP Conference Proceedings*. AIP Publishing LLC, 150002.

Hitabatuma, A., Tuyishime, M. A. and Komera, I. 2017. Integration of Recent Biosensor into Community-Based Reduction Method to Reduce Food Mycotoxin Contamination. *American Journal of Food Science and Nutrition Research*, 4 (6): 184-196.

Ho, T. A., Bae, C., Nam, H., Kim, E., Lee, S. Y., Park, J. H. and Shin, H. 2018. Metallic Ni3S2 films grown by atomic layer deposition as an efficient and stable electrocatalyst for overall water splitting. *ACS applied materials & interfaces*, 10 (15): 12807-12815.

Hoffmann, A. A., Dias, S. L., Rodrigues, J. R., Pavan, F. A., Benvenutti, E. V. and Lima, E. C. 2008. Methylene blue immobilized on cellulose acetate with titanium dioxide: an application as sensor for ascorbic acid. *Journal of the Brazilian Chemical Society*, 19 (5): 943-949.

Hohenberg, P. and Kohn, W. 1964. Inhomogeneous electron gas. *Physical review*, 136 (3B): B864-B871.

Hou, S.-l., Ma, Z.-e., Meng, H., Xu, Y. and He, Q.-h. 2019. Ultrasensitive and green electrochemical immunosensor for mycotoxin ochratoxin A based on phage displayed mimotope peptide. *Talanta*, 194: 919-924.

Hoyos-Arbeláez, J., Vázquez, M. and Contreras-Calderón, J. 2017. Electrochemical methods as a tool for determining the antioxidant capacity of food and beverages: A review. *Food chemistry*, 221: 1371-1381.

Huang, L., Santiago, D., Loyselle, P. and Dai, L. 2018. Graphene-Based Nanomaterials for Flexible and Wearable Supercapacitors. *Small*, 14 (43): 1800879-1800889.

Huang, X., Du, Z., Wu, B., Jia, L., Wang, X. and Jing, X. 2020. Dispersive liquid–liquid microextraction based on the solidification of floating organic droplets for HPLC determination of three strobilurin fungicides in cereals. *Food Additives & Contaminants: Part A*, 37 (8): 1279-1288.

Huertas-Pérez, J. F., Arroyo-Manzanares, N., García-Campaña, A. M. and Gámiz-Gracia, L. 2017. Solid phase extraction as sample treatment for the determination of Ochratoxin A in foods: A review. *Critical reviews in food science and nutrition*, 57 (16): 3405-3420.

Husain, A., Chakkamalayath, J. and Al-Bahar, S. 2017. Electrochemical impedance spectroscopy as a rapid technique for evaluating the failure of fusion bonded epoxy powder coating. *Engineering Failure Analysis*, 82: 765-775.

Husnah, M., Fakhri, H. A., Rohman, F., Aimon, A. H. and Iskandar, F. 2017. A modified Marcano method for improving electrical properties of reduced graphene oxide (rGO). *Materials Research Express*, 4 (6): 064001-064006.

Ilager, D., Shetti, N. P., Malladi, R. S., Shetty, N. S., Reddy, K. R. and Aminabhavi, T. M. 2021. Synthesis of Ca-doped ZnO nanoparticles and its application as highly efficient electrochemical sensor for the determination of anti-viral drug, acyclovir. *Journal of Molecular Liquids*, 322: 114552-114559.

Inam, O., Demir, E. and Uslu, B. 2020. Voltammetric pathways for the analysis of ophthalmic drugs. *Current Pharmaceutical Analysis*, 16 (4): 367-391.

Intanoo, M., Kongkeitkajorn, M., Pattarajinda, V., Bernard, J., Callaway, T., Suriyasathaporn, W. and Phasuk, Y. 2018. Isolation and screening of aflatoxin-detoxifying yeast and bacteria from ruminal fluids to reduce aflatoxin B1 contamination in dairy cattle feed. *Journal of applied microbiology*, 125 (6): 1603-1613.

Ioi, J. D., Zhou, T., Tsao, R. and F Marcone, M. 2017. Mitigation of patulin in fresh and processed foods and beverages. *Toxins*, 9 (5): 157-174.

Iqbal, S. Z., Jinap, S., Pirouz, A. and Faizal, A. A. 2015. Aflatoxin M1 in milk and dairy products, occurrence and recent challenges: A review. *Trends in Food Science & Technology*, 46 (1): 110-119.

Irakli, M. N., Skendi, A. and Papageorgiou, M. D. 2017. HPLC-DAD-FLD method for simultaneous determination of mycotoxins in wheat bran. *Journal of chromatographic science*, 55 (7): 690-696.

Iskandar, F., Hikmah, U., Stavila, E. and Aimon, A. H. 2017. Microwave-assisted reduction method under nitrogen atmosphere for synthesis and electrical conductivity improvement of reduced graphene oxide (rGO). *RSC advances*, 7 (83): 52391-52397.

Ismail, I., Oluleye, G. and Oluwafemi, I. 2017. Mathematical modelling of an enzyme-based biosensor. *Int. J. Biosens. Bioelectron*, 3: 265-268.

Itti, L. and Koch, C. 2001. Computational modelling of visual attention. *Nature reviews neuroscience*, 2 (3): 194-203.

Ivanova, M., Kareth, S. and Petermann, M. 2018. Supercritical carbon dioxide and imidazolium based ionic liquids applied during the sol–gel process as suitable candidates for the replacement of classical organic solvents. *The Journal of Supercritical Fluids*, 132: 76-82.

Jahdi, M., Mishra, S. B., Nxumalo, E. N., Mhlanga, S. D. and Mishra, A. K. 2020. Synergistic effects of sodium fluoride (NaF) on the crystallinity and band gap of Fe-doped TiO2 developed via microwave-assisted hydrothermal treatment. *Optical Materials*, 104: 109844-109852.

Jalili, M. and Scotter, M. 2015. A review of aflatoxin M1 in liquid milk. *Iranian Journal of Health, Safety and Environment*, 2 (2): 283-295.

Jász, Á., Rák, Á., Ladjánszki, I. and Cserey, G. 2019. Optimized GPU implementation of Merck molecular force field and universal force field. *Journal of Molecular Structure*, 1188: 227-233.

Jeddi, I. and Saiz, L. 2017. Three-dimensional modeling of single stranded DNA hairpins for aptamer-based biosensors. *Scientific reports*, 7 (1): 1-13.

Jeyaramraja, P., Meenakshi, S. N. and Woldesenbet, F. 2018. Relationship between drought and preharvest aflatoxin contamination in groundnut (Arachis hypogaea L.). *World Mycotoxin Journal*, 11 (2): 187-199.

Ji, J., Zhu, P., Cui, F., Pi, F., Zhang, Y. and Sun, X. 2017. The disorder metabolic profiling in kidney and spleen of mice induced by mycotoxins deoxynivalenol through gas chromatography mass spectrometry. *Chemosphere*, 180: 267-274.

Ji, M., Xia, J., Di, J., Liu, Y., Chen, R., Chen, Z., Yin, S. and Li, H. 2018. Graphene-like boron nitride induced accelerated charge transfer for boosting the photocatalytic behavior of Bi4O5I2 towards bisphenol a removal. *Chemical Engineering Journal*, 331: 355-363.

Jiang, C., Lan, L., Yao, Y., Zhao, F. and Ping, J. 2018. Recent progress in application of nanomaterial-enabled biosensors for ochratoxin A detection. *TrAC Trends in Analytical Chemistry*, 102: 236-249.

Jiang, F., Li, P., Zong, C. and Yang, H. 2020. Surface-plasmon-coupled chemiluminescence amplification of silver nanoparticles modified immunosensor for high-throughput ultrasensitive detection of multiple mycotoxins. *Analytica chimica acta*, 1114: 58-65.

Jiao, Y., Hou, W., Fu, J., Guo, Y., Sun, X., Wang, X. and Zhao, J. 2017. A nanostructured electrochemical aptasensor for highly sensitive detection of chlorpyrifos. *Sensors and Actuators B: Chemical*, 243: 1164-1170.

Jo, J. H., Singh, P., Kim, Y. J., Wang, C., Mathiyalagan, R., Jin, C.-G. and Yang, D. C. 2016. Pseudomonas deceptionensis DC5-mediated synthesis of extracellular silver nanoparticles. *Artificial cells, nanomedicine, and biotechnology*, 44 (6): 1576-1581.

John, A., Benny, L., Cherian, A. R., Narahari, S. Y., Varghese, A. and Hegde, G. 2021. Electrochemical sensors using conducting polymer/noble metal nanoparticle nanocomposites for the detection of various analytes: a review. *Journal of Nanostructure in Chemistry*: 1-31.

Johnson, R. W., Hultqvist, A. and Bent, S. F. 2014. A brief review of atomic layer deposition: from fundamentals to applications. *Materials today*, 17 (5): 236-246.

Johra, F. T. and Jung, W.-G. 2015. Hydrothermally reduced graphene oxide as a supercapacitor. *Applied Surface Science*, 357: 1911-1914.

Joint, F., Organization, W. H. and Additives, W. E. C. o. F. 2017. *Evaluation of certain contaminants in food: eighty-third report of the Joint FAO/WHO Expert Committee on Food Additives*. Geneva, Switzerland: World Health Organization. Available: https://apps.who.int/iris/handle/10665/254893 (Accessed 24 June 2020).

Jorio, A. 2012. Raman spectroscopy in graphene-based systems: prototypes for nanoscience and nanometrology. *International Scholarly Research Notices*, 2012: 234216. Available: https://www.hindawi.com/journals/isrn/2012/234216/ (Accessed 12 November 2020).

Jung, J.-Y., Song, B.-K. and Kim, Y.-K. 2019. Tunable color emission of transparent boron nitride nanophosphors towards anti-counterfeiting application. *Journal of Alloys and Compounds*, 791: 81-86.

Kafil, V., Saei, A. A., Tohidkia, M. R., Barar, J. and Omidi, Y. 2020. Immunotargeting and therapy of cancer by advanced multivalence antibody scaffolds. *Journal of Drug Targeting*, 28 (10): 1018-1033.

Kamika, I. and Tekere, M. 2016. Occurrence of aflatoxin contamination in maize throughout the supply chain in the Democratic Republic of Congo. *Food control*, 69: 292-296.

Kang'ethe, E., Korhonen, H., Marimba, K., Nduhiu, G., Mungatu, J., Okoth, S., Joutsjoki, V., Wamae, L. and Shalo, P. 2017. Management and mitigation of health risks associated with the occurrence of mycotoxins along the maize value chain in two counties in Kenya. *Food Quality and Safety*, 1 (4): 268-274.

Kannan, P., Maiyalagan, T., Marsili, E., Ghosh, S., Niedziolka-Jönsson, J. and Jönsson-Niedziolka, M. 2016. Hierarchical 3-dimensional nickel–iron nanosheet arrays on carbon fiber paper as a novel electrode for non-enzymatic glucose sensing. *Nanoscale*, 8 (2): 843-855.

Kara, R. and Ince, S. 2014. Aflatoxin M1 in buffalo and cow milk in Afyonkarahisar, Turkey. *Food Additives & Contaminants: Part B*, 7 (1): 7-10.

Karapetis, S., Nikolelis, D. and Hianik, T. 2018. Label-free and redox markers-based electrochemical aptasensors for aflatoxin M1 detection. *Sensors*, 18 (12): 4218-4231.

Karczmarczyk, A., Baeumner, A. J. and Feller, K.-H. 2017. Rapid and sensitive inhibition-based assay for the electrochemical detection of Ochratoxin A and Aflatoxin M1 in red wine and milk. *Electrochimica Acta*, 243: 82-89.

Karimi-Maleh, H., Karimi, F., Alizadeh, M. and Sanati, A. L. 2020. Electrochemical sensors, a bright future in the fabrication of portable kits in analytical systems. *The Chemical Record*, 20 (7): 682-692.

Kathiravan, V., Ravi, S. and Ashokkumar, S. 2014. Synthesis of silver nanoparticles from Melia dubia leaf extract and their in vitro anticancer activity. *Spectrochimica Acta Part A: Molecular and Biomolecular Spectroscopy*, 130: 116-121.

Kaur, N., Bharti, A., Batra, S., Rana, S., Rana, S., Bhalla, A. and Prabhakar, N. 2019. An electrochemical aptasensor based on graphene doped chitosan nanocomposites for determination of ochratoxin A. *Microchemical Journal*, 144: 102-109.

Kaushik, A., Solanki, P. R., Ansari, A. A., Ahmad, S. and Malhotra, B. D. 2009. A nanostructured cerium oxide film-based immunosensor for mycotoxin detection. *Nanotechnology*, 20 (5): 055105-055113.

Kavitha, E., Sundaraganesan, N. and Sebastian, S. 2010. Molecular structure, vibrational spectroscopic and HOMO, LUMO studies of 4-nitroaniline by density functional method, 48 (1): 20-30.

Kawrani, S., Nada, A. A., Bekheet, M. F., Boulos, M., Viter, R., Roualdes, S., Miele, P., Cornu, D. and Bechelany, M. 2020. Enhancement of calcium copper titanium oxide photoelectrochemical performance using boron nitride nanosheets. *Chemical Engineering Journal*, 389: 124326-124337.

Keller, A. A., McFerran, S., Lazareva, A. and Suh, S. 2013. Global life cycle releases of engineered nanomaterials. *Journal of nanoparticle research*, 15 (6): 1-17.

Khadka, R., Aydemir, N., Carraher, C., Hamiaux, C., Colbert, D., Cheema, J., Malmström, J., Kralicek, A. and Travas-Sejdic, J. 2019. An ultrasensitive electrochemical impedance-based biosensor using insect odorant receptors to detect odorants. *Biosensors and Bioelectronics*, 126: 207-213.

Khalil, M. M., Ismail, E. H. and El-Magdoub, F. 2012. Biosynthesis of Au nanoparticles using olive leaf extract: 1st nano updates. *Arabian journal of chemistry*, 5 (4): 431-437.

Khan, A. I., Navid, I. A., Noshin, M. and Subrina, S. 2017. Thermal transport characterization of hexagonal boron nitride nanoribbons using molecular dynamics simulation. *Aip Advances*, 7 (10): 105110-105121.

Khan, I., Saeed, K. and Khan, I. 2019. Nanoparticles: Properties, applications and toxicities. *Arabian journal of chemistry*, 12 (7): 908-931.

Khan, M. M., Ansari, S. A., Pradhan, D., Ansari, M. O., Lee, J. and Cho, M. H. 2014. Band gap engineered TiO 2 nanoparticles for visible light induced photoelectrochemical and photocatalytic studies. *Journal of Materials Chemistry A*, 2 (3): 637-644.

Khan, M. T., Irfan, M., Ahsan, H., Ali, S., Malik, A., Pech-Cervantes, A., Cui, Z., Zhang, Y. and Wei, D. 2021. CYP1A2, 2A13, and 3A4 network and interaction with aflatoxin B1. *World Mycotoxin Journal*, 14 (2): 179-189.

Khlangwiset, P., Shephard, G. S. and Wu, F. 2011. Aflatoxins and growth impairment: a review. *Critical reviews in toxicology*, 41 (9): 740-755.

Khodaei, D., Javanmardi, F. and Khaneghah, A. M. 2020. The global overview of the occurrence of mycotoxins in Cereals: A three-year survey. *Current Opinion in Food Science*, 39:36-42.

Kholová, A., Lhotská, I., Uhrová, A., Špánik, I., Machyňáková, A., Solich, P., Švec, F. and Šatínský, D. 2020. Determination of Ochratoxin A and Ochratoxin B in Archived Tokaj Wines (Vintage 1959–2017) Using On-Line Solid Phase Extraction Coupled to Liquid Chromatography. *Toxins*, 12 (12): 739-749.

Khoshbin, Z., Housaindokht, M. R. and Verdian, A. 2020. A low-cost paper-based aptasensor for simultaneous trace-level monitoring of mercury (II) and silver (I) ions. *Analytical biochemistry*, 597: 113689-113699.

Khoshnamvand, Z., Nazari, F., Mehrasebi, M. R. and Hosseini, M. J. 2019. Occurrence and Safety Evaluation of Ochratoxin A in Cereal-based Baby Foods Collected from Iranian Retail Market. *Journal of food science*, 84 (3): 695-700.

Klvana, M. and Bren, U. 2019. Aflatoxin B1–formamidopyrimidine DNA adducts: Relationships between structures, free energies, and melting temperatures. *Molecules*, 24 (1): 150-169.

Kong, L., Chen, J., Chen, Z., Feng, J., Fan, D. and Wei, Q. 2018. A Label-Free Photoelectrochemical Aptasensor Based on N-GQDs Sensitized Zn-SnS 2 for Aflatoxin B1 Detection. *IEEE Sensors Journal*, 19 (5): 1633-1639.

Kongor, A., Panchal, M., Athar, M., Vora, M., Makwana, B., Jha, P. and Jain, V. 2020. Calix [4] pyrrole stabilized PdNPs as an efficient heterogeneous catalyst for enhanced degradation of water-soluble carcinogenic Azo dyes. *Catalysis Letters*: 1-11.

Kora, A. J. and Rastogi, L. 2018. Green synthesis of palladium nanoparticles using gum ghatti (Anogeissus latifolia) and its application as an antioxidant and catalyst. *Arabian journal of chemistry*, 11 (7): 1097-1106.

Kos, J., Janić Hajnal, E., Šarić, B., Jovanov, P., Mandić, A., Đuragić, O. and Kokić, B. 2018. Aflatoxins in maize harvested in the Republic of Serbia over the period 2012–2016. *Food Additives & Contaminants: Part B*, 11 (4): 246-255.

Kosimaningrum, W. E., Le, T. X. H., Holade, Y., Bechelany, M., Tingry, S., Buchari, B., Noviandri, I., Innocent, C. and Cretin, M. 2017. Surfactant-and binder-free hierarchical platinum nanoarray directly grown onto a carbon felt electrode for efficient electrocatalysis. *ACS applied materials & interfaces*, 9 (27): 22476-22489.

Krishna, R., Titus, E., Okhay, O., Gil, J. C., Ventura, J., Ramana, E. V. and Gracio, J. J. 2014. Rapid electrochemical synthesis of hydrogenated graphene oxide using Ni nanoparticles. *Int. J. Electrochem. Sci*, 9: 4054-4069.

Kulikov, L., Kalinina, M., Makeeva, D., Maximov, A., Kardasheva, Y., Terenina, M. and Karakhanov, E. 2020. Palladium Catalysts Based on Porous Aromatic Frameworks, Modified with Ethanolamino-Groups, for Hydrogenation of Alkynes, Alkenes and Dienes. *Catalysts*, 10 (10): 1106-1122.

Kumar, A., Purohit, B., Maurya, P. K., Pandey, L. M. and Chandra, P. 2019. Engineered nanomaterial assisted signal-amplification strategies for enhancing analytical performance of electrochemical biosensors. *Electroanalysis*, 31 (9): 1615-1629.

Kumar, C. G. and Poornachandra, Y. 2015. Biodirected synthesis of Miconazole-conjugated bacterial silver nanoparticles and their application as antifungal agents and drug delivery vehicles. *Colloids and Surfaces B: Biointerfaces*, 125: 110-119.

Kunene, K., Weber, M., Sabela, M., Voiry, D., Kanchi, S., Bisetty, K. and Bechelany, M. 2020. Highly-efficient electrochemical label-free immunosensor for the detection of ochratoxin A in coffee samples. *Sensors and Actuators B: Chemical*, 305: 127438-127446.

Kunene, K. W. 2018. Fabrication of electrochemical biosensors for the determination of phenolic compounds by experimental and computational methods. Masters degree, Durban University of Technology.

Laaniste, A., Leito, I. and Kruve, A. 2019. ESI outcompetes other ion sources in LC/MS trace analysis. *Analytical and bioanalytical chemistry*, 411 (16): 3533-3542.

Labib, M., Sargent, E. H. and Kelley, S. O. 2016. Electrochemical methods for the analysis of clinically relevant biomolecules. *Chemical reviews*, 116 (16): 9001-9090.

Lalah, J. O., Omwoma, S. and Orony, D. A. 2019. Aflatoxin B1: Chemistry, environmental and diet sources and potential exposure in human in Kenya. In: Blumenberg, M. *Aflatoxin B1 Occurrence, Detection and Toxicological Effects*. London, United Kingdom: IntechOpen. Available: https://www.intechopen.com/chapters/69028 (Accessed 11 March 2020).

Lan, L., Yao, Y., Ping, J. and Ying, Y. 2017. Recent advances in nanomaterial-based biosensors for antibiotics detection. *Biosensors and Bioelectronics*, 91: 504-514.

Lee, S., Han, J.-H., Lee, S.-H., Baek, G.-H. and Park, J.-S. 2019a. Review of organic/inorganic thin film encapsulation by atomic layer deposition for a flexible OLED display. *Jom*, 71 (1): 197-211.

Lee, S. H. and Jun, B.-H. 2019. Silver nanoparticles: synthesis and application for nanomedicine. *International journal of molecular sciences*, 20 (4): 865-888.

Lee, X. J., Hiew, B. Y. Z., Lai, K. C., Lee, L. Y., Gan, S., Thangalazhy-Gopakumar, S. and Rigby, S. 2019b. Review on graphene and its derivatives: Synthesis methods and potential industrial implementation. *Journal of the Taiwan Institute of Chemical Engineers*, 98: 163-180.

Leitão, A. L. 2019. Occurrence of ochratoxin A in coffee: Threads and solutions—A mini-review. *Beverages*, 5 (2): 36-49.

Leung, K. C. F. and Xuan, S. 2016. Noble Metal-Iron Oxide Hybrid Nanomaterials: Emerging Applications. *The Chemical Record*, 16 (1): 458-472.

Lewars, E. 2011. Computational chemistry. 3rd ed. Switzerland: Springer.Cham.

Li, D., Song, H., Meng, X., Shen, T., Sun, J., Han, W. and Wang, X. 2020a. Effects of particle size on the structure and photocatalytic performance by alkali-treated TiO2. *Nanomaterials*, 10 (3): 546-559.

Li, G., Xu, L., Wu, W., Wang, D., Jiang, J., Chen, X., Zhang, W., Poapolathep, S., Poapolathep, A. and Zhang, Z. 2018. On-Site ultrasensitive detection paper for multiclass chemical contaminants via universal bridge-antibody labeling: Mycotoxin and illegal additives in milk as an example. *Analytical chemistry*, 91 (3): 1968-1973.

Li, H., Guo, Z., Xie, W., Sun, W., Ji, S., Tian, J. and Lv, L. 2019. A label-free fluorometric aptasensor for adenosine triphosphate (ATP) detection based on aggregation-induced emission probe. *Analytical biochemistry*, 578: 60-65.

Li, H., Yang, D., Li, P., Zhang, Q., Zhang, W., Ding, X., Mao, J. and Wu, J. 2017. Palladium nanoparticles-based fluorescence resonance energy transfer aptasensor for highly sensitive detection of aflatoxin M1 in milk. *Toxins*, 9 (10): 318-327.

Li, Q., Michaelis, M., Wei, G. and Ciacchi, L. C. 2015. A novel aptasensor based on single-molecule force spectroscopy for highly sensitive detection of mercury ions. *Analyst*, 140 (15): 5243-5250.

Li, Q., Zeng, L., Wang, J., Tang, D., Liu, B., Chen, G. and Wei, M. 2011 Magnetic mesoporous organic–inorganic $NiCo_2O_4$ hybrid nanomaterials for electrochemical immunosensors *ACS applied materials & interfaces*, 3 1366-1373.

Li, W., Wang, J., Liu, T. and Luo, M. 2020b. Electromechanical impedance instrumented circular piezoelectric-metal transducer for corrosion monitoring: modeling and validation. *Smart Materials and Structures*, 29 (3): 035008-035021.

Li, Y., Liu, D., Zhu, C., Shen, X., Liu, Y. and You, T. 2020c. Sensitivity programmable ratiometric electrochemical aptasensor based on signal engineering for the detection of aflatoxin B1 in peanut. *Journal of hazardous materials*, 387: 122001-122008.

Li, Z., Ye, Z., Fu, Y., Xiong, Y. and Li, Y. 2016. A portable electrochemical immunosensor dor rapid detection of trace aflatoxin B_1 in rice. *Analytical Methods*, 8 (3): 548-553.

Liaqat, M., Riaz, S., Nawaz, M. H., Badea, M., Hayat, A. and Marty, J. L. 2021. Fabrication of electro-active nano-trans surfaces to design label free electrochemical aptasensor for ochratoxin A detection. *Electrochimica Acta*, 379: 138172-132180.

Limonciel, A. and Jennings, P. 2014. A review of the evidence that ochratoxin A is an Nrf2 inhibitor: implications for nephrotoxicity and renal carcinogenicity. *Toxins*, 6 (1): 371-379.

Liu, H., Zhang, X. H., Li, Y. X., Li, X., Dong, C. K., Wu, D. Y., Tang, C. C., Chou, S. L., Fang, F. and Du, X. W. 2020a. Conductive boron nitride as promising catalyst support for the oxygen evolution reaction. *Advanced Energy Materials*, 10 (25): 1902521-1902527.

Liu, H., Zhao, P., Wang, Y., Li, S., Zhang, L., Zhang, Y., Ge, S. and Yu, J. 2020b. based sandwich type SERS sensor based on silver nanoparticles and biomimetic recognizer. *Sensors and Actuators B: Chemical*, 313: 127989-127997.

Liu, R., Li, W., Cai, T., Deng, Y., Ding, Z., Liu, Y., Zhu, X., Wang, X., Liu, J. and Liang, B. 2018a. TiO2 nanolayer-enhanced fluorescence for simultaneous multiplex mycotoxin detection by aptamer microarrays on a porous silicon surface. *ACS applied materials & interfaces*, 10 (17): 14447-14453.

Liu, S.-H., Wen, B.-Y., Lin, J.-S., Yang, Z.-W., Luo, S.-Y. and Li, J.-F. 2020c. Rapid and Quantitative Detection of Aflatoxin B1 in Grain by Portable Raman Spectrometer. *Applied Spectroscopy*, 74 (11): 1365-1373.

Liu, S., Wang, Y., Xu, W., Leng, X., Wang, H., Guo, Y. and Huang, J. 2017a. A novel sandwich-type electrochemical aptasensor based on GR-3D Au and aptamer-AuNPs-HRP for sensitive detection of oxytetracycline. *Biosensors and Bioelectronics*, 88: 181-187.

Liu, S., Xing, X., Yu, J., Lian, W., Li, J., Cui, M. and Huang, J. 2012. A novel label-free electrochemical aptasensor based on graphene–polyaniline composite film for dopamine determination. *Biosensors and Bioelectronics*, 36 (1): 186-191.

Liu, X., Shi, D., Zhou, S., Liu, H., Liu, H. and Yao, X. 2018b. Molecular dynamics simulations and novel drug discovery. *Expert opinion on drug discovery*, 13 (1): 23-37.

Liu, Y., Yu, J., Wang, Y., Liu, Z. and Lu, Z. 2016. An ultrasensitive aptasensor for detection of Ochratoxin A based on shielding effect-induced inhibition of fluorescence resonance energy transfer. *Sensors and Actuators B: Chemical*, 222: 797-803.

Liu, Z., Liu, Y., Zeng, G., Shao, B., Chen, M., Li, Z., Jiang, Y., Liu, Y., Zhang, Y. and Zhong, H. 2018c. Application of molecular docking for the degradation of organic pollutants in the environmental remediation: A review. *Chemosphere*, 203: 139-150.

Liu, Z., Wu, H.-L., Xie, L.-X., Hu, Y., Fang, H., Sun, X.-D., Wang, T., Xiao, R. and Yu, R.-Q. 2017b. Chemometrics-enhanced liquid chromatography-full scan-mass spectrometry for interference-free analysis of multi-class mycotoxins in complex cereal samples. *Chemometrics and Intelligent Laboratory Systems*, 160: 125-138.

Lopa, N. S., Rahman, M. M., Ahmed, F., Ryu, T., Sutradhar, S. C., Lei, J., Kim, J., Kim, D. H., Lee, Y. H. and Kim, W. 2019. Simple, low-cost, sensitive and label-free aptasensor for the detection of cardiac troponin I based on a gold nanoparticles modified titanium foil. *Biosensors and Bioelectronics*, 126: 381-388.

Lou, S., Ye, J.-y., Li, K.-q. and Wu, A. 2011. A Gold nanoparticles-based immunochromatogaphic assay: The infuance of nanoparticle size. *Analyst*, 137 (5): 1174-1181.

Lu, L., Seenivasan, R., Wang, Y.-C., Yu, J.-H. and Gunasekaran, S. 2016. An electrochemical immunosensor for rapid and sensitive detection of mycotoxins fumonisin B1 and deoxynivalenol. *Electrochimica Acta*, 213: 89-97.

Lu, L., Yuan, W., Xiong, Q., Wang, M., Liu, Y., Cao, M. and Xiong, X. 2021a. One-step grain pretreatment for ochratoxin A detection based on bipolar electrode-electrochemiluminescence biosensor. *Analytica chimica acta*, 1141: 83-90.

Lu, S., Wang, H., Zhou, J., Wu, X. and Qin, W. 2017. Atomic layer deposition of ZnO on carbon black as nanostructured anode materials for high-performance lithium-ion batteries. *Nanoscale*, 9 (3): 1184-1192.

Lu, T., Peng, H., Zhong, L., Wu, P., He, J., Deng, Z. and Huang, Y. 2021b. The Tree Shrew as a Model for Cancer Research. *Frontiers in Oncology*, 11: 660-669.

Luczkowska, K., Stekelenburg, C., Sloan-Béna, F., Ranza, E., Gastaldi, G., Schwitzgebel, V. and Maechler, P. 2020. Hyperinsulinism associated with GLUD1 mutation: allosteric regulation and functional characterization of p. G446V glutamate dehydrogenase. *Human genomics*, 14 (1): 1-8.

Lunghi, A. and Sanvito, S. 2019. A unified picture of the covalent bond within quantum-accurate force fields: From organic molecules to metallic complexes' reactivity. *Science advances*, 5 (5): eaaw2210- eaaw2217.

Luo, Z., Sun, D., Tong, Y., Zhong, Y. and Chen, Z. 2019. DNA nanotetrahedron linked dual-aptamer based voltammetric aptasensor for cardiac troponin I using a magnetic metal-organic framework as a label. *Microchimica Acta*, 186 (6): 1-10.

Lv, L., Cui, C., Liang, C., Quan, W., Wang, S. and Guo, Z. 2016. Aptamer-based single-walled carbon nanohorn sensors for ochratoxin A detection. *Food control*, 60: 296-301.

Lv, Z., He, S., Wang, Y. and Zhu, X. 2021. Noble Metal Nanomaterials for NIR-Triggered Photothermal Therapy in Cancer. *Advanced Healthcare Materials*, 10 (6): 2001806-2001822.

Ma, H., Sun, J., Zhang, Y. and Xia, S. 2016. Disposable amperometric immunosensor for simple and sensitive determination of aflatoxin B1 in wheat. *Biochemical Engineering Journal* 115: 38-46.

Maghsoudi, A. S., Hassani, S., Rezael Akmal, M., Ganjali, M. R., Mirnia, K., Norouzi, P. and Abdollahi, M. 2020. An electrochemical aptasensor platform based on flower-like gold microstructure-modified screen-printed carbon electrode for detection of serpin A 12 as a type 2 diabetes biomarker. *International Journal of Nanomedicine*, 15: 2219-2230.

Mahato, D. K., Lee, K. E., Kamle, M., Devi, S., Dewangan, K. N., Kumar, P. and Kang, S. G. 2019. Aflatoxins in food and feed: an overview on prevalence, detection and control strategies. *Frontiers in microbiology*, 10: 2266-2275.

Mahfuz, M., Gazi, M. A., Hossain, M., Islam, M. R., Fahim, S. M. and Ahmed, T. 2018. General and advanced methods for the detection and measurement of aflatoxins and aflatoxin metabolites: a review. *Toxin Reviews*, 39 (2): 123-137.

Mahshid, S., Mepham, A. H., Mahshid, S. S., Burgess, I. B., Saberi Safaei, T., Sargent, E. H. and Kelley, S. O. 2016. Mechanistic control of the growth of three-dimensional gold sensors. *The Journal of Physical Chemistry C*, 120 (37): 21123-21132.

Malas, A., Bharati, A., Verkinderen, O., Goderis, B., Moldenaers, P. and Cardinaels, R. 2017. Effect of the GO reduction method on the dielectric properties, electrical conductivity and crystalline behavior of PEO/rGO nanocomposites. *Polymers*, 9 (11): 613-633.

Malik, P. and Bhushan, R. 2018. Thin Layer Chromatographic Resolution of Some β-adrenolytics and a β 2-Agonist Using Bovine Serum Albumin as Chiral Additive in Stationary Phase. *Journal of chromatographic science*, 56 (1): 92-98.

Malir, F., Ostry, V., Pfohl-Leszkowicz, A., Malir, J. and Toman, J. 2016. Ochratoxin A: 50 years of research. *Toxins*, 8 (7): 191-239.

Malir, F., Ostry, V., Pfohl-Leszkowicz, A. and Novotna, E. 2013. Ochratoxin A: Developmental and reproductive toxicity—An overview. *Birth Defects Research Part B: Developmental and Reproductive Toxicology*, 98 (6): 493-502.

Mally, A. 2012. Ochratoxin A and mitotic disruption: mode of action analysis of renal tumor formation by ochratoxin A. *Toxicological Sciences*, 127 (2): 315-330.

Malvano, F., Albanese, D., Pilloton, R. and Matteo, M. D. 2016. A highly sensitive impedimetric label free immunosensor for Ochratoxin measurement in cocoa beans. *Food chemistry*, 212 688-694.

Malygin, A. A., Drozd, V. E., Malkov, A. A. and Smirnov, V. M. 2015. From VB Aleskovskii's "Framework" hypothesis to the method of molecular layering/atomic layer deposition. *Chemical Vapor Deposition*, 21 (10-11-12): 216-240.

Mananghaya, M. R. 2019. Titanium-decorated boron nitride nanotubes for hydrogen storage: a multiscale theoretical investigation. *Nanoscale*, 11 (34): 16052-16062.

Mannaa, M. and Kim, K. D. 2017. Influence of temperature and water activity on deleterious fungi and mycotoxin production during grain storage. *Mycobiology*, 45 (4): 240-254.

Marchese, S., Polo, A., Ariano, A., Velotto, S., Costantini, S. and Severino, L. 2018. Aflatoxin B1 and M1: Biological properties and their involvement in cancer development. *Toxins*, 10 (6): 214-232.

Marijani, E., Charo-Karisa, H., Kigadye, E. and Okoth, S. 2020. Occurrence and Exposure Assessment of Aflatoxin B1 in Omena (Rastrineobola argentea) from Kenya. *Journal of Food Quality*, 2020: 8823340. Available: https://www.hindawi.com/journals/jfq/2020/8823340/ (Accessed 15 October 2020).

Marin, S., Ramos, A., Cano-Sancho, G. and Sanchis, V. 2013. Mycotoxins: Occurrence, toxicology, and exposure assessment. *Food and Chemical Toxicology*, 60: 218-237.

Masurkar, N., Thangavel, N. K., Yurgelevic, S., Varma, S., Auner, G. W. and Arava, L. M. R. 2021. Reliable and highly sensitive biosensor from suspended MoS2 atomic layer on nano-gap electrodes. *Biosensors and Bioelectronics*, 172: 112724-112732.

Mehri, F., Esfahani, M., Heshmati, A., Jenabi, E. and Khazaei, S. 2020. The prevalence of ochratoxin A in dried grapes and grape-derived products: a systematic review and meta-analysis. *Toxin Reviews*: 1-10.

Mishra, R. K., Hayat, A., Catanante, G., Istamboulie, G. and Marty, J.-L. 2016. Sensitive quantitation of Ochratoxin A in cocoa beans using differential pulse voltammetry based aptasensor. *Food chemistry*, 192: 799-804.

Moghtada, A., Shahrouzianfar, A. and Ashiri, R. 2017. Low-temperature ultrasound synthesis of nanocrystals CoTiO3 without a calcination step: effect of ultrasonic waves on formation of the crystal growth mechanism. *Advanced Powder Technology*, 28 (4): 1109-1117.

Mohammadi, H. 2011. A review of aflatoxin M1, milk, and milk products. *Aflatoxins-Biochemistry and Molecular Biology; InTech: Houston, TX, USA*: 397-414.

Mokhena, T. C., John, M., Sibeko, M., Agbakoba, V., Mochane, M., Mtibe, A., Mokhothu, T., Motsoeneng, T., Phiri, M. and Phiri, M. 2020. Nanomaterials: Types, synthesis and characterization. In: *Nanomaterials in Biofuels Research*. Springer, 115-141.

Moldoveanu, S. and David, V. 2016. *Selection of the HPLC method in chemical analysis*. Britain: Elsevier Science. Available: https://books.google.co.za/books?id=mky0DAAAQBAJ (Accessed 15 July 2020).

Molinero-Fernández, Á., Jodra, A., Moreno-Guzmán, M., López, M. Á. and Escarpa, A. 2018. Magnetic reduced graphene oxide/nickel/platinum nanoparticles micromotors for mycotoxin analysis. *Chemistry–A European Journal*, 24 (28): 7172-7176.

Mottaghianpour, E., Nazari, F. and Hosseini, M.-J. 2021. Determination of Aflatoxin B1 Contamination in Wheat and Rice Flour Collected from Iranian Market Using Simple and Reliable HPLC Method. *Journal of Food and Nutrition Research*, 9 (1): 50-54.

Mousavi Khaneghah, A., Eş, I., Raeisi, S. and Fakhri, Y. 2018. Aflatoxins in cereals: State of the art. *Journal of Food Safety*, 38 (6): e12532-e12538.

Muhammad, H., Tahiri, I. A., Muhammad, M., Masood, Z., Versiani, M. A., Khaliq, O., Latif, M. and Hanif, M. 2016. A comprehensive heterogeneous electron transfer rate constant evaluation of dissolved oxygen in DMSO at glassy carbon electrode measured by different electrochemical methods. *Journal of Electroanalytical Chemistry*, 775: 157-162.

Mulchandani, A. 2011. Microbial biosensors for organophosphate pesticides. *Applied biochemistry and biotechnology*, 165 (2): 687-699.

Muñoz, J., Montes, R. and Baeza, M. 2017. Trends in electrochemical impedance spectroscopy involving nanocomposite transducers: Characterization, architecture surface and bio-sensing. *TrAC Trends in Analytical Chemistry*, 97: 201-215.

Mupunga, I., Lebelo, S. L., Mngqawa, P., Rheeder, J. and Katerere, D. R. 2014. Natural occurrence of aflatoxins in peanuts and peanut butter from Bulawayo, Zimbabwe. *Journal of Food Protection*, 77 (10): 1814-1818.

Murashiki, T. C., Chidewe, C., Benhura, M. A., Maringe, D. T., Dembedza, M. P., Manema, L. R., Mvumi, B. M. and Nyanga, L. K. 2017. Levels and daily intake estimates of aflatoxin B1 and fumonisin B1 in maize consumed by rural households in Shamva and Makoni districts of Zimbabwe. *Food control*, 72: 105-109.

Nabila, M. I. and Kannabiran, K. 2018. Biosynthesis, characterization and antibacterial activity of copper oxide nanoparticles (CuO NPs) from actinomycetes. *Biocatalysis and agricultural biotechnology*, 15: 56-62.

Naidoo, L., Suvardhan, K., Sabela, M. I. and Bisetty, K. 2020. Multivariate optimization of field-flow fractionation of nanoscale synthetic amorphous silica in processed foods supported by computational modelling. *New Journal of Chemistry*, 44 (40): 17542-17551.

Nantaphol, S., Chailapakul, O. and Siangproh, W. 2015. Sensitive and selective electrochemical sensor using silver nanoparticles modified glassy carbon electrode for determination of cholesterol in bovine serum. *Sensors and Actuators B: Chemical*, 207: 193-198.

Narváez, A., Rodríguez-Carrasco, Y., Castaldo, L., Izzo, L. and Ritieni, A. 2020. Ultra-high-performance liquid chromatography coupled with quadrupole Orbitrap high-resolution mass spectrometry for multi-residue analysis of mycotoxins and pesticides in botanical nutraceuticals. *Toxins*, 12 (2): 114-129.

Naseem, T. and Farrukh, M. A. Antibacterial Activity of Green Synthesis of Iron Nanoparticles Using Lawsonia inermis and Gardenia jasminoides leaves extract. *Journal of Chemistry*, 2015: 912342. Available: https://www.hindawi.com/journals/jchem/2015/912342/ (Accessed 3 May 2021).

Navale, S., Yang, Z., Liu, C., Cao, P., Patil, V., Ramgir, N., Mane, R. and Stadler, F. 2018. Enhanced acetone sensing properties of titanium dioxide nanoparticles with a sub-ppm detection limit. *Sensors and Actuators B: Chemical*, 255: 1701-1710.

Nayebi, B., Rabiee, N., Nayebi, B., Asl, M. S., Ramakrishna, S., Jang, H. W., Varma, R. S. and Shokouhimehr, M. 2020. Boron nitride-palladium nanostructured catalyst: efficient reduction of nitrobenzene derivatives in water. *Nano Express*, 1 (3): 030012-030023.

Nazari, M., Kashanian, S., Rafipour, R. and Omidfar, K. 2019. Biosensor design using an electroactive label-based aptamer to detect bisphenol A in serum samples. *Journal of biosciences*, 44 (4): 1-10.

Nazhand, A., Durazzo, A., Lucarini, M., Souto, E. B. and Santini, A. 2020. Characteristics, occurrence, detection and detoxification of aflatoxins in foods and feeds. *Foods*, 9 (5): 644-669.

Ndagijimana, R., Shahbaz, U. and Sun, X. 2020. Aflatoxin B1 in food and feed: an overview on prevalence, determination and control tactics. *JAIR*, 8: 144-152.

Nganou, N., Tchinda, E., Noumo, T., Mouafo, H., Sokamte, A. and Tatsadjieu, L. 2020. Fungal Diversity and Evaluation of Ochratoxin A Content of Coffee from Three Cameroonian Regions.

Journal of Food Quality, 2020: 8884514. Available: https://www.hindawi.com/journals/jfq/2020/8884514/ (Accessed 4 March 2021).

Nguyen, H. H., Lee, S. H., Lee, U. J., Fermin, C. D. and Kim, M. 2019. Immobilized enzymes in biosensor applications. *Materials*, 12 (1): 121-154.

Niederberger, M. and Pinna, N. 2009. *Metal oxide nanoparticles in organic solvents: synthesis, formation, assembly and application*. 1st ed. London: Springer Science & Business Media.Springer Science & Business Media.

Nleya, N., Adetunji, M. C. and Mwanza, M. 2018. Current status of mycotoxin contamination of food commodities in Zimbabwe. *Toxins*, 10 (5): 89-100.

Noble, M. I. 2017. Commentary: The number of Electrons in the Nernst Equation: Energetic Considerations. *Open J Cardiatic Res*, 1 (2): 000502-000504.

Novoselov, K. S., Geim, A. K., Morozov, S. V., Jiang, D., Zhang, Y., Dubonos, S. V., Grigorieva, I. V. and Firsov, A. A. 2004. Electric field effect in atomically thin carbon films. *science*, 306 (5696): 666-669.

Obot, I., Macdonald, D. and Gasem, Z. 2015. Density functional theory (DFT) as a powerful tool for designing new organic corrosion inhibitors. Part 1: an overview. *Corrosion Science*, 99: 1-30.

Oliveira, G., Evangelista, S. R., Passamani, F. R. F., Santiago, W. D., das Graças Cardoso, M. and Batista, L. R. 2019. Influence of temperature and water activity on Ochratoxin A production by Aspergillus strain in coffee south of Minas Gerais/Brazil. *LWT*, 102: 1-7.

Olsson, J., Börjesson, T., Lundstedt, T. and Schnürer, J. 2002. Detection and quantification of ochratoxin A and deoxynivalenol in barley grains by GC-MS and electronic nose. *International Journal of Food Microbiology*, 72 (3): 203-214.

Omotayo, O. P., Omotayo, A. O., Babalola, O. O. and Mwanza, M. 2019. Comparative study of aflatoxin contamination of winter and summer ginger from the North West Province of South Africa. *Toxicology reports*, 6: 489-495.

Organization, W. H. and Cancer, I. A. f. R. o. 1993. Some naturally occurring substances: food items and constituents, heterocyclic aromatic amines and mycotoxins. Paper presented at the *IARC Monographs on the Evaluation of the Carcinogenic Risk of Chemicals to Humans*. Lyon, France, 9-16 June 1992. Geneva, Switzerland: World Health Organization, Available: https://www.ncbi.nlm.nih.gov/books/NBK513574/ (Accessed 10 May 2021).

Orlandi, C., Deredge, D., Ray, K., Gohain, N., Tolbert, W., DeVico, A. L., Wintrode, P., Pazgier, M. and Lewis, G. K. 2020. Antigen-Induced Allosteric Changes in a Human IgG1 Fc Increase Low-Affinity Fcγ Receptor Binding. *Structure*, 28 (5): 516-527.

Oteiza, J. M., Khaneghah, A. M., Campagnollo, F. B., Granato, D., Mahmoudi, M. R., Sant'Ana, A. S. and Gianuzzi, L. 2017. Influence of production on the presence of patulin and ochratoxin A in fruit juices and wines of Argentina. *LWT*, 80: 200-207.

Owumi, S., Najophe, E. S., Farombi, E. O. and Oyelere, A. K. 2020. Gallic acid protects against Aflatoxin B1-induced oxidative and inflammatory stress damage in rats kidneys and liver. *Journal of Food Biochemistry*, 44 (8): e13316-e13327.

Pagadala, N. S., Syed, K. and Tuszynski, J. 2017. Software for molecular docking: a review. *Biophysical reviews*, 9 (2): 91-102.

Paleico, M. L. and Behler, J. 2020. A flexible and adaptive grid algorithm for global optimization utilizing basin hopping Monte Carlo. *The Journal of chemical physics*, 152 (9): 094109-094122.

Pan, M., Yang, J., Liu, K., Yin, Z., Ma, T., Liu, S., Xu, L. and Wang, S. 2020. Noble metal nanostructured materials for chemical and biosensing systems. *Nanomaterials*, 10 (2): 209-233.

Pang, X., Cui, C., Wan, S., Jiang, Y., Zhang, L., Xia, L., Li, L., Li, X. and Tan, W. 2018. Bioapplications of cell-SELEX-generated aptamers in cancer diagnostics, therapeutics, theranostics and biomarker discovery: a comprehensive review. *Cancers*, 10 (2): 47-64.

Panhwar, S., Hassan, S. S., Mahar, R. B., Canlier, A., Uddin, S. and Arain, M. 2018. Synthesis of l-Cysteine Capped Silver Nanoparticles in Acidic Media at Room Temperature and Detailed Characterization. *Journal of Inorganic and Organometallic Polymers and Materrials*, 28 (3): 863-870.

Paosen, S., Saising, J., Septama, A. W. and Voravuthikunchai, S. P. 2017. Green synthesis of silver nanoparticles using plants from Myrtaceae family and characterization of their antibacterial activity. *Materials Letters*, 209: 201-206.

Parashar, M., Shukla, V. K. and Singh, R. 2020. Metal oxides nanoparticles via sol–gel method: A review on synthesis, characterization and applications. *Journal of Materials Science: Materials in Electronics*, 31 (5): 3729-3749.

Patel, S. V., Bosamia, T. C., Bhalani, H. N., Singh, P. and Kumar, A. 2015. Aflatoxins: Causes and effects. *Journal of Agricultural and Biological Sciences*, 13 (9): 140-141.

Patil, S. B., Basavarajappa, P. S., Ganganagappa, N., Jyothi, M., Raghu, A. and Reddy, K. R. 2019. Recent advances in non-metals-doped TiO2 nanostructured photocatalysts for visible-light driven

hydrogen production, CO2 reduction and air purification. *International Journal of Hydrogen Energy*, 44 (26): 13022-13039.

Pelaez, M., Nolan, N. T., Pillai, S. C., Seery, M. K., Falaras, P., Kontos, A. G., Dunlop, P. S., Hamilton, J. W., Byrne, J. A. and O'shea, K. 2012. A review on the visible light active titanium dioxide photocatalysts for environmental applications. *Applied Catalysis B: Environmental*, 125: 331-349.

Peng, H., Hui, Y., Ren, R., Wang, B., Song, S., He, Y. and Zhang, F. 2019. A sensitive electrochemical aptasensor based on MB-anchored GO for the rapid detection of Cronobacter sakazakii. *Journal of Solid State Electrochemistry*, 23 (12): 3391-3398.

Pereira, C. S., Cunha, S. C. and Fernandes, J. O. 2020. Validation of an Enzyme-Linked Immunosorbent Assay (ELISA) Test Kit for Determination of Aflatoxin B 1 in Corn Feed and Comparison with Liquid-Chromatography Tandem Mass Spectrometry (LC-MS/MS) Method. *Food Analytical Methods*, 13 (9): 1806-1816.

Pereira, V., Fernandes, J. and Cunha, S. 2014. Mycotoxins in cereals and related foodstuffs: A review on occurrence and recent methods of analysis. *Trends in Food Science & Technology*, 36 (2): 96-136.

Pérez-Fernández, B., Mercader, J. V., Checa-Orrego, B. I., de la Escosura-Muñiz, A. and Costa-García, A. 2019. A monoclonal antibody-based immunosensor for the electrochemical detection of imidacloprid pesticide. *Analyst*, 144 (9): 2936-2941.

Pilehvar, S., Dierckx, T., Blust, R., Breugelmans, T. and De Wael, K. 2014. An electrochemical impedimetric aptasensing platform for sensitive and selective detection of small molecules such as chloramphenicol. *Sensors*, 14 (7): 12059-12069.

Pitt, J., Taniwaki, M. H. and Cole, M. 2013. Mycotoxin production in major crops as influenced by growing, harvesting, storage and processing, with emphasis on the achievement of Food Safety Objectives. *Food control*, 32 (1): 205-215.

Pohanka, M. 2018. Overview of piezoelectric biosensors, immunosensors and DNA sensors and their applications. *Materials*, 11 (3): 448-460.

Postupolski, J., Starski, A., Ledzion, E., Kurpinska-Jaworska, J. and Szczesna, M. 2019. Assessment of changes in the occurrence of Fusarium toxin and ochratoxin A in Poland related to extreme weather phenomena. *Roczniki Państwowego Zakładu Higieny*, 70 (2): 127-135

Pradhan, S. and Ananthanarayan, L. 2020. Standardization and validation of a high-performance thin-layer chromatography method for the quantification of aflatoxin B1 and its application in surveillance of contamination level in marketed food commodities from the Mumbai region. *JPC–Journal of Planar Chromatography–Modern TLC*, 33 (6): 617-630.

Prieto-Simón, B., Campàs, M., Marty, J.-L. and Noguer, T. 2008. Novel highly-performing immunosensor-based strategy for ochratoxin A detection in wine samples. *Biosensors and Bioelectronics*, 23 (7): 995-1002.

Purushothama, H., Nayaka, Y. A., Vinay, M., Manjunatha, P., Yathisha, R. and Basavarajappa, K. 2018. Pencil graphite electrode as an electrochemical sensor for the voltammetric determination of chlorpromazine. *Journal of Science: Advanced Materials and Devices*, 3 (2): 161-166.

Putri, A. D., Murti, B. T., Kanchi, S., Sabela, M. I., Bisetty, K., Tiwari, A. and Asiri, A. M. 2019. Computational studies on the molecular insights of aptamer induced poly (N-isopropylacrylamide)-graft-graphene oxide for on/off-switchable whole-cell cancer diagnostics. *Scientific reports*, 9 (1): 1-14.

Puvača, N., Bursić, V., Petrović, A., Prodanović, R., Kharud, M. M., Obućinski, D., Vuković, G. and Marić, M. 2019. Influence of tea tree essential oil on the synthesis of mycotoxins: Ochratoxin A. *Maced. J. Anim. Sci*, 9: 25-29.

Qi, D., Fei, T., Liu, H., Yao, H., Wu, D. and Liu, B. 2017. Development of multiple heart-cutting two-dimensional liquid chromatography coupled to quadrupole-orbitrap high resolution mass spectrometry for simultaneous determination of aflatoxin B1, B2, G1, G2, and ochratoxin A in snus, a smokeless tobacco product. *Journal of agricultural and food chemistry*, 65 (45): 9923-9929.

Qi, N., Yu, H., Yang, C., Gong, X., Liu, Y. and Zhu, Y. 2019. Aflatoxin B1 in peanut oil from Western Guangdong, China, during 2016–2017. *Food Additives & Contaminants: Part B*, 12 (1): 45-51.

Qu, L.-L., Jia, Q., Liu, C., Wang, W., Duan, L., Yang, G., Han, C.-Q. and Li, H. 2018. Thin layer chromatography combined with surface-enhanced raman spectroscopy for rapid sensing aflatoxins. *Journal of chromatography A*, 1579: 115-120.

Quan, X., Xu, H., Sun, B. and Xiao, Z. 2018. Anode modification with palladium nanoparticles enhanced Evans Blue removal and power generation in microbial fuel cells. *International biodeterioration & biodegradation*, 132: 94-101.

Radi, A.-E., Munoz-Berbel, X., Lates, V. and Marty, J.-L. 2009. Label-free impedimetric immunosensor for sensitive detection of ochratoxin A *Biosensors and Bioelectronics*, 24: 1888-1892.

Rane, A. V., Kanny, K., Abitha, V. and Thomas, S. 2018. Methods for synthesis of nanoparticles and fabrication of nanocomposites. In: *Synthesis of inorganic nanomaterials*. Elsevier, 121-139.

Rani, P., Kumar, V., Singh, P. P., Matharu, A. S., Zhang, W., Kim, K.-H., Singh, J. and Rawat, M. 2020. Highly stable AgNPs prepared via a novel green approach for catalytic and photocatalytic removal of biological and non-biological pollutants. *Environment International*, 143: 105924-105936.

Rastegar, H., Shoeibi, S., Yazdanpanah, H., Amirahmadi, M., Khaneghah, A. M., Campagnollo, F. B. and Sant'Ana, A. S. 2017. Removal of aflatoxin B1 by roasting with lemon juice and/or citric acid in contaminated pistachio nuts. *Food control*, 71: 279-284.

Raza, M. A., Kanwal, Z., Rauf, A., Sabri, A. N., Riaz, S. and Naseem, S. 2016. Size-and shape-dependent antibacterial studies of silver nanoparticles synthesized by wet chemical routes. *Nanomaterials*, 6 (4): 74-88.

Reimers, J. R., Sajid, A., Kobayashi, R. and Ford, M. J. 2018. Understanding and calibrating density-functional-theory calculations describing the energy and spectroscopy of defect sites in hexagonal boron nitride. *Journal of chemical theory and computation*, 14 (3): 1602-1613.

Ren, G., Hu, Y., Zhang, J., Zou, L. and Zhao, G. 2018a. Determination of multi-class mycotoxins in tartary buckwheat by ultra-fast liquid chromatography coupled with triple quadrupole mass spectrometry. *Toxins*, 10 (1): 28-38.

Ren, X., Lu, P., Feng, R., Zhang, T., Zhang, Y., Wu, D. and Wei, Q. 2018b. An ITO-based point-of-care colorimetric immunosensor for ochratoxin A detection. *Talanta*, 188: 593-599.

Reyneri, A. 2006. The role of climatic condition on micotoxin production in cereal. *Veterinary research communications*, 30 (1): 87-92.

Rivas, L., Mayorga-Martinez, C. C., Quesada-González, D., Zamora-Gálvez, A., de la Escosura-Muñiz, A. and Merkoçi, A. 2015. Label-free impedimetric aptasensor for ochratoxin-A detection using iridium oxide nanoparticles. *Analytical chemistry*, 87 (10): 5167-5172.

Rizwan, M., Elma, S., Lim, S. A. and Ahmed, M. U. 2018. AuNPs/CNOs/SWCNTs/chitosan-nanocomposite modified electrochemical sensor for the label-free detection of carcinoembryonic antigen. *Biosensors and Bioelectronics*, 107: 211-217.

Rojas, L. M., Qu, Y. and He, L. 2021. A facile solvent extraction method facilitating surface-enhanced Raman spectroscopic detection of ochratoxin A in wine and wheat. *Talanta*, 224: 121792-121797.

Rong, C., Wang, B., Zhao, D. and Liu, S. 2020. Information-theoretic approach in density functional theory and its recent applications to chemical problems. *Wiley Interdisciplinary Reviews: Computational Molecular Science*, 10 (4): e1461-e1482.

Rosado, G., Valenzuela-Muñiz, A. M., Miki-Yoshida, M. and Gómez, Y. V. 2020. Facile method to obtain anatase and anatase-brookite nanoparticles (TiO2) with MWCNT towards reducing the bandgap. *Diamond and Related Materials*, 109: 108015-108026.

Roy, I., Sarkar, G., Mondal, S., Rana, D., Bhattacharyya, A., Saha, N. R., Adhikari, A., Khastgir, D., Chattopadhyay, S. and Chattopadhyay, D. 2016. Synthesis and characterization of graphene from waste dry cell battery for electronic applications. *RSC Advances*, 6 (13): 10557-10564.

Rubert, J., Soriano, J. M., Mañes, J. and Soler, C. 2013. Occurrence of fumonisins in organic and conventional cereal-based products commercialized in France, Germany and Spain. *Food and Chemical Toxicology*, 56: 387-391.

Rushing, B. R. and Selim, M. I. 2017. Structure and oxidation of pyrrole adducts formed between aflatoxin B2a and biological amines. *Chemical research in toxicology*, 30 (6): 1275-1285.

Rushing, B. R. and Selim, M. I. 2019. Aflatoxin B1: A review on metabolism, toxicity, occurrence in food, occupational exposure, and detoxification methods. *Food and Chemical Toxicology*, 124: 81-100.

Saberi, Z., Rezaei, B. and Ensafi, A. A. 2019. Fluorometric label-free aptasensor for detection of the pesticide acetamiprid by using cationic carbon dots prepared with cetrimonium bromide. *Microchimica Acta*, 186 (5): 1-7.

Saha, A., Gajbhiye, N. A., Basak, B. B. and Manivel, P. 2018. High-performance liquid chromatography tandem mass spectrometry for simultaneous detection of aflatoxins B1, B2, G1 and G2 in Indian medicinal herbs using QuEChERS-based extraction procedure. *International Journal of Environmental Analytical Chemistry*, 98 (7): 622-643.

Saldan, I., Semenyuk, Y., Marchuk, I. and Reshetnyak, O. 2015. Chemical synthesis and application of palladium nanoparticles. *Journal of Materials Science*, 50 (6): 2337-2354.

Saleh, T. A. 2020. Nanomaterials: Classification, properties, and environmental toxicities. *Environmental Technology & Innovation*: 101067-101082.

Sanati, A., Jalali, M., Raeissi, K., Karimzadeh, F., Kharaziha, M., Mahshid, S. S. and Mahshid, S. 2019. A review on recent advancements in electrochemical biosensing using carbonaceous nanomaterials. *Microchimica Acta*, 186 (12): 1-22.

Santos, A. O., Vaz, A., Rodrigues, P., Veloso, A. C., Venâncio, A. and Peres, A. M. 2019. Thin films sensor devices for mycotoxins detection in foods: Applications and challenges. *Chemosensors*, 7 (1): 3-25.

Sarker, Y. A., Hasan, M. M., Paul, T. K., Rashid, S. Z., Alam, M. N. and Sikder, M. H. 2018. Screening of antibiotic residues in chicken meat in Bangladesh by thin layer chromatography. *Journal of Advanced Veterinary and Animal Research*, 5 (2): 140-145.

Sasaki, K. and Yamashita, T. 2021. Modification and Validation of the DREIDING Force Field for Molecular Liquid Simulations (DREIDING-UT). *Journal of chemical information and modeling*, 61 (3): 1172-1179.

Savin, A. V. and Mazo, M. A. 2020. The COMPASS force field: Validation for carbon nanoribbons. *Physica E: Low-dimensional Systems and Nanostructures*, 118: 113937.

Saw, E. N., Grasmik, V., Rurainsky, C., Epple, M. and Tschulik, K. 2016. Electrochemistry at single bimetallic nanoparticles–using nano impacts for sizing and compositional analysis of individual AgAu alloy nanoparticles. *Faraday discussions*, 193: 327-338.

Sayadi, M. H., Salmani, N., Heidari, A. and Rezaei, M. R. 2018. Bio-synthesis of palladium nanoparticle using Spirulina platensis alga extract and its application as adsorbent. *Surfaces and Interfaces*, 10: 136-143.

Schlösser, I. and Prange, A. 2019. Effects of selected natural preservatives on the mycelial growth and ochratoxin A production of the food-related moulds Aspergillus westerdijkiae and Penicillium verrucosum. *Food Additives & Contaminants: Part A*, 36 (9): 1411-1418.

Scholz, F. 2011. The anfractuous pathways which led to the development of electrochemical stripping techniques. *Journal of Solid State Electrochemistry*, 15 (7-8): 1509-1521.

Scholz, F. 2015. Voltammetric techniques of analysis: the essentials. *ChemTexts*, 1 (4): 1-24.

Schütz, M. B., Xiao, L., Lehnen, T., Fischer, T. and Mathur, S. 2018. Microwave-assisted synthesis of nanocrystalline binary and ternary metal oxides. *International Materials Reviews*, 63 (6): 341-374.

Schwerdt, G., Holzinger, H., Sauvant, C., Königs, M., Humpf, H.-U. and Gekle, M. 2007. Long-term effects of ochratoxin A on fibrosis and cell death in human proximal tubule or fibroblast cells in primary culture. *Toxicology*, 232 (1-2): 57-67.

Şen, B., Aygün, A., Okyay, T. O., Şavk, A., Kartop, R. and Şen, F. 2018. Monodisperse palladium nanoparticles assembled on graphene oxide with the high catalytic activity and reusability in the dehydrogenation of dimethylamine-borane. *International Journal of Hydrogen Energy*, 43 (44): 20176-20182.

Sengupta, M., Pal, R., Nath, A., Chakraborty, B., Singh, L. M., Das, B. and Ghosh, S. K. 2018. Anticancer efficacy of noble metal nanoparticles relies on reprogramming tumor-associated macrophages through redox pathways and pro-inflammatory cytokine cascades. *Cellular & molecular immunology*, 15 (12): 1088-1090.

Seo, S., Jeong, S., Park, H., Shin, H. and Park, N.-G. 2019. Atomic layer deposition for efficient and stable perovskite solar cells. *Chemical Communications*, 55 (17): 2403-2416.

Serrano, A., Font, G., Mañes, J. and Ferrer, E. 2013. Emerging Fusarium mycotoxins in organic and conventional pasta collected in Spain. *Food and Chemical Toxicology*, 51: 259-266.

Seyedjafarri, S. 2021. Detoxification of Aflatoxin M1 in Milk by Lactic Acid Bacteria. *Asian Journal of Dairy & Food Research*, 40 (1): 30-34.

Shafiei, M., Bradford, J., Khan, H., Piloto, C., Wlodarski, W., Li, Y. and Motta, N. 2018. Low-operating temperature NO2 gas sensors based on hybrid two-dimensional SnS2-reduced graphene oxide. *Applied Surface Science*, 462: 330-336.

Shang, R., Goulas, A., Tang, C. Y., de Frias Serra, X., Rietveld, L. C. and Heijman, S. G. 2017. Atmospheric pressure atomic layer deposition for tight ceramic nanofiltration membranes: Synthesis and application in water purification. *Journal of Membrane Science*, 528: 163-170.

Sharma, A., Ahmed, A., Singh, A., Oruganti, S., Khosla, A. and Arya, S. 2021. Recent advances in tin oxide nanomaterials as electrochemical/chemiresistive sensors. *Journal of the Electrochemical Society*, 168 (2): 027505-027521.

Sharma, G., Kumar, D., Kumar, A., Ala'a, H., Pathania, D., Naushad, M. and Mola, G. T. 2017a. Revolution from monometallic to trimetallic nanoparticle composites, various synthesis methods and their applications: a review. *Materials Science and Engineering: C*, 71: 1216-1230.

Sharma, G., Sharma, A., Kurian, M., Bhavesh, R., Nam, J. and Lee, S. 2014. Green synthesis of silver nanoparticle using myristica fragrans (nutmeg) seed extract and its biological activity. *Digest Journal of Nanomaterials & Biostructures (DJNB)*, 9 (1): 325-332.

Sharma, N., Sharma, V., Jain, Y., Kumari, M., Gupta, R., Sharma, S. and Sachdev, K. 2017b. Synthesis and characterization of graphene oxide (GO) and reduced graphene oxide (rGO) for gas sensing application. In: Proceedings of *Macromolecular Symposia*. Wiley Online Library, 376 (1): 1700006-1700010.

Shende, S., Ingle, A. P., Gade, A. and Rai, M. 2015. Green synthesis of copper nanoparticles by Citrus medica Linn.(Idilimbu) juice and its antimicrobial activity. *World Journal of Microbiology and Biotechnology*, 31 (6): 865-873.

Sherma, J. 2017. Review of thin-layer chromatography in pesticide analysis: 2014–2016. *Journal of Liquid Chromatography & Related Technologies*, 40 (5-6): 226-238.

Shetti, N. P., Malode, S. J., Nayak, D. S., Aminabhavi, T. M. and Reddy, K. R. 2019. Nanostructured silver doped TiO2/CNTs hybrid as an efficient electrochemical sensor for detection of anti-inflammatory drug, cetirizine. *Microchemical Journal*, 150: 104124-104131.

Shi, L., Wang, Z., Yang, G., Yang, H. and Zhao, F. 2020. A novel electrochemical immunosensor for aflatoxin B1 based on Au nanoparticles-poly 4-aminobenzoic acid supported graphene. *Applied Surface Science*, 527: 146934-146939.

Shiau, B.-W., Lin, C.-H., Liao, Y.-Y., Lee, Y.-R., Liu, S.-H., Ding, W.-C. and Lee, J.-R. 2018. The characteristics and mechanisms of Au nanoparticles processed by functional centrifugal procedures. *Journal of Physics and Chemistry of Solids*, 116: 161-167.

Shirman, T., Toops, T. J., Shirman, E., Shneidman, A. V., Liu, S., Gurkin, K., Alvarenga, J., Lewandowski, M. P., Aizenberg, M. and Aizenberg, J. 2021. Raspberry colloid-templated approach for the synthesis of palladium-based oxidation catalysts with enhanced hydrothermal stability and low-temperature activity. *Catalysis Today*, 360: 241-251.

Sholl, D. and Steckel, J. 2009. DFT calculations for surfaces of solids. *Density Functional Theory*: 83-112.

Shtansky, D. V., Firestein, K. L. and Golberg, D. V. 2018. Fabrication and application of BN nanoparticles, nanosheets and their nanohybrids. *Nanoscale*, 10 (37): 17477-17493.

Shukla, S., Kim, D.-H., Chung, S. and Kim, M. 2017. Occurrence of aflatoxins in fermented food products. In: *Fermented Foods in Health and Disease Prevention*. Elsevier, 653-674.

Siddiqui, S., Dai, Z., Stavis, C. J., Zeng, H., Moldovan, N., Hamers, R. J., Carlisle, J. A. and Arumugam, P. U. 2012. A quantitative study of detection mechanism of a label-free impedance biosensor using ultrananocrystalline diamond microelectrode array. *Biosensors and Bioelectronics*, 35: 284-290.

Simão, E. P., Barbieri, G. J. L. S., Andrade, C. A. S. and Oliveira, M. D. L. 2016. Biosensor Based on Cysteine Monolayer and Monoclonal Antibody for Specific Detection of Aflatoxin B_1 in Rice. *J. Braz. Chem. Soc*, 27 (6): 1040-1047.

Singh, B., Singh, P., Singh, K., Sharma, J., Kumar, M., Bala, R., Meena, R., Sharma, S. K. and Kumar, A. 2017. Nanostructured BN–TiO 2 composite with ultra-high photocatalytic activity. *New Journal of Chemistry*, 41 (20): 11640-11646.

Singh, J. and Mehta, A. 2020. Rapid and sensitive detection of mycotoxins by advanced and emerging analytical methods: A review. *Food science & nutrition*, 8 (5): 2183-2204.

Singh, M., Goyal, M. and Devlal, K. 2018. Size and shape effects on the band gap of semiconductor compound nanomaterials. *Journal of Taibah University for Science*, 12 (4): 470-475.

Singh, P., Kim, Y. J., Wang, C., Mathiyalagan, R., El-Agamy Farh, M. and Yang, D. C. 2016. Biogenic silver and gold nanoparticles synthesized using red ginseng root extract, and their applications. *Artificial cells, nanomedicine, and biotechnology*, 44 (3): 811-816.

Smaniotto, A., Mezalira, D. Z., Zapp, E., Gallardo, H. and Vieira, I. C. 2017. Electrochemical immunosensor based on an azo compound for thyroid-stimulating hormone detection. *Microchemical Journal*, 133: 510-517.

Smith, B. R. and Gambhir, S. S. 2017. Nanomaterials for in vivo imaging. *Chemical reviews*, 117 (3): 901-986.

Sneharani, A., Prabhudev, S. and Sachin, H. 2019. Effect of phytochemicals on optical absorption spectra during biogenic synthesis of self-assembled silver nanoparticles and studies relevant to food applications. *Spectroscopy Letters*, 52 (7): 413-422.

Solanki, P. R., Patel, M. K., Ali, M. A. and Malhotra, B. 2015a. A chitosan modified nickel oxide plaform for biosensing applications. *Journal of Materials Chemistry B*, 3 (32): 6698-6708.

Solanki, P. R., Patel, M. K., Ali, M. A. and Malhotra, B. 2015b. A chitosan modified nickel oxide platform for biosensing applications *Journal of Materials Chemistry B*, 3 6698-6708.

Soleymani, L. and Li, F. 2017. *Mechanistic challenges and advantages of biosensor miniaturization into the nanoscale. ACS Sens. 2, 458–467*.

Song, D., Zheng, J., Myung, N. V., Xu, J. and Zhang, M. 2021. Sandwich-type electrochemical immunosensor for CEA detection using magnetic hollow Ni/C@ SiO2 nanomatrix and boronic acid functionalized CPS@ PANI@ Au probe. *Talanta*, 225: 122006-122016.

Song, L., Liu, W., Xin, F. and Li, Y. 2020. " Materials studio" simulation study of the adsorption and polymerization mechanism of sodium silicate on active silica surface at different temperatures. *International Journal of Metalcasting*: 1-8.

Sreenivasan, S. and Berry, V. 2013. How Do the Electrical Properties of Graphene Change with its Functionalization? *Small (Weinheim an der Bergstrasse, Germany)*, 9 (30): 341-350.

Su, W., Kim, S.-E., Cho, M., Nam, J.-D., Choe, W.-S. and Lee, Y. 2013. Selective detection of endotoxin using an impedance aptasensor with electrochemically deposited gold nanoparticles. *Innate immunity*, 19 (4): 388-397.

Sun, C., Liao, X., Huang, P., Shan, G., Ma, X., Fu, L., Zhou, L. and Kong, W. 2020. A self-assembled electrochemical immunosensor for ultra-sensitive detection of ochratoxin A in medicinal and edible malt. *Food chemistry*, 315: 126289-126296.

Sun, W., Meng, Y., Fu, Q., Wang, F., Wang, G., Gao, W., Huang, X. and Lu, F. 2016. High-yield production of boron nitride nanosheets and its uses as a catalyst support for hydrogenation of nitroaromatics. *ACS applied materials & interfaces*, 8 (15): 9881-9888.

Sun, X., Gao, C., Zhang, L., Yan, M., Yu, J. and Ge, S. 2017a. Photoelectrochemical sensor based on molecularly imprinted film modified hierarchical branched titanium dioxide nanorods for chlorpyrifos detection. *Sensors and Actuators B: Chemical*, 251: 1-8.

Sun, Z., Duan, Z., Liu, X., Deng, X. and Tang, Z. 2017b. Development of a nanobody-based competitive dot ELISA for visual screening of ochratoxin A in cereals. *Food Analytical Methods*, 10 (11): 3558-3564.

Suntola, T. and Antson, J. 1977. *Method for producing compound thin films*. United States 4058430. Available: https://patents.google.com/patent/US4058430A/en (Accessed 28 February 2021).

Suresh, L., Brahman, P. K., Reddy, K. R. and Bondili, J. 2018. Development of an electrochemical immunosensor based on gold nanoparticles incorporated chitosan biopolymer nanocomposite film for the detection of prostate cancer using PSA as biomarker. *Enzyme and microbial technology*, 112: 43-51.

Švorc, Ľ., Haššo, M., Sarakhman, O., Kianičkova, K., Stanković, D. M. and Otřísal, P. 2018. A progressive electrochemical sensor for food quality control: Reliable determination of theobromine in chocolate products using a miniaturized boron-doped diamond electrode. *Microchemical Journal*, 142: 297-304.

Syafiuddin, A., Salim, M. R., Beng Hong Kueh, A., Hadibarata, T. and Nur, H. 2017. A review of silver nanoparticles: research trends, global consumption, synthesis, properties, and future challenges. *Journal of the Chinese Chemical Society*, 64 (7): 732-756.

Tabarani, A., Zinedine, A. and Bouchriti, N. 2020. Exposure assessment to ochratoxin A through the intake of three cereal derivatives from the Moroccan market. *Food Research International*, 137: 109464-109470.

Tabrizi, M. A., Ferré-Borrull, J., Kapruwan, P. and Marsal, L. F. 2019. A photoelectrochemical sandwich immunoassay for protein S100β, a biomarker for Alzheimer's disease, using an ITO electrode modified with a reduced graphene oxide-gold conjugate and CdS-labeled secondary antibody. *Microchimica Acta*, 186 (2): 1-9.

Tadyszak, K., Wychowaniec, J. K. and Litowczenko, J. 2018. Biomedical applications of graphene-based structures. *Nanomaterials*, 8 (11): 944-963.

Tagad, C. K., Dugasani, S. R., Aiyer, R., Park, S., Kulkarni, A. and Sabharwal, S. 2013. Green synthesis of silver nanoparticles and their application for the development of optical fiber based hydrogen peroxide sensor. *Sensors and Actuators B: Chemical*, 183: 144-149.

Tai, B., Chang, J., Liu, Y. and Xing, F. 2020. Recent progress of the effect of environmental factors on Aspergillus flavus growth and aflatoxins production on foods. *Food Quality and Safety*, 4 (1): 21-28.

Taib, M., Tan, L. L., Abd Karim, N. H., Ta, G. C., Heng, L. Y. and Khalid, B. 2020. Reflectance aptasensor based on metal salphen label for rapid and facile determination of insulin. *Talanta*, 207: 120321-120329.

Tajik, S., Beitollahi, H. and Biparva, P. 2018. Methyldopa electrochemical sensor based on a glassy carbon electrode modified with Cu/TiO2 nanocomposite. *Journal of the Serbian Chemical Society*, 83 (7-8): 863-874.

Tamileswari, R., Nisha, M. H., Jesurani, S., Kanagesan, S., Hashim, M. and Alexander, S. C. P. 2015. Synthesis of silver nanoparticles using the vegetable extract of raphanus sativus (Radish) and assessment of their antibacterial activity. *Int J Adv Technol Eng Sci*, 3 (5): 207-212.

Taniwaki, M., Teixeira, A., Teixeira, A., Copetti, M. and Iamanaka, B. 2014. Ochratoxigenic fungi and ochratoxin A in defective coffee beans. *Food Research International*, 61: 161-166.

Tarcan, R., Todor-Boer, O., Petrovai, I., Leordean, C., Astilean, S. and Botiz, I. 2020. Reduced graphene oxide today. *Journal of Materials Chemistry C*, 8 (4): 1198-1224.

Taşpınar, H., Elik, A., Kaya, S. and Altunay, N. 2021. Optimization of green and rapid analytical procedure for the extraction of patulin in fruit juice and dried fruit samples by air-assisted natural deep eutectic solvent-based solidified homogeneous liquid phase microextraction using experimental design and computational chemistry approach. *Food chemistry*, 358: 129817-129823.

Tebele, S. M., Gbashi, S., Adebo, O., Changwa, R., Naidu, K. and Njobeh, P. B. 2020. Quantification of multi-mycotoxin in cereals (maize, maize porridge, sorghum and wheat) from Limpopo province of South Africa. *Food Additives & Contaminants: Part A*, 37 (11): 1922-1938.

Thangavel, P., Kannan, R., Ramachandran, B., Moorthy, G., Suguna, L. and Muthuvijayan, V. 2018. Development of reduced graphene oxide (rGO)-isabgol nanocomposite dressings for enhanced vascularization and accelerated wound healing in normal and diabetic rats. *Journal of colloid and interface science*, 517: 251-264.

Thiagarajan, S., Yang, R.-F. and Chen, S.-M. 2009. Palladium nanoparticles modified electrode for the selective detection of catecholamine neurotransmitters in presence of ascorbic acid. *Bioelectrochemistry*, 75 (2): 163-169.

Thipe, V. C., Thatyana, M., Ajayi, F. R., Njobeh, P. B. and Katti, K. V. 2020. Hybrid nanomaterials for detection, detoxification, and management mycotoxins. In: *Multifunctional Hybrid Nanomaterials for Sustainable Agri-Food and Ecosystems*. Elsevier, 271-285.

Ting, W. E., Chang, C.-H., Szonyi, B. and Gizachew, D. 2020. Growth and Aflatoxin B1, B2, G1, and G2 Production by Aspergillus flavus and Aspergillus parasiticus on Ground Flax Seeds (Linum usitatissimum). *Journal of Food Protection*, 83 (6): 975-983.

Tiwari, S., Gupta, N., Malairaman, U. and Shankar, J. 2017a. Anti-aspergillus properties of phytochemicals against aflatoxin producing Aspergillus flavus and Aspergillus parasiticus. *National Academy science letters*, 40 (4): 267-271.

Tiwari, S., Gupta, P. K., Bagbi, Y., Sarkar, T. and Solanki, P. R. 2017b. L-cysteine capped lanthanum hydroxie nanostructures for non-invasive detection of oral cancer biomarker. *Biosensors and Bioelectronics*, 89: 1042-1052.

Tola, M. and Kebede, B. 2016. Occurrence, importance and control of mycotoxins: A review. *Cogent Food & Agriculture*, 2 (1): 1191103.

Tolosa, J., Barba, F. J., Font, G. and Ferrer, E. 2019. Mycotoxin incidence in some fish products: QuEChERS methodology and liquid chromatography linear ion trap tandem mass spectrometry approach. *Molecules*, 24 (3): 527-537.

Tran, L. T., Tran, T. Q., Ho, H. P., Chu, X. T. and Mai, T. A. 2019. Simple label-free electrochemical immunosensor in a microchamber for detecting newcastle disease virus. *Journal of Nanomaterials*, 2019: 3835609. Available: https://www.hindawi.com/journals/jnm/2019/3835609/ (Accessed 10 June 2021).

Tripathy, A., Raichur, A. M., Chandrasekaran, N., Prathna, T. and Mukherjee, A. 2010. Process variables in biomimetic synthesis of silver nanoparticles by aqueous extract of Azadirachta indica (Neem) leaves. *Journal of nanoparticle research*, 12 (1): 237-246.

Tu, J., Torrente-Rodríguez, R. M., Wang, M. and Gao, W. 2020. The era of digital health: A review of portable and wearable affinity biosensors. *Advanced Functional Materials*, 30 (29): 1906713-1906742.

Turner, N. W., Subrahmanyam, S. and Piletsky, S. A. 2009. Analytical methods for determination of mycotoxins: a review. *Analytica chimica acta*, 632 (2): 168-180.

Turner, P. C. 2013. The molecular epidemiology of chronic aflatoxin driven impaired child growth. *Scientifica*, 2013: 152879. Available: https://www.hindawi.com/journals/scientifica/2013/152879/ (Accessed 7 August 2020).

Ulicny, J. and Kozar, T. 2018. Roadmap for Computer-Aided Modeling of Theranostics and Related Nanosystems. In: Proceedings of *EPJ Web of Conferences*. EDP Sciences,173: 05017-05020.

Umadevi, M., Shalini, S. and Bindhu, M. 2012. Synthesis of silver nanoparticle using D. carota extract. *Advances in Natural Sciences: Nanoscience and Nanotechnology*, 3 (2): 025008-025014.

Vaclavikova, M., Malachova, A., Veprikova, Z., Dzuman, Z., Zachariasova, M. and Hajslova, J. 2013. 'Emerging'mycotoxins in cereals processing chains: Changes of enniatins during beer and bread making. *Food chemistry*, 136 (2): 750-757.

VALENTINA, M., Giacomo, L., MICHELE, V., GRAZIA, G., FRANCESCA, P. and LUIGI, I. 2016. Serum levels of ochratoxin A in dogs with chronic kidney disease (CKD): a retrospective study. *Journal of Veterinary Medical Science*: 16-0226.

Van der Merwe, K., Steyn, P., Fourie, L., Scott, D. B. and Theron, J. 1965. Ochratoxin A, a toxic metabolite produced by Aspergillus ochraceus Wilh. *Nature*, 205 (4976): 1112-1113.

Van Egmond, H. 1991. Worldwide regulations for ochratoxin A. *IARC scientific publications*, (115): 331-336.

Varga, E., Fodor, P. and Soros, C. 2021. Multi-mycotoxin LC-MS/MS method validation and its application to fifty-four wheat flours in Hungary. *Food Additives & Contaminants: Part A*: 1-11.

Vaseghi, Z. and Nematollahzadeh, A. 2020. Nanomaterials: Types, Synthesis, and Characterization. *Green Synthesis of Nanomaterials for Bioenergy Applications*: 23-82.

Veerakumar, P., Madhu, R., Chen, S.-M., Veeramani, V., Hung, C.-T., Tang, P.-H., Wang, C.-B. and Liu, S.-B. 2014. Highly stable and active palladium nanoparticles supported on porous carbon for practical catalytic applications. *Journal of Materials Chemistry A*, 2 (38): 16015-16022.

Veisi, H., Azizi, S. and Mohammadi, P. 2018. Green synthesis of the silver nanoparticles mediated by Thymbra spicata extract and its application as a heterogeneous and recyclable nanocatalyst for catalytic reduction of a variety of dyes in water. *Journal of cleaner production*, 170: 1536-1543.

Verma, A. and Mehata, M. S. 2016. Controllable synthesis of silver nanoparticles using Neem leaves and their antimicrobial activity. *Journal of radiation research and applied sciences*, 9 (1): 109-115.

Vettorazzi, A., González-Peñas, E. and de Cerain, A. L. 2014. Ochratoxin A kinetics: A review of analytical methods and studies in rat model. *Food and Chemical Toxicology*, 72: 273-288.

Victorious, A., Saha, S., Pandey, R., Didar, T. F. and Soleymani, L. 2019. Affinity-based detection of biomolecules using photo-electrochemical readout. *Frontiers in chemistry*, 7: 617-640.

Vieira, T., Cunha, S. and Casal, S. 2015. Analysis of the mycotoxin Ochratoxin A in coffee. In: *Coffee in Health and Disease Prevention*. Elsevier, 1023-1031.

Wallace, P. R. 1947. The band theory of graphite. *Physical review*, 71 (9): 622-634.

Wang, C., García-Fernández, D., Mas, A. and Esteve-Zarzoso, B. 2015a. Fungal diversity in grape must and wine fermentation assessed by massive sequencing, quantitative PCR and DGGE. *Frontiers in microbiology*, 6: 1156-1163.

Wang, C., Li, Y. and Zhao, Q. 2019. A signal-on electrochemical aptasensor for rapid detection of aflatoxin B1 based on competition with complementary DNA. *Biosensors and Bioelectronics*, 144: 111641-111646.

Wang, C., Qian, J., An, K., Ren, C., Lu, X., Hao, N., Liu, Q., Li, H., Huang, X. and Wang, K. 2018. Fabrication of magnetically assembled aptasensing device for label-free determination of aflatoxin B1 based on EIS. *Biosensors and Bioelectronics*, 108: 69-75.

Wang, H., Zhang, Y., Wang, Y., Ma, H., Du, B. and Wei, Q. 2017a. Facile synthesis of cuprous oxide nanowires decorated graphene oxide nanosheets nanocomposites and its application in label-free electrochemical immunosensor. *Biosensors and Bioelectronics*, 87: 745-751.

Wang, J., Ma, F. and Sun, M. 2017. Graphene, hexagonal boron nitride, and their heterostructures: properties and applications. *RSC Advances*, 7 (27): 16801-16822.

Wang, K.-N., Cao, Q., Liu, L.-Y., Zhao, Z.-J., Liu, W., Zhou, D.-J., Tan, C.-P., Xia, W., Ji, L.-N. and Mao, Z.-W. 2019. Charge-driven tripod somersault on DNA for ratiometric fluorescence imaging of small molecules in the nucleus. *Chemical science*, 10 (43): 10053-10064.

Wang, L., Zhang, T., Li, P., Huang, W., Tang, J., Wang, P., Liu, J., Yuan, Q., Bai, R. and Li, B. 2015b. Use of synchrotron radiation-analytical techniques to reveal chemical origin of silver-nanoparticle cytotoxicity. *ACS nano*, 9 (6): 6532-6547.

Wang, S., Yin, T., Zeng, S., Che, H., Yang, F., Chen, X., Shen, G. and Wu, Z. 2012. A piezoelectric immunosensor using hybrid self-assembled monolayers for detection of Schistosoma japonicum. *PloS one*, 7 (1): e30779-e30785.

Wang, X., Tang, C., Wang, Q., Li, X. and Hao, J. 2017b. Selection of optimal polymerization degree and force field in the molecular dynamics simulation of insulating paper cellulose. *Energies*, 10 (9): 1377-1387.

Wang, X., Yuan, L., Deng, H. and Zhang, Z. 2021. Structural characterization and stability study of green synthesized starch stabilized silver nanoparticles loaded with isoorientin. *Food chemistry*, 338: 127807-127816.

Wang, Y., Zhou, J. and Li, J. 2017. Construction of Plasmonic Nano-Biosensor-Based Devices for Point-of-Care Testing. *Small Methods*, 1 (11): 1700197-1700209.

Waszkowycz, B., Clark, D. E. and Gancia, E. 2011. Outstanding challenges in protein–ligand docking and structure-based virtual screening. *Wiley Interdisciplinary Reviews: Computational Molecular Science*, 1 (2): 229-259.

Weber, M., Collot, P., El Gaddari, H., Tingry, S., Bechelany, M. and Holade, Y. 2018. Enhanced Catalytic Glycerol Oxidation Activity Enabled by Activated-Carbon-Supported Palladium Catalysts Prepared through Atomic Layer Deposition. *ChemElectroChem*, 5 (5): 743-747.

Weber, M., Kim, J.-Y., Lee, J.-H., Kim, J.-H., Iatsunskyi, I., Coy, E., Miele, P., Bechelany, M. and Kim, S. S. 2019a. Highly Efficient Hydrogen Sensors Based on Pd Nanoparticles Supported on Boron Nitride Coated ZnO Nanowires. *Journal of Materials Chemistry A*, 7 (14): 8107-8116.

Weber, M., Koonkaew, B., Balme, S., Utke, I., Picaud, F., Iatsunskyi, I., Coy, E., Miele, P. and Bechelany, M. 2017. Boron nitride nanoporous membranes with high surface charge by atomic layer deposition. *ACS applied materials & interfaces*, 9 (19): 16669-16678.

Weber, M., Tuleushova, N., Zgheib, J., Lamboux, C., Iatsunskyi, I., Coy, E., Flaud, V., Tingry, S., Cornu, D., Miele, P., Bechelany, M. and Holade, Y. 2019d. Enhanced electrocatalytic perfomanve triggered by atomically bridged boron nitride between palladium nanoparticles and caron fibers in gas-diffusion electrodes. *Applied Catalysis B: Environmental* 257: 117917-117926.

Wu, F., Groopman, J. D. and Pestka, J. J. 2014. Public health impacts of foodborne mycotoxins. *Annual review of food science and technology*, 5: 351-372.

Wu, F., Xu, C., Jiang, N., Wang, J. and Ding, C.-F. 2018. Poly (methacrylic acid-co-diethenyl-benzene) monolithic microextraction column and its application to simultaneous enrichment and analysis of mycotoxins. *Talanta*, 178: 1-8.

Wu, S. S., Wei, M., Wei, W., Liu, Y. and Liu, S. 2019. Electrochemical aptasensor for aflatoxin B1 based on smart host-guest recognition of β-cyclodextrin polymer. *Biosensors and Bioelectronics*, 129: 58-63.

Wu, X., Chen, J., Wu, M. and Zhao, J. X. 2015. Aptamers: active targeting ligands for cancer diagnosis and therapy. *Theranostics*, 5 (4): 322-344.

Xing, Y., Ouyang, Q., Wang, S. and Zhou, X. 2017. Simultaneous determination of aflatoxins B 1, B 2, G 1, G 2, and M 1 in dairy products by high-performance liquid chromatography/fluorescence. *New Journal of Chemistry*, 41 (18): 9840-9846.

Xiong, J., Wang, Y., Nennich, T., Li, Y. and Liu, J. 2015. Transfer of dietary aflatoxin B1 to milk aflatoxin M1 and effect of inclusion of adsorbent in the diet of dairy cows. *Journal of Dairy Science*, 98 (4): 2545-2554.

Xiong, J., Xiong, L., Zhou, H., Liu, Y. and Wu, L. 2018. Occurrence of aflatoxin B1 in dairy cow feedstuff and aflatoxin M1 in UHT and pasteurized milk in central China. *Food control*, 92: 386-390.

Xu, C., Shi, X., Ji, A., Shi, L., Zhou, C. and Cui, Y. 2015. Fabrication and characteristics of reduced graphene oxide produced with different green reductants. *PloS one*, 10 (12): e0144842-e0144856.

Xu, J., Han, X., Liu, H. and Hu, Y. 2006. Synthesis and optical properties of silver nanoparticles stabilized by gemini surfactant. *Colloids and Surfaces A: Physicochemical and Engineering Aspects*, 273 (1-3): 179-183.

Xu, W., Xiong, Y., Lai, W., Xu, Y., Li, C. and Xie, M. 2014. A homogeneous immunosensor for AFB1 detection based on FRET between different-sized quantum dots. *Biosensors and Bioelectronics*, 56: 144-150.

Xue, K. S., Tang, L., Sun, G., Wang, S., Hu, X. and Wang, J.-S. 2019a. Mycotoxin exposure is associated with increased risk of esophageal squamous cell carcinoma in Huaian area, China. *BMC cancer*, 19 (1): 1-10.

Xue, Q., Bian, C., Tong, J., Sun, J., Zhang, H. and Xia, S. 2012. FET immunosensor for hemoglobon A1c using a gold nanofilm grown by a seed-mediated technique and covered with mixed sekf-assembled monolayers. *Microchimica Acta*, 176 (1-2): 65-72.

Xue, Z., Zhang, Y., Yu, W., Zhang, J., Wang, J., Wan, F., Kim, Y., Liu, Y. and Kou, X. 2019b. Recent advances in aflatoxin B1 detection based on nanotechnology and nanomaterials-A review. *Analytica chimica acta*, 1069: 1-27.

Yan, B., Li, X., Bai, Z., Song, X., Xiong, D., Zhao, M., Li, D. and Lu, S. 2017. A review of atomic layer deposition providing high performance lithium sulfur batteries. *Journal of Power Sources*, 338: 34-48.

Yang, G., Chen, D., Lv, P., Kong, X., Sun, Y., Wang, Z., Yuan, Z., Liu, H. and Yang, J. 2016. Core-shell Au-Pd nanoparticles as cathode catalysts for microbial fuel cell applications. *Scientific reports*, 6 (1):1-9.

Yang, G. and Park, S.-J. 2019. Conventional and microwave hydrothermal synthesis and application of functional materials: A review. *Materials*, 12 (7): 1177-1194.

Yang, H.-C., Waldman, R. Z., Chen, Z. and Darling, S. B. 2018a. Atomic layer deposition for membrane interface engineering. *Nanoscale*, 10 (44): 20505-20513.

Yang, S., Su, H.-C., Hou, J.-L., Luo, W., Zou, D.-H., Zhu, Q.-Y. and Dai, J. 2017. The effects of transition-metal doping and chromophore anchoring on the photocurrent response of titanium-oxo-clusters. *Dalton Transactions*, 46 (29): 9639-9645.

Yang, X., Li, Q., Li, L., Lin, J., Yang, X., Yu, C., Liu, Z., Fang, Y., Huang, Y. and Tang, C. 2019. CuCo binary metal nanoparticles supported on boron nitride nanofibers as highly efficient catalysts for hydrogen generation from hydrolysis of ammonia borane. *Journal of Power Sources*, 431: 135-143.

Yang, Y., Yan, Q., Liu, Q., Li, Y., Liu, H., Wang, P., Chen, L., Zhang, D., Li, Y. and Dong, Y. 2018b. An ultrasensitive sandwich-type electrochemical immunosensor based on the signal amplification strategy of echinoidea-shaped Au@ Ag-Cu2O nanoparticles for prostate specific antigen detection. *Biosensors and Bioelectronics*, 99: 450-457.

Yao, C., Zhang, Q., Su, Y., Xu, L., Wang, H., Liu, J. and Hou, S. 2019. Palladium nanoparticles encapsulated into hollow N-doped graphene microspheres as electrocatalyst for ethanol oxidation reaction. *ACS Applied Nano Materials*, 2 (4): 1898-1908.

Ye, Y., Ding, S., Ye, Y., Xu, H., Cao, X., Liu, S. and Sun, H. 2015. Enzyme-based sensing of glucose using a glassy carbon electrode modified with a one-pot synthesized nanocomposite consisting of chitosan, reduced graphene oxide and gold nanoparticles. *Microchimica Acta*, 182 (9-10): 1783-1789.

You, H., Mu, Z., Zhao, M., Zhou, J., Yuan, Y. and Bai, L. 2020. Functional fullerene-molybdenum disulfide fabricated electrochemical DNA biosensor for Sul1 detection using enzyme-assisted target recycling and a new signal marker for cascade amplification. *Sensors and Actuators B: Chemical*, 305: 127483-127489.

Yu, J., Mikiashvili, N. and Liang, C. L. 2019. Deoxynivalenol and Ochratoxin A in North Carolina grown organic wheat grains. *Journal of Food Safety*, 39 (6): e12687-e12693.

Yu, L., Zhang, Y., Hu, C., Wu, H., Yang, Y., Huang, C. and Jia, N. 2015. Highly sensitive electrochemical impedance spectroscopy immunosensor for the detection of AFB1 in olive oil. *Food chemistry*, 176: 22-26.

Yu, S., Wang, X., Pang, H., Zhang, R., Song, W., Fu, D., Hayat, T. and Wang, X. 2018. Boron nitride-based materials for the removal of pollutants from aqueous solutions: a review. *Chemical Engineering Journal*, 333: 343-360.

Yuan, Y.-G. and Gurunathan, S. 2017. Combination of graphene oxide–silver nanoparticle nanocomposites and cisplatin enhances apoptosis and autophagy in human cervical cancer cells. *International Journal of Nanomedicine*, 12: 6537-6558.

YURDAKUL, O., SAHINDOKUYUCU, F., YALCIN, H. and Keyvan, E. 2019. Survey of Ochratoxin A in coffee, dried grapes and grape pekmez samples in Burdur, Turkey. *Journal of research in veterinary medicine*, 38 (1): 46-51.

Zaaba, N., Foo, K., Hashim, U., Tan, S., Liu, W.-W. and Voon, C. 2017. Synthesis of graphene oxide using modified hummers method: solvent influence. *Procedia engineering*, 184: 469-477.

Zahid, M., Irshad, A., Shakoor, S., Samiullah, T. R., Shahid, N., Iqbal, A., Tanveer, S., Akram, S. J., Ali, M. A. and Ahmed, S. 2020. Engineered Recombinant NDV-Fusion Protein and Its Polyclonal Antibodies Production. *Pakistan Veterinary Journal*, 40 (4): 499-503.

Zahra, N., Saeed, M. K., Sheikh, A., Kalim, I., Ahmad, S. R. and Jamil, N. 2019. A Review of Mycotoxin Types, Occurrence, Toxicity, Detection Methods and Control. *Biological Sciences-PJSIR*, 62 (3): 206-218.

Zain, M. E. 2011. Impact of mycotoxins on humans and animals. *Journal of Saudi chemical society*, 15 (2): 129-144.

Zareshahrabadi, Z., Bahmyari, R., Nouraei, H., Khodadadi, H., Mehryar, P., Asadian, F. and Zomorodian, K. 2020. Detection of Aflatoxin and Ochratoxin A in Spices by High-Performance Liquid Chromatography. *Journal of Food Quality*, 2020: 8858889. Available: https://www.hindawi.com/journals/jfq/2020/8858889/ (Accessed 11 March 2021).

Zarringhalam, M., Ahmadi-Danesh-Ashtiani, H., Toghraie, D. and Fazaeli, R. 2019. The effects of suspending Copper nanoparticles into Argon base fluid inside a microchannel under boiling flow condition by using of molecular dynamic simulation. *Journal of Molecular Liquids*, 293: 111474-111481.

Zejli, H., Goud, K. Y. and Marty, J. L. 2019. An electrochemical aptasensor based on polythiophene-3-carboxylic acid assisted methylene blue for aflatoxin B1 detection. *Sensing and Bio-Sensing Research*, 25: 100290-100297.

Zeng, H., Zhi, C., Zhang, Z., Wei, X., Wang, X., Guo, W., Bando, Y. and Golberg, D. 2010. "White graphenes": boron nitride nanoribbons via boron nitride nanotube unwrapping. *Nano letters*, 10 (12): 5049-5055.

Zhang, D., Li, W. and Ma, Z. 2018. Improved sandwich-format electrochemical immunosensor based on "smart" SiO2@ polydopamine nanocarrier. *Biosensors and Bioelectronics*, 109: 171-176.

Zhang, G., Liu, Z., Fan, L. and Guo, Y. 2018a. Electrochemical prostate specific antigen aptasensor based on hemin functionalized graphene-conjugated palladium nanocomposites *Microchimica Acta*, 185 (3): 1-8.

Zhang, G., Zhu, C., Huang, Y., Yan, J. and Chen, A. 2018b. A lateral flow strip based aptasensor for detection of ochratoxin A in corn samples. *Molecules*, 23 (2): 291-302.

Zhang, H.-X., Zhang, P., Fu, X.-F., Zhou, Y.-X. and Peng, X.-T. 2020a. Rapid and Sensitive Detection of Aflatoxin B1, B2, G1 and G2 in Vegetable Oils Using Bare Fe3O4 as Magnetic Sorbents Coupled with High-Performance Liquid Chromatography with Fluorescence Detection. *Journal of chromatographic science*, 58 (7): 678-685.

Zhang, H., Yin, C., Jiang, Y. and van der Spoel, D. 2018c. Force field benchmark of amino acids: I. hydration and diffusion in different water models. *Journal of chemical information and modeling*, 58 (5): 1037-1052.

Zhang, J., Xia, Y.-K., Chen, M., Wu, D.-Z., Cai, S.-X., Liu, M.-M., He, W.-H. and Chen, J.-H. 2016a. A fluorescent aptasensor based on DNA-scaffolded silver nanoclusters coupling with Zn (II)-ion signal-enhancement for simultaneous detection of OTA and AFB1. *Sensors and Actuators B: Chemical*, 235: 79-85.

Zhang, J., Xu, X. and Qiang, Y. 2020. Ultrasensitive electrochemical aptasensor for ochratoxin A detection using AgPt bimetallic nanoparticles decorated iron-porphyrinic metal-organic framework for signal amplification. *Sensors and Actuators B: Chemical*, 312: 127964-127971.

Zhang, K., Wong, J. W., Krynitsky, A. J. and Trucksess, M. W. 2016b. Perspective on advancing FDA regulatory monitoring for mycotoxins in foods using liquid chromatography and mass spectrometry. *Journal of AOAC International*, 99 (4): 890-894.

Zhang, S., Zhang, C., Jia, Y., Zhang, X., Dong, Y., Li, X., Liu, Q., Li, Y. and Zhao, Z. 2019a. Sandwich-type electrochemical immunosensor based on Au@ Pt DNRs/NH2-MoSe2 NSs nanocomposite as signal amplifiers for the sensitive detection of alpha-fetoprotein. *Bioelectrochemistry*, 128: 140-147.

Zhang, X., Cheng, Z., Ma, L. and Li, J. 2017a. A study on accumulation of volatile organic compounds during ochratoxin a biosynthesis and characterization of the correlation in Aspergillus carbonarius isolated from grape and dried vine fruit. *Food chemistry*, 227: 55-63.

Zhang, X., Li, C.-R., Wang, W.-C., Xue, J., Huang, Y.-L., Yang, X.-X., Tan, B., Zhou, X.-P., Shao, C. and Ding, S.-J. 2016c. A novel electrochemical immunosensor for highly sensitive detection of aflatoxin B1 in corn using single-walled carbon nanotubes/chitosan. *Food chemistry*, 192: 197-202.

Zhang, X., Li, M., Cheng, Z., Ma, L., Zhao, L. and Li, J. 2019b. A comparison of electronic nose and gas chromatography–mass spectrometry on discrimination and prediction of ochratoxin A content in Aspergillus carbonarius cultured grape-based medium. *Food chemistry*, 297: 124850-124858.

Zhang, X., Wang, Z., Xie, H., Sun, R., Cao, T., Paudyal, N., Fang, W. and Song, H. 2018d. Development of a magnetic nanoparticles-based screen-printed electrodes (MNPs-SPEs) biosensor for the quantification of Ochratoxin A in cereal and feed samples. *Toxins*, 10 (8): 317-328.

Zhang, X., Zeng, T., Hu, C. and Hu, S. 2016d. Studies on fabrication and application of arsenic electrochemical sensors based on titanium dioxide nanoparticle modified gold strip electrodes. *Analytical Methods*, 8 (5): 1162-1169.

Zhang, X., Zhang, X., Song, L., Huang, X., Li, Y., Qiao, M., Liu, W., Zhang, T., Qi, Y. and Wang, W. 2021. An ultrasensitive, homogeneous fluorescence quenching immunoassay integrating separation and detection of aflatoxin M 1 based on magnetic graphene composites. *Microchimica Acta*, 188 (2): 1-11.

Zhang, Y., Wang, L., Shen, X., Wei, X., Huang, X., Liu, Y., Sun, X., Wang, Z., Sun, Y. and Xu, Z. 2017b. Broad-specificity immunoassay for simultaneous detection of ochratoxins A, B, and C in millet and maize. *Journal of agricultural and food chemistry*, 65 (23): 4830-4838.

Zhang, Z., Zhao, Y., Zhao, Z., Huang, G. and Mei, Y. 2020b. Atomic Layer Deposition-Derived Nanomaterials: Oxides, Transition Metal Dichalcogenides, and Metal–Organic Frameworks. *Chemistry of Materials*, 32 (21): 9056-9077.

Zhao, S., Zhao, Z., Yang, Z., Ke, L., Kitipornchai, S. and Yang, J. 2020. Functionally graded graphene reinforced composite structures: A review. *Engineering Structures*, 210: 110339-110354.

Zhdanov, V. P. 2019. Formation of a protein corona around nanoparticles. *Current Opinion in Colloid & Interface Science*, 41: 95-103.

Zheng, K. and Boccaccini, A. R. 2017. Sol-gel processing of bioactive glass nanoparticles: A review. *Advances in colloid and interface science*, 249: 363-373.

Zheng, Y., Matsuo, Y., Nakagawa, H. and Kushiro, M. 2016. Separation of aflatoxin M1 and aflatoxin G1 on reverse-phase HPLC. *JSM Mycotoxins*, 66 (1): 7-8.

Zhou, C., Liu, D., Xu, L., Li, Q., Song, J., Xu, S., Xing, R. and Song, H. 2015. A sensitive label–free amperometric immunosensor for alpha-fetoprotein based on gold nanorods with different aspect ratio. *Scientific reports*, 5 (1): 1-7.

Zhou, R., Liu, M., Liang, X., Su, M. and Li, R. 2019. Clinical features of aflatoxin B1-exposed patients with liver cancer and the molecular mechanism of aflatoxin B1 on liver cancer cells. *Environmental toxicology and pharmacology*, 71: 103225-103231.

Zhu, S. 2019. Validation of the generalized force fields GAFF, CGenFF, OPLS-AA, and PRODRGFF by testing against experimental osmotic coefficient data for small drug-like molecules. *Journal of chemical information and modeling*, 59 (10): 4239-4247.

Zhu, W., Ren, C., Nie, Y. and Xu, Y. 2016. Quantification of ochratoxin A in Chinese liquors by a new solid-phase extraction clean-up combined with HPLC-FLD method. *Food control*, 64: 37-44.

Zhuang, Z., Huang, Y., Yang, Y. and Wang, S. 2016. Identification of AFB1-interacting proteins and interactions between RPSA and AFB1. *Journal of hazardous materials*, 301: 297-303.

Ziegler, T., Seth, M., Krykunov, M. and Autschbach, J. 2008. A revised electronic Hessian for approximate time-dependent density functional theory. *The Journal of chemical physics*, 129 (18): 184114-184123.

Zorlugenç, B., Zorlugenç, F. K., Öztekin, S. and Evliya, I. B. 2008. The influence of gaseous ozone and ozonated water on microbial flora and degradation of aflatoxin B1 in dried figs. *Food and Chemical Toxicology*, 46 (12): 3593-3597.